High Temperature Sodium Sulfate Interactions with Ytterbium Disilicate Environmental Barrier Coating Systems and Silicon Carbide Matrix Composite Materials

---

A
Dissertation
Presented to
the faculty of the School of Engineering and Applied Science
University of Virginia

---

in partial fulfillment
of the requirements for the degree

Doctor of Philosophy

by

Lucas A Herweyer

August 2020

APPROVAL SHEET

This

Dissertation

is submitted in partial fulfillment of the requirements
for the degree of

Doctor of Philosophy

Author: Lucas A Herweyer

This Dissertation has been read and approved by the examing committee:

Advisor: Elizabeth Opila

Advisor:

Committee Member: Rob Kelly, Chair

Committee Member: Bill Soffa

Committee Member: Bob Davis

Committee Member: Prasanna Balachandran

Committee Member: Bryan Harder, NASA GRC

Committee Member:

Accepted for the School of Engineering and Applied Science:

Craig H. Benson, School of Engineering and Applied Science

August 2020

Acknowledgements

I would like to acknowledge the Office of Naval Research for funding this research and Rolls Royce North America for providing material described in the last two chapters of my thesis. My first two thesis chapters were funded under "Hot Corrosion of SiC-based Composites" ONR award no. N00014-11-1-0607, while my last two thesis chapters were funded under "Hot-Corrosion of Rare Earth Silicate Environmental Barrier Coatings" ONR award no. N00014-18-1-2628. Without this funding, I would not have been able to obtain my doctoral degree from the University of Virginia. This entire experience gave me an invaluable learning experience on how to apply basic science and engineering to real-world problems. I would also like to thank my group members, current and past for helping me whilst completing my degree. Although not written in this dissertation, everything that I learned, observed, and discussed with everyone over the years was equally as valuable as the things written in this dissertation. Lastly, I would like to the thank my advisor, Dr. Beth Opila, the University of Virginia's Materials Science and Engineering department, and the University of Virginia for giving me the opportunity for pursuing my doctoral degree. The lessons learned during my tenure as a Ph.D. student in the Materials Science and Engineering program at the University of Virginia has given me invaluable insights, a world-class education, and the tools in becoming apart of this country's next great scientific and engineering endeavors.

Remember, "*Go Deep*."

Abstract

It has been known for decades that turbines engines operating in marine environments form molten Na_2SO_4 species due to an *in-situ* reaction between ingested NaCl species and S impurities in the fuel. This liquid species leads to a form of deposit-based degradation of Ni-base superalloy hot-section components known as hot corrosion. Currently, SiC ceramic matrix composites (CMCs) have entered service in the hot-section of GE Aviation's LEAP engines as non-loading bearing components, with future implementation to replace load-bearing Ni-base superalloy components a current research and development focus. SiC CMC turbine engine components have many attractive properties which include a slow-forming SiO_2 thermally grown oxide (TGO), excellent high temperature capability, and lower density relative to their Ni-based superalloy counterparts. Their SiC fiber reinforcement phase/BN matrix fiber interphase/SiC matrix allows for increased toughness relative to monolithic SiC. An environmental barrier coating system is required to prevent rapid recession to the underlying SiC CMC component due to reaction with steam present as a product of combustion. A $Yb_2Si_2O_7$ topcoat + Si bond coat bi-layer is a highly studied EBC system due to many of its attractive properties. However, many aspects of the performance of the SiC CMCs and $Yb_2Si_2O_7$ + Si bond coat EBC systems are unaddressed, including its reaction with Na_2SO_4 deposits. This dissertation investigated; (i) the high-temperature interaction of Na_2SO_4 deposits with Hi Nicalon, Hi Nicalon S, Sylramic, and Sylramic-iBN SiC fibers relevant for application in SiC CMCs; (ii) Na_2SO_4 reaction with the BN interphase material and their on SiC oxidation rates, surface degradation, and reaction layer crystallization; (iii) the interaction and penetration behavior of Na_2SO_4 deposits with state-of-the-art air plasma sprayed (APS) $Yb_2Si_2O_7$ topcoat-Si bond coat EBC systems on SiC CMC substrates; and (iv) the influence of Na_2SO_4 on Si bond coat oxidation kinetics and thermally grown oxide (TGO) crystallization behavior. Numerous characterization techniques revealed that exposure of SiC CMC and $Yb_2Si_2O_7$ topcoat and Si bond coat EBC systems to Na_2SO_4 results in a range of degradation mechanisms including rapid SiC fiber corrosion, accelerated SiC corrosion due to formation of low-melting sodium borosilicate phases resulting from reaction with the BN matrix fiber interphase, granulation of $Yb_2Si_2O_7$ EBC topcoats and reaction to form Yb_2SiO_5 and Na silicates, and increased TGO growth kinetics and crystallization.

Table of Contents

List of Figures

List of Tables

1 | Introduction

Components in the hot-section of current turbine engines are comprised of nickel (Ni) base superalloys. The maximum temperature capability of turbine engine materials has increased over the past several decades through careful materials engineering to increase Ni-base alloy high temperature strength, oxidation resistance and phase stability, through the usage of internal air cooling channels and application of thermally insulating ceramic coatings known as thermal barrier coatings (TBCs).[1] These increases in maximum temperature capability have allowed for higher engine efficiencies and fuel savings. However, increases in maximum temperature capability of turbine engines components can no longer be achieved with current material systems. Instead, silicon carbide (SiC) ceramic matrix composites (CMCs) are being developed to replace Ni-base alloy hot section components for usage in next-generation turbine engines allowing for further maximum temperature capability. Some SiC CMCs entered service into GE Aviation's LEAP engines in 2016 as non-load bearing components.[2, 3] An image of a manufactured SiC CMC component for usage in a turbine engine can be seen in Figure 1.1. However, further research and development is required for the full replacement of Ni-base superalloy components with SiC CMCs.

1.1 Architecture and Chemistry of SiC CMCs

Monolithic SiC possesses many properties that make its usage in turbine engines desirable, including low density ($\rho = 3.21$ g/cm^3) and ability to form a protective thermally grown oxide. However, due to the brittle fracture behavior of monolithic SiC, a reinforcing SiC fiber phase is used to provide damage tolerance by hindering crack propagation through the composite material. This damage tolerance is achieved through a weakly bonded SiC fiber/SiC matrix (SiC_f/SiC_m) boron nitride (BN) interphase fiber

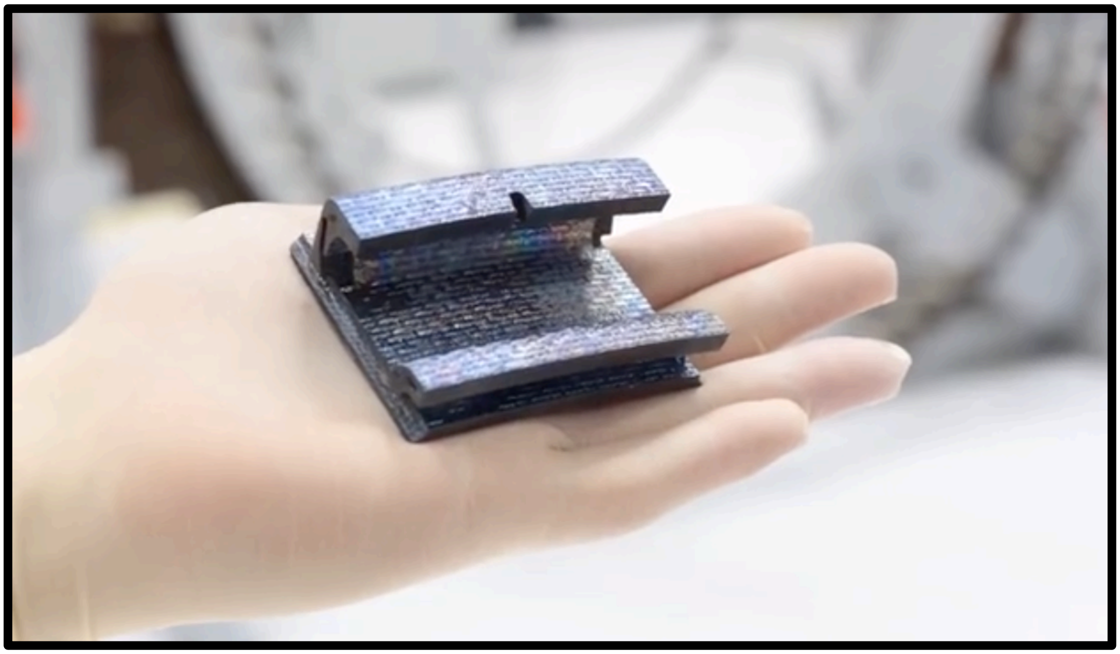

Figure 1.1. Image showing a SiC CMC component manufactured for usage in turbine engines. Image courtesy of Instagram account @rollsroycegroup

coating. BN has a hexagonal, layered crystal structure, allowing for easy fiber debonding from the matrix.

SiC CMC processing begins with weaving tows of hundreds (500-800) of SiC fibers together into SiC preforms. These fiber preforms vary significantly in structure as multiple fiber orientation and weaving strategies are employed, ranging from directionally aligned, stacked one-dimensional (1D) layers, two-dimensional (2D) mats, and three-dimensional (3D) weaves whose orientation vary layer-to-layer.[4–6] BN fiber coatings are gas-phase deposited ~1 μm or less in thickness onto the SiC fiber preforms. An additional SiC layer intended to protect the BN fiber coating is gas-phase deposited, followed by the processing of the SiC matrix using chemical vapor infiltration (CVI), liquid infiltration in-situ reaction techniques such as polymer infiltration pyroloysis (PIP) or Si melt-infiltration (MI).[7–9] Several SiC fibers have been developed for application as the fiber-reinforcing phase in CMCs over the past several decades, with Hi Nicalon and Hi Nicalon S as some of the most researched and developed.[10–14] SiC fibers are processed from polymer pre-cursor materials, heat-treated to bake out organics, and spooled into bundles of hundreds of fibers resulting in fine-diameter (~10 μm) strong, creep-resistant fibers with desired C:Si stoichiometric ratios near one.

1.2 High Temperature Oxidation of SiC

Turbine engines create extreme environments, using high temperature and high-pressure gases flowing at high velocities to generate thrust. Due to the ingestion of air and particulate matter (i.e. dirt, salt fly-ash), the solid-gas and solid-liquid reactions of airborne species are of concern for SiC CMC component durability. It is well known that SiC oxidizes at high temperature in dry $O_2(g)$ environments to form SiO_2 and CO(g), seen in Equation (1.1)[15–17]:

$$SiC + 3/2\ O_2(g) \rightarrow SiO_2 + CO(g) \tag{1.1}$$

This reaction is well studied, and closely follows the Deal-Grove oxidation model used to predict the formation of SiO_2 on Si.[18] The oxidation of Si contrasts with SiC, as no gaseous reaction by-products are released, seen in Equation (1.2):

$$Si + O_2(g) \rightarrow SiO_2 \tag{1.2}$$

This slow-growing, thermally grown SiO_2 layer on SiC acts as a self-protective diffusion barrier, limiting oxidation to the underlying Si or SiC substrate. The phase of this layer and the presence of low-melting eutectics from oxide additions from the surrounding environment are important to the effectiveness of thermally grown SiO_2 as diffusion barrier.

1.2.1 SiO_2: Polymorphism and Structure

SiO_2 is a highly studied material due to its immense technological importance. Pure SiO_2 has three equilibrium crystalline phases at atmospheric pressure, namely quartz, tridymite and cristobalite. Quartz is the room temperature stable phase, while tridymite and cristobalite are stable at high temperature. A commonly accepted polymorphic transition for these SiO_2 phases occur at 867°C for the quartz → tridymite transition, 1460°C for the tridymite → cristobalite transition, while melting of SiO_2 occurs at 1723°C.[19–22] Currently, it is still debated if tridymite is an impurity stabilized-phase (i.e. Na_2O, B_2O_3) as cristobalite is known to exist in the tridymite phase field despite tridymite being the stable SiO_2 phase.[23, 24] Because of this controversy over tridymite being pure SiO_2 phase, it is believed that only a single polymorphic phase transition at 1050°C (quartz → cristobalite) occurs in the pure SiO_2 system. Quartz, tridymite and cristobalite each undergo a displacive phase transformation from their equilibrium, high temperature phase (β) to a low-temperatures phase (α), however, tridymite and cristobalite are the most relevant SiO_2 phases for SiC CMC components due to their phase stability at temperatures relevant for turbine engine service. Cristobalite transforms from β-to-α between 200-300°C, as sample purity, synthesis temperature, and number of inversion cycles are known to influence the inversion temperature.[22, 25–28] This phase transformation causes cracking due to a ~5% density increase (2.20 to 2.32 g/cm^3) upon cooling. This phase-transformation induced cracking is known to limit the usage of high temperature high-purity SiO_2 glassware at high temperature.[29] Tridymite has multiple low temperature inversions upon cooling, all of which are hardly studied.[24, 30–32]

1.2.2 Thermally Grown SiO_2: Growth Kinetics and Structure

Due to the importance of Si and SiC in high temperature applications, many studies have been devoted to their high temperature oxidation behavior in both dry and wet $O_2(g)$. Both materials oxidize to form a SiO_2 layer (Equations (1.1) and (1.2)) growth kinetics are defined by linear-parabolic oxidation kinetics. For shorter time periods or at low temperatures, the growth can be described by Equation (1.3):[18, 33]

$$x = k_l t \tag{1.3}$$

where x is the 1-D SiO_2 thickness, k_l the linear rate constant, and t time. The SiO_2 growth kinetics for long times and at high temperatures can be described by the parabolic equation below in Equation (1.4):

$$x^2 = k_p t \tag{1.4}$$

where k_p is the parabolic rate constant. The linear growth of SiO_2 is limited by the oxidation reaction kinetics, while SiO_2 formation during parabolic oxidation is limited by the transport of oxidizing species (i.e. O_2, H_2O) through the SiO_2 layer. Most of the oxidation studies on Si have been performed at temperatures up to 1200°C for times ranging from several minutes to hours, while SiC oxidation studies have been performed for temperatures up to 1500°C for much longer times ranging from several days to weeks.[16, 18, 34–36] Oxidation studies of both bulk SiC (i.e. sintered, CVD) and fibers have been performed. [37–41] Their thermally grown SiO_2 oxides initially form as amorphous scales, but crystallize into β-cristobalite after prolonged exposure.[17, 42] β-cristobalite nucleates at the surface of the prior grown amorphous TGO as spherulitic crystals, which then grow radially outward and into the amorphous SiO_2 matrix.[43] The β-cristobalite spherulites subsequently crack upon cooling through the β-to-α cristobalite inversion temperature. The presence of impurity oxides leads to the formation of a globular microstructure, which has been reported to crystallize into tridymite.[44–46]

SiC oxidation rates are increased in contaminated and steam-containing environments relative to impurity-free, dry O_2(g) environments. Borosilicate reaction layers, including those formed by the oxidation of BN fiber coatings in CMCs, increase the oxidation rates of SiC. [47–49] The oxidation of BN can be expressed in the chemical reaction seen below in Equation (1.5):[45]

$$2\ BN + 3/2\ O_2(g) \rightarrow B_2O_3 + N_2(g) \tag{1.5}$$

The mixture of thermally grown SiO_2 and B_2O_3 leads to the formation of borosilicate glass, seen in Equation (1.6):

$$SiO_2 + xB_2O_3 \rightarrow SiO_2{\bullet}xB_2O_3 \tag{1.6}$$

where x denotes molar composition of B_2O_3. The formation of a borosilicate glass can easily be explained by examination of the B_2O_3-SiO_2 binary phase diagram seen in Figure 1.2. Additionally, it should be noted that B_2O_3 is a highly hygroscopic material that forms gaseous boron hydroxide species during high temperature exposure due to reaction with water even in environments with water levels as low as ~10 ppm H_2O.[49] Due to this volatilization, the B_2O_3 content of thermally grown borosilicate layers decreases over time.

The presence of alkali contaminants such as Na_2O and K_2O have also been found to increase SiC oxidation rates.[34, 51] These oxides exist as testing impurities in high temperature furnaces, but are also known environmental impurities during turbine engine service. Just like borosilicate formation, exposure of SiO_2 in the presence of Na_2O and K_2O leads to the formation of sodium and potassium silicates, seen below in Equations (1.7) and (1.8)[34, 51, 52]

$$SiO_2 + xNa_2O \rightarrow SiO_2{\bullet}xNa_2O \tag{1.7}$$

$$SiO_2 + xK_2O \rightarrow SiO_2{\bullet}xNa_2O \tag{1.8}$$

where x denotes molar Na_2O and K_2O composition. The formation of sodium and potassium silicates can easily be explained by examination of the Na_2O-SiO_2 and K_2O-SiO_2 binary phase diagrams seen in Figures 1.3 and 1.4. The addition of B_2O_3, Na_2O, and K_2O to SiO_2 leads to the formation of low-melting silicates, which in turn allow for rapid oxygen transport through these highly permeable surface silicate layers, increasing the oxidation rates of SiC. Oxygen diffusivity through crystalline SiO_2 is 6-9 orders of magnitude slower than through liquid sodium silicate.[55] The B_2O_3-SiO_2 system has a single low-melting eutectic temperature at~420°C, while multiple low-melting eutectic temperatures ranging from ~750°C to 1000°C exist on the SiO_2 rich side of the Na_2O-SiO_2 and K_2O-SiO_2 and phase diagrams. These temperatures are all within turbine engine operating range, and allow for rapid SiC CMC consumption due to the formation of silicate reaction layer.

1.2.3 SiO_2 Steam Volatilization

The interaction of SiC and steam at high temperature is important, as steam is a combustion by-product of ingested air and jet fuel. Steam oxidation of SiC is faster than in dry O_2(g) and follows paralinear oxidation kinetics similar to the oxidation of Cr- containing alloys.[58–61] Upon exposure to H_2O(g), SiC simultaneously reacts to form SiO_2 and the gaseous silicon hydroxide species $Si(OH)_4$.[62] This two-step chemical reaction can be seen below in Equations (1.9) and (1.10):

$$SiC + 3\ H_2O\ (g) \rightarrow SiO_2 + 3\ H_2(g) + CO(g) \tag{1.9}$$

$$SiO_2 + 2\ H_2O\ (g) \rightarrow Si(OH)_4(g) \tag{1.10}$$

The volatilization of SiO_2 leads to unacceptably high SiC recession, with predicted rates of ~1 μm/h at temperatures above 1200°C.[63, 64] Over thousands of hours, these rates translate into millimeters of SiC CMC component recession, rendering component lifetimes too short for service in

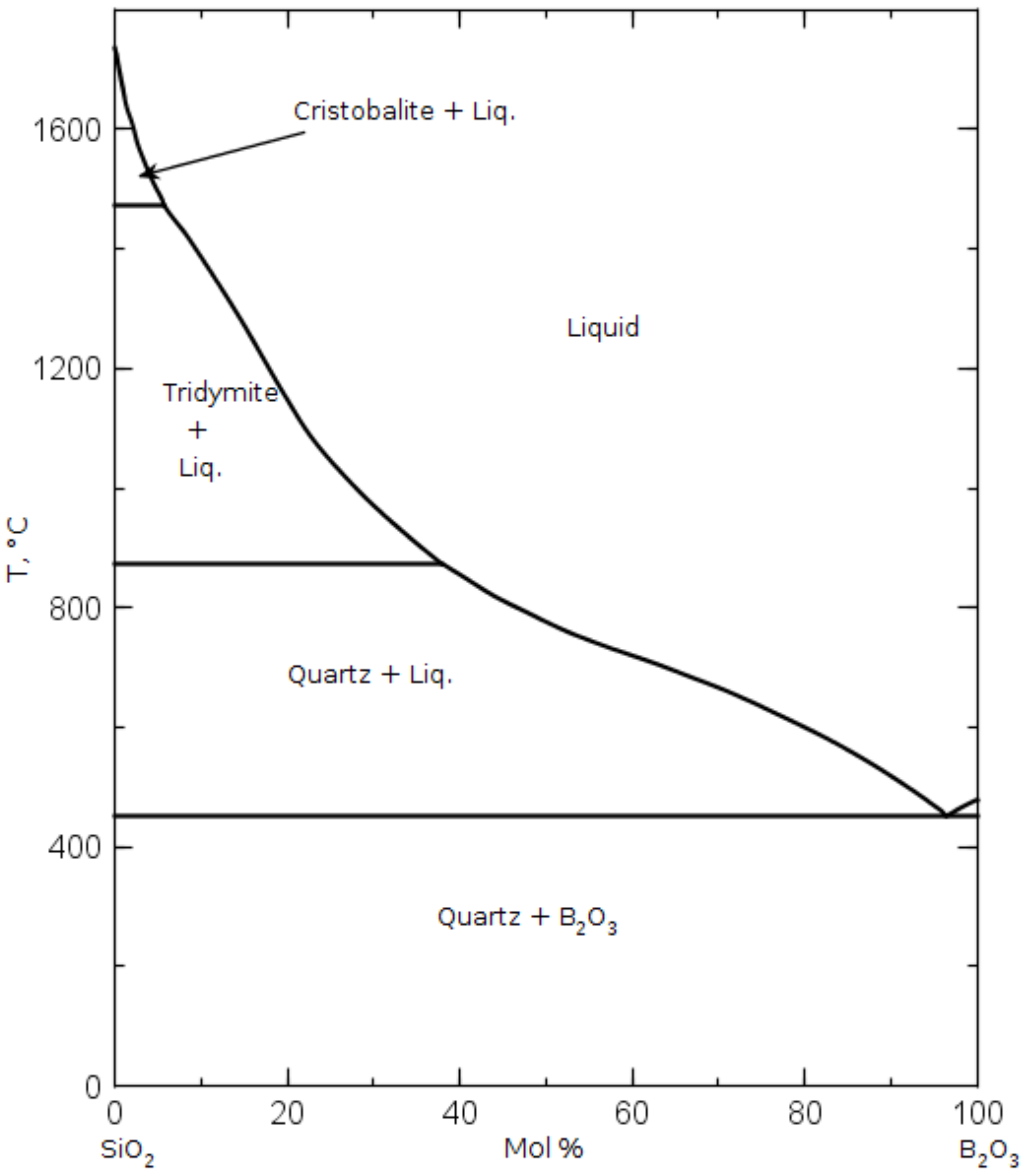

Figure 1.2. The experimental B_2O_3-SiO_2 binary phase diagram.[53, 54]

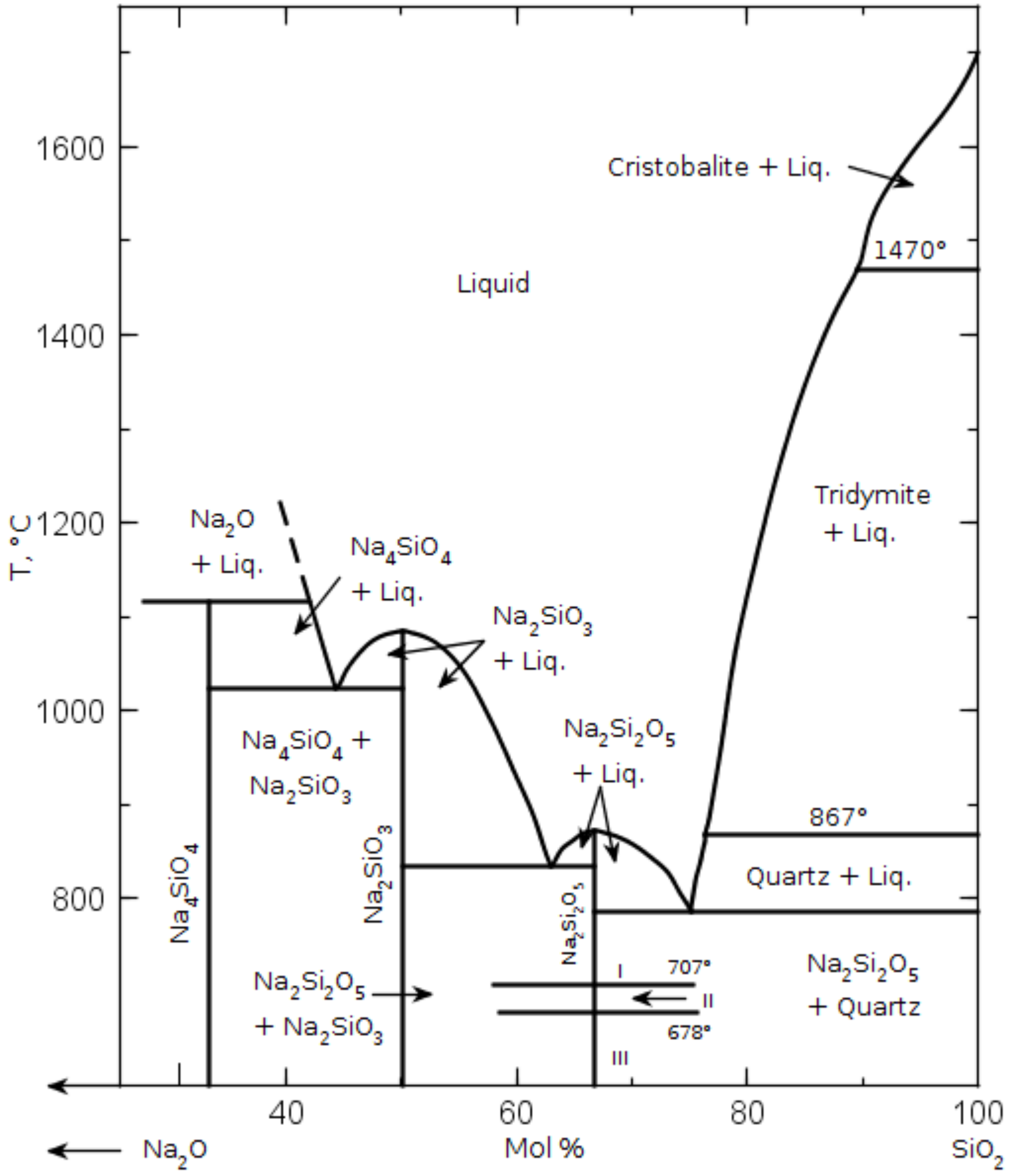

Figure 1.3. The SiO_2 rich portion of the experimental Na_2O-SiO_2 binary phase diagram.[56]

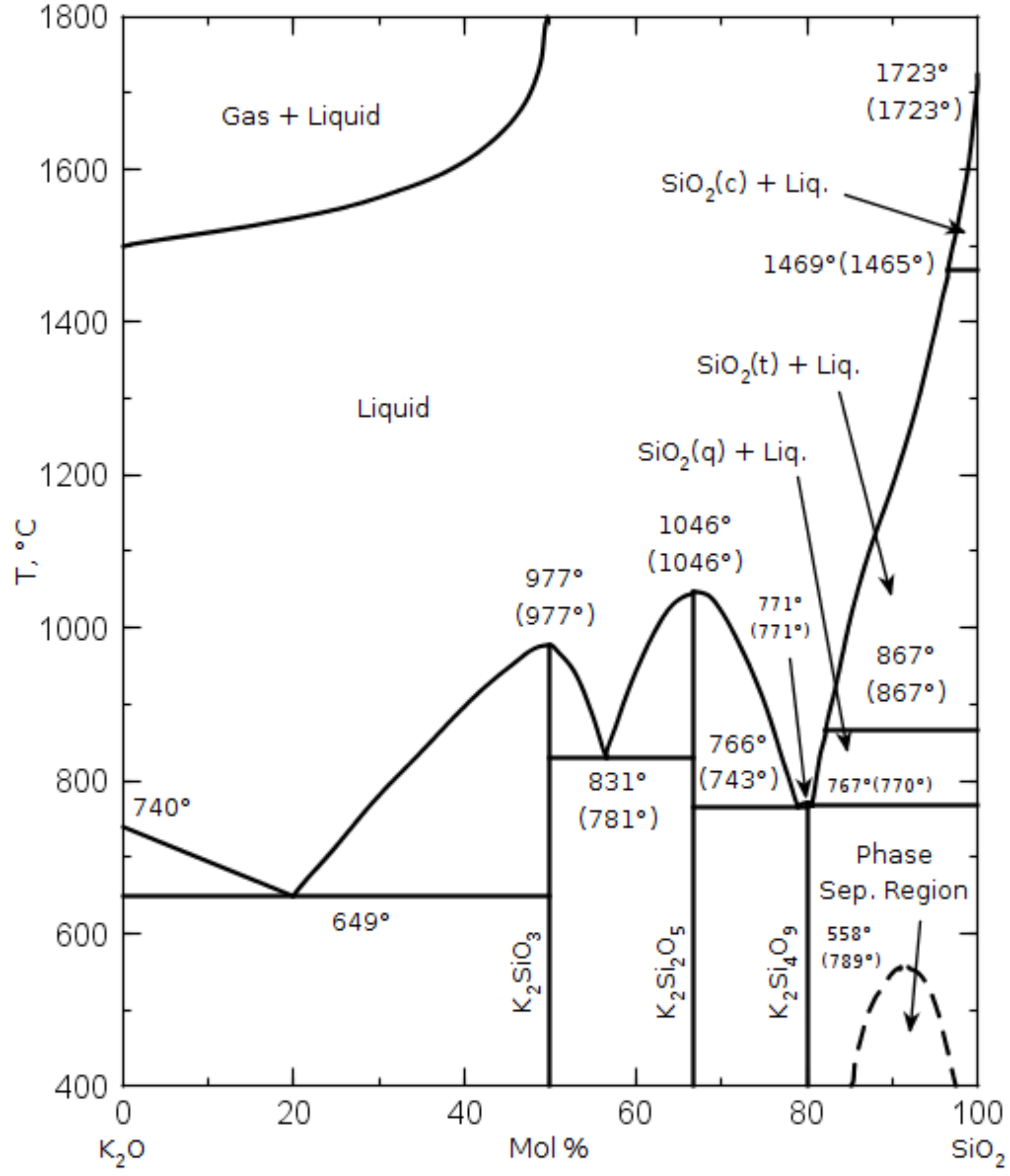

Figure 1.4. The experimental K_2O-SiO_2 binary phase diagram.[57]

turbine engines. Thus, steam along with silicate formation due to alkali contaminants and B_2O_3 from SiC CMC oxidation, render thermally grown SiO_2 of insufficient stability to protect SiC CMCs from environmental degradation during service.

1.3 Environmental Barrier Coatings (EBCs)

Further protection of SiC CMC components from degrading chemical reactions has necessitated the development of EBCs.[65] These coatings must be a (i) protective reaction barrier from steam volatilization (ii) a permeation barrier from inward diffusing oxidizing species (i.e. O_2, H_2O), and also (iii) must be adherent to CMC components. Over the past several decades, EBC research and development has focused on mullite ($2Al_2O_3 \bullet 3SiO_2$), mullite + yttria-stabilized zirconia (YSZ) multilayers, BSAS ($BaO \bullet SrO \bullet Al_2O_3 \bullet SiO_2$), BSAS + mullite multilayers, rare earth monosilicates (RE_2SiO_5), and disilicates ($RE_2Si_2O_7$).[66–69] Currently, ytterbium disilicate ($Yb_2Si_2O_7$) is one of the most researched and developed EBCs as it satisfies many of the above-mentioned criteria of a successful EBC system. $Yb_2Si_2O_7$ is a line compound that melts congruently at 1850°C as seen in the Yb_2O_3-SiO_2 phase diagram in Figure 1.5. Furthermore, a Si bond coat between SiC CMC components and the $Yb_2Si_2O_7$ EBC or topcoat layer has been utilized to prevent the formation of interfacial gas-phase induced porosity (Equations (1.1) and (1.7)) while also alleviating thermal stresses. This layer is sacrificially oxidized instead of the underlying SiC CMC component, leading to the build-up of a buried SiO_2 thermally grown oxide (TGO) between the Si bond coat and EBC topcoat. Due to many attractive features the $Yb_2Si_2O_7$ topcoat + Si bond coat EBC system, the system is state-of-the art and will be the focus of a portion of this dissertation.[65]

1.3.1 Air Plasma Spray and Coating Microstructure

Air plasma spray (APS) is a processing technique used to deposit EBCs such as $Yb_2Si_2O_7$ onto SiC CMC components due to its low cost and rapid application rates.[71] The coating is formed by injecting powder into a high-velocity plasma whose core temperature is 5,000°C, which is well above the powdered material melting temperature. The plasma is directed onto substrates allowing for deposition of the semi-molten powders. The deposited coatings have a "splat-microstructure" filled with microcracking, porosity, non-equilibrium crystalline and amorphous phase content and trapped gases. As result of the porosity and non-equilibrium crystalline + amorphous phase content, a stabilization anneal is employed to heal cracks, restore stoichiometry, and also to promote crystallization of equilibrium phases. It has been reported in literature that annealed APS $Yb_2Si_2O_7$ EBCs post-annealing can have up to 15 vol.% porosity and up to 10 vol.% Yb_2SiO_5 balance $Yb_2Si_2O_7$.[72] Furthermore, volatilization of SiO(g) has been shown to occur during APS deposition of $Yb_2Si_2O_7$ coatings, leaving behind a SiO_2-depleted coating comprised of both Yb_2SiO_5 and $Yb_2Si_2O_7$.[73, 74]

1.4 High Temperature Behavior of SiC CMC + EBC Systems

There are many known high-temperature behavioral phenomena in EBC systems that are of concern to lifetime requirements upwards of 10,000h (~1 year) that include but are not limited to (i) Si bond coat degradation (ii) reaction between coating layers and (iii) deposit-induced degradation to the topcoat. Other degradation phenomena such as steam volatilization of the topcoat, spallation due to CTE mismatch between coating system layers, and phase stability within layers are also important, but are not studied in this dissertation. The application of the Si bond coat limits SiC CMC oxidation as inward permeation of diffusing oxidizing species (i.e. O_2, H_2O) through EBC topcoats first oxidizes the Si bond coat (see Equation (1.2)). Only limited information on transport through the topcoat exists, however the formation of a buried SiO_2 layer formed between the topcoat and bondcoat has been reported. Only two studies have reported oxidation kinetics of Si bond coats in EBC systems, both of which were performed on $Yb_2Si_2O_7$ topcoat-Si bond coat EBC systems in steam containing environments at 1316°C.[75, 76] Both of these works reported TGO thicknesses less than that predicted by the Deal-

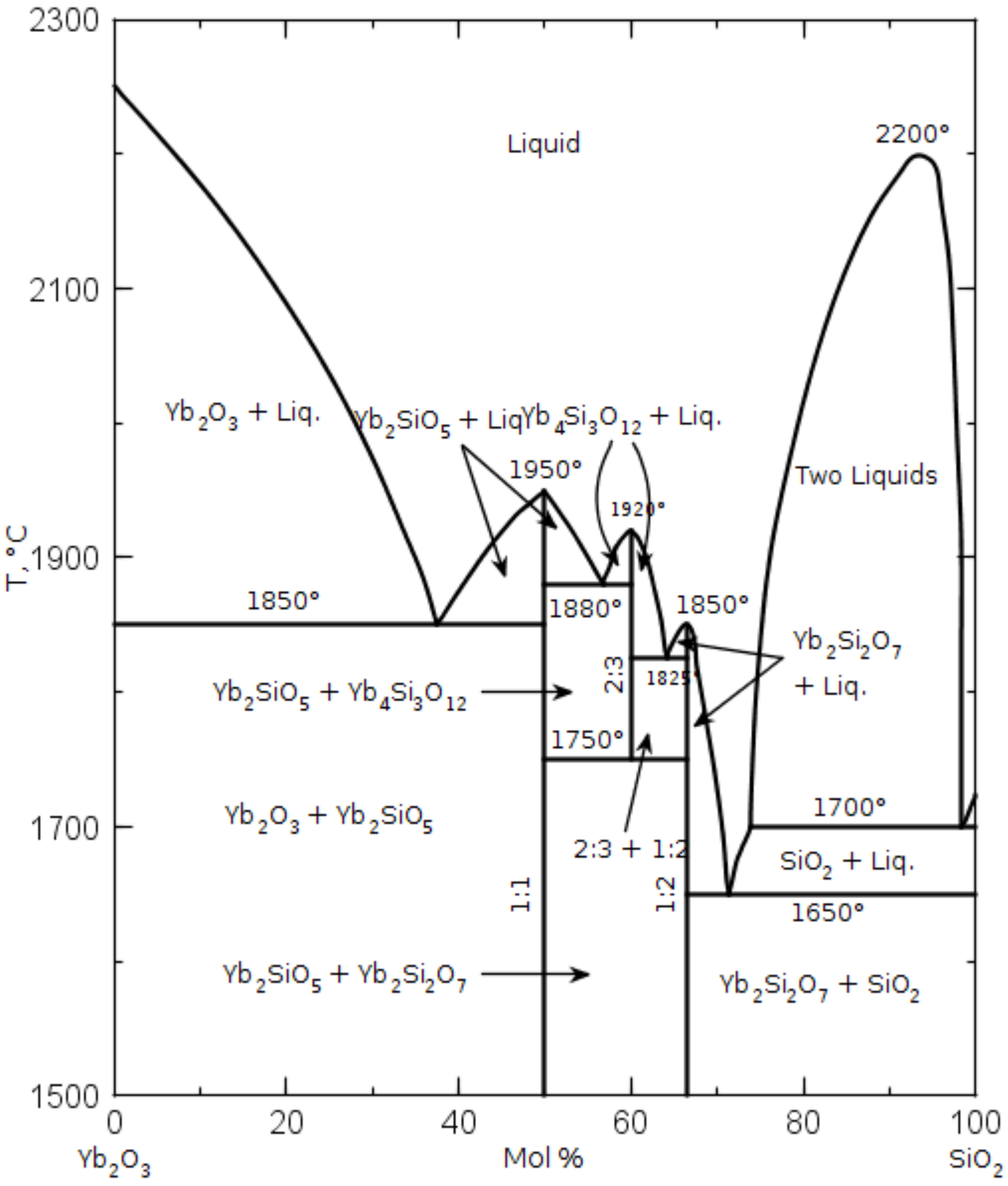

Figure 1.5. The experimental binary Yb_2O_3-SiO_2 phase diagram.[70]

Grove model, however the TGO thickness reported by Lee was an order of magnitude thicker than that reported by Richards despite having a $Yb_2Si_2O_7$ topcoat nearly twice as thick. Additionally, it has been identified that the SiO_2 TGO crystallizes into β-cristobalite, which cracks upon cooling through the β-to-α cristobalite inversion temperature (T = 200-300°C). It is believed large tensile forces within the TGO, estimated to be several GPa, lead to vertical cracking through the TGO layer causing enhanced Si bond coat oxidation and possible EBC spallation.[75, 77] However, crystallization kinetics of the TGO have not been studied.

Thermodynamic instability can cause reaction between layers in an EBC system. Reactions between Yb_2SiO_5 + mullite layers led to the formation of a solid unidentified Yb_2O_3-SiO_2-Al_2O_3 compound, while reaction between the SiO_2 TGO with BSAS and Y_2SiO_5 topcoats has also been observed. The reaction products in the Yb_2SiO_5 + Mullite and Y_2SiO_5 + SiC system were benign due to the formation of high melting temperature Yb_2O_3-SiO_2-Al_2O_3 and $Y_2Si_2O_7$ phases. The reaction between SiO_2 and BSAS was degrading due to the formation of a liquid reaction product, and led to the development of other EBC systems. There has been no assessment of any reaction between $Yb_2Si_2O_7$ topcoat + Si bond coat layers over time.[67, 77–79]

Deposit based degradation to EBC systems from siliceous debris known as CMAS (CaO-MgO-Al_2O_3-SiO_2) and Na_2SO_4 are expected to occur. CMAS studies investigating the interaction with EBC systems including $Yb_2Si_2O_7$ are numerous, however only limited studies have reported the high temperature interaction between Na_2SO_4 deposits and EBC topcoats.[80–84] CMAS interaction occurs above the melting temperature of CMAS which is generally no less than 1200°C depending upon composition. No studies have investigated the interaction of $Yb_2Si_2O_7$ topcoats with Na_2SO_4 (T_m = 884°C) despite being a known high-temperature reactant in metallics based systems.

1.4 Na_2SO_4 Deposit-Induced Hot Corrosion

Turbine engines operating in a marine environment ingest NaCl which can react with sulfur (S) impurities in the fuel or environment, leading to the formation of liquid sodium sulfate (Na_2SO_4), as seen below in in Equation (1.11)[85]:

$$2NaCl + SO_3\,(g) + H_2O(g) \rightarrow Na_2SO_4(l) + 2HCl(g) \qquad (1.11)$$

This *in-situ* formed Na_2SO_4 has been known for decades to deposit onto metallic components in the hot-section of turbine engines, leading to a form of severe environmental degradation known as hot-corrosion.[86, 87] Hot-corrosion causes accelerated oxidation and pitting of metallic components and is another concern for long-term operation of turbine engines. Liquid Na_2SO_4 can only form between the melting temperature of Na_2SO_4 (T_m = 884°C) and the dewpoint of Na_2SO_4 which is a function of P_{SO_3}, ingested Na levels, and the total gas pressure inside of the turbine engine. A plot generated using the chemical software program FACTSAGE seen in Figure 1.6 shows the dewpoint of Na_2SO_4 as a function of temperature and pressure in dry O_2 with a molar O_2/Na_2SO_4 ratio of 10^5. This plot demonstrates that Na_2SO_4 will remain as a liquid phase to high temperatures at the high pressures representative of a turbine environment.Na_2SO_4 deposit-based degradation is expected to occur on EBC coated SiC CMC components, especially due to the higher operating pressures used in next-generation turbine engines. However, Na_2SO_4 deposit-based hot corrosion of state-of-the art $Yb_2Si_2O_7$ topcoat-Si bond EBC + SiC CMC systems, and their constituent phases is not well-studied.

1.6. Hot Corrosion of SiC CMCs and Constituent Phases

Usage of EBCs will protect SiC CMCs from Na_2SO_4 deposit-based attack, however if uncoated SiC CMCs or spalled coating regions are exposed to Na_2SO_4, attack could occur. Very few studies have investigated the interaction of Na_2SO_4 with SiC CMCs, as most studies have investigated the

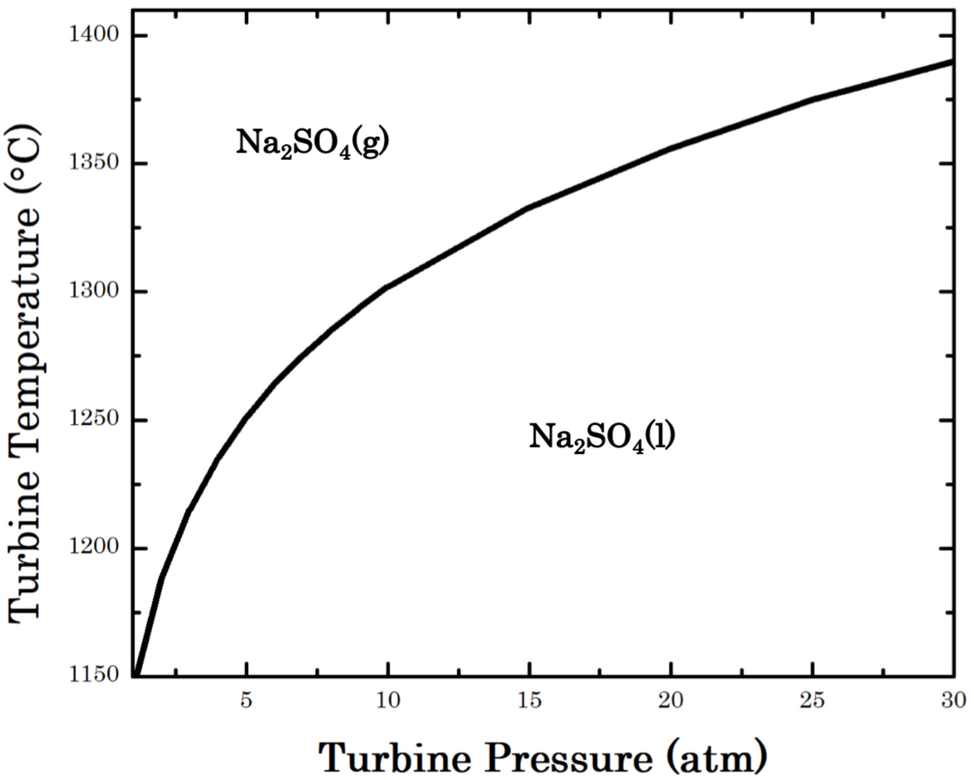

Figure 1.6. Plot showing the dewpoint of Na_2SO_4 calculated using the chemical software program FACTSAGE assuming a molar O_2/Na_2SO_4 ratio of 10^5.

interaction of Na_2SO_4 with commercially sintered α-SiC.[88] Na_2SO_4 dissolves the thermally grown oxide formed during oxidation of SiC, leading to enhanced oxidation kinetics whilst severely corroding the SiC substrate. Investigations using single salt loadings found the formation of a liquid sodium silicate layer consistent with the Na_2O-SiO_2 phase diagram (Figure 1.3). This silicate layer allows for rapid O_2 transport through the layer, leading to rapid SiC oxidation. Ten-to-twenty times more SiO_2 was produced after exposure to ~2.5 mg/cm^2 of Na_2SO_4 for 48h at 1000°C than in similar testing conditions without Na_2SO_4.[53] Time-dependent testing at 1000°C revealed SiC was rapidly consumed during the first few hours of exposure but exhibited a kinetic plateau at longer exposure times.[45, 52] This kinetic plateau is attributed to porosity removal from the reaction layer, formation of a continuous SiO_2 crystalline tridymite layer, and consumption or volatilization of Na_2SO_4. Additionally, the formation of ~50 µm deep pits into SiC surfaces were found to reduce strength of SiC. However, there currently only has been a single study reporting the effect of BN on SiC oxidation rates, while no studies on the hot corrosion of SiC fibers have been performed.[46]

1.7 Na_2SO_4 Interaction with $Yb_2Si_2O_7$-Si EBC + SiC CMC Systems

The products that form from the reaction of Na_2SO_4 and rare earth silicate EBCs will be dictated by phase equilibrium of the deposit and coating system. However, very few studies have investigated the interaction of Na_2SO_4 with $Yb_2Si_2O_7$ and no phase equilibrium diagram exists for the Yb_2O_3-SiO_2-Na_2O system. Only equilibria in the Yb_2O_3-SiO_2 and Na_2O-SiO_2 systems have been investigated (Figures 1.3 and 1.5). Synthesis of ternary Yb_2O_3-SiO_2-Na_2O compounds including $NaYb_9Si_6O_{26}$, $Na_3YbSi_2O_7$, Na_2YbSiO_4 and $NaYbSiO_4$ have been reported, however no other works have been able to verify their existence.[89–91] No peer-reviewed literature studies have investigated the interaction of Na_2SO_4 with $Yb_2Si_2O_7$ topcoat-Si bond coat EBC systems on SiC. Therefore it is unknown what phases form and how quickly Na_2SO_4 or other Na-containing species will penetrate $Yb_2Si_2O_7$ topcoats. A single patent on the hot corrosion resistance of $Yb_2Si_2O_7$ was filed by General Electric, however no details were reported on phases formed or Na transport behavior through the topcoat.[92] Studies on the interaction of Na_2SO_4 with other EBC materials, including mullite and $Y_2Si_2O_7$, led to formation of ternary Y_2O_3-SiO_2-Na_2O and Al_2O_3-SiO_2-Na_2O crystalline reaction products at the EBC surface.[93–95] It was suspected by Jacobson that at longer exposure times, Na diffusion through the mullite topcoat could cause durability issues due to reaction with underlying layers.

1.8 Dissertation Objectives

A comprehensive understanding on the behavior of Na_2SO_4 deposits with SiC CMCs components, their constituent phases, and state-of-the-art $Yb_2Si_2O_7$ topcoat-Si bond coat EBC systems is lacking. This dissertation explores the interaction of Na_2SO_4 with SiC fibers relevant for SiC CMC applications, BN fiber interphase coatings, and state-of-the-art $Yb_2Si_2O_7$ topcoat-Si bond coat EBC systems. Throughout this dissertation, emphasis is placed on phase formation, structure of reaction products, and reaction mechanisms and rates. *Chapter 2* of this dissertation titled " Na_2SO_4 Deposit Induced Corrosion of SiC Fibers Relevant for SiC CMCs" investigates the interaction between Na_2SO_4 deposits and SiC fibers relevant for application in SiC CMCs. The questions this chapter addresses are:

(1) Are some commercially available SiC fibers more resistant to Na_2SO_4 deposit based attack than others, and if so, why?
(2) What is the microstructure of SiC fibers after exposure to Na_2SO_4?
(3) What is the chemistry and crystal structure of the reaction products?

Staying within the SiC CMC, *Chapter 3* of this dissertation titled "BN Effects on Na_2SO_4 Deposit Induced Hot Corrosion of α-SiC" investigates the effect of BN fiber interphase coating on Na_2SO_4 deposit-induced hot corrosion of SiC. The questions this chapter addresses are:

(1) Does BN affect the temperature range in which Na_2SO_4 deposit induced hot-corrosion of SiC occurs? If so, by how much?
(2) How will SiC consumption vary across time and temperature due to exposure to BN, Na_2SO_4, $O_2(g)$?
(3) How does Na_2SO_4-induced degradation to the SiC surfaces vary with temperature?
(4) What reaction products form and what are their crystallization kinetics?

The last two chapters of this dissertation focus on the interaction between Na_2SO_4 deposits and the state-of-the art $Yb_2Si_2O_7$ topcoat-Si bond coat EBC/CMC system. The interaction of Na_2SO_4 with the topcoat is studied in *Chapter 4* of this dissertation titled "High Temperature Na_2SO_4 Interaction with an Air Plasma Sprayed $Yb_2Si_2O_7$-Si-SiC Coating System." The questions this dissertation chapter addresses are:

(1) What phases will form in $Yb_2Si_2O_7$ topcoat due to reaction with Na_2SO_4. How quickly will this reaction happen across time and temperature?
(2) Will the reaction with Na_2SO_4 be limited to the surface of the $Yb_2Si_2O_7$ topcoat?
(3) Will Na_2SO_4 or other Na species transport through the topcoat down to the Si bond coat? If so, how quickly?

Si bond coat oxidation and crystallization of the TGO studied in *Chapter 5* titled "Na_2SO_4 Effects on Environmental Degradation to Si Bond Coats For Applications in Turbine Engines" addresses the following questions:

(1) How will Na effect the Si bond coat oxidation kinetics? Will Na alter the oxidation rates relative to Na-free environments?
(2) How will Na effect the thermally grown oxide crystallization? When will the thermally grown oxide crystallize?
(3) If the thermally grown oxide crystallizes, will it be cristobalite, tridymite or even some other crystalline phase?
(4) What kind of damage will Na cause to the thermally grown oxide or other coating system layers? Will porosity or cracking develop?

The summation of these chapters provide a new and comprehensive understanding of Na_2SO_4 deposit -induced degradation of SiC based CMC/EBC systems.

References

1. Perepezko JH. The Hotter the Engine, the Better. *Science*. 2009;326(5956):1068–1069.
2. Melissae Fellet. Ceramic-Matrix Composites Take The Heat. *MRS Bull*. 2015;40:916–7.
3. Zok FW. Ceramic Matrix Composites Enable Revolutionary Gains in Turbine Efficiency. 2016;95:22–28.
4. Morscher GN, Yun HM, DiCarlo JA. In-Plane Cracking Behavior and Ultimate Strength for 2D Woven and Braided Melt-Infiltrated SiC/SiC Composites Tensile Loaded in Off-Axis Fiber Directions. *J Am Ceram Soc*. 2007;90(10):3185–3193.
5. Morscher GN, Yun HM, DiCarlo JA. Matrix Cracking in 3D Orthogonal Melt-Infiltrated SiC/SiC Composites with Various Z-Fiber Types. *J Am Ceram Soc*. 2005;88(1):146–153.
6. Morscher GN, DiCarlo JA, Kiser JD, Yun HM. Effects of Fiber Architecture on Matrix Cracking for Melt-Infiltrated SiC/SiC Composites. *Int J Appl Ceram Technol*. 2010;7(3):276–290.
7. Naslain R. Design, Preparation and Properties of Non-Oxide CMCs for Application in Engines and Nuclear Reactors: An Overview. *Compos Sci Technol*. 2004;64(2):155 – 170.
8. Naslain RR. SiC-Matrix Composites: Nonbrittle Ceramics for Thermo-Structural Application. *Int J Appl Ceram Technol*. 2005;2(2):75–84.
9. Naslain R, Guette A, Rebillat F, Pailler R, Langlais F, Bourrat X. Boron-Bearing Species in Ceramic Matrix Composites for Long-Term Aerospace Applications. *J Solid State Chem*. 2004;177(2):449–456.
10. Ichikawa H. Polymer-Derived Ceramic Fibers. *Annu Rev Mater Res*. 2016;46(1):335–356.
11. Lipowitz J, Rabe JA. Structure and Properties of Sylramic Silicon Carbide Fiber- A Polycrystalline, Stoichiometric β-SiC Composition. 1997;18(3):147–157.
12. Baldus P, Jansen M, Sporn D. Ceramic Fibers for Matrix Composites in High-Temperature Engine Applications. *Science*. 1999;285(5428):699–703.
13. Flores O, Bordia RK, Nestler D, Krenkel W, Motz G. Ceramic Fibers Based on SiC and SiCN Systems: Current Research, Development, and Commercial Status. *Adv Eng Mater*. 2014;16(6):621–636.
14. Schawaller D, Clauß B, Buchmeiser MR. Ceramic Filament Fibers – A Review. *Macromol Mater Eng*. 2012;297(6):502–522.
15. Guy E. Oxidation Behavior of Silicon Carbide. *J Am Ceram Soc*. 1958;41(9):347–352.
16. Costello JA, Tressler ER. Oxidation Kinetics of Silicon Carbide Crystals and Ceramics: I, In Dry Oxygen. *J Am Ceram Soc*. 1986;69(9):674–681.
17. Presser V, Nickel KG. Silica on Silicon Carbide. *Crit Rev Solid State Mater Sci*. 2008;33(1):1–99.

18. Deal BE, Grove AS. General Relationship for the Thermal Oxidation of Silicon. *J Appl Phys*. 1965;36(12):3770–3778.
19. Flörke OW. Des Kriställrten des SiO_2 und ihr Umwandlungsverhalten. *Berichte Dtsch Keram Ges*. 1961;38(3):89–97.
20. Flörke OW. Uber das Einstoffsystem SiO. *Naturwissenschaften*. 1956;43:419.
21. Fenner CN. Stability Relations of the Silica Minerals. *Am J Sci*. 1913;36(4):331–384.
22. Fenner CN. The Relations Between Tridymite and Cristobalite. *Trans Soc Glass Technol*. 1919;3:116.
23. Buerger MJ, Lukesh J. The Tridymite Problem. *Science*. 1952;95:20.
24. Rockett TJ. The Thermal Stability of Purified Tridymite. *Am Mineral*. 1967;52:1233–1239.
25. Flörke OW. Strukturanomalien bei Tridimyt und Cristobalit. *Berichte Dtsch Keram Ges*. 1955;32:369–381.
26. Hatch DM, Ghose S. The α-β phase transition in cristobalite, SiO_2. *Phys Chem Miner*. 1991;17(6):554–562.
27. Hill VG, Roy R. Silica Structure Studies: V, The Variable Inversion in Cristobalite. *J Am Ceram Soc*. 1958;41(12):532–537.
28. Sandford SS. The Conversion of Quartz into Cristobalite below 1000°C and Some Properties of the Cristobalite Formed. *J Am Ceram Soc*. 1935;18(1–12):149–154.
29. Crookes W. On the devitrification of silica glass. *Proc R Soc Lond Ser Contain Pap Math Phys Character*. 1912;86(588):406–408.
30. Withers RL, Thompson JG, Xiao Y, Kirkpatrick RJ. An electron diffraction study of the polymorphs of SiO_2-tridymite. *Phys Chem Miner*. 1994;21(7):421–433.
31. Garofalini SH, Miller AD. Kinetics of Tridymite Formation. *J Cryst Growth*. 1986;78:85–96.
32. Jones JB, Segnit ER. Genesis of Cristobalite and Tridymite at Low Temperatures. *J Geol Soc Aust*. 1972;18(4):419–422.
33. Ramberg EC, Gary C, Spear KE, Tressler RE, Ramberg CF. Passive-Oxidation Kinetics of High-Purity Silicon Carbide from 800° to 1100°C. *J Am Ceram Soc*. 1996;79(11):2897–2911.
34. Jacobson NS. Corrosion of Silicon-Based Ceramics in Combustion Environments. *J Am Ceram Soc*. 1993;76(1):3–28.
35. Fox DS, Opila EJ, Hann RE. Paralinear Oxidation of CVD SiC in Simulated Fuel-Rich Combustion. *J Am Ceram Soc*. 2000;83(7):1761–1767.
36. Cristy SS, Condon JB. A Model for Oxidation of Silicon by Oxygen. *J Electrochem Soc*. 1981;128(10):2170–2174.
37. Hay RS, Corns R. Passive oxidation kinetics for glass and cristobalite formation on Hi-Nicalon™-S SiC fibers in steam. *J Am Ceram Soc*. 2018;101(11):5241–5256.

38. Hay RS, Fair GE, Bouffioux R, *et al.* Relationships Between Fiber Strength, Passive Oxidation and Scale Crystallization Kinetics of Hi-Nicalon™-S SiC Fibers. *J Am Ceram Soc.* 2011;94(11):3983–3991.
39. Hay RS, Fair GE, Bouffioux R, *et al.* Hi-Nicalon™-S SiC Fiber Oxidation and Scale Crystallization Kinetics. *J Am Ceram Soc.* 2011;94(11):3983–3991.
40. Zhu Yuntian T, Taylor Seth T, Stout Michael G, Butt Darryl P, Lowe Terry C. Kinetics of Thermal, Passive Oxidation of Nicalon Fibers. *J Am Ceram Soc.* n.d.;81(3):655–660.
41. Wilson M, Opila EJ. A Review of SiC Fiber Oxidation with a New Study of Hi-Nicalon SiC Fiber Oxidation. *Adv Eng Mater.* 2016;18(10):1698–1709.
42. Opila EJ. Influence of Alumina Reaction Tube Impurities on the Oxidation of Chemically-Vapor-Deposited Silicon Carbide. *J Am Ceram Soc.* n.d.;78(4):1107–1110.
43. Presser V, Loges A, Hemberger Y, Nickel KG. Microstructural Evolution of Silica on Single-Crystal Silicon Carbide. Part I: Devitrification and Oxidation Rates. *J Am Ceram Soc.* 2009;92(3):724–731.
44. Presser V, Loges A, Wirth R, Nickel KG. Microstructural Evolution of Silica on Single Crystal Silicon Carbide. Part II: Influence of Impurities and Defects. *J Am Ceram Soc.* 2009;92(8):1796–1805.
45. Hagan JM, Opila EJ. High-Temperature Na_2SO_4 Deposit-Assisted Corrosion of Silicon Carbide – I: Temperature and Time Dependence. *J Am Ceram Soc.* 2015;98(4):1275–1284.
46. Hagan JM, Opila EJ. High-temperature Na_2SO_4 deposit-assisted corrosion of silicon carbide–II: Effects of B, C, and Si. *J Am Ceram Soc.* 2017;100(2):761–773.
47. McFarland B, Opila EJ. Silicon Carbide Fiber Oxidation Behavior in the Presence of Boron Nitride. *J Am Ceram Soc.* 2018;101:5534–5551.
48. Schlichting J. Oxygen transport through glass layers formed by a gel process. *J Non-Cryst Solids.* 1984;63(1):173–181.
49. Jacobson NS, Morscher GN, Bryant DR, Tressler RE. High-Temperature Oxidation of Boron Nitride: II, Boron Nitride Layers in Composites. *J Am Ceram Soc.* 1999;82(6):1473–1482.
50. Jacobson NS, Serene F, Arthur M, Haluk S. High-Temperature Oxidation of Boron Nitride: I, Monolithic Boron Nitride. *J Am Ceram Soc.* 1999;82(2):393–398.
51. Pareek V, Shores DA. Oxidation of Silicon Carbide in Environments Containing Potassium Salt Vapor. *J Am Ceram Soc.* 1991;74(3):556–563.
52. Jacobson NS. Kinetics and Mechanism of Corrosion of SiC by Molten Salts. *J Am Ceram Soc.* 1986;69(1):74–82.
53. Jacobson NS, Smialek JL. Hot Corrosion of Sintered α-SiC at 1000°C. *J Am Ceram Soc.* 1985;68(8):432–439.

54. Rockett TJ. Phase Relations in the Systems Silica, Boron Oxide-Silica, and Sodium Oxide-Boron Oxide-Silica. The Ohio State University; Mineralogy; 1963
55. Rockett TJ, Foster WR. Phase Relations in the System Boron Oxide–Silica. *J Am Ceram Soc*. 1965;48(2):75–80.
56. Kracek FC. The System Sodium Oxide-Silica. *J Phys Chem*. 1929;34(7):1583–1598.
57. Wu P, Eriksson G, Pelton AD. Optimization of the Thermodynamic Properties and Phase Diagrams of the Na_2O–SiO_2 and K_2O–SiO_2 Systems. *J Am Ceram Soc*. 1993;76(8):2059–2064.
58. Tedmon CS. The Effect of Oxide Volatilization on the Oxidation Kinetics of Cr and Fe-Cr Alloys. *J Electrochem Soc*. 1966;113(8):766–768.
59. Opila EJ, Hann RE. Paralinear Oxidation of CVD SiC in Water Vapor. *J Am Ceram Soc*. 1997;80(1):197–205.
60. Opila EJ. Variation of the Oxidation Rate of Silicon Carbide with Water-Vapor Pressure. *J Am Ceram Soc*. 1999;82(3):625–636.
61. Opila EJ. Oxidation and Volatilization of Silica Formers in Water Vapor. *J Am Ceram Soc*. 2003;86(8):1238–1248.
62. Opila EJ, Fox DS, Jacobson NS. Mass Spectrometric Identification of Si–O–H(g) Species from the Reaction of Silica with Water Vapor at Atmospheric Pressure. *J Am Ceram Soc*. 1997;80(4):1009–1012.
63. Robinson RC, Smialek JL. SiC Recession Caused by SiO_2 Scale Volatility under Combustion Conditions: I, Experimental Results and Empirical Model. *J Am Ceram Soc*. 1999;82(7):1817–1825.
64. Opila EJ, Smialek JL, Robinson RC, Fox DS, Jacobson NS. SiC Recession Caused by SiO_2 Scale Volatility under Combustion Conditions: II, Thermodynamics and Gaseous-Diffusion Model. *J Am Ceram Soc*. 1999;82(7):1826–1834.
65. Dongming Zhu, Bryan Harder, Janet B. Hurst, *et al.* Advanced Environmental Barrier Coating Development for SiC-SiC Ceramic Matrix Composite Components. 12th Pacific Rim Conference on Ceramic and Glass Technology (PACRIM 12): 2017
66. Lee KN, Jacobson NS, Miller RA. Refractory Oxide Coatings on SiC Ceramics. *MRS Bull*. 1994;19(10):35–38.
67. K.N. Lee, Fox DS, Eldridge JI, *et al.* Upper Temperature Limit of Environmental Barrier Coatings Based on Mullite and BSAS. *J Am Ceram Soc*. n.d.;86(8):1299–1306.
68. Lee KN. Current status of environmental barrier coatings for Si-Based ceramics. *Surf Coat Technol*. 2000;133–134:1 – 7.
69. Dongming Zhu, Serene Farmer, Terry R. McCue, Bryan Harder, Janet B. Hurst. Environmental Stability and Oxidation Behavior of HfO_2-Si and YbGd(O) Based Environmental Barrier Coating Systems for SiC/SiC Ceramic Matrix Composites. 41st Internation Conference and Expo on Advanced Ceramics and Composites (ICACC'17): 2017

70. Davis JR. Handbook of Thermal Spray Technology. ASM International; 2004
71. Garcia E, Lee H, Sampath S. Phase and microstructure evolution in plasma sprayed $Yb_2Si_2O_7$ coatings. *J Eur Ceram Soc*. 2019;39(4):1477–1486.
72. Richards BT, Wadley HNG. Plasma spray deposition of tri-layer environmental barrier coatings. *J Eur Ceram Soc*. 2014;34(12):3069 – 3083.
73. Richards BT, Zhao H, Wadley HNG. Structure, composition, and defect control during plasma spray deposition of ytterbium silicate coatings. *J Mater Sci*. 2015;50(24):7939–7957.
74. Toropov NA, Bondar IA. Silicate of Rare Earth Elements. VI. Phase Diagrams for the Binary Systems Sm_2O_3-SiO_2 and Yb_2O_3-SiO_2 and a Comparison of them with Silicates of other Rare Earth Elements. *Uch Zap Kazan Gos Univ*. 1961;1372–1379.
75. Richards BT, Young KA, Francqueville F, Sehr S, Begley MR, Wadley HNG. Response of ytterbium disilicate–silicon environmental barrier coatings to thermal cycling in water vapor. *Acta Mater*. 2016;106:1 – 14.
76. Lee KN. $Yb_2Si_2O_7$ Environmental barrier coatings with reduced bond coat oxidation rates via chemical modifications for long life. *J Am Ceram Soc*. 2019;102(3):1507–1521.
77. Richards BT, Begley M, Wadley HNG. Mechanisms of Ytterbium Monosilicate/Mullite/Silicon Coating Failure During Thermal Cycling in Water Vapor. *J Am Ceram Soc*. n.d.;98(12):4066–4075.
78. Cojocaru CV, Lévesque D, Moreau C, Lima RS. Performance of thermally sprayed Si/mullite/BSAS environmental barrier coatings exposed to thermal cycling in water vapor environment. *Surf Coat Technol*. 2013;216:215 – 223.
79. Mechnich P. Y_2SiO_5 coatings fabricated by RF magnetron sputtering. *Surf Coat Technol*. 2013;237:88–94.
80. Poerschke DL, Hass DD, Eustis S, Seward GGE, Van Sluytman JS, Levi CG. Stability and CMAS Resistance of Ytterbium-Silicate/Hafnate EBCs/TBC for SiC Composites. *J Am Ceram Soc*. 2015;98(1):278–286.
81. Turcer LR, Krause AR, Garces HF, Zhang L, Padture NP. Environmental-barrier coating ceramics for resistance against attack by molten calcia-magnesia-aluminosilicate (CMAS) glass: Part II, β-Yb2Si2O7 and β-Sc2Si2O7. *J Eur Ceram Soc*. 2018;38(11):3914–3924.
82. Stokes JL, Harder BJ, Wiesner VL, Wolfe DE. High-Temperature thermochemical interactions of molten silicates with $Yb_2Si_2O_7$ and $Y_2Si_2O_7$ environmental barrier coating materials. *J Eur Ceram Soc*. 2019;39(15):5059–5067.
83. Stolzenburg F, Johnson MT, Lee KN, Jacobson NS, Faber KT. The interaction of calcium–magnesium–aluminosilicate with ytterbium

silicate environmental barrier materials. *Surf Coat Technol*. 2015;284:44–50.

84. Poerschke DL, Jackson WR, Levi CG. Silicate Deposit Degradation of Engineered Coatings in Gas Turbines: Progress Toward Models and Materials Solutions. *Annu Rev Mater Res*. 2017;47(1):297–330.
85. Stearns CA, Kohl FJ, Rosner DE. Combustion System Processes Leading to Corrosive Deposits. San Diego, California: 1981
86. Pettit F. Hot Corrosion of Metals and Alloys. *Oxid Met*. 2011;76(1):1–21.
87. Stringer J. Hot Corrosion of High-Temperature Alloys. *Annu Rev Mater Sci*. 1977;7(1):477–509.
88. Hagan JM. High Temperature Salt Deposit-Assisted of Silicon Carbide Ceramic Matrix Composites:Effects of Composite Chemistry and Architecture. University of Virginia, Materials Science and Engineering; 2015
89. Felsche J. Rare earth silicates with the apatite structure. *J Solid State Chem*. 1972;5(2):266 – 275.
90. Latshaw AM, Wilkins BO, Chance WM, Smith MD, Loye H-C zur. Influence of rare earth cation size on the crystal structure in rare earth silicates, Na_2RESiO_4 (RE = Sc, Yb) and $NaRESiO_4$ (RE = La, Yb). *Solid State Sci*. 2016;51:59 – 65.
91. Latshaw AM, Yeon J, Smith MD, Loye H-C zur. Synthesis, structure, and polymorphism of $A_3LnSi_2O_7$ (A=Na, K; Ln=Sm, Ho, Yb). *J Solid State Chem*. 2016;235:100 – 106.
92. Meschter P, Rowe R. Hot-Corrosion-Resistant Coatings and Components Protected Therewith. US 9,945,036 B2. 2018.
93. Jacobson NS, Lee KN, Yoshio T. Corrosion of Mullite by Molten Salts. *J Am Ceram Soc*. 1996;79(8):2161–2167.
94. Ziqi S, Meishuan L, Yanchun Z. Kinetics and Mechanism of Hot Corrosion of γ-$Y_2Si_2O_7$ in Thin-Film Na_2SO_4 Molten Salt. *J Am Ceram Soc*. 2008;91(7):2236–2242.
95. Sun Z, Li M, Li Z, Zhou Y. Hot corrosion of γ-$Y_2Si_2O_7$ in strongly basic Na_2CO_3 molten salt environment. *J Eur Ceram Soc*. 2008;28(1):259 – 265.

2 | Na_2SO_4 Deposit-Induced Hot Corrosion of SiC Fibers Relevant for SiC CMCs

2.1 Introduction

Silicon carbide (SiC) ceramic matrix composites (CMCs) have entered service in GE Aviation's LEAP engines in 2016 as non-load bearing components.[1, 2] SiC CMCs are comprised of a SiC matrix phase that is reinforced by fine-diameter (~10 μm), polycrystalline SiC fibers. These fibers serve as a reinforcement phase inside of the SiC matrix phase, allowing for increased toughness compared to monolithic SiC whilst retaining the attractive high temperature capability properties of bulk SiC. While in service, SiC CMCs will be exposed to high temperature oxidizing environments, causing degrading chemical reactions to occur. Despite the implementation of SiC CMCs into turbine engine service and numerous studies devoted to understanding their environmental degradation mechanism, there still remains uncertainty in their high temperature behavior.

It is well known that SiC is unstable in high temperature oxidizing environments. SiC reacts to form a slow-growing protective SiO_2 scale, whilst liberating CO(g) in oxidizing environments, given by Equation (2.1):

$$SiC(s) + 3/2O_2(g) \rightarrow SiO_2(s) + CO(g) \tag{2.1}$$

The growth of SiO_2 on SiC is a well-studied reaction, and closely follows the thermal oxidation model of Si developed by Deal and Grove.[3, 4] Unlike Si though, oxidation of SiC results in the formation of gaseous-byproducts. For long reaction times and high temperatures, the reaction rate of SiC is defined by the parabolic rate constant (k_p), which easily can be determined through thickness measurement of thermally grown SiO_2. Oxidation studies in dry O_2(g) of SiC fibers relevant for application in SiC CMC have been the focus of many high temperature studies.[5–13] SiC fibers developed for application in

SiC CMCs each have their own processing routes, resulting in unique compositions and microstructures, which in turn can affect their high temperature oxidation resistance.

2.1.1 SiC Fibers: Processing, Chemistry and Microstructure

Fine diameter SiC fibers developed for application in SiC CMCs, which include Hi Nicalon, Hi Nicalon S, Syralmic and Sylramic iBN, are uniquely different materials, which as a result of their processing routes, possess different microstructures and chemistries.[14, 15] Properties of these fibers are summarized in Table 2.1. Hi Nicalon fibers are created through a thermal treatment of polycarbosilane (PCS) materials, and are subsequently melt-spun. Further thermal treatment results in a SiC fiber comprised of 5-10 nm size β-SiC crystallites and regions of amorphous Si-C-O and free C. Hi Nicalon S fibers are processed identically to Hi Nicalon fibers, except that sintering aids and further thermal treatment are used, resulting in β-SiC grains 50-100 nm in diameter and minimal amounts of amorphous Si-C-O and free C. Sylramic and Sylramic iBN fibers are processed from polytitanocarbosilane (PTC) precursor materials and then boron (B) doped from gas phase processing. The fibers are heat-treated at elevated temperatures to remove excess C and O, leaving behind a polycrystalline β-SiC fiber with TiB_2 and B_4C crystallites.[16] Sylramic iBN fibers are processed identically to Sylramic fibers, except that an additional thermal treatment in a nitrogen gas-containing environments causes the formation of an *in-situ* boron nitride (iBN) ~200 nm thick surface layer due to outward B diffusion and subsequent reaction with the nitrogen gas. An important difference between these four fibers is the C:Si ratio of ~1.4 for Hi Nicalon and ~1 for Hi Nicalon, Sylramic and Sylramic iBN and fibers. It is unknown how the differing chemistries and microstructures of these SiC fibers will impact their corrosion resistance in the presence of molten Na_2SO_4 deposits.

Fiber Type	Manufacturer	Density (g/cm^3)	Fiber Diameter (μm)	Composition (at.%)	Phases
Hi Nicalon	Nippon-Carbon	2.74	14	41.5 Si 57.9 C 0.6 O *(1.4 C:Si)*	β-SiC, Free C, Amorphous SiCO
Hi Nicalon S	Nippon-Carbon	3.10	12	48.6 Si 51.1 C 0.3 O *(1.05 C:Si)*	β-SiC
Sylramic	COI Ceramics	3.2	10	46.7 Si 2.3 B 46.7 C 2.1 Ti 0.8 O 0.4 N *(1.01 C:Si)*	β-SiC, TiB_2, B_4C
Sylramic iBN	COI Ceramics	3.2	10	46.7 Si 2.3 B 46.7 C 2.1 Ti 0.8 O 0.4 N *(1.01 C:Si)*	β-SiC, TiB_2, B_4C, BN surface layer

Table 2.1. Properties of SiC fibers tested in this dissertation chapter.[15, 22, 23]

2.1.2 SiO_2 Polymorphism Basics

Pure SiO_2 is a polymorphic material that can exist as at least two equilibrium phases at ambient pressure up to its melting point (T_m = 1723°C), namely quartz and cristobalite. However, debate still exists in literature if another SiO_2 phase tridymite, is stabilized by impurities including Na_2O.[17–21] A single transition from quartz to cristobalite occurs at 1050°C in the two-phase SiO_2 system, while a widely accepted view for SiO_2 polymorphism in the three-phase SiO_2 system puts SiO_2 transition temperatures of quartz to tridymite at ~867°C and tridymite to cristobalite at ~1460°C.[24–26] Cristobalite and tridymite are the SiO_2 phases most of interest for SiC fiber oxidation due to their stability at temperatures relevant for turbine engine application. Both cristobalite and tridymite invert from their high-temperature or β-form to their low-temperature or α-form upon cooling to room temperature. The β-to-α cristobalite inversion is well studied, and is associated with cracking within thermally grown SiO_2 layers due to a ~5% density increase upon cooling.[27, 28] Tridymite has multiple low temperature polymorphs, resulting in more complex inversion behavior than cristobalite.[29] High temperature oxidation studies of Hi Nicalon S fibers up to 1400°C in dry air revealed thermally grown SiO_2 layers consisting of both cristobalite and tridymite, while exposures in steam produced mainly cristobalite layers.[10, 13] A high temperature study in a NaCl containing environment of Nicalon CG fibers, a predecessor of Hi Nicalon and Hi Nicalon S fibers, revealed the reaction product crystallized into tridymite.[38] No high temperature studies of Hi Nicalon, Hi Nicalon S, Sylramic and Sylramic iBN fibers in Na-containing environments have been reported in the literature.

2.1.3 Hot Corrosion of SiC Fibers

The ingestion of NaCl into turbine engines operating in marine environments causes an *in-situ* reaction with S impurities from the jet fuel or environment, resulting in the formation of liquid Na_2SO_4, as seen below in Equation (2.2)[30]:

$$2NaCl(l) + SO_3(g) + H_2O(g) \rightarrow Na_2SO_4(l) + 2HCl(g) \qquad (2.2)$$

The deposition of Na_2SO_4 onto current metallic turbine hot-section components causes a form of high temperature degradation known as hot corrosion to occur. Hot corrosion of SiC CMCs is also expected to occur, but is less studied than the hot corrosion of metals and alloys.[31, 32] Laboratory testing on commercially sintered α-SiC has shown the reaction of Na_2SO_4 causes enhanced oxidation and surface pitting.[33–39] The accelerated oxidation of α-SiC by molten Na_2SO_4 is attributed to the dissolution of thermally grown SiO_2 into a liquid and a highly oxidant permeable sodium silicate, whose formation can be expressed in Equations (2.1) and (2.3):

$$Na_2O + xSiO_2 \rightarrow Na_2O\bullet xSiO_2 \quad (2.3)$$

where x denotes variable SiO_2 molar composition in the sodium silicate reaction product. The formation of liquid silicates are highly nonprotective for further SiC oxidation, as oxygen diffusivity through liquid sodium silicates are 6-9 orders of magnitude faster than crystalline or amorphous SiO_2.[36, 40] However, the acceleration to SiC oxidation kinetics only lasts for an initial exposure period of several hours, which is followed by a kinetic plateau due to porosity removal from the reaction layer or volatilization and consumption of Na_2SO_4, allowing the build-up of a continuous SiO_2 layer.[34, 35] Additionally, Jacobson also showed that SiC oxidizes more rapidly in the presence of Na_2SO_4 relative to other SiO_2 forming materials (i.e. Si, Si_3N_4).[41, 42] It was believed that C present in SiC either as C sintering aids or CO(g) produced from the oxidation of SiC (Equation (2.1)), promotes the decomposition of Na_2SO_4 to Na_2O, which can be seen in Equations (2.4), (2.5) and (2.6):

$$Na_2SO_4 + 2C(s) \rightarrow Na_2S + 2CO_2(g) \quad (2.4)$$

$$Na_2SO_4 + CO(g) \rightarrow Na_2S + CO_2 + 3/2O_2 \quad (2.5)$$

$$Na_2S + 3Na_2SO_4 \rightarrow 4Na_2O + 4SO_2 \quad (2.6)$$

In accordance with the acid-base description of oxide mixing, C in SiC creates more basic conditions in Na_2SO_4, which in turn allows for more easy SiO_2 dissolution into sodium silicates (Equation 2.3), resulting in rapid SiC oxidation. Hot-corrosion testing of SiC CMCs with various SiC fiber types in burner rig studies performed by Hagan, showed certain CMCs were more corroded based upon SiC fiber type employed.[43] Currently, the interaction of Na_2SO_4 deposits with SiC fibers relevant for application in SiC CMCs is lacking. This work aims to establish an understanding how the differences in processing, chemistry, and microstructures for SiC fibers relevant for application in SiC CMCs will affect their resistance to Na_2SO_4 deposit-induced hot corrosion. Emphasis is placed on the growth kinetics of the reaction layer, microstructure of the reaction product and fiber surface, and the chemistry and crystal structure of the reaction product.

2.2 Experimental

2.2.1 Materials

Hot corrosion testing was performed on four different SiC fiber types, namely Hi Nicalon™ (Nippon Carbon, Japan), Hi Nicalon Type S™ (Nippon Carbon, Japan), Sylramic™ (COI Ceramics, San Diego, CA) and Sylramic iBN™ (COI Ceramics, San Diego, CA). Each fiber type was received in spools as bundles (tows) of 500 fibers (Hi Nicalon and Hi Nicalon S) or 800 fibers (Sylramic and Sylramic iBN). All fibers except for Syramic iBN possessed a PVA surface layer used to improve handleability of fiber tows.

2.2.2 Sample Preparation

Fiber tows used for all hot corrosion testing were cut from the fiber spools into 11 cm lengths, and then twisted into 5.5 cm long "lanyards", to allow for easy handling of fiber tow specimens during experimentation and characterization. Hi Nicalon, Hi Nicalon S, and Sylramic fibers were exposed at 600°C for 30 minutes in air to remove or desize their PVA layer. No desizing was required for Sylramic iBN samples as these fibers do not employ a PVA coating. Fiber lanyards were weighed after desizing using an analytical balance to determine their starting weight (Mettler Toledo, Columbus, OH). SiC fiber lanyards were immersed in a room-temperature Na_2SO_4-containing aqueous solution for approximately 2 minutes. Hi Nicalon S, Sylramic and Sylramic iBN specimens were soaked in a 100 mL aqueous solution containing 6g of Na_2SO_4, while Hi Nicalon specimens were soaked in a 100mL aqueous solution containing 3g of Na_2SO_4. The fiber tows were placed in a convection oven (MTI Corporation, Richmond, CA) at 120°C to evaporate the water, leaving behind only Na_2SO_4. Fiber tows were re-weighed after drying in the convection oven to confirm salt loadings of approximately 60 ± 20 μg/cm^2 for all fiber types.

2.2.3 Hot Corrosion Procedure

All hot corrosion experiments were conducted in a horizontal tube furnace (CM Furnaces, Bloomfield, NJ) with a 50 mm outer diameter and 47 mm inner diameter fused quartz tube (99.995% purity, Quartz Scientific, Harbor, OH). Stainless steel endcaps were fitted with inlet and outlet ports for gas flow, and a thermocouple inlet port to simultaneously control the gaseous environment and to measure the temperature inside the tube furnace. Exhaust gas was filtered through a water filled gas wash bottle at the end of the tube furnace to visually determine if gas was flowing. Samples were suspended across an Al_2O_3 boat that was wrapped with platinum (Pt) during experimentation, as seen in Figure 2.1. Experiments were conducted for times between 0.75h-24h at 1000°C, in a 0.1% SO_2-O_2 gaseous environment. Upon heating to the experimental temperature, samples were loaded, endcaps sealed, and the 0.1% SO_2-O_2 gas mixture was introduced to the furnace at a flow rate of 100 sccm (Model 1179, Mass Flow Controller, MKS Instruments, Andover, MA) to provide well defined SO_3/Na_2O activity and to limit the rapid volatilization of Na_2SO_4. Approximately 5-10 minutes before exposures ended, the gas mixture was switched to pure O_2 to flush the furnace of SO_2 prior to sample removal. Samples were removed at temperature to terminate the exposure at the desired time.

2.2.4 Characterization

The extent of the reaction with Na_2SO_4 on fiber surfaces and cross-sections before and after exposure was assessed using a scanning electron microscope (SEM) (Quanta 650, FEI Company, Hillsboro, OR). Specimens were cross-sectioned with a sharp blade or fractured by hand after exposure, allowing for easy specimen preparation for cross-sectional analysis via SEM. Approximately 15 oxide thickness measurements for each fiber type tested

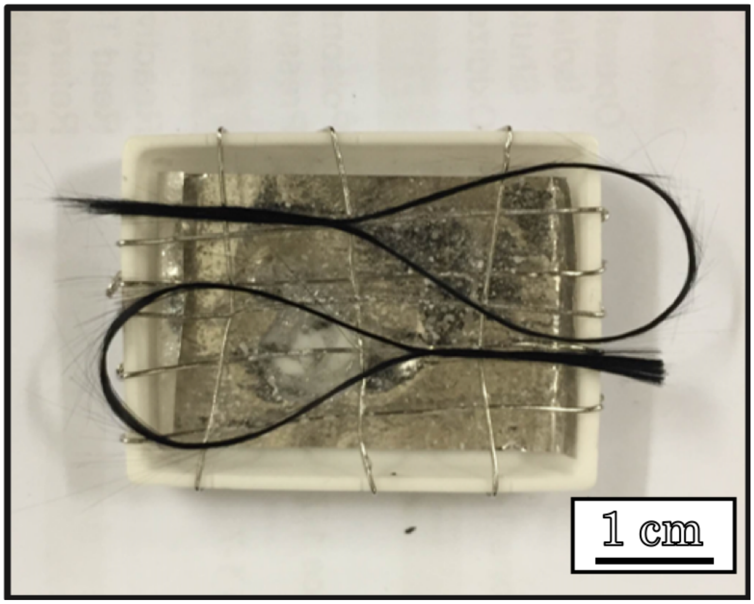

Figure 2.1. Macro image showing two SiC fiber tows twisted into “lanyards”, resting on a Pt-wire wrapped Al_2O_3 sample boat used for testing.

per exposure condition were gathered for determination of the average oxide thickness measurement. Energy dispersive spectroscopy (EDS) (Oxford Instruments) was used to determine the reaction product local chemistry. Higher magnification microscopy of fiber specimens was performed using transmission electron microscopy (TEM) (Titan 300, FEI Company, Hillsboro, OR), selected area diffraction (SAED) was used for crystal structure determination, while energy-filtered transmission electron microscopy (EFTEM) was used for local chemistry determination. Fiber specimens were prepared for TEM analysis using a dual beam focused Ga^+ ion beam scanning electron microscope (FIB-SEM) (Quanta 3D FEG, FEI Company, Hillsboro, OR). Quantification of the corrosion product composition was determined using an inductively coupled plasma optical emission spectrometer (ICP-OES) (iCAP 6200, Thermo Scientific, Waltham, MA). The reaction layer was removed from the SiC fiber tows using a two-step digestion process. Specimens were first placed in a 10 mL aqueous solution to remove water soluble corrosion products (i.e. silicates, Na_2SO_4) and then in a 1 mL hydrogen fluoride (HF) + 9 mL aqueous solution to remove any water insoluble phases (i.e. SiO_2). Each H_2O- or acid- soak was performed by suspending the solution container for 48h in a 35°C heated water bath with sonication. Several Na, Si and S spectral emission lines were selected for corrosion layer analysis, and were subsequently averaged for elemental composition analysis. One fiber specimen per experimental condition was analyzed using ICP-OES. Fibers in the as-received condition after PVA removal were digested in water + acid to determine their stability during digestion as a baseline comparison. One fiber lanyard specimen per condition was analyzed using ICP-OES.

2.3 Results

2.3.1 Salt Loading Study

Previous studies in literature employed an aqueous solution method to deposit Na_2SO_4 salt onto SiC materials prior to high temperature testing.[8, 33, 44] This method can allow for significant loadings onto specimens due to the appreciable solubility of Na_2SO_4 in water at 20°C (50g of Na_2SO_4 per 100mL of water). A similar aqueous-solution deposition method was thus adopted in this dissertation chapter. Before testing could be performed, a suitable Na_2SO_4 loading amount needed to be identified for observable degradation rates. A salt loading study revealed the amount of Na_2SO_4 deposited on SiC fiber types as a function of Na_2SO_4 dissolved in aqueous solution, which can be seen in Figure 2.2. The uncertainty bars reported in this figure represent variation in Na_2SO_4 deposition between two SiC fiber lanyard specimens. In addition to salt-loading, the reaction severity of salt-loaded specimens were assessed to ensure microstructural and quantitative analysis could be performed via exposure for 3h at 1000°C. Fibers soaked in solutions containing more than 25 g of Na_2SO_4 in 100 mL of H_2O were reduced to fiber fragments after exposure, while fibers soaked in salt solutions containing 1-10 g of Na_2SO_4 were degraded considerably less. Resultantly, salt solutions containing less than 10g of Na_2SO_4 were used. Fibers soaked in these 1-10g

Na_2SO_4 containing solutions led to deposition of no more than ~100 μg/cm^2 of Na_2SO_4. However, Hi Nicalon fibers experienced nearly twice as much salt deposition as Hi Nicalon, Sylramic and Sylramic iBN. Hi-Nicalon fiber specimens were therefore immersed in a 100 mL aqueous solution containing 3g of Na_2SO_4 while Hi Nicalon S, Sylramic and Sylramic iBN fiber specimens would be immersed in a solution containing 6g of Na_2SO_4 to ensure salt loadings of approximately 60 ± 20 μg/cm^2, given an estimated fiber surface area of 10-15 cm^2. The surface area of fiber tow "lanyards" or specimens was calculated by assuming each fiber as a cylinder with length equal to 11 cm and diameter equal to their average diameter reported in Table 2.1. The total surface area of the fiber tow was then obtained by multiplying the surface area of a single fiber times the number of fibers in each tow, 500 for Hi Nicalon and Hi Nicalon S fiber types and 800 for Sylramic and Sylramic iBN fiber types.

2.3.2 Reaction Product Structure and Chemistry

Visual inspection of all fibers after exposure revealed that no color difference or morphological changes relative to pre-exposure conditions occurred after all exposure times. The fibers could easily be fractured by hand unlike their pre-exposure condition. SEM images of Hi Nicalon, Hi Nicalon S, Sylramic and Sylramic iBN fibers in cross-section prior to salt loading and exposure can be seen in Figure 2.3. SEM images of fiber specimens in cross-section after exposure for 24h at 1000°C seen in Figure 2.4, revealed the formation of a reaction product on all fiber specimens, whose scale thickness, morphology and porosity within the reaction layer varied amongst each of the fiber types. Reaction products developed on Hi Nicalon fibers, seen in Figure 2.4a), were the thickest and also were filled with the highest degree of porosity relative to all fiber types tested. The porosity in the observed scales are indicative of gas evolution throughout exposure. The other fibers types, seen in Figure 2.4b)-2.4d), developed nearly equally thick reaction products

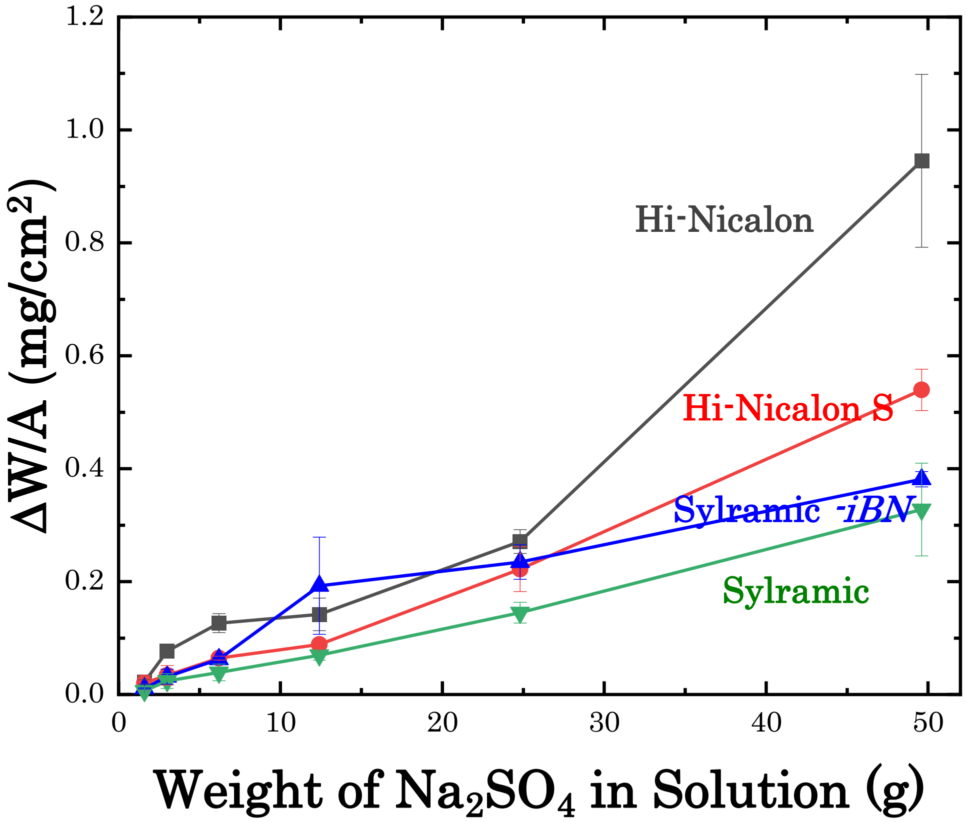

Figure 2.2. Plot showing the amount of Na_2SO_4 salt deposited on Hi Nicalon (dark grey), Hi Nicalon S (red), Sylramic (green) and Sylramic iBN (blue) fiber tow specimens after two minute depositions in varying Na_2SO_4 + 150 mL DI water solutions.

and were visibly less porous than the scale formed on Hi Nicalon. The reaction products formed on both Sylramic and Sylramic iBN have similar microstructures due to their identical starting chemistry and microstructure. Higher magnification imaging of the fiber scale interface of a Hi Nicalon fiber exposed for 24h at 1000°C can be seen in Figure 2.5. The SEM image seen in Figure 2.5a) reveals that a dark phase contrast region existed between the fiber and porous reaction layer formed, while the TEM image of the fiber-scale interface seen in Figure 2.5b) revealed the presence of 10-100 nm size pores in the dark, phase contrast layer scale. The porosity present in the

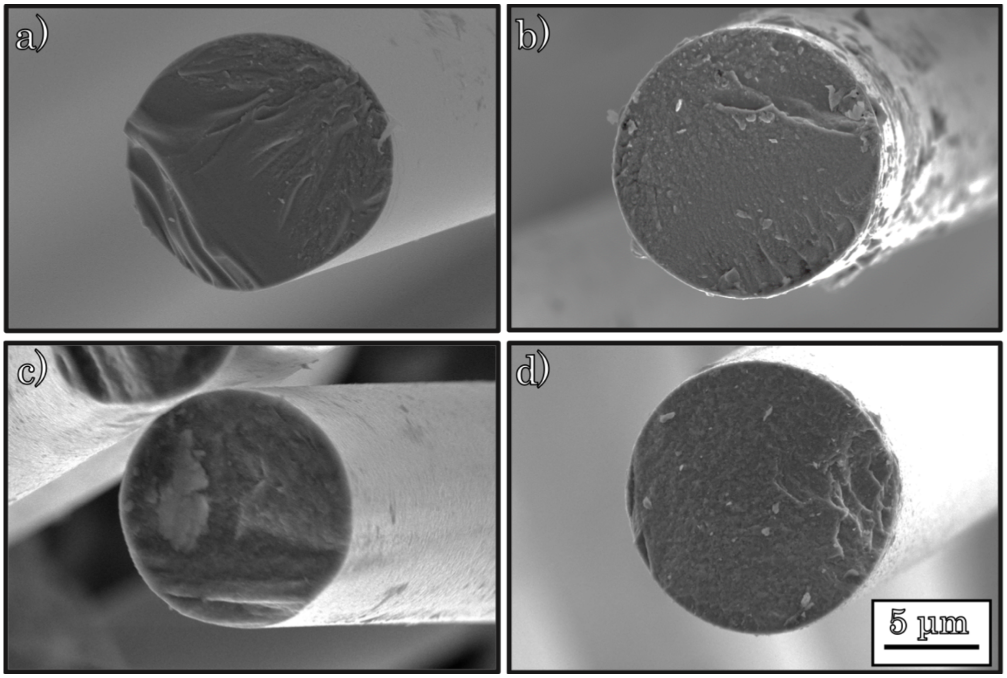

Figure 2.3. Backscattered electron SEM images of a) Hi Nicalon b) Hi Nicalon S c) Sylramic and d) Sylramic iBN fiber types in the as-received condition in cross-section.

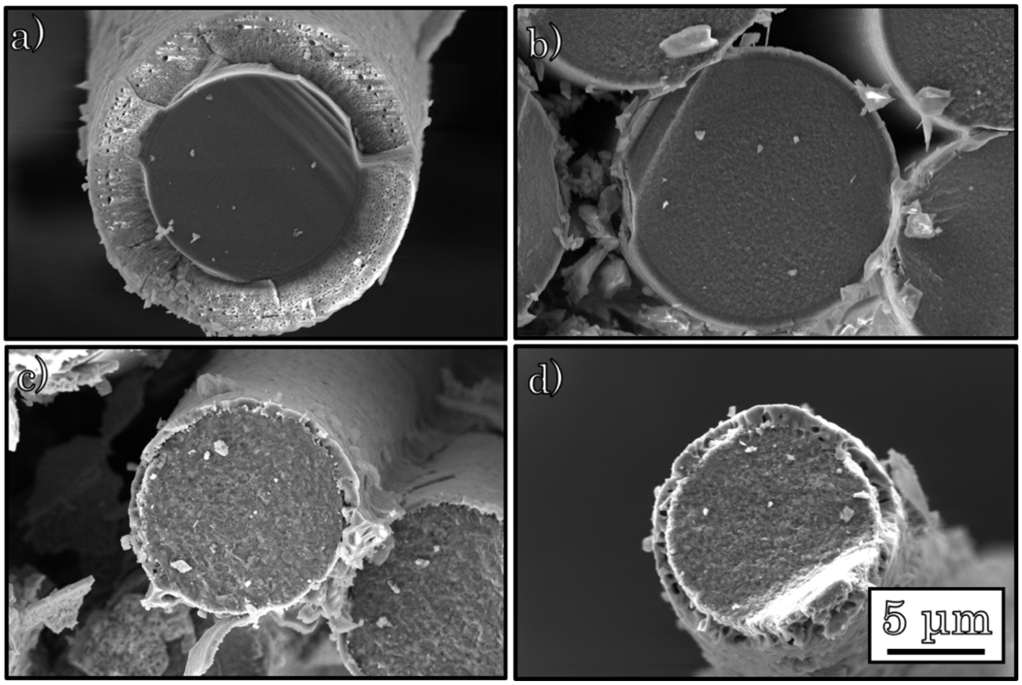

Figure 2.4. Backscattered SEM images of a) Hi Nicalon b) Hi Nicalon S c) Sylramic d) Sylramic iBN fibers after exposure to ~60 µg/cm^2 of Na_2SO_4 for 24h at 1000°C in a 0.1% SO_2-O_2 gaseous environment.

scales present on Hi Nicalon fibers increases in size from the fiber-scale interface outwards towards the scale-gas interface. This indicates gas evolution from the fiber and that pore coalescence occurs during exposure.

The crystallinity of scales formed on Hi Nicalon, Hi Nicalon S and Sylramic iBN fiber types after exposure to Na_2SO_4 for 24h at 1000°C was determined using electron diffraction. TEM images and the corresponding electron diffraction patterns collected from areas circled in red can be seen in Figures 2.6-2.8. The scale formed on Hi Nicalon seen in Figure 2.6, is filled throughout with porosity identical to the microstructure observed in Figures 2.4a) and 2.5, much more than in the scales formed on Hi Nicalon S and Sylramic iBN fibers. The pores are smallest at the fiber-scale interface (10-100 nm), and increase in size with the largest pores residing nearest the scale-gas interface. The SAED results from these figures show polycrystalline corrosion products exist, although the crystalline phases were not identified. Additionally, twinned regions and grains ~500 nm in size can easily be observed throughout the scales in these figures, indicating that crystallization of the entire scale in the presence of Na_2SO_4 occurs less than 24h into exposure at 1000°C. Lastly, it should be noted that higher magnification TEM imaging and electron diffraction analysis was not possible due to electron beam-induced amorphization to the crystalline SiO_2 scales from the 300 kV electron beam, an example of which can be seen in Appendix A.

Microscopy of fiber surfaces after exposure for 24h at 1000°C, seen in Figure 2.9, revealed cracking occurred within the reaction product of all SiC fibers types. However, the morphology and phases present within the reaction products were not the same between fiber types. Non uniform surface morphologies of the oxide were observed for Hi Nicalon, seen in Figure 2.9a), while Hi Nicalon S exhibited a smooth oxide surface. A bright-contrast rod-shaped phase (identified by the white arrows) some of which are

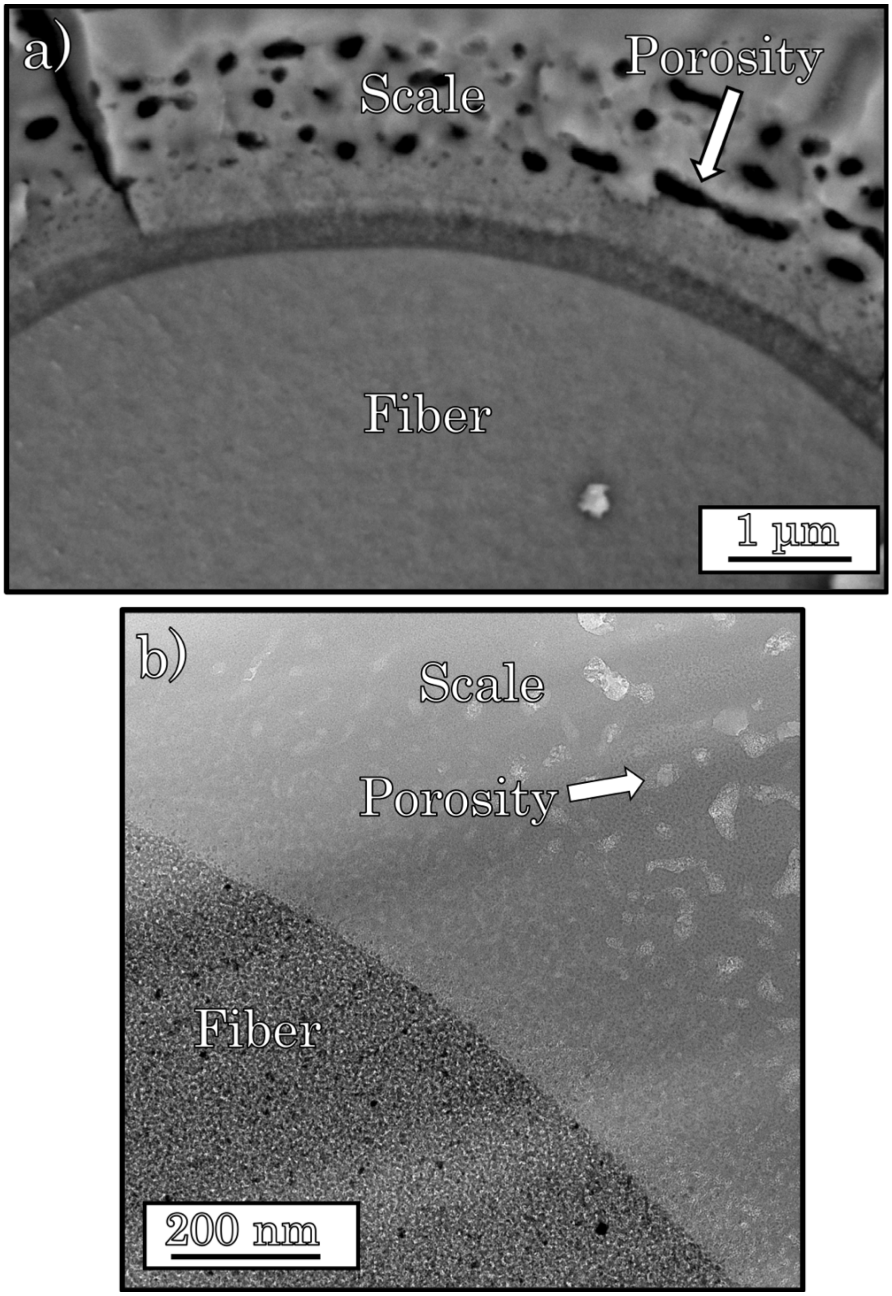

Figure 2.5. a) Backscattered SEM image and b) TEM image of the fiber-scale interface on a Hi Nicalon fiber after exposure to ~60 µg/cm^2 of Na_2SO_4 for 24h at 1000°C in a 0.1% SO_2-O_2 gaseous environment.

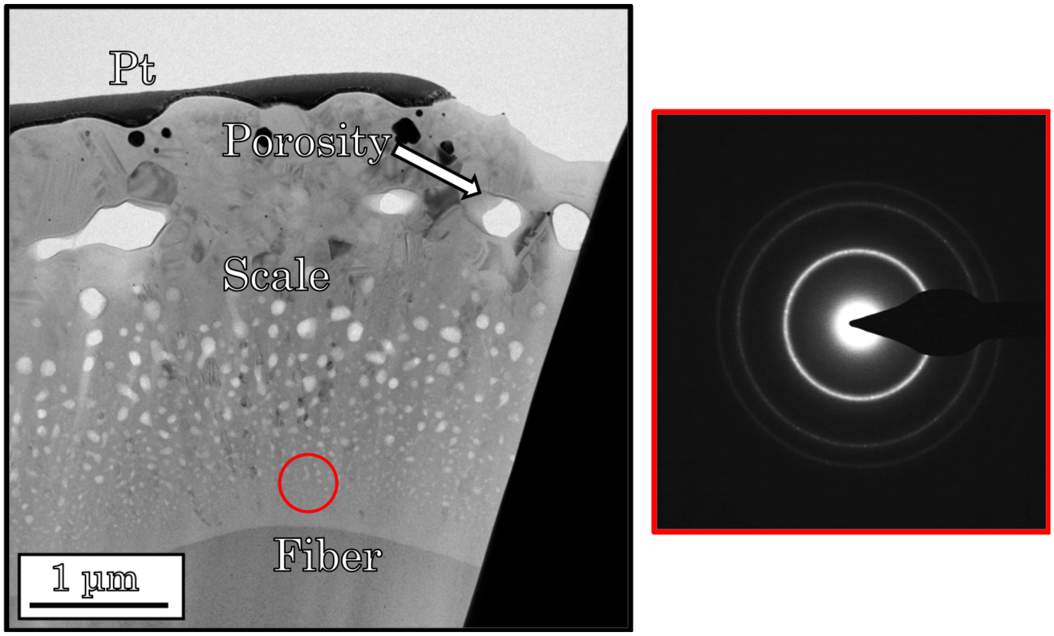

Figure 2.6. TEM image (left) of the fiber-scale interface on a Hi Nicalon fiber after exposure to ~60 μg/cm^2 of Na_2SO_4 for 24h at 1000°C in a 0.1% SO_2-O_2 gaseous environment and the selected diffraction area (right) from the region circled in red.

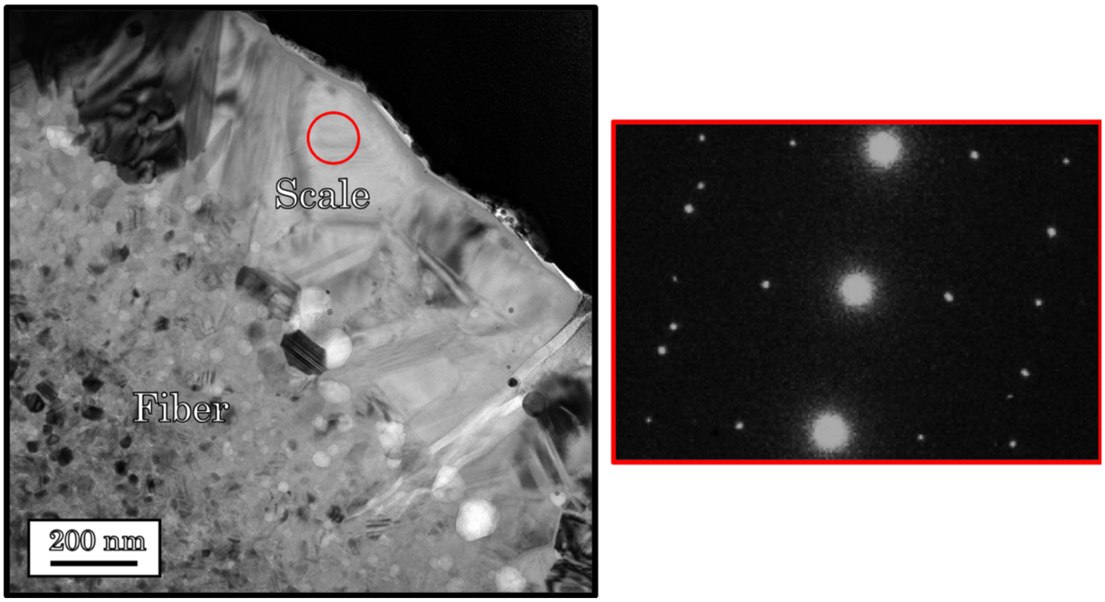

Figure 2.7. TEM image (left) of the fiber-scale interface on a Hi Nicalon S fiber after exposure to ~60 μg/cm^2 of Na_2SO_4 for 24h at 1000°C in a 0.1% SO_2-O_2 gaseous environment and the selected diffraction area (right) from the region circled in red.

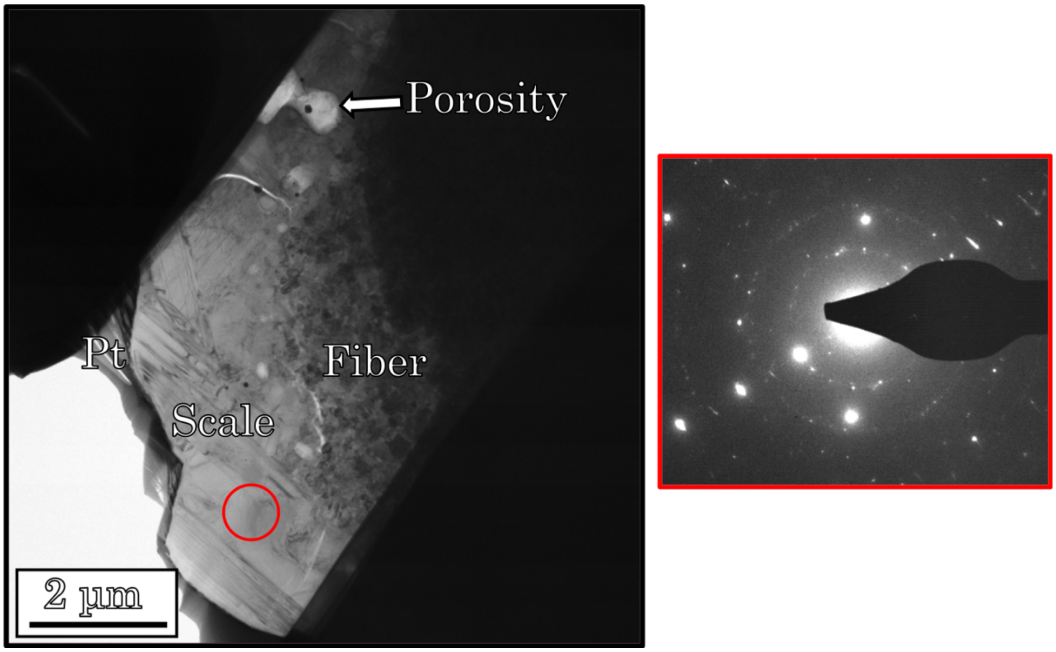

Figure 2.8. TEM image (left) of the fiber-scale interface on a Sylramic iBN fiber after exposure to ~60 μg/cm^2 of Na_2SO_4 for 24h at 1000°C in a 0.1% SO_2-O_2 gaseous environment and the selected diffraction area (right) from the region circled in red.

several microns long, are found only in the surface of Sylramic and Sylramic iBN fibers, which can be seen in Figure 2.9c) and 2.9d). SEM images and corresponding elemental maps in plan-view of the reaction products formed on Hi Nicalon and Sylramic iBN fibers after exposure to Na_2SO_4 for 24h at 1000°C were analyzed to determine the local chemistry, which can be seen in Figures 2.10 and 2.11. EDS was not able to detect B and Na in the reaction products, indicating levels of those elements in this area were below the detection limits of EDS, which is ~1% for light elements. It can be seen from the Si and O maps, that a continuous, silicon oxide reaction product formed on both Hi Nicalon and Sylramic iBN fiber types. The bright-phase contrast particles residing within the SiO_2 reaction product of Sylramic and Sylramic iBN fibers seen in Figure 2.9c)-d) were identified as titanium oxide. Higher magnification imaging and chemical analysis using TEM and EFTEM of the

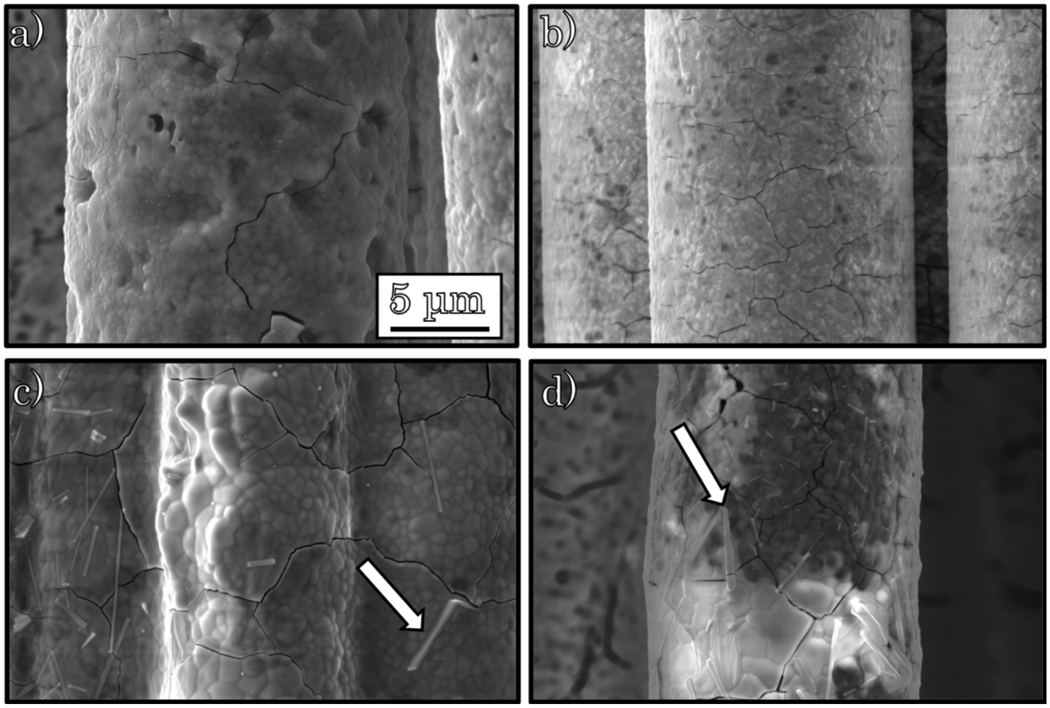

Figure 2.9. Backscattered SEM images of a) Hi Nicalon b) Hi Nicalon S c) Sylramic and d) Sylramic iBN fibers in plan-view after exposure to ~60 μg/cm^2 for 24h at 1000°C in a 0.1% SO_2-O_2 gaseous environment.

fiber-scale interface of Sylramic and Sylramic iBN fibers after exposure for 24h at 1000°C was performed, which can be seen in Figures 2.12 and 2.13. In both of these figures, the TEM images can be seen on the left while the corresponding color-coded B (red), Ti(green) and O(blue) EFTEM maps can be seen on the right. Within the fiber are the yellow TiB_2 (green+red→yellow) and red B_4C crystallites. The scale itself is purple, indicating it contains both B and O (blue+red →purple), while within the scale are green Ti oxide particles. EFTEM mapping results suggest that the TiB_2 and B_4C phases also oxidize during exposure.

Time dependent ICP-OES analysis on all SiC fibers tested was conducted to determine elemental composition of corrosion product levels, well below the resolution limits of EDS, which can be seen in Figure 2.14. The water digestion results can be seen in the left-hand side of this figure,

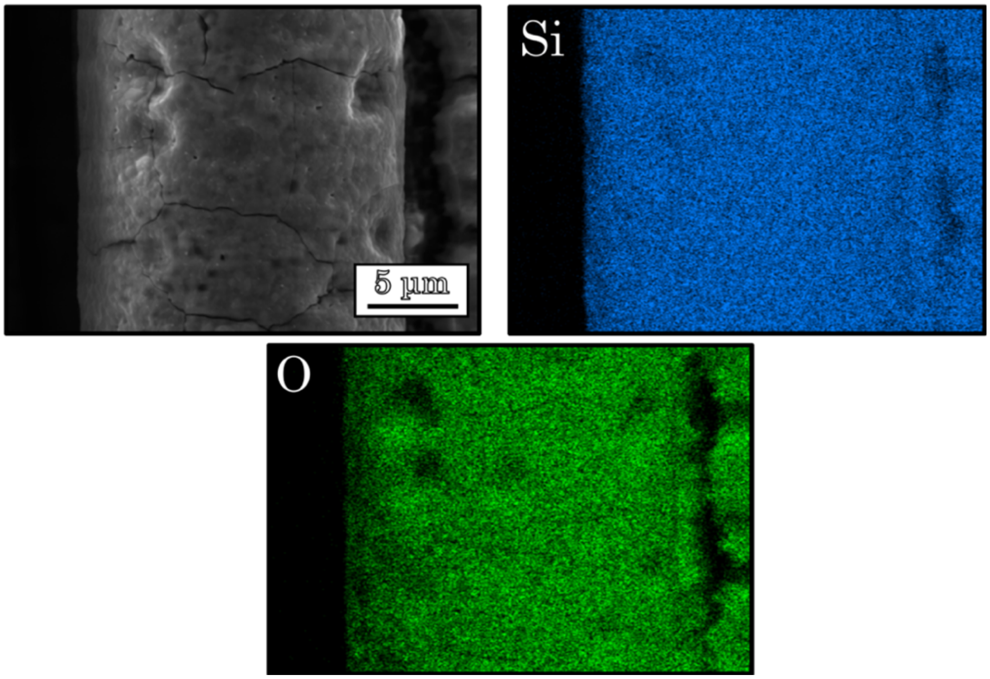

Figure 2.10. Backscattered electron SEM image and corresponding Si and O EDS maps of the surface of a Hi Nicalon fiber after exposure to ~60 µg/cm^2 of Na_2SO_4 for 24h at 1000°C in a 0.1% SO_2-O_2 gaseous environment.

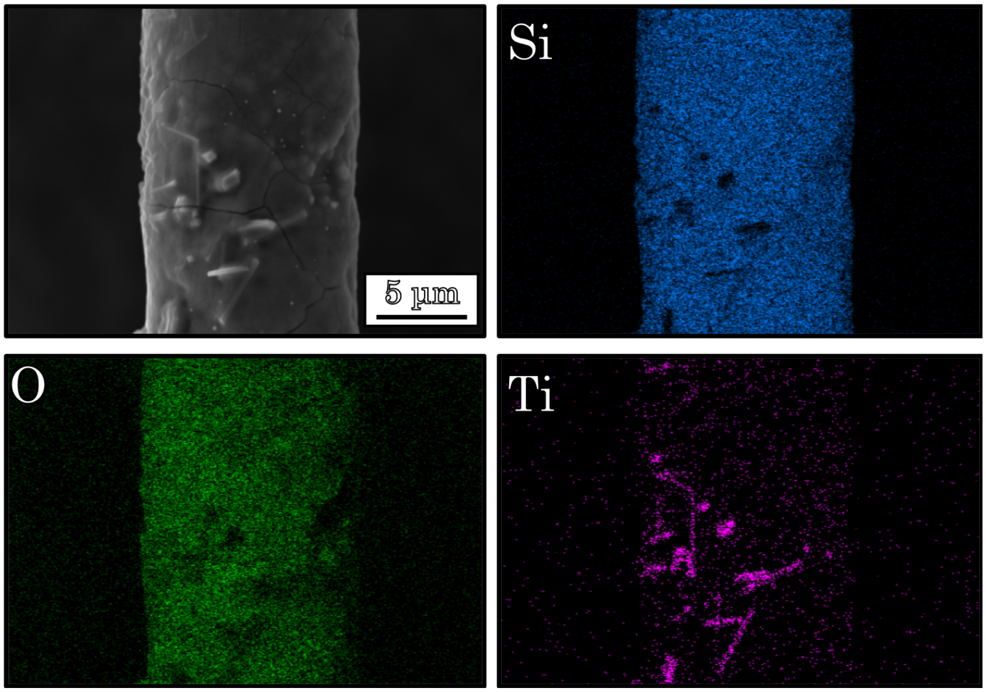

Figure 2.11. Backscattered electron SEM image and corresponding Si, O, and Ti EDS maps of the surface of a Sylramic iBN fiber after exposure to ~60 µg/cm^2 of Na_2SO_4 for 24h at 1000°C in a 0.1% SO_2-O_2 gaseous environment.

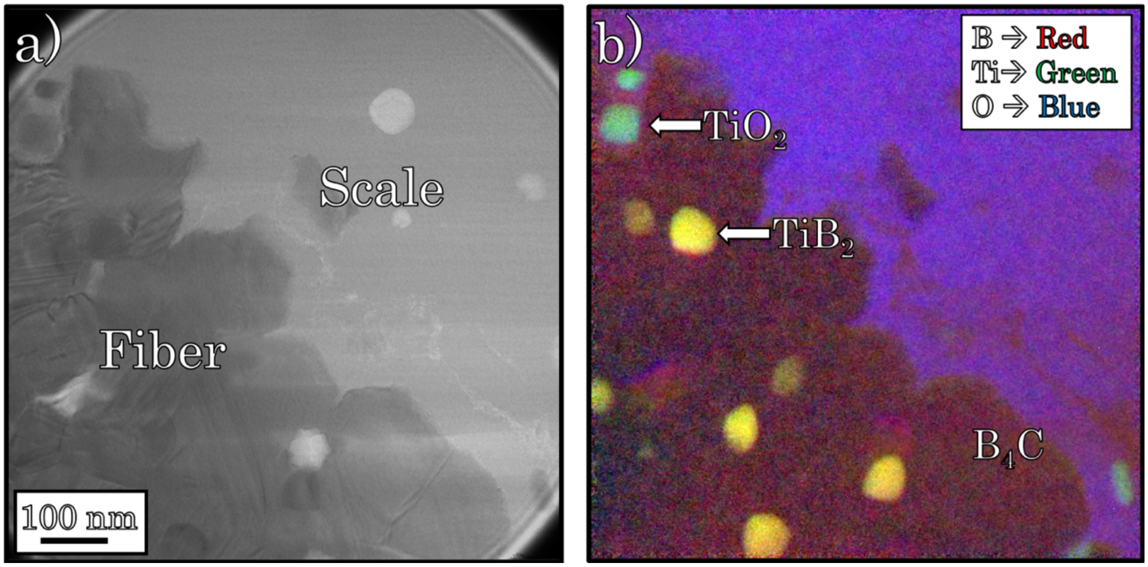

Figure 2.12. a) Dark-field TEM image of the fiber-scale interface of a Sylramic fiber after exposure to ~60 μg/cm^2 of Na_2SO_4 for 24h at 1000°C in a 0.1% SO_2-O_2 gaseous environment and b) B (red) Ti (green) and O (blue) EFTEM map of the same area.

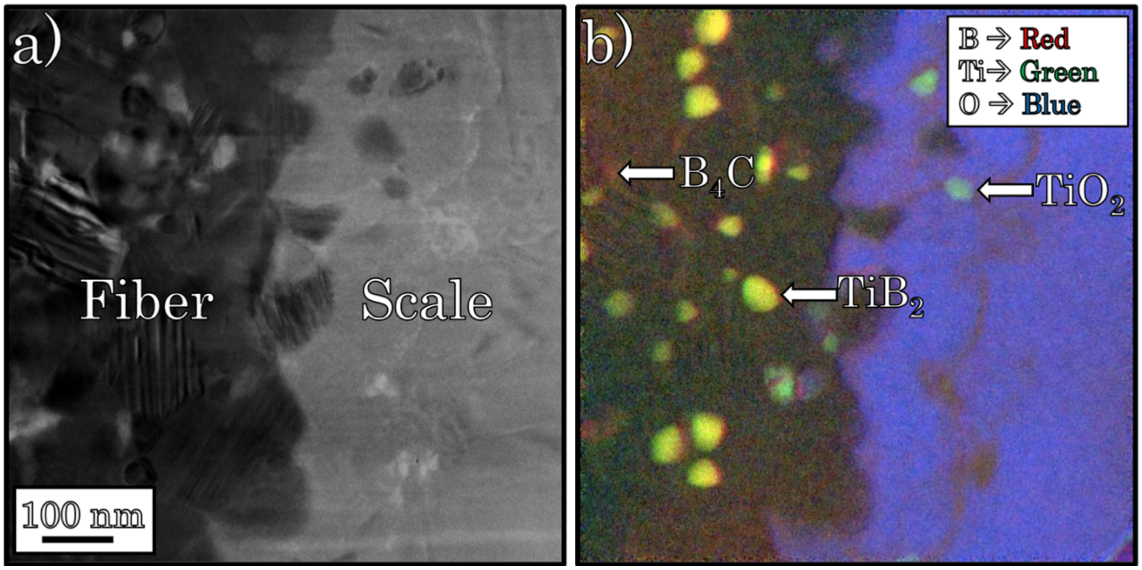

Figure 2.13. a) Dark-field TEM image of the fiber-scale interface of a Sylramic iBN fiber after exposure to ~60 μg/cm^2 of Na_2SO_4 for 24h at 1000°C in a 0.1% SO_2-O_2 gaseous environment and b) B (red) Ti (green) and O (blue) EFTEM map of the same area.

while the acid-digestion results can be seen on the right-hand side. The water and acid ICP-OES results for Hi Nicalon can be seen in Figure 2.14a)-b), Figure 2.14c)-d) for Hi Nicalon S, Figure 2.14e)-f) for Sylramic, and Figure 2.14g)-h) for Sylramic iBN. As seen in the left-hand side of Figure 2.14, water digestion suggest a sodium silicate layer formed on Hi Nicalon and Hi Nicalon S fiber types, indicated by the detection of both Si and Na. However, no water soluble reaction product was detected in the water digestion of Sylramic and Sylramic-iBN fibers across the entire exposure period. Additionally, low levels of S detected in the water digestion in all four fiber types is consistent with complete consumption or volatilization of Na_2SO_4 during exposure, as Na_2SO_4 is water soluble. Acid digestion, seen in the right-hand side of Figure 2.14, revealed that a SiO_2 reaction product formed on all fiber types as SiO_2 is soluble in HF. Total Si levels revealed that Hi Nicalon fibers were consumed the most rapidly after exposure for 24h at 1000°C. However, a flattening in Si consumption over time did occur for the other three fiber types. It should be noted that only ~10 μg of Si, an insignificant amount, were detected in baseline water + acid from all fiber types. Ti, Na and B levels detected in the acid digestion of Sylramic and Sylramic iBN fibers after exposure can be seen in Figure 2.15. Na levels in both fiber types dropped to near zero levels after 24h of exposure, indicating complete Na_2SO_4 volatilization or consumption likely occurred. Ti and B levels in both fiber types were generally constant over time, with more Ti and B residing in the reaction product of Sylramic iBN fibers.

2.3.3 SiC Fiber Oxidation Kinetics

Assessment of the SiC fiber oxidation reaction kinetics with Na_2SO_4 were performed using oxide thickness measurement, which can be seen in Figure 2.16. Average oxide thickness values are reported for all fibers for

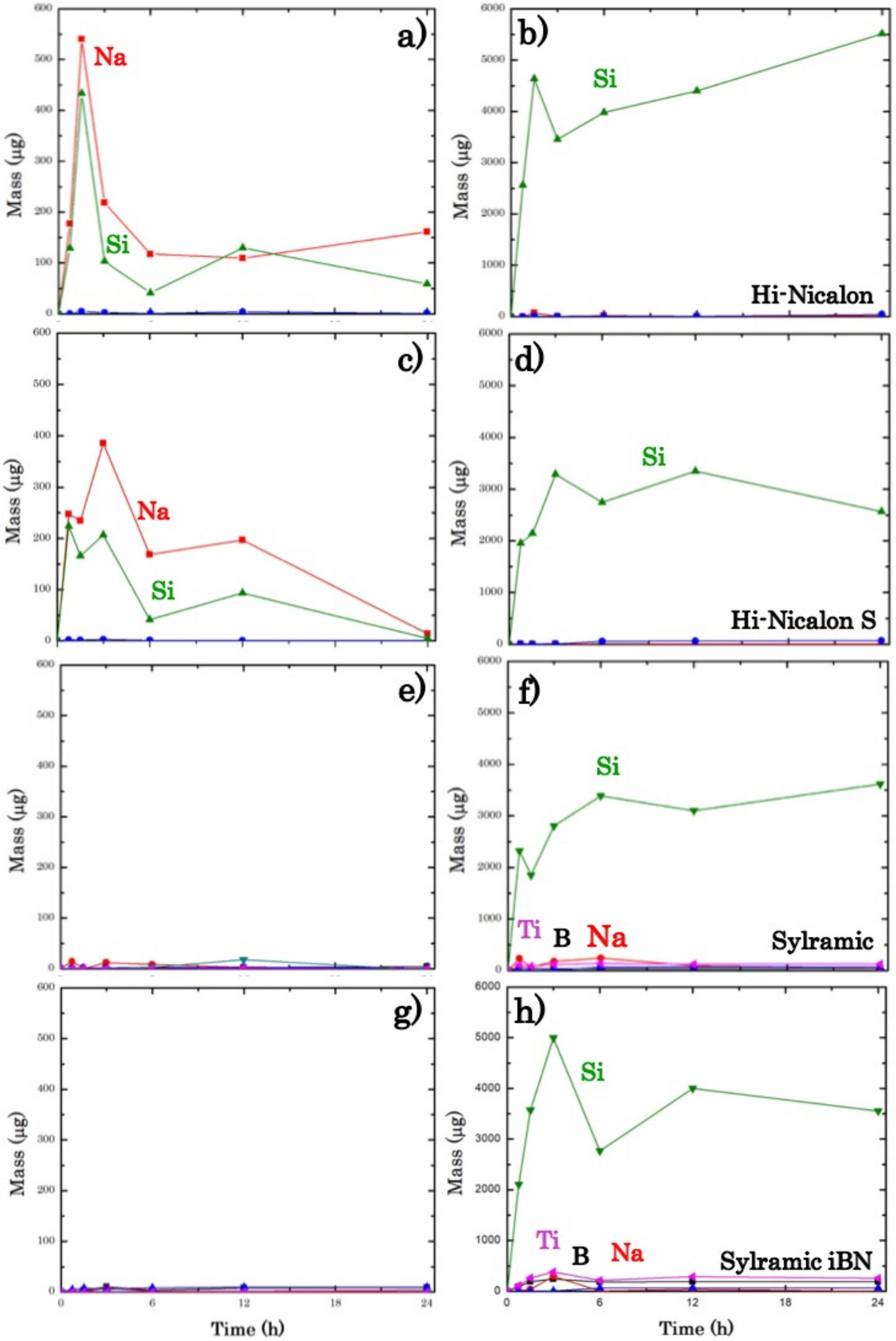

Figure 2.14. Elemental composition (in μg) of the reaction products formed on SiC fibers after exposure to ~60 μg/cm² Na_2SO_4 at 1000°C in a 0.1% SO_2-O_2 gaseous environment as a function of time. Results from the water digestion are reported on the left-hand side and after acid digestion on the right-hand side.

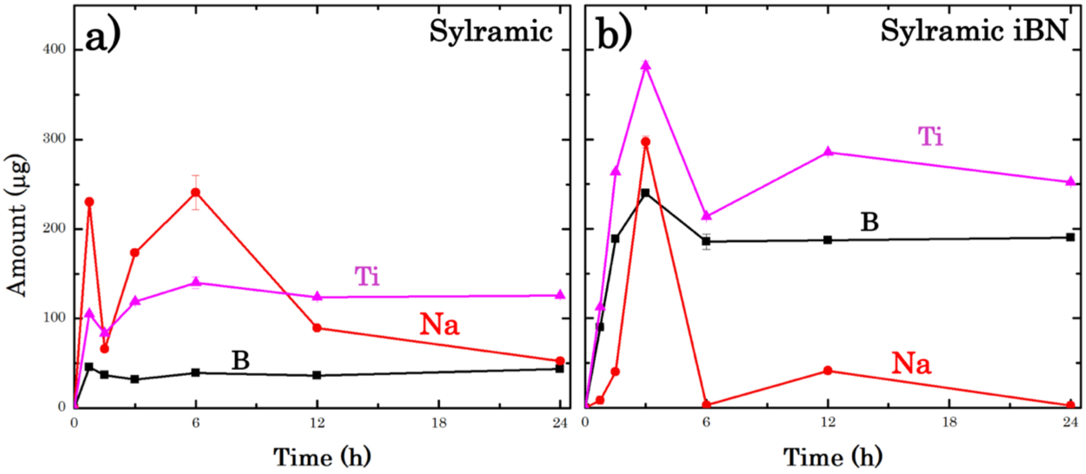

Figure 2.15 Na, Ti and B composition (in μg) in the acid digestion reaction product formed on Sylramic and Sylramic iBN fibers after exposure to ~60 μg/cm^2 Na_2SO_4 at 1000°C in a 0.1% SO_2-O_2 gaseous environment as a function of time.

exposure times up to 24h after exposure at 1000°C. The uncertainty bars seen in Figure 2.16 represent variation in oxide thickness within a specimen used for measurement and not measurement error. Hi Nicalon (dark gray) fibers oxidized most rapidly after exposure for 24h with average oxide thicknesses of ~2 μm, Sylramic iBN fibers produced average TGO thickness ~0.75 μm over the same period. Both Hi Nicalon S and Sylramic fibers produced nearly equally thick oxides of ~0.5 μm after 24h of exposure. Hi Nicalon S, Sylramic and Sylramic iBN fiber types produced oxides ~3-4x less thick than those formed on Hi Nicalon. Another important observation is that oxides formed on Hi Nicalon fibers increased in average thickness over time, while Hi Nicalon S, Sylramic and Sylramic iBN fiber types had an initial rapid oxidation period lasting only a few hours, that was followed by a kinetic plateau that lasted throughout the 24h exposure period.

The effect of Na_2SO_4 on the fiber oxidation rates both with and without Na_2SO_4 at 1000°C in dry O_2(g) were compared. No studies reported in literature have investigated the oxidation of Sylramic iBN at 1000°C in dry

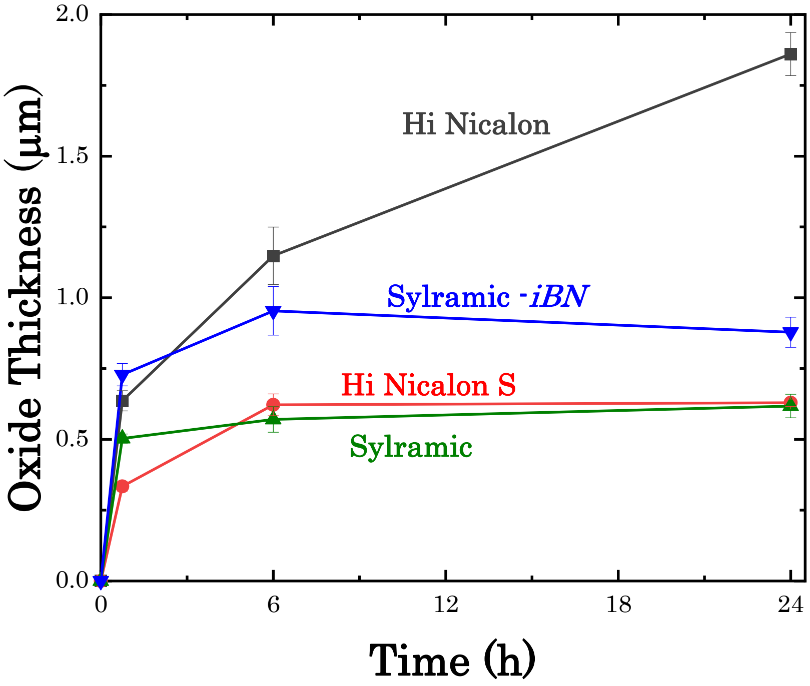

Figure 2.16. Plots showing the average oxide thickness of Hi Nicalon, Hi Nicalon S, Sylramic and Sylramic iBN fibers after to ~60 µg/cm^2 of Na_2SO_4 at 1000°C in a 0.1% SO_2-O_2 gaseous environment as function of time.

O_2(g). No currently published studies in the literature exist for the hot corrosion of any SiC fibers. Several studies have investigated the oxidation kinetics of Hi Nicalon, Hi Nicalon S and Sylramic fibers at 1000°C in Na_2SO_4-free, dry O_2(g) environments. The effect of Na_2SO_4 on the oxidation kinetics of Hi Nicalon, Hi Nicalon S and Sylramic fibers relative to exposure in Na_2SO_4-free, dry O_2(g) environments at 1000°C can be seen plotted in Figure 2.17. The values from literature in this figure were reported as oxide thickness values or as parabolic oxidation rates (k_p).[7, 9, 10, 45, 46] This comparison reveals that in the presence of Na_2SO_4 all SiC fiber types exhibit increased oxide growth kinetics relative to exposure in Na_2SO_4-free, dry O_2(g) environments. Relative to Na_2SO_4-free environments, Na_2SO_4 increases average oxide thickness by a factor of ~2x for Hi Nicalon S and

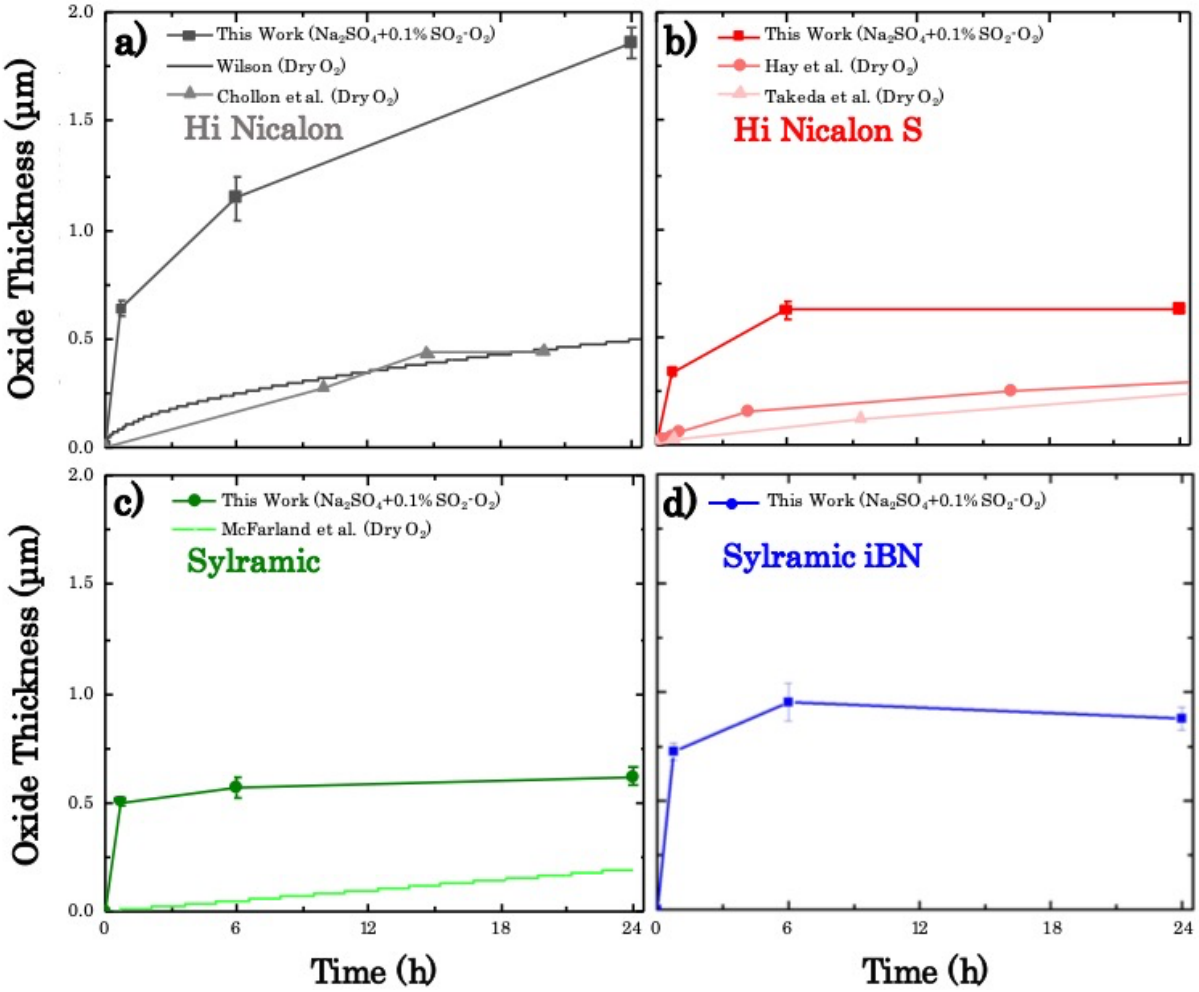

Figure 2.17. Plots showing the oxide thickness of a) Hi-Nicalon b) Hi-Nicalon S and c) Sylramic fibers exposed to ~60 $\mu g/cm^2$ Na_2SO_4 for times up to 24h at 1000°C in 0.1% SO_2-O_2 gaseous environment compared to oxide thickness values reported in literature at 1000°C without Na_2SO_4 in dry $O_2(g)$ present.[7, 9, 10, 45, 46]

Sylramic fiber types and nearly a factor of ~4x for Hi Nicalon fiber types relative to Na_2SO_4 free environments after 24h exposures.

2.3.4 SiC Fiber Surface Degradation

Imaging of the surfaces of as-received SiC fibers in plan-view after baseline soaking in the same two-step water +acid digestion used to for ICP-

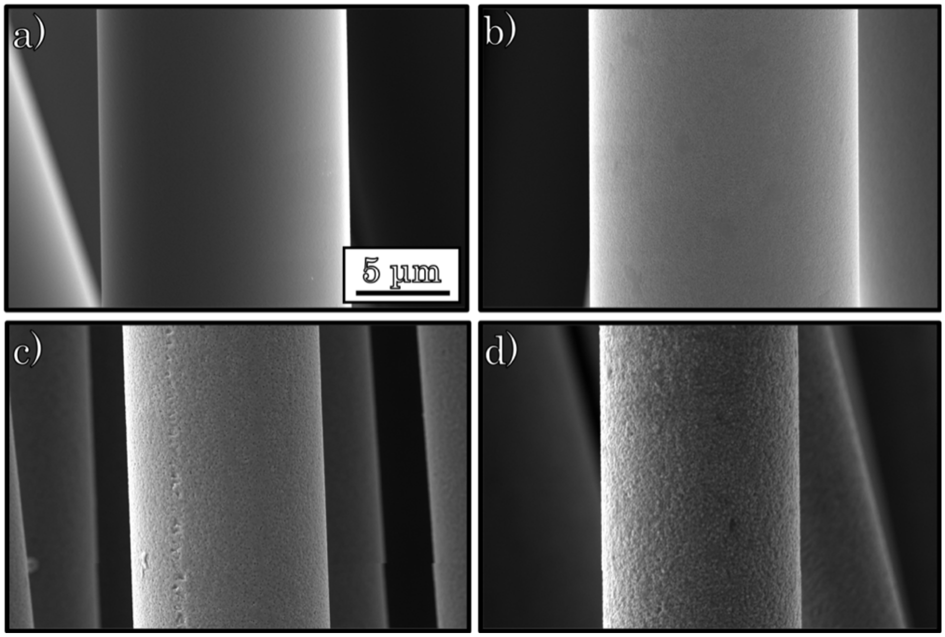

Figure 2.18. Backscattered SEM images of a) Hi Nicalon b) Hi Nicalon S c) Sylramic and d) Sylramic iBN fibers after a baseline soak in water then HF without Na_2SO_4 deposition and exposure.

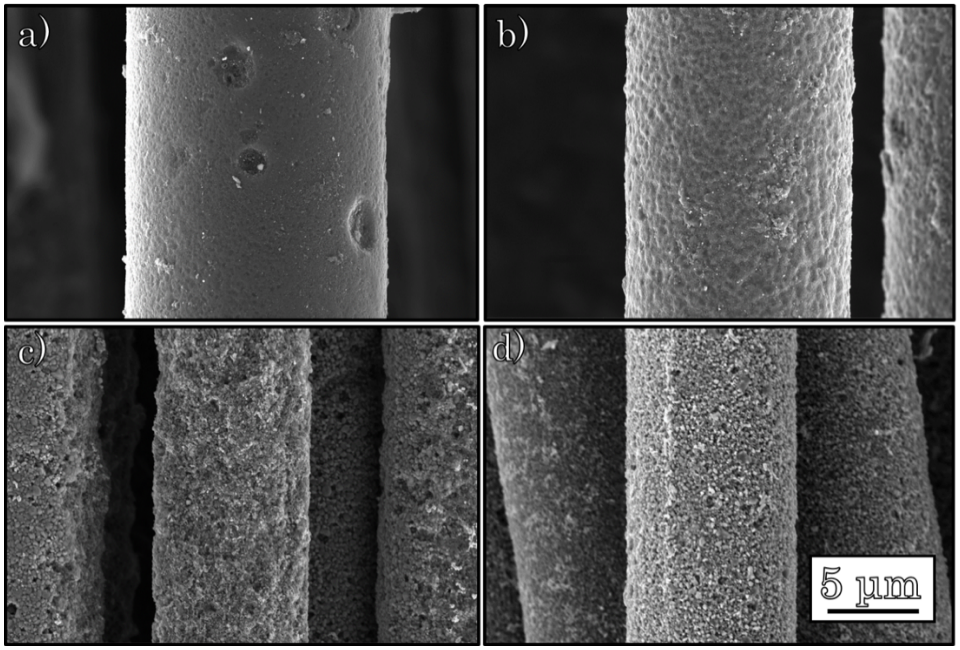

Figure 2.19. Backscattered electron SEM images after reaction product removal using water + acid digestion on a) Hi Nicalon b) Hi Nicalon S c) Sylramic and d) Sylramic iBN exposed to ~60 µg/cm^2 Na_2SO_4 for 6h at 1000°C in 0.1% SO_2-O_2 gaseous environment.

OES composition determination water + acid digestion, revealed the digestion left no visible attack features on all fiber types, seen in Figure 2.18. Additionally, all fiber types were stable in digestion solutions, as only ~10 µg of Si was detected for all SiC fiber types. However, imaging of fiber surfaces after removal of reaction products formed on specimens after exposure for 6h at 1000°C revealed significant attack to the fiber occurred, seen in Figure 2.19. These features formed in less than 6h, indicating attack of the surface of SiC fibers after exposure to Na_2SO_4 is rapid.

2.4 Discussion

2.4.1 Hot Corrosion of SiC Fibers

High temperature oxidation of Hi Nicalon, Hi Nicalon S, Sylramic and Sylramic iBN fibers relevant for application in SiC CMCs in the presence of Na_2SO_4 resulted in rapid oxidation and pitting. All SiC fibers oxidized faster (~2-4x) in the presence of Na_2SO_4 than in Na_2SO_4-free environments at 1000°C, indicating their high susceptibility to rapid environmental degradation from Na_2SO_4 deposits. Additionally, the hot corrosion of these fibers resulted in localized pitting into their surfaces, with pits forming within a few hours. These pits are not desired, as they serve as stress concentration sites that can lead to premature fracture. Microscopy and electron diffraction also revealed that the reaction product on all fiber types were completely crystalline after exposure for 24h, but were also highly cracked. Although not confirmed, the layers are likely α-cristobalite, α-tridymite or a mixture of the two phases, as both of these SiO_2 phases are known to form after inverting during cooling from their high-temperature β-forms. The observed cracking is likely a result of the β-to-α inversion of these phases. The combination of rapid oxidation, pitting into the load-bearing phase of SiC CMCs from Na_2SO_4 deposits, and cracking within the oxide layer are all problems for SiC CMCs.

Both pitting and the increased oxidation behavior relative to Na_2SO_4-free environments observed with SiC fibers is consistent with previously reported hot corrosion studies of bulk SiC. This enhanced oxidation behavior is attributed to rapid O_2(g) transport through a liquid sodium silicate layer. Analysis of the SiO_2 rich side of the Na_2O-SiO_2 binary phase diagram in Figure 2.20, reveals that Na_2O additions to thermally grown SiO_2 at 1000°C will result in liquid sodium silicate formation due to several low melting eutectics.[47] This liquid layer is highly nonprotective, as O_2(g) transport in liquid sodium silicate is 6-9 orders of magnitude faster than through crystalline and amorphous SiO_2.[36, 40] However, an oxidation kinetic plateau occurs after formation of a continuous or non-porous SiO_2 (crystalline or amorphous) layer between the SiC substrate and highly-permeable sodium silicate layer.[34, 35] This kinetic plateau behavior was observed through a multitude of characterization techniques for Hi Nicalon S, Sylramic and Sylramic iBN fibers within 0.75h-3h of exposure. Microscopy and electron diffraction determined the reaction product on Hi Nicalon S, Sylramic, and Sylramic iBN fibers types were relatively low in porosity and completely crystalline, while the reaction product on Hi Nicalon fibers were highly porous and completely crystalline. A possible explanation for this lack of kinetic plateau behavior in Hi Nicalon fibers lies in its highly porous reaction layer, a layer more porous than those formed on the other three fiber types. The scales formed on Hi Nicalon possessed pores whose size ranged from tens to hundreds of nanometers in diameter, and existed from the fiber-scale interface all the way to the scale-gas interface. These pores formed as a result of oxidation of C-containing β-SiC, free C and amorphous SiCO phases into CO(g), which can be seen below in Equations (2.1), (2.7) and (2.8):

$$SiC + 3/2O_2(g) \rightarrow SiO_2 + CO(g) \tag{2.1}$$

$$C(s) + 1/2O_2(g) \rightarrow CO(g) \tag{2.7}$$

$$SiCO + O_2 \rightarrow SiO_2 + CO(g) \tag{2.8}$$

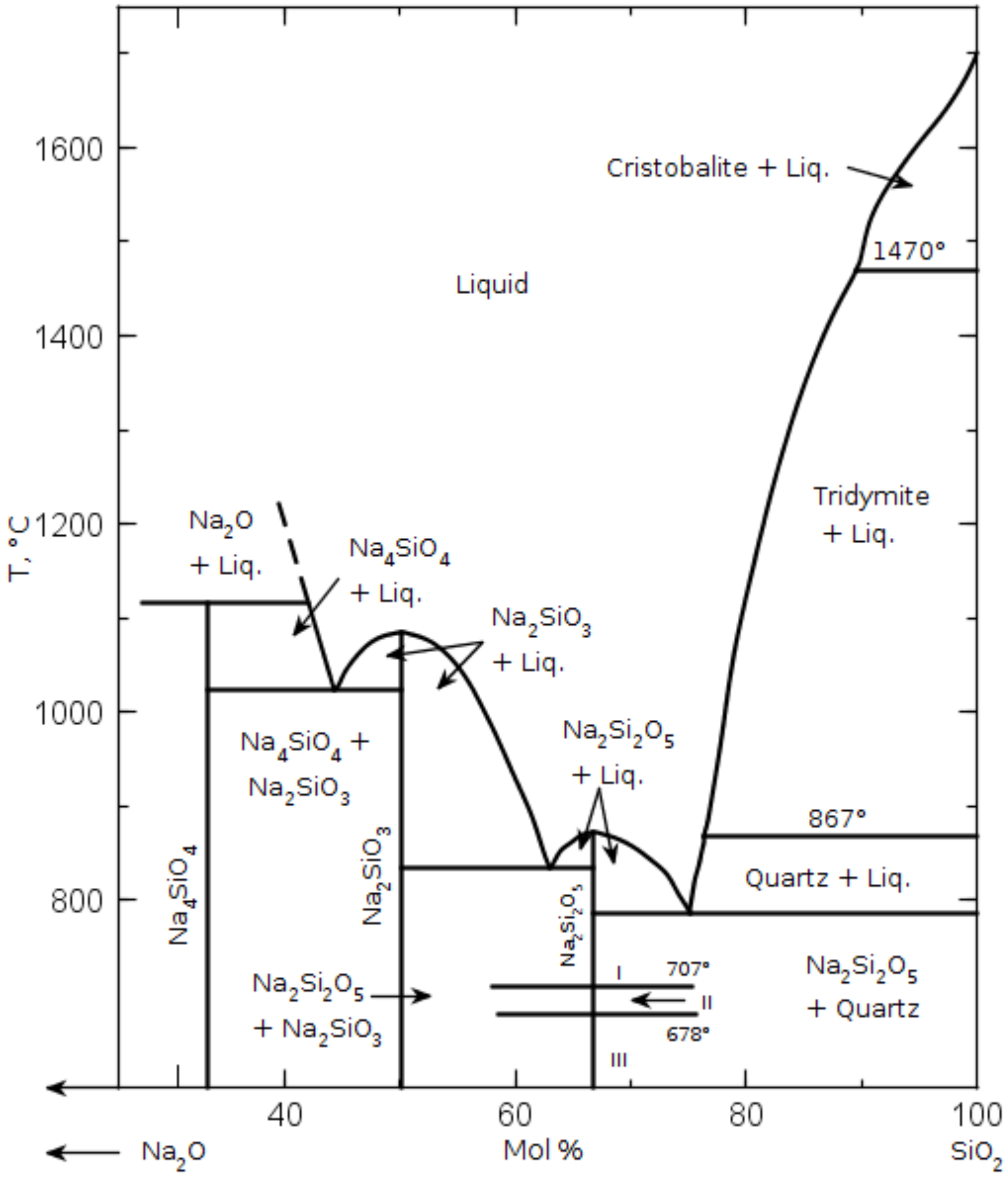

Figure 2.20. SiO_2 rich side of the experimental Na_2O-SiO_2 phase diagram.[47]

Due to 40% more C residing within Hi Nicalon than the other three fiber types, more CO(g) is produced than the other fibers, as they have C:Si stoichiometries equal to ~1 as compared to ~1.4 for Hi Nicalon. The outward migrating CO(g) produces a reaction-layer wide, pore network that serves as a fast-diffusion pathway for inward transporting O_2(g). Despite being crystalline, these gas-phase formed pores prevent a kinetic plateau from occurring.

Along with creating more porosity than the other fibers types, the extra C present in Hi Nicalon fibers increases the basicity of the Na_2SO_4 melt. This increase in basicity explained by Jacobson, allows for increased Na_2O to be released from Na_2SO_4 due to reaction with C or CO(g) (Equations (2.5) and (2.6)). ICP-OES measurement revealed that Na levels in both acid and water digestion of the other fiber types were consistently lower than in the reaction product formed on Hi Nicalon fibers. This higher Na content can be observed in the first 1.5h of exposure in Figure 2.14. This liquid sodium silicate allows for the observed rapid reaction due to fast O_2(g) transport through the layer. However, it seems unlikely that C enhanced SiO_2 dissolution explained by Jacobson entirely explains both the (i) increased oxidation kinetics and (ii) the absence of a kinetic plateau for Hi Nicalon. As mentioned previously, Hi Nicalon was confirmed to possess a highly crystalline SiO_2 scale. This reaction layer should be highly protective due to a 6-9 order of magnitude decrease in O_2(g) diffusivity through the SiO_2 layer relative to a sodium silicate layer. However, despite being completely crystalline just like the other fiber types, no oxidation kinetic plateau in Hi Nicalon occurred. More work is needed to understand how C, gas-phase induced porosity within reaction product layers, and SiO_2 layer build-up effects the oxidation kinetics of Hi Nicalon fibers exposed to Na_2SO_4.

2.4.2 Hot Corrosion of Sylramic and Sylramic iBN

The corrosion mechanism in the presence of Na_2SO_4 is slightly different for Sylramic and Sylramic iBN than for Hi Nicalon and Hi Nicalon S fiber types. A difference between Hi Nicalon + Hi Nicalon S and Sylramic + Sylramic iBN, is the presence of TiB_2 and B_4C crystallites within Sylramic and Sylramic iBN fiber types, and a BN surface layer present on Sylramic iBN fiber types. Along with oxidation of the β-SiC grains, oxidation of the TiB_2 + B_4C crystallites and BN surface layer also occurs. Likely oxidation equations for these phase can be seen below in Equations (2.9), (2.10), and (2.11):

$$TiB_2 + 5/2O_2(g) \rightarrow TiO_2 + B_2O_3 \tag{2.9}$$

$$B_4C + 4O_2(g) \rightarrow 2B_2O_3 + CO_2\,(g) \tag{2.10}$$

$$2BN + 3/2O_2(g) \rightarrow B_2O_3(g) + N_2(g) \tag{2.11}$$

It is known that Na_2O, SiO_2 and B_2O_3 mix to form a water-soluble, sodium borosilicate.[26, 48] However, B, Na and Si were only present in the acid digestion (Figure 2.14), indicating sodium borosilicate formation did not occur, rapid volatilization (< 0.75h) occurred, or the silicate reaction product was water insoluble due to a high SiO_2 content. Analysis of the acid digestion of both fiber types (Figure 2.14), reveals Na volatilization did occur after several hours of exposure, while Ti and B levels were relatively constant over time indicating very little volatilization occurred. Due to the existence of the BN layer, more B is detected (Figure 2.15) in the reaction product of Sylramic iBN than Sylramic fibers, while the higher Ti levels detected in Sylramic iBN are an anomaly as Sylramic and Sylramic iBN fibers have the same phase content. The B was soluble in the crystalline SiO_2 layer formed on Sylramic and Sylramic iBN fibers, while the Ti resided in TiO_2 rods within the crystalline SiO_2 oxide.

2.5 Implications For Turbine Engine Application

SiC fibers are the reinforcement phase inside of SiC CMCs, serving as the load-bearing phase for SiC CMCs. However, Na_2SO_4 deposition onto exposed regions of SiC CMCs will result in increased oxidation kinetics and pitting of the load bearing fiber phase. This increased consumption rate and pitting of the load-bearing fiber phase within the CMC could lead to component fracture and failure. As evident by the more rapid hot corrosion of Hi Nicalon relative to Hi Nicalon S, Sylramic, and Sylramic iBN, an important strategy to limit SiC fiber damage is to employ fibers comprised mainly of SiC, and also which are highly stoichiometric. Further strategies that will improve stoichiometric SiC fiber resistance from environmental damage from Na_2SO_4 deposits is the usage of an EBC system that will prevent Na from reaching the CMC. This implies that EBCs should be highly adherent to CMCs while also be highly impermeable to Na. Additionally, free C within the SiC matrix should be removed as this will promote more basic conditions and will oxidize into gaseous species. These extra gas species, just like that observed in Hi-Nicalon will produce porosity within corrosion products in the CMC and EBC system, possibly leading to more rapid coating spallation.

2.6 Conclusions

Hi Nicalon, Hi Nicalon S, Sylramic and Sylramic iBN SiC fibers were exposed to ~60 μg/cm^2 of Na_2SO_4 for times up to 24h at 1000°C in a 0.1% SO_2-O_2(g) environment. Hi Nicalon fibers reacted the most severely of all the fiber types after exposure to Na_2SO_4. Hi Nicalon's enhanced oxidation was attributed to it's high C:Si stoichimetry of ~1.4. The high carbon content led to more basic Na_2O dissolution of SiO_2 scale and more CO(g) generated pores in the corrosion products, both mechanisms decreasing the protective capability of the SiO_2 scale and increasing the fibers oxidation rate. Pitting in all fiber surfaces after removal of reaction products was also observed, suggesting hot corrosion will degrade load-bearing capability of all SiC fibers.

References

1. Zok FW. Ceramic Matrix Composites Enable Revolutionary Gains in Turbine Efficiency. 2016;95:22–28.
2. Melissae Fellet. Ceramic-Matrix Composites Take The Heat. *MRS Bull*. 2015;40:916–7.
3. Deal BE, Grove AS. General Relationship for the Thermal Oxidation of Silicon. *J Appl Phys*. 1965;36(12):3770–3778.
4. Ramberg EC, Gary C, Spear KE, Tressler RE, Ramberg CF. Passive-Oxidation Kinetics of High-Purity Silicon Carbide from 800° to 1100°C. *J Am Ceram Soc*. 1996;79(11):2897–2911.
5. Hay RS, Fair GE, Bouffioux R, *et al.* Relationships Between Fiber Strength, Passive Oxidation and Scale Crystallization Kinetics of Hi-Nicalon™-S SiC Fibers. *J Am Ceram Soc*. 2011;94(11):3983–3991.
6. Hay RS, Corns R. Passive oxidation kinetics for glass and cristobalite formation on Hi-Nicalon™-S SiC fibers in steam. *J Am Ceram Soc*. 2018;101(11):5241–5256.
7. Wilson M, Opila EJ. A Review of SiC Fiber Oxidation with a New Study of Hi-Nicalon SiC Fiber Oxidation. *Adv Eng Mater*. 2016;18(10):1698–1709.
8. Parthasarathy TA, Mah T, Folsom CA, Allan KP. Microstructural Stability of Nicalon at 1000°C in Air after Exposure to Salt (NaCl) Water. *J Am Ceram Soc*. 1995;78(7).
9. Chollon G, Pailler R, Naislan R, Laanani F, Monthouix M, Olry P. Thermal stability of a PCS-derived SiC fibre with a low oxygen content (Hi-Nicalon). *J Mater Sci*. 1997;32(2):327–347.
10. Hay RS, Fair GE, Bouffioux R, *et al.* Hi-Nicalon™-S SiC Fiber Oxidation and Scale Crystallization Kinetics. *J Am Ceram Soc*. 2011;94(11):3983–3991.
11. Wu S, Cheng L, Zhang L, Xu Y, Zhang J, Mei H. Wet oxidation behaviors of Hi-Nicalon fibers. *Appl Surf Sci*. 2006;253(3):1447 – 1450.
12. Clark TJ, Arons RM, Stamatoff JB, Rabe J. Thermal Degradation of Nicalon™ SiC Fibers. *Proc. 9th Annu. Conf. Compos. Adv. Ceram. Mater. Ceram. Eng. Sci. Proc.* John Wiley & Sons, Ltd; 2008:576–588.
13. Hay RS. Crystallization kinetics for SiO_2 formed during SiC fiber oxidation in steam. *J Am Ceram Soc*. 2019;102(9):5587–5602.
14. Ichikawa H. Polymer-Derived Ceramic Fibers. *Annu Rev Mater Res*. 2016;46(1):335–356.
15. Flores O, Bordia RK, Nestler D, Krenkel W, Motz G. Ceramic Fibers Based on SiC and SiCN Systems: Current Research, Development, and Commercial Status. *Adv Eng Mater*. 2014;16(6):621–636.
16. Lipowitz J, Rabe JA. Structure and Properties of Sylramic Silicon Carbide Fiber- A Polycrystalline, Stoichiometric β-SiC Composition. 1997;18(3):147–157.
17. Buerger MJ, Lukesh J. The Tridymite Problem. *Science*. 1952;95:20.

18. Rockett TJ. The Thermal Stability of Purified Tridymite. *Am Mineral*. 1967;52:1233–1239.
19. Fenner CN. Stability Relations of the Silica Minerals. *Am J Sci*. 1913;36(4):331–384.
20. Flörke OW. Strukturanomalien bei Tridimyt und Cristobalit. *Berichte Dtsch Keram Ges*. 1955;32:369–381.
21. Fenner CN. The Relations Between Tridymite and Cristobalite. *Trans Soc Glass Technol*. 1919;3:116.
22. Council NR. Ceramic Fibers and Coatings: Advanced Materials for the Twenty-First Century. Washington, DC: The National Academies Press; 1998
23. Dong SM, Chollon G, Labrugère C, *et al.* Characterization of nearly stoichiometric SiC ceramic fibres. *J Mater Sci*. 2001;36(10):2371–2381.
24. Flörke OW. Des Kriställrten des SiO_2 und ihr Umwandlungsverhalten. *Berichte Dtsch Keram Ges*. 1961;38(3):89–97.
25. Flörke OW. Uber das Einstoffsystem SiO. *Naturwissenschaften*. 1956;43:419.
26. Rockett TJ. Phase Relations in the Systems Silica, Boron Oxide-Silica, and Sodium Oxide-Boron Oxide-Silica. The Ohio State University; Mineralogy; 1963
27. Hatch DM, Ghose S. The α-β phase transition in cristobalite, SiO_2. *Phys Chem Miner*. 1991;17(6):554–562.
28. Hill VG, Roy R. Silica Structure Studies: V, The Variable Inversion in Cristobalite. *J Am Ceram Soc*. 1958;41(12):532–537.
29. Withers RL, Thompson JG, Xiao Y, Kirkpatrick RJ. An electron diffraction study of the polymorphs of SiO_2-tridymite. *Phys Chem Miner*. 1994;21(7):421–433.
30. Stearns CA, Kohl FJ, Rosner DE. Combustion System Processes Leading to Corrosive Deposits. San Diego, California: 1981
31. Stringer J. Hot Corrosion of High-Temperature Alloys. *Annu Rev Mater Sci*. 1977;7(1):477–509.
32. Pettit F. Hot Corrosion of Metals and Alloys. *Oxid Met*. 2011;76(1):1–21.
33. Hagan JM. High Temperature Salt Deposit-Assisted of Silicon Carbide Ceramic Matrix Composites:Effects of Composite Chemistry and Architecture. University of Virginia, Materials Science and Engineering; 2015
34. Hagan JM, Opila EJ. High-Temperature Na_2SO_4 Deposit-Assisted Corrosion of Silicon Carbide – I: Temperature and Time Dependence. *J Am Ceram Soc*. 2015;98(4):1275–1284.
35. Jacobson NS. Kinetics and Mechanism of Corrosion of SiC by Molten Salts. *J Am Ceram Soc*. 1986;69(1):74–82.
36. Jacobson NS, Smialek JL. Hot Corrosion of Sintered α-SiC at 1000°C. *J Am Ceram Soc*. 1985;68(8):432–439.

37. Jacobson NS, Smialek JL. Corrosion Pitting of SiC by Molten Salts. 1986;133(12):2615–2621.
38. Carruth M, Baxter D, Oliveira F, Coley K. Hot-corrosion of silicon carbide in combustion gases at temperatures above the dew point of salts. *J Eur Ceram Soc*. 1998;18(16):2331 – 2338.
39. Fox DS, Smialek JL. Burner Rig Hot Corrosion of Silicon Carbide and Silicon Nitride. *J Am Ceram Soc*. 1990;73(2):303–311.
40. Lamkin MA, Riley FL, Fordham RJ. Oxygen mobility in silicon dioxide and silicate glasses: a review. *J Eur Ceram Soc*. 1992;10(5):347 – 367.
41. Jacobson NS. Corrosion of Silicon-Based Ceramics in Combustion Environments. *J Am Ceram Soc*. 1993;76(1):3–28.
42. Jacobson NS, Fox DS. Molten-Salt Corrosion of Silicon Nitride: II, Sodium Sulfate. *J Am Ceram Soc*. 1988;71(2):139–148.
43. Jacobson NS. Sodium sulfate: Deposition and dissolution of silica. *Oxid Met*. 1989;31(1):91–103.
44. Parthasarathy TA, Folsom CA, Zawada LP. Combined Effects of Exposure to Salt (NaCl) Water and Oxidation on the Strength of Uncoated and BN-Coated Nicalon™ Fibers. *J Am Ceram Soc*. 1998;81(7):1812–1818.
45. Takeda M, Urano A, Sakamoto J, Imai Y. Microstructure and Oxidation Behavior of Silicon Carbide Fibers Derived from Polycarbosilane. *J Am Ceram Soc*. 2000;83(5):1171–1176.
46. McFarland B, Opila EJ. Silicon Carbide Fiber Oxidation Behavior in the Presence of Boron Nitride. *J Am Ceram Soc*. 2018;101:5534–5551.
47. Kracek FC. The System Sodium Oxide-Silica. *J Phys Chem*. 1929;34(7):1583–1598.
48. Hagan JM, Opila EJ. High-temperature Na_2SO_4 deposit-assisted corrosion of silicon carbide–II: Effects of B, C, and Si. *J Am Ceram Soc*. 2017;100(2):761–773.

3 | BN Effects on Na_2SO_4 Deposit-Induced Hot Corrosion of α-SiC

3.1 Introduction

Non-load bearing components fabricated from silicon carbide (SiC) ceramic matrix composites (CMCs) have entered service into the hot section of GE Aviation's LEAP engines in 2016. CMCs lower operating costs and reduce harmful engine emissions due to their low density, high temperature capability, and reduced cooling load.[1, 2] The CMCs are comprised of small diameter, boron nitride (BN)-coated SiC fibers embedded in a SiC matrix. This structure allows for the required toughness needed for CMC components to serve in turbine engines. However, the high temperature oxidation and corrosion resistance of SiC CMCs remains a concern.

In dry O_2(g) containing environments, SiC reacts to form a SiO_2 reaction layer, as given in Equation (3.1)[3, 4]:

$$SiC + 3/2\ O_2(g) \rightarrow SiO_2 + CO(g) \tag{3.1}$$

The growth of SiO_2 on SiC is slow, forming a self-protective O_2(g) diffusion barrier to further reduce SiC oxidation.[3, 5–7] However, in environments which include B_2O_3- and Na_2O- containing species, SiC oxidation rates are increased due to the formation of thermally grown low-melting silicates. Molecular oxygen transport rates are faster through silicates than through pure SiO_2.[8–11] The formation of low-melting silicates on SiC CMC components during service is a concern, as B_2O_3 is present from the oxidation of SiC/BN/SiC CMC oxidation and Na_2O species are present in marine environments.

Boron nitride fiber coatings present as the fiber/matrix interphase in SiC CMCs will oxidize to form low-melting B_2O_3 (T_m = 450°C) whilst also liberating N_2(g), as seen in Equation (3.2):

$$2BN + 3/2O_2(g) \rightarrow B_2O_3 + N_2(g) \tag{3.2}$$

In the presence of thermally grown SiO_2, B_2O_3 mixes with SiO_2 to form a borosilicate ($SiO_2 \cdot xB_2O_3$) glass, as seen in Equation (3.3):

$$SiO_2 + xB_2O_3 \rightarrow SiO_2 \cdot xB_2O_3 \quad (3.3)$$

where x denotes variable molar B_2O_3 composition values. The oxidation of SiC with B- containing materials increases SiC oxidation rates by several orders of magnitude due to the formation of a borosilicate glass.[11, 12] Additionally, B-containing species in monolithic BN and borosilicate layers are known to produce various volatile gaseous boron hydroxide species of the form $H_xB_yO_z(g)$.[11, 13–17] This causes thermally grown borosilicate layers to become more SiO_2- rich over time as B_2O_3 levels decrease due to volatilization.

During operation in a marine environment, turbine engines undergo a form of deposit-based attack known as hot corrosion due to the reaction of ingested NaCl sea salt and S from the fuel or atmosphere. This *in-situ* turbine engine reaction can form liquid sodium sulfate (Na_2SO_4), as seen in Equation (3.4)[18]:

$$2NaCl(l) + SO_3(g) + H_2O(g) \rightarrow Na_2SO_4(l) + 2HCl(g) \quad (3.4)$$

Once this sodium sulfate deposits on hot section components, rapid dissolution of protective metal oxides, accelerated oxidation and localized pitting of alloy components can occur.[19–22] It has been shown in literature that Na_2SO_4 deposits cause similar oxide dissolution, accelerated oxidation and pitting of SiC and SiC CMCs.[8, 23–25] The increased oxidation kinetics of SiC have been attributed to the dissolution of thermally grown SiO_2 into liquid sodium silicate ($SiO_2 \cdot xNa_2O$), seen in Equation (3.5):

$$SiO_2(s) + xNa_2O \rightarrow SiO_2 \cdot xNa_2O \quad (3.5)$$

where x denotes variable Na_2O molar composition. SiC consumption rates were shown to increase relative to Na_2SO_4 free environments within the first few hours of exposure at 1000°C. Longer exposure times resulted in a SiC consumption kinetic plateau after the formation of a non-porous, SiO_2 layer.[9] Localized and deep (~30-50 μm) pits or craters into SiC surfaces after exposure to Na_2SO_4 formed, acting as stress concentrators, decreasing the strength of SiC.[26]

It is expected during service in marine environments that BN fiber coatings in SiC CMCs, and Na_2SO_4 will form thermally grown sodium borosilicate reaction layers on SiC CMC components. The SiO_2-rich portion of the SiO_2-Na_2O-B_2O_3 ternary system has been studied extensively over the past several decades, but there are very little available studies on the effect of thermally grown SiO_2-Na_2O-B_2O_3 layers on SiC oxidation rates. [15–17, 27–30] The only quantitative work in this area, established that BN-coated α-SiC exposed to Na_2SO_4 in dry O_2(g), enhanced SiC oxidation rates, and the reaction layer was comprised of amorphous and crystalline tridymite phases.[24] However, only a singular exposure for 24h at 1000°C was performed, leaving time and temperature dependence of B_2O_3 and Na_2O containing species on SiC oxidation rates unexplored.

3.1.1 The SiO_2-Na_2O-B_2O_3 System

The phase and composition of thermally grown SiO_2 is of technological importance to SiC CMCs in turbine engines. Pure SiO_2 is a polymorphic material that has at least two equilibrium phases at ambient pressure up to its melting point (T_m = 1723°C), namely quartz and cristobalite. A debate still exists in literature if tridymite is water and impurity stabilized or a slow-forming phase.[31–33] A widely accepted view on pure SiO_2 polymorphism established by Fenner, puts SiO_2 transition temperatures of quartz to tridymite at ~867°C and tridymite to cristobalite at ~1460°C, while a differing view established by Flörke places a single transition from quartz to cristobalite at 1050°C.[34–38] Regardless, work in the past century has proven that the addition of many metal oxides including, Na_2O and B_2O_3, to SiO_2 lead to equilibrium formation of tridymite between ~867°C and ~1460°C. [17, 27, 39–46] Multiple equilibrium studies in the SiO_2-Na_2O-B_2O_3 system have been conducted, with the most thorough study performed by Rockett and Foster.[15–17, 47] Three main observations for SiO_2 rich SiO_2-Na_2O-B_2O_3 phase equilibria include (i) transformation temperatures from quartz to tridymite at ~870°C and tridymite to cristobalite at ~1460°C; (ii) the low refractory nature of this system evident by the rapidly downward sloping liquidus surface; and (iii) the long times needed to crystallize several compositions ranging from minutes up to months.[15–17, 33] During the oxidation of SiC in clean dry and wet O_2(g) containing environments, it is generally accepted that amorphous SiO_2 initially forms and thereafter crystallization into cristobalite occurs.[3, 48–53] However, it has been shown that in the presence of impurities, SiC will form a thermally grown tridymite layer.[24, 54, 55]

The focus of this work is to understand how BN affects Na_2SO_4-induced hot corrosion of SiC. This interaction was studied for times to 144h, and at temperatures between 700°C and 1100°C. SiC consumption kinetics and composition, phase formation and crystallinity of the thermally grown layers were characterized. Implications for hot corrosion of SiC/BN/SiC CMCs are discussed.

3.2 Experimental

3.2.1 Materials

Experiments were conducted on commercially sintered α-SiC Hexoloy™ (Hexoloy SA, Saint-Gobain, Niagara Falls, NY) substrates with approximate dimensions of 1.25 cm x 1.25 cm x 0.1 cm. The B and C sintering aids present in Hexoloy are more representative of the SiC matrix composition in CMCs than pure SiC.[56, 57] The BN interphase fiber coatings present in CMCs were simulated using a BN thin film deposited onto α-SiC substrates using a RF Magnetron sputtering system (LGA Thin Films, Santa Clara, CA). The chemical composition and thickness of the as-deposited BN coated SiC was measured using auger electron spectroscopy (AES) depth profiling done by Evans Analytical Group (East Windsor, NJ).

3.2.2 Hot Corrosion Procedure

The effect of BN on the hot corrosion of SiC was isolated by performing high temperature exposures with and without Na_2SO_4. For exposures with Na_2SO_4, an aqueous solution (3g Na_2SO_4 in 100 mL DI water), was loaded onto specimen surfaces using a pipetter followed by convection oven (MTI Corporation, Richmond, CA) drying at 120°C to obtain Na_2SO_4 loadings of ~2.5 mg/cm^2. Specimens were weighed before and after salt-loading using a high precision analytical balance (Mettler Toledo, Columbus, OH) to confirm Na_2SO_4 salt loadings. All experiments were conducted in high purity fused quartz tubes (99.995%, Quartz Scientific, Fairport Harbor, OH) in a horizontal tube furnace (CM Furnaces, Bloomington, NJ). Fused quartz tubes were O-ring sealed, terminated with stainless-steel endcaps, and a bubbler was used for visual determination of exhaust gas flow. For experiments conducted with Na_2SO_4, a 100 sccm (Model 1179, Mass Flow Controller, MKS Instruments, Andover, MA) flowing 0.1% (1000 ppm) SO_2-O_2 gas mixture was used to control Na_2O activities, while flowing dry O_2 was used for experiments without Na_2SO_4. Temperature dependent experiments were run for 24h at temperatures between 700°C-1100°C, while time dependent experiments were performed between 0.75-144h at 800°C and 1000°C, below and above the melting temperature of Na_2SO_4. All SiC coupons were placed inside of an Al_2O_3 boat and then loaded into the tube furnace hot-zone at temperature, and were air quenched upon completion of experimentation. For exposures performed in 0.1% SO_2-O_2 environments, the tube was flushed with O_2(g) for several minutes prior to quenching, while specimens exposed in O_2(g) were air quenched immediately. Specimens were weighed after removal from tube furnace testing. Two SiC coupons were exposed per condition, one for reaction layer composition analysis and the other specimen for phase, microstructure and morphological determination.

3.2.3 Characterization

The reaction kinetics, reaction layer composition and structure, along with the SiC surface degradation were characterized using several techniques. X-ray diffraction (XRD) was conducted on all specimens before and after exposure to determine the formation of any new crystalline products. Data were collected using a diffractometer (X'Pert, PANalytical, Almelo, the Netherlands) with Cu Kα (0.1541 nm) radiation over a range of 15-70 degrees 2θ, while peak identification was done using Highscore Plus software. The morphology and chemical composition of specimen surfaces was characterized using scanning electron microscopy (SEM) (Quanta 650, FEI Company, Hillsboro, OR) and energy dispersive spectroscopy (EDS) (X-max 150, Oxford Instruments, Abingdon, England). Specimens were cross-sectioned using a slow-speed diamond loaded saw and polished in ethylene glycol to minimize the removal of water-soluble products. Polishing was performed using diamond based-media, with the last polishing step performed down at 0.25 μm.

The elemental composition of the reaction layer was determined using an inductively coupled plasma optical emission spectrometer, or ICP-OES (iCAP Duo Spectrometer 6200, Thermo Scientific, Waltham, MA). Samples were first soaked for 48h in a 35°C heated water bath with sonication in 10 mL of water followed by a second soak in a 1 mL HF + 9 mL water mixture in two-step digestion to selectively remove reaction products from α-SiC substrates. For specimens exposed to Na_2SO_4, the water digestion step was used to remove Na_2SO_4 and water soluble Na_2O and B_2O_3 containing silicates, while SiO_2 was removed in the acid digestion. For specimens that were exposed without Na_2SO_4, water soluble borosilicates high in B_2O_3 content were removed in the water digestion step, while SiO_2 was removed with acid. Three to four spectral lines each for Na, S Si and B were analyzed by ICP-OES for both digestions, and then averaged to determine the elemental concentration in the dissolved reactions products. Only one specimen per experimental condition was analyzed using ICP-OES. Baseline digestion of as-received BN-coated α-SiC specimens in two-steps followed by ICP-OES analysis measured less than 10 μg of Si and 80 μg of B.

Optical profilometry (NewView 7300, Zygo Corporation, Middlefield, CT) was used to visualize and quantify surface attack morphologies and depths after the removal of the reaction products in the water and acid digestion. 3D contour plots were constructed and maximum pit depth values were measured using MountainMaps (Digital Surf, Besancon, France) software.

3.3 Results

3.3.1 BN Coating Characterization

A macro image of a BN-coated α-SiC specimen prior to salt loading can be seen in Figure 3.1a), while a SEM image of the BN coating surface can be seen in Figure 3.1b). The green color of the surface is attributed to thin film interference of the BN coating with visible light. The chemical composition and thickness of as-deposited BN coated α-SiC specimens are seen in Figure 3.2. From this plot, the BN coating thickness is approximately 600 nm evident by the intersection of the B and Si composition profiles.

3.3.2 Temperature Dependent Results

(i) Reaction Layer Phases and Chemistry

Visual inspection of BN-coated SiC specimen surfaces after exposure revealed changes to their color and shape. The formation of opaque droplets between 700°C-900°C, and a surface-wide, transparent reaction layer on specimen surfaces at exposures above 900°C can be seen in Figure 3.3.

The crystalline phases of the reaction layer on α-SiC specimens post-exposure were determined by XRD diffraction, seen in Figure 3.4. No BN diffraction peaks could be detected either before or after exposure, only α-SiC diffraction peaks from the substrate were observed. Unreacted Na_2SO_4 was

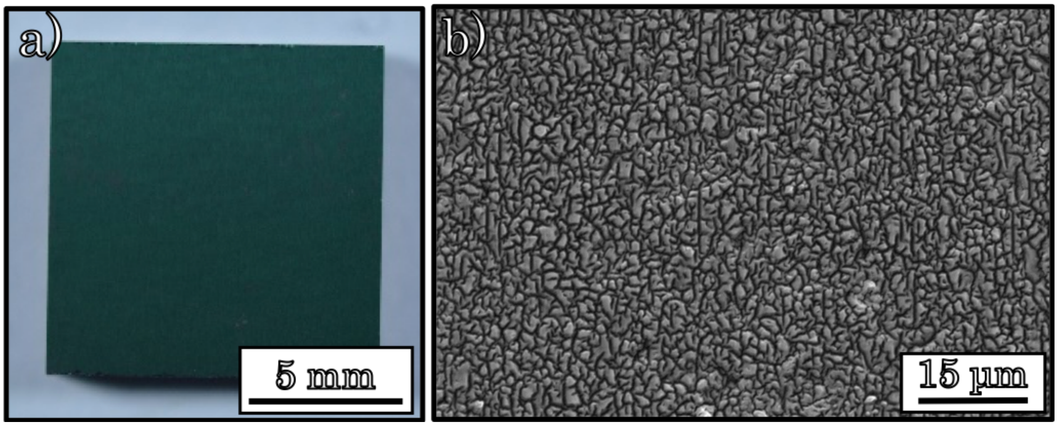

Figure 3.1. a) Macro image of a BN coated α-SiC specimen and b) SEM micrograph displaying the BN coating microstructure at higher magnification.

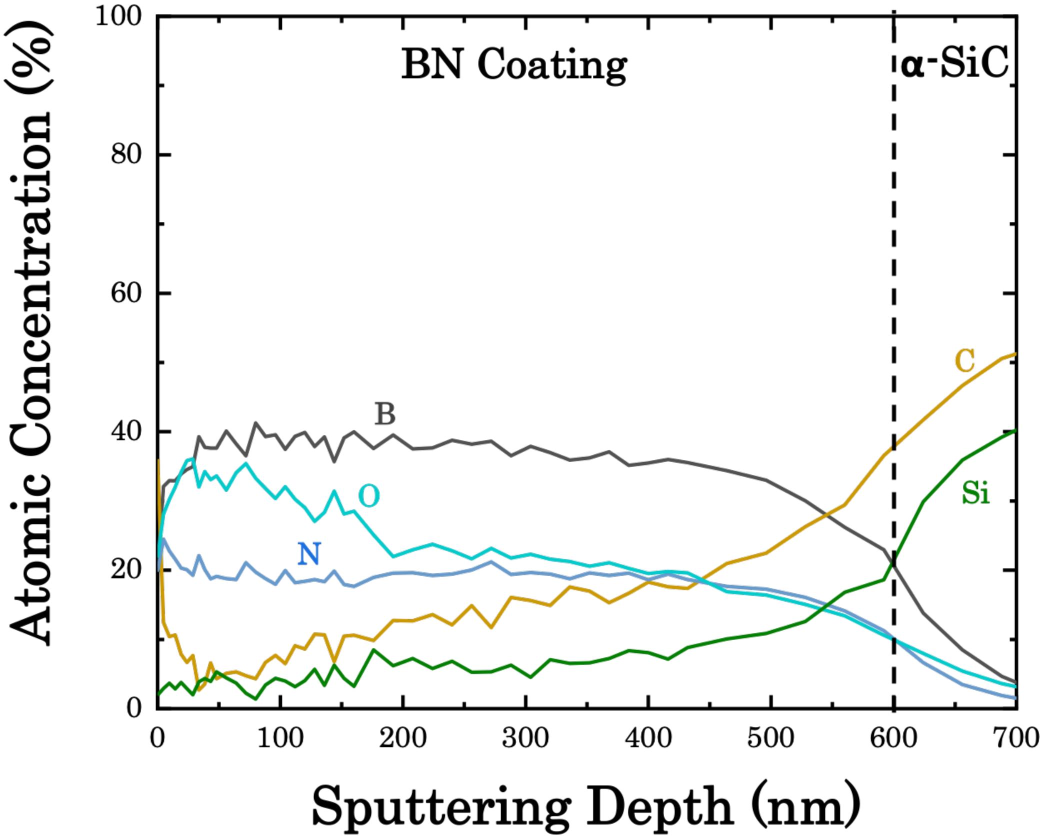

Figure 3.2. Depth profile gathered using AES of the elemental composition of the RF magnetron BN sputtered coating on a α-SiC specimen used for this study.

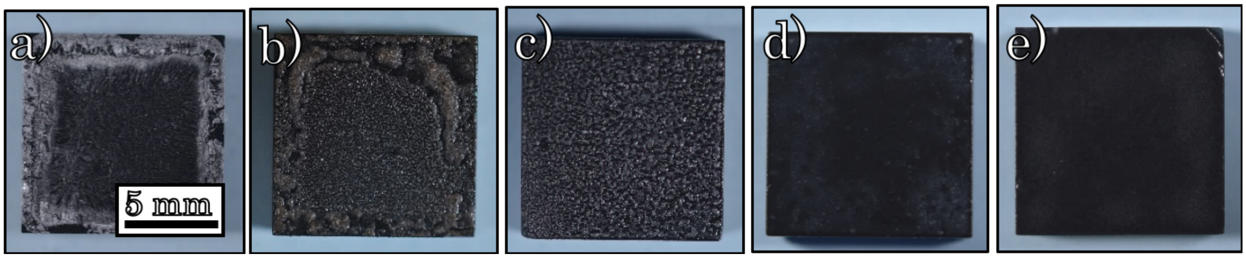

Figure 3.3. Macro images of BN coated α-SiC specimens after exposure to ~2.5 mg/cm^2 of Na_2SO_4 for 24h a) 700°C b) 800°C c) 900°C d) 1000°C e) 1100°C in a 0.1% SO_2-O_2 gaseous environment.

detected after exposures below 900°C, but not at 900°C and above. A single sodium borosilicate $Na_2Si_2O_5$ peak was tentatively identified after exposure at 900°C and below at ~22.5° 2θ. At all exposures above 750°C, the reaction layer contained either as α-cristobalite or mixtures of both α-cristobalite and α-tridymite. A single peak belonging to α-cristobalite near 22° 2θ was found to first form at 750°C, and was still present at higher exposure temperatures. α-tridymite was first detected at 900°C, increasing in peak intensity at higher exposure temperatures. No crystalline peaks belonging to SiO_2 and $Na_2Si_2O_5$ could be detected after exposure at 700°C. Microstructural and compositional measurements of the reaction layer revealed a silicate and SiO_2 bi-layer reaction product. A cross-sectional SEM micrograph coupled with elemental maps of a specimen after exposure for 24h at 1000°C is shown in Figure 3.5. A ~15 μm thick reaction bi-layer consisting of sodium silicate was found on top of a nearly continuous, Si and O- containing lath-like layer, which is associated with tridymite, over the SiC substrate. The elemental maps reveal that the dark phase contrast areas in the α-SiC substrate are the B and C sintering aids used for processing.

Due to the known solubilities of Na_2SO_4 and silicates in water and SiO_2 in HF acid, chemical analysis using ICP-OES revealed elemental Si, Na, S and B compositions of all silicate and SiO_2 reaction layers, as seen in Figure 3.6a) and 3.6b). Uncertainty bars reported in this work represent the standard deviation of the average of all spectral lines for a given element. Sulfur was only detected in the water digestion and at temperatures below 900°C, indicating Na_2SO_4 volatilization or rapid reaction kinetics occurred at higher temperatures. The detection of Si, B and residual Na not belonging to Na_2SO_4 in the water digestion revealed the formation of a sodium borosilicate layer ($SiO_2 \cdot xNa_2O \cdot yB_2O_3$), but only below 900°C as B completely volatilized from the reaction layer above 900°C. Boron levels in the reaction layer relative to the other elements were nearly an order of magnitude less and are re-plotted on an enlarged scale in Figure 3.6b). The acid digestion revealed the presence of Na_2O- and B_2O_3-containing SiO_2 at temperatures below 900°C, while a Na_2O- containing thermally grown SiO_2 formed at temperatures above 900°C. Total Si levels in the reaction layer increased with temperature from a minimum at 700°C to a maximum at 1100°C, indicating faster reaction kinetics with increasing temperature as expected.

(ii) Substrate Attack: Pitting vs. Rivulets

Optical profilometry was performed on specimens to determine surface attack morphology after removal of the reaction layer using the two-step digestion method for ICP-OES analysis. Seen in Figure 3.7 are a series of three-dimensional (3D) topographical maps of specimen surface recession inverted features displaying pits and rivulet valleys inverted. Recession features from all exposure temperatures were scaled to the same 35 μm scale bar. Evident by the topographical maps, attack on the α-SiC substrate surfaces exhibited differing morphologies at lower and higher temperatures. At 900°C and below, the surface attack features was observed to be a random network of 3-5 μm deep "rivulets" that are tens of microns wide, while localized craters or pits 10-30 μm deep were observed at exposure temperatures above 900°C. The rivulets are deeper and wider at 900°C than those seen at 750°C and 800°C, while the pitting observed at 1000°C is deeper than that seen at 1100°C.

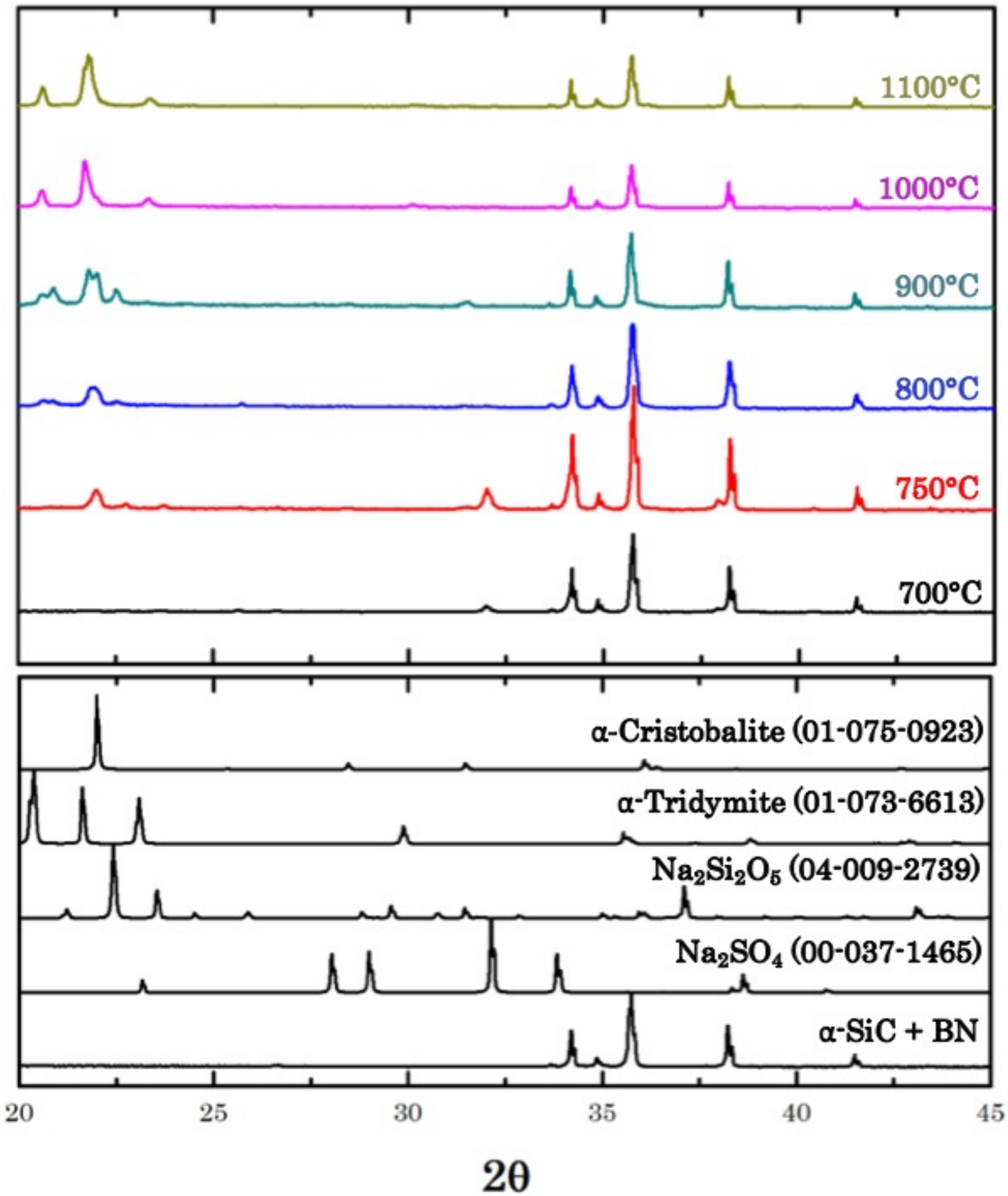

Figure 3.4. XRD patterns of BN-coated α-SiC specimens after exposure to ~2.5 mg/cm^2 of Na_2SO_4 for 24h between 700°C- 1100°C in a 0.1% SO_2-O_2 gaseous environment.

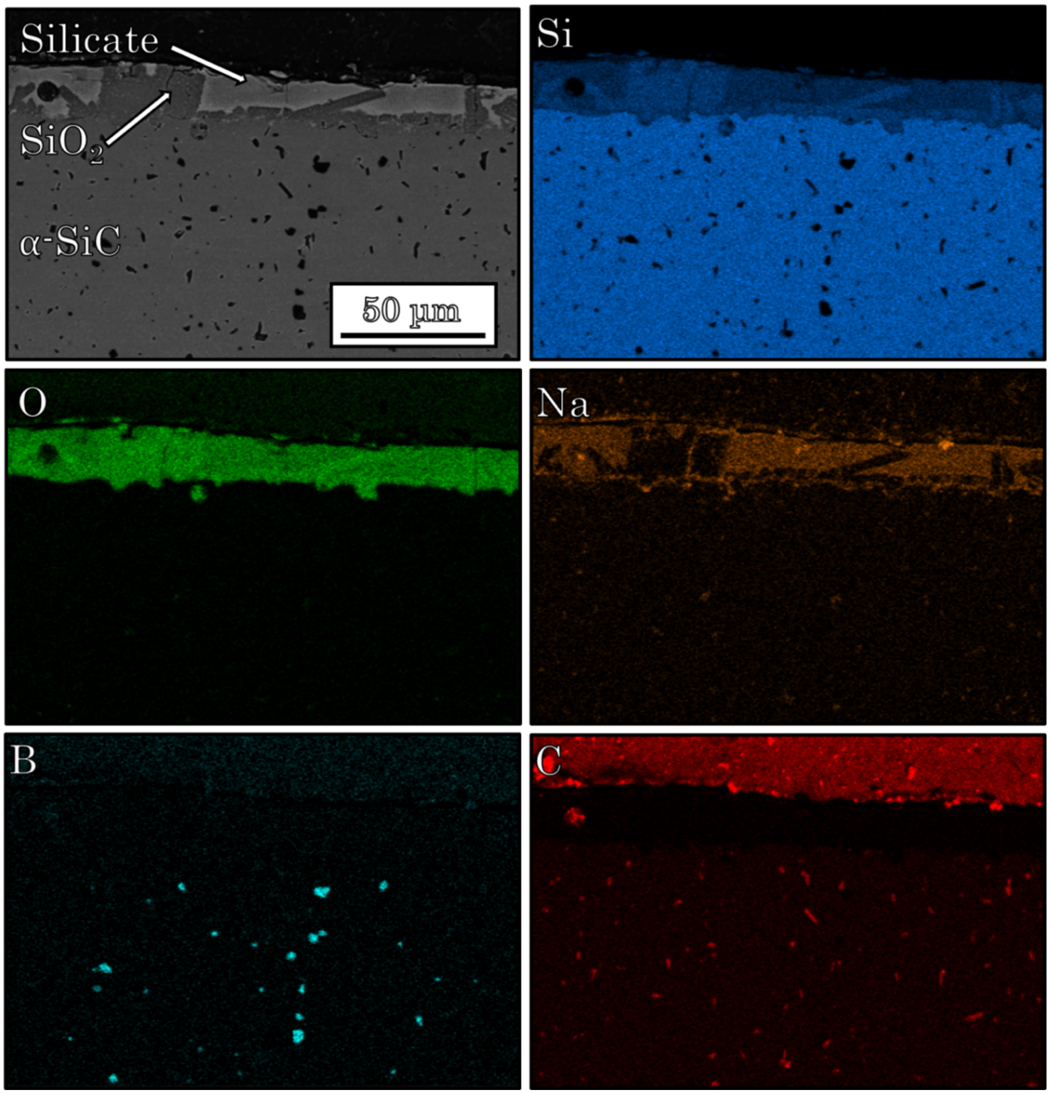

Figure 3.5. Backscattered SEM image and corresponding EDS elemental maps of a BN-coated α-SiC specimen in cross-section after exposure to ~2.5 mg/cm^2 of Na_2SO_4 for 24h at 1000°C in a gaseous 0.1% SO_2-O_2 environment.

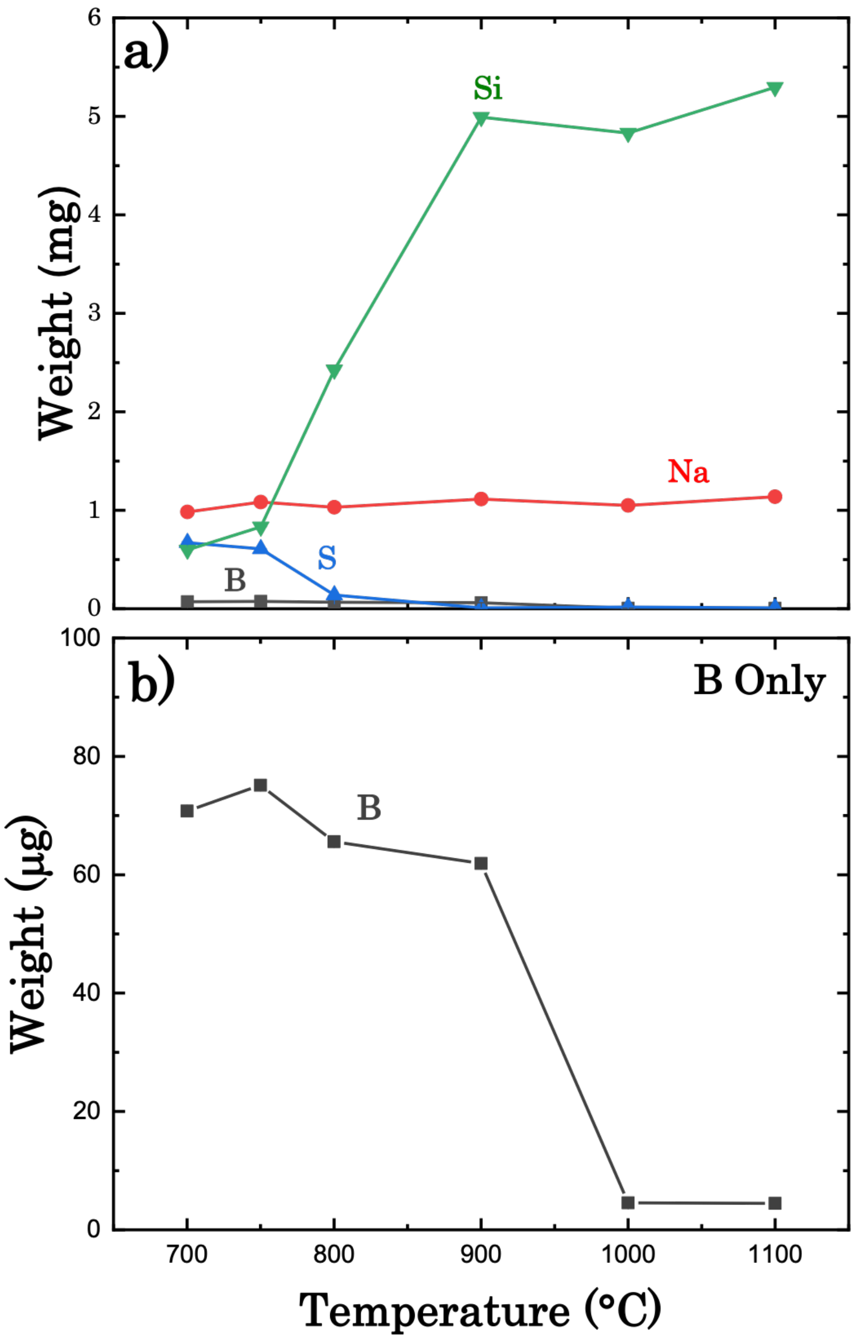

Figure 3.6. Plots showing the a) Si, Na, S and B (in mg) and b) B (in µg) content of the entire corrosion products of BN-coated α-SiC specimens exposed to ~2.5 mg/cm^{2}of Na_2SO_4 for 24h between 700°C-1100°C in a 0.1% SO_2-O_2 gaseous environment.

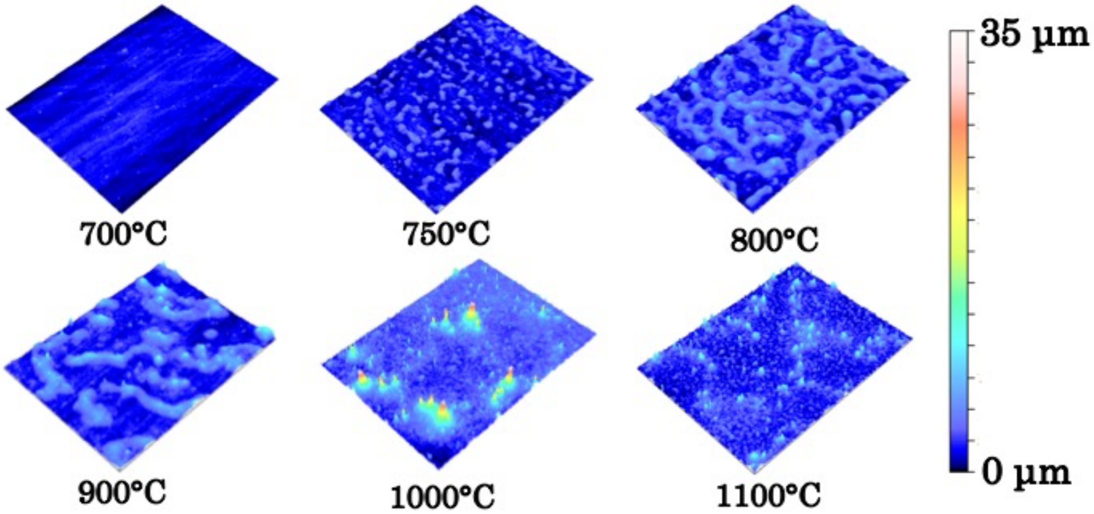

Figure 3.7. 3D contour plots of specimen surfaces after exposure to 2.5 mg/cm^2 of Na_2SO_4 for 24 between 700-1100°C in 0.1% SO_2-O_2 gaseous environment. The surface recession features are inverted to become peaks, and the scale bar is plotted in units of µm. The scan size is 1044 µm x 788 µm.

(iii) SiC Oxidation Rates: BN vs. Na_2SO_4 vs. BN + Na_2SO_4

The amount of SiC consumed in the presence of (i) ~2.5 mg/cm^2 Na_2SO_4 + BN (ii) ~2.5 mg/cm^2 Na_2SO_4 only (iii) BN only and (iv) no additional condensed phase species for 24h between 700°C-1100°C in O_2(g), can be seen in Figure 3.8. The SiC values reported from exposure to both Na_2SO_4 and BN, only Na_2SO_4 and only BN in Figure 3.8 were calculated by converting the elemental Si into SiC from the reaction layer measured using ICP-OES assuming SiC substrates tested possessed 1:1 Si:C stoichiometry. Values for SiC consumed with no additional condensed phase species present (dry oxidation) were calculated from Ramberg et al. using reported rate constant values, assuming an oxidation time of 24h, and no initial oxide on specimens surfaces.[7] SiC consumption values in the presence of Na_2SO_4 only were obtained from Hagan et al.[23] It can be seen from Figure 3.8, that SiC has the most oxidation resistance when no BN or Na_2SO_4 is present. With the addition of a thin 600nm BN layer, SiC consumption is greater than pure SiC from 700°C-1000°C. However, the introduction of both Na_2SO_4 and BN causes more SiC consumption to occur than individually BN or Na_2SO_4 until ~1050°C, as Na_2SO_4 causes more SiC consumption above this temperature. It should be noted that Si levels values reported by Hagan et al.[23] have large uncertainty values (~10-20%) associated with repeat experiments, while only 1 sample per condition was analyzed for values reported in Figure 3.8 in this dissertation. However, due to the identical testing set-up, ICP-OES characterization analysis, similar uncertainty in the Si levels can be assumed in this work.

3.3.3 Time Dependent Results

(i) 800°C vs. 1000°C

Visual inspection of specimen surfaces exposed up to 24h at 800°C, seen in Figure 3.9, revealed the formation of opaque droplets in the middle of specimens identical to those observed during temperature dependent experiments. Morphological and color changes of specimens exposed at 800°C were not evident until 24h of exposure. Inspection of specimen surfaces exposed up to 24h at 1000°C, seen in Figure 3.10, showed a more uniform surface reaction layer with larger droplets than those formed at 800°C. Additionally, evidence of a vigorous reaction is indicated by the formation of bubble filled regions after exposure for 0.75h at 1000°C. Determination of newly formed crystalline phase during exposure at 800°C and 1000°C can be seen in Figures 3.11 and 3.12. Only α-SiC peaks from the substrate were observed as no BN peaks could be measured before and after exposure at both temperatures. Trace Na_2SO_4 peaks were observed up until 6h of exposure at 800°C, while Na_2SO_4 peaks could not be measured even after 0.75h exposure at 1000°C, indicating rapid reaction kinetics and/or volatilization. Crystalline SiO_2 peaks were observed on specimens at both temperatures, however the crystallization phase formation and kinetics

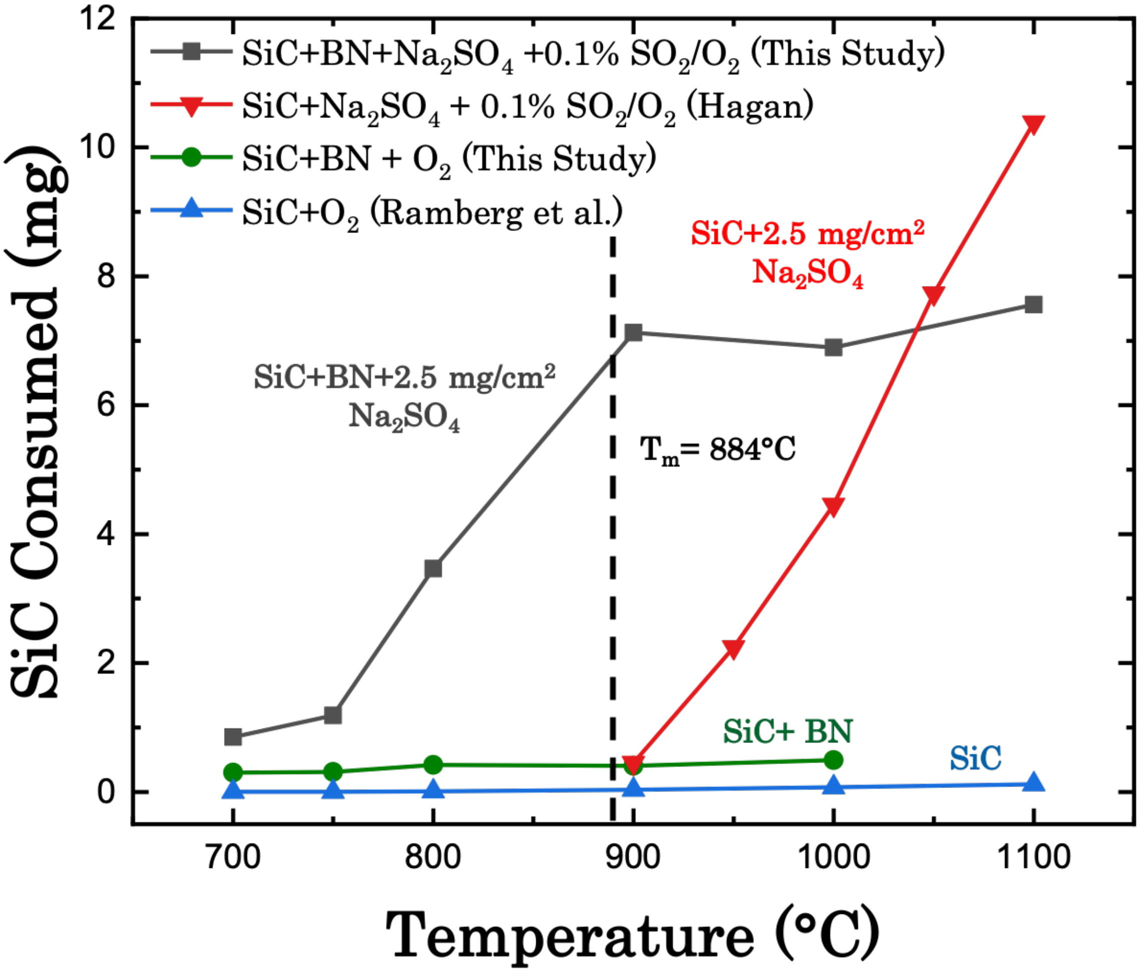

Figure 3.8. Plot showing the total SiC consumed as function of temperature after exposure for 24h to ~2.5 mg/cm^2 Na_2SO_4 +BN (dark grey), ~2.5 mg/cm^2 Na_2SO_4 only (red)[49], BN only (green) and no additional species in dry O_2(g) using Ramberg et al. (blue)[7].

differed. XRD measurements at 800°C, seen in Figure 3.11, reveal that α-cristobalite first formed between 3h-6h and persisted as the only crystalline phase up until 24h. For exposures times beyond 24h, both α-cristobalite and α-tridymite coexisted indefinitely. A silicate phase matching with $Na_2Si_2O_5$ was found to form after 96h and existed indefinitely. Seen in Figure 3.12, XRD measurements after exposure at 1000°C revealed cristobalite initially

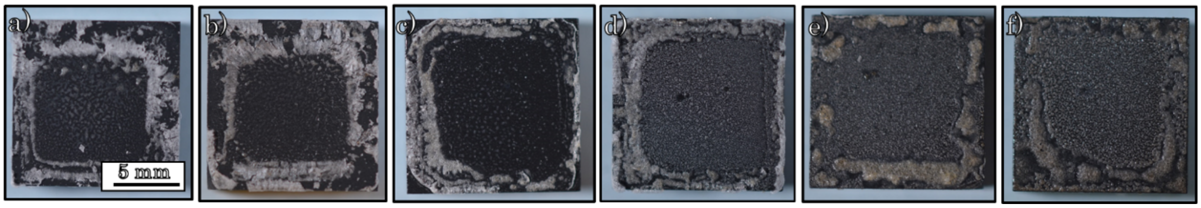

Figure 3.9. Macro images of BN-coated α-SiC specimens after exposure to ~2.5 mg/cm^2 of Na_2SO_4 at 800°C for a) 0.75h b) 1.5h c) 3h d) 6h e) 12h f) 24h in a 0.1% SO_2-O_2 gaseous environment.

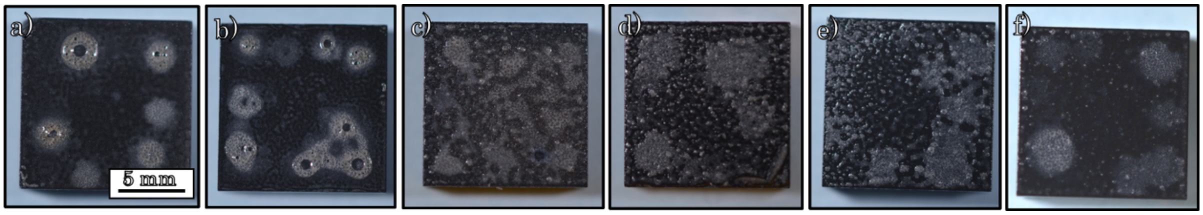

Figure 3.10. Macro images of BN-coated SiC specimens after exposure to ~2.5 mg/cm^2 of Na_2SO_4 at 1000°C for a) 0.75h b) 1.5h c) 3h d) 6h e) 12h f) 24h in a 0.1% SO_2-O_2 gaseous environment.

crystallized from the reaction layer melt between 1.5-3h, co-existing with tridymite between 6h-24h of exposure. For times longer than 24h, the equilibrium phase α-tridymite became the dominant crystalline phase present evident by its strong diffraction peaks up to 96h of exposure. Relative to the crystalline SiO_2 peaks observed at 800°C, the crystalline peaks formed at 1000°C were more intense, indicating long-range ordering from potentially larger crystals.

The elemental composition of the reaction layer determined using ICP-OES seen in Figure 3.13, revealed that nearly equal amounts of Si consumption occurred at both temperatures after prolonged exposure. However, the reaction kinetics at both temperatures differed, evident by evolution of the elemental species detected in the reaction layer. Exposures at both temperatures resulted in parabolic Si consumption behavior that eventually exhibited a slope change or kinetic plateau with prolonged exposure. Between 6-12h of exposure at 1000°C, a flattening or kinetic plateau in Si consumption occurred and similarly after 96h of exposure at 800°C. From the water digestion, it was found that S was detected after 800°C exposures up to 24h, while S levels less than ~100 μg of S could be detected after exposure for 0.75h at 1000°C, indicating high Na_2SO_4 reactivity and/or volatilization. Si, B and residual Na not associated with Na_2SO_4 in the water digestion revealed that a sodium borosilicate formed at both temperatures, but due to rapid B volatilization, a sodium silicate formed at 1000°C after 12-24h, seen in Figure 3.14. The amount of B plotted (in μg) on an enlarged scale versus time at both 800°C and 1000°C can be seen in Figure 3.14. Acid digestion revealed that Na- and B- containing SiO_2 formed at both 800°C and 1000°C, but that the product formed at 1000°C was richer in Si and poorer in B content than the phase formed at 800°C.

(ii) Thermally Grown Oxide Composition vs. Time

SiO_2, Na_2O and B_2O_3 compositions (in wt%) in the thermally grown oxide over time were calculated using elemental Si, B and Na levels from ICP-OES measurements. Si and B measured were assumed to belong only to SiO_2, B_2O_3 or silicates, while Na_2O levels belonging to Na_2SO_4 were subtracted leaving the remainder to silicates or SiO_2. The calculated composition values were overlaid on top of the high-SiO_2 liquidus region in the SiO_2-Na_2O-B_2O_3 ternary established by Rocket and Foster, seen in Figure 3.15.[17] This figure reveals that irrespective of temperature, longer exposure times produced more SiO_2 rich thermally grown reaction layers, doing so faster at 1000°C. Additionally, due to B volatility, the thermally grown oxide at 1000°C reduced to a two component Na_2O-SiO_2 reaction whilst remaining a three component SiO_2-Na_2O-B_2O_3 reaction layer at 800°C.

(iii) 800°C vs. 1000°C: BN vs. Na_2SO_4 vs. BN + Na_2SO_4

The individual and combined effects of BN and Na_2SO_4 on the oxidation of SiC at 800°C and 1000°C were compared using values generated from this work and from literature. SiC consumption values plotted in Figure

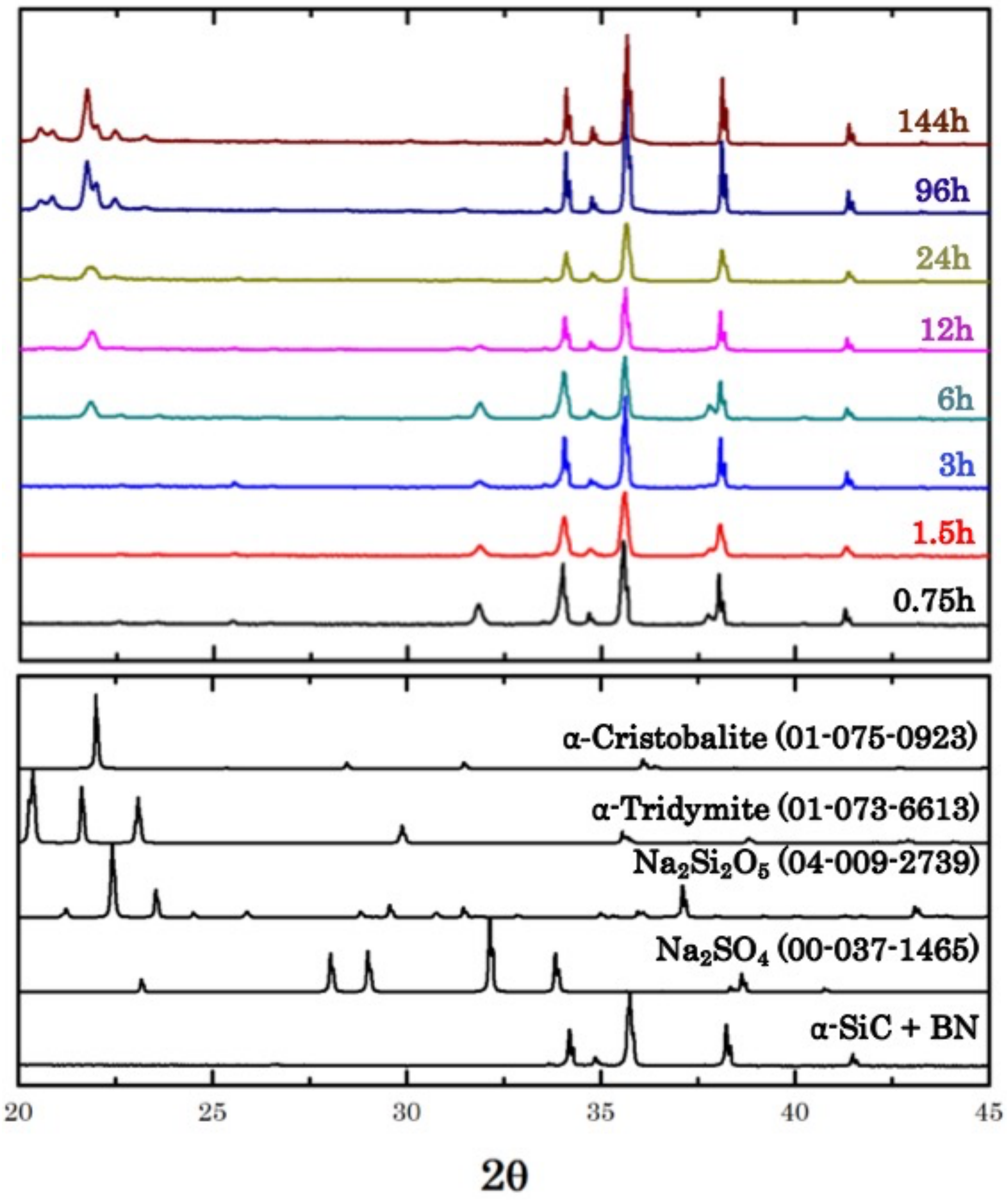

Figure 3.11. XRD pattern for BN-coated α-SiC specimens after exposure to ~2.5 mg/cm^2 of Na_2SO_4 for 0.75h-144h at 800°C in a 0.1% SO_2-O_2 gaseous environment.

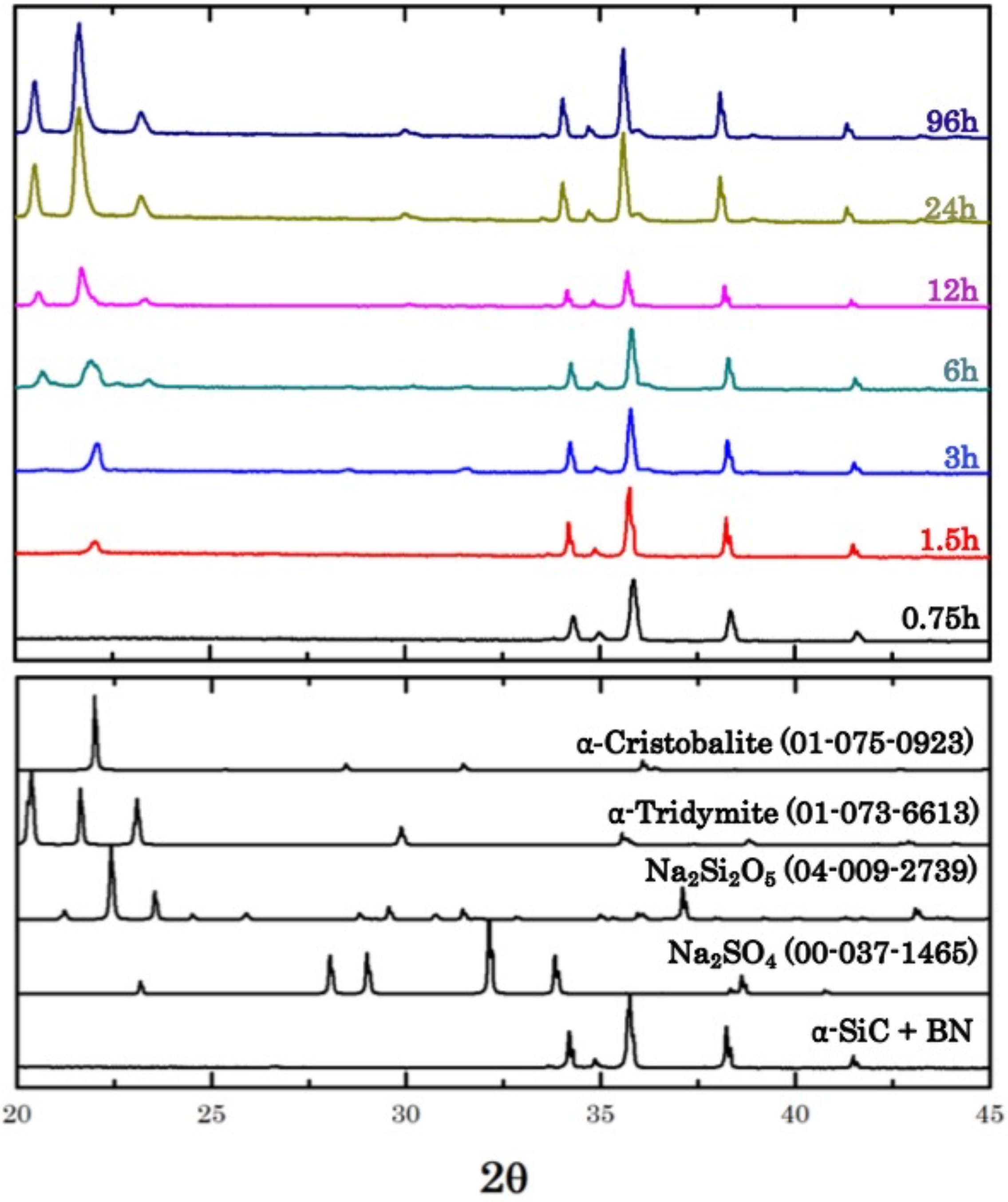

Figure 3.12. XRD patterns of BN-coated α-SiC specimens after exposure to ~2.5 mg/cm^2 of Na_2SO_4 for 0.75-96h between 1000°C in a 0.1% SO_2-O_2 gaseous environment.

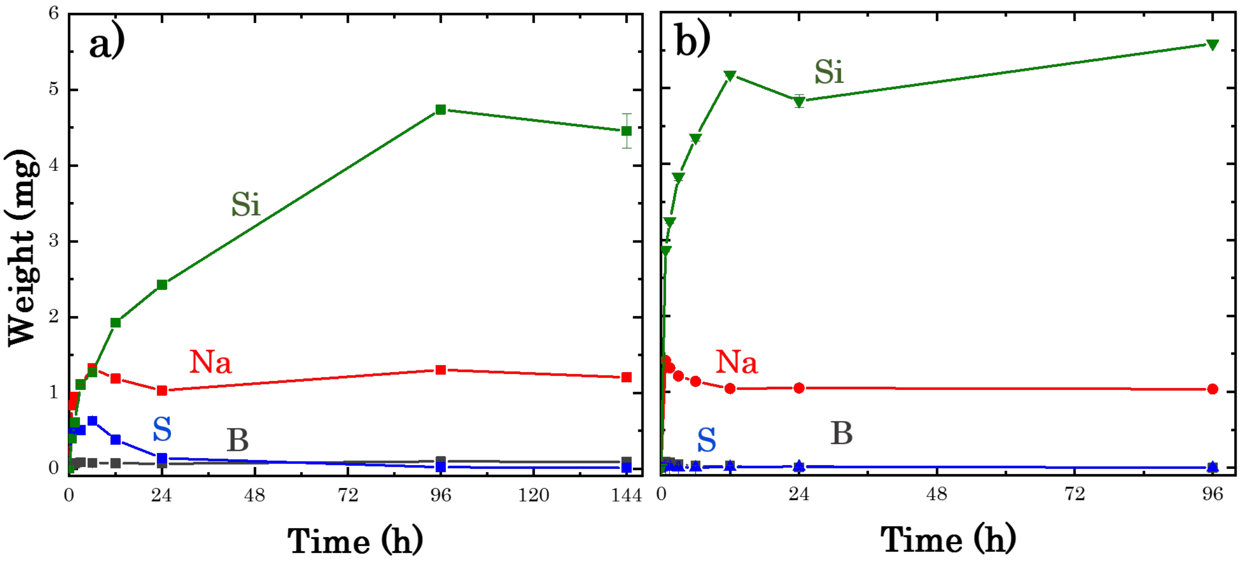

Figure 3.13. Plots showing the total Si, Na, S and B levels (in mg) of the corrosion products on BN-coated α-SiC specimens after exposure to ~2.5 mg/cm^2 Na_2SO_4 for 0.75h-144h at a) 800°C and b) 1000°C in a 0.1% SO_2-O_2 gaseous environment.

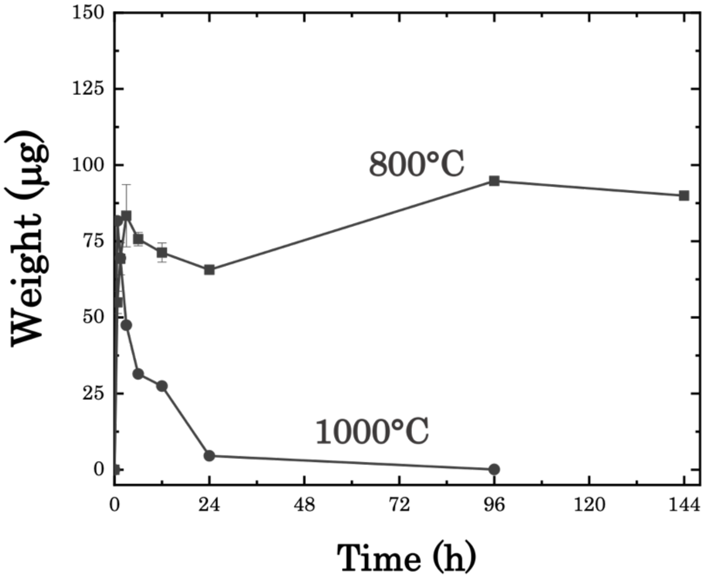

Figure 3.14. Plot showing the total amount of B (in µg) in the reaction layer of BN-coated α-SiC specimens after exposure to ~2.5 mg/cm^2 Na_2SO_4 for 0.75-144h at 800°C (top curve) and 1000°C (bottom curve) in a 0.1% SO_2-O_2 gaseous environment.

3.16 and 3.17 exposed to both BN and Na_2SO_4, only Na_2SO_4 and only BN were calculated in this work. Values for the amount of SiC consumed were calculated identically as those from temperature dependent measurements, assuming 1:1 SiC in the substrates. SiC consumption values with O_2(g) only were calculated using reaction rate constants reported by Ramberg et al.[7] It can be seen at both temperatures that SiC has the most oxidation resistance without BN or Na_2SO_4 present. The addition of only BN increased the amount of SiC consumption relative to no species present at both 800°C and 1000°C by a factor of ~2-3. At 800°C the addition of both BN and Na_2SO_4 increased the amount of SiC consumed by 1-2 orders of magnitude relative to exposure with BN or no additional species in dry O_2(g). No data are available for SiC + Na_2SO_4 in dry O_2(g) although no effect is expected below the melting of Na_2SO_4 ($T_m = 884°C$) consistent with Hagans observations. At 1000°C, the addition of BN to Na_2SO_4-induced hot corrosion of SiC was not found to statistically enhance the amount of SiC consumed relative to exposure of only Na_2SO_4 compared to values reported in literature, as these works report 10-20% uncertainly in their SiC consumption values measured using ICP-OES. Due to the identical testing set-up, ICP-OES characterization analysis, similar uncertainty in the SiC consumption levels can be assumed in this work. Validation of ICP-OES in determining SiC consumption levels reported in Figure 3.16 and Figure 3.17 compared against benchtop weight change before salt-loading and after removal of the reaction product using the two-step digestion procedure can be seen in Appendix C.

3.4 Discussion

3.4.1 SiC Oxidation + Hot Corrosion Behavior

High purity, thermally grown SiO_2 is protective to further SiC oxidation in clean, oxidizing high-temperature environments due to slow oxygen diffusivity.[58–60] It is generally accepted that amorphous SiO_2 forms initially, which upon prolonged exposure subsequently crystallizes into β-cristobalite. The crystallization kinetics into cristobalite are sluggish at

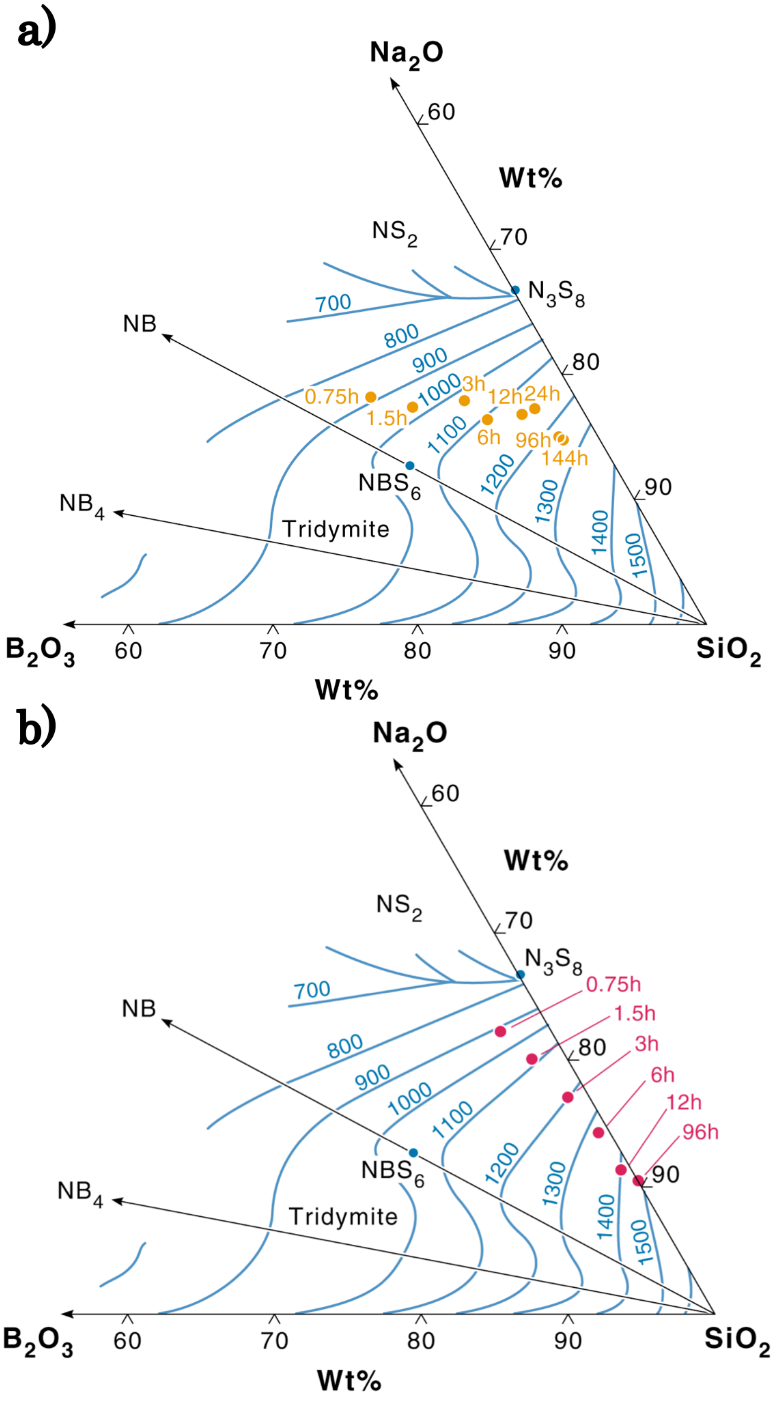

Figure 3.15. Composition of the thermally grown oxide between 0.75h-144h calculated using ICP-OES after exposure at a) 800°C (gold points) and b) 1000°C (magenta points) plotted over SiO_2 rich portion of the SiO_2-Na_2O-B_2O_3 ternary liquidus.[17] (N=Na_2O, B=B_2O_3, and S=SiO_2)

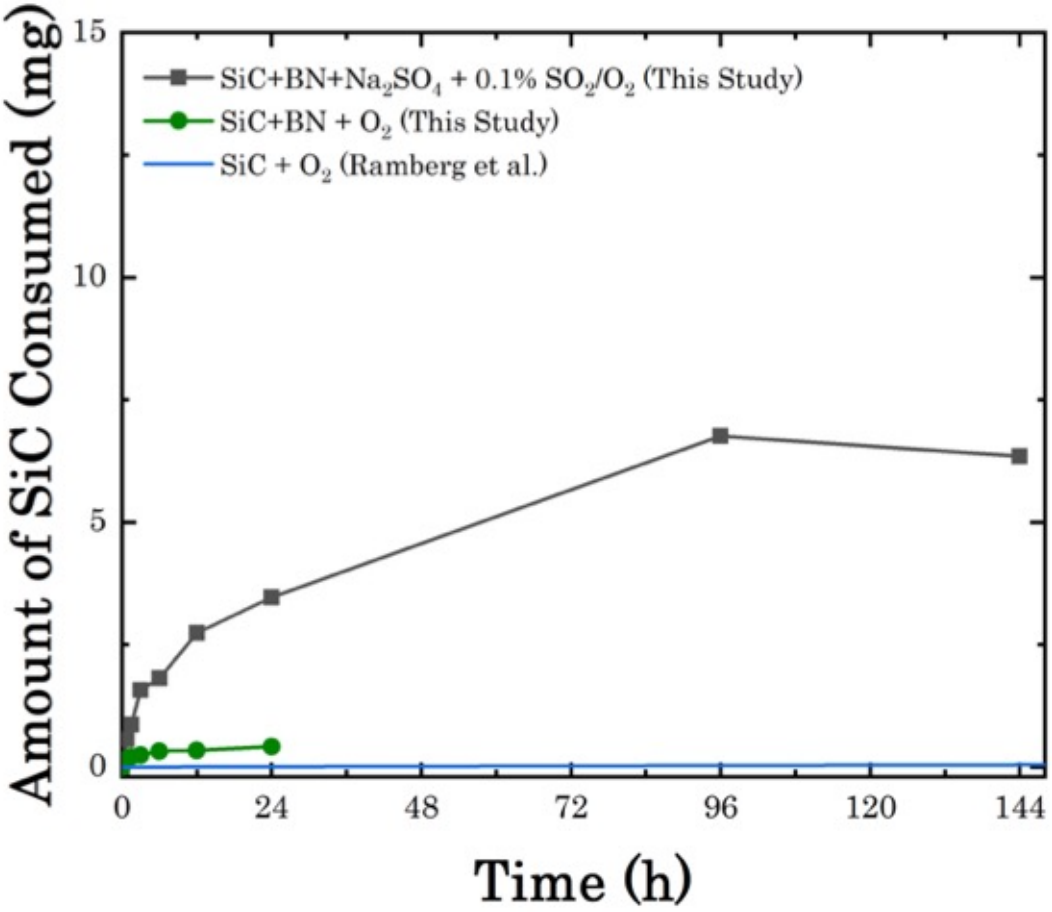

Figure 3.16. Plot showing the amount of SiC consumed after exposure to 2.5 mg/cm^2 of Na_2SO_4+BN (grey), BN (green) and no additional species (blue) at 800°C in dry O_2(g). The values from the reaction of SiC+BN+Na_2SO_4 and SiC+BN were measured using ICP-OES by this work, while the amount of SiC consumed during oxidation at 800°C were calculated from Ramberg et al.[7]

temperatures near 1200°C, but are increased at higher temperature and in the presence of impurities and steam. However, B_2O_3 and Na_2O incorporation in thermally grown SiO_2 can result in liquid formation due to the presence of low-melting eutectic temperatures in this system. Examination of the SiO_2-Na_2O-B_2O_3 liquidus surface in Figure 3.15 reveals that SiO_2 mixtures dilute in B_2O_3 and Na_2O (~95 wt% SiO_2) melt around 1400°C-1500°C and with

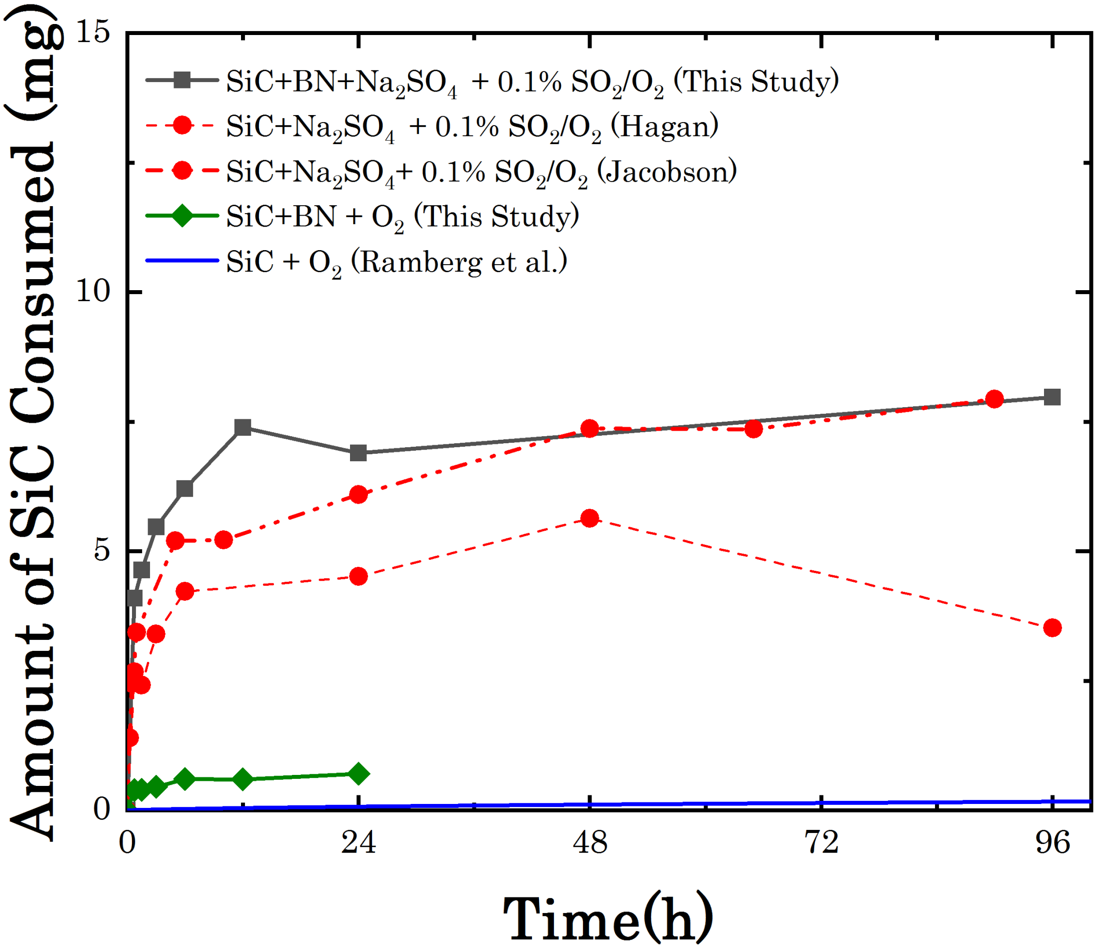

Figure 3.17. Plot showing the amount of SiC consumed after exposure to ~2.5 mg/cm^2 of Na_2SO_4+BN (dark grey), Na_2SO_4 (red), BN (green) and no additional species (blue) at 1000°C in dry O_2(g). The values from the reaction of SiC+BN+Na_2SO_4 and SiC+BN were measured using ICP-OES by this work, while the amount of SiC consumed during oxidation at 1000°C were calculated from Ramberg et al. [7] and from exposure to Na_2SO_4 from Jacobson an Hagan et al.[9, 23]

increased mixtures of B_2O_3 or Na_2O (60-70 wt% SiO_2) the liquidus temperature decreases to 700°C. Furthermore, formation of sodium borosilicates results in increased oxygen diffusivity, accelerating the oxidation kinetics of SiC. Values reported in literature suggest that oxygen diffusivity through crystalline or amorphous SiO_2 versus liquid silicates could decrease by 6 to 9 orders of magnitude.[8, 61] However, thermally grown silicate surface layers do not possess equilibrium compositions at a given time and temperature, as continual SiC oxidation combined with Na_2O and B_2O_3 volatilization increases the reaction layer SiO_2 content. Thus it is generally expected as SiO_2 levels increase or Na_2O and B_2O_3 levels decrease in the reaction layer melt, a subsequent increase in the liquidus temperature of the reaction layer melt will result in the formation of thermodynamically favorable solid phases.

The combination of ICP-OES and XRD revealed that SiC initially formed a thermally grown silicate, presumably liquid at temperature, that crystallized into a tridymite containing layer after prolonged exposure. Time and temperature dependent XRD measurement revealed that initially a sequence of phase transformations occurred, starting with a silicate layer or crystalline reaction layer too minimal to be detected using XRD that transformed into β-cristobalite, and later into β-tridymite. These phases then inverted to their low temperature or α-phases upon cooling to room temperature. The detection of both α-tridymite and α-cristobalite in room temperature XRD suggests that a phase transformation from the β-to-α phase occurred upon cooling. Tridymite crystallization began in less than 12h at 1000°C while beginning between sometime 24h-96h at 800°C. Si composition measurements in the reaction layer made using ICP-OES, revealed that tridymite crystallization from XRD measurements occurred at the same time the Si levels of the reaction layer reached a plateau, seen in Figures 3.12 and 3.13. This flattening in Si consumption and presence of strong tridymite peaks occur after 12h at 1000°C and between 24h-96h at 800°C.

At exposures of 900°C and above, the presence of only tridymite at prolonged exposure is consistent with known phase relations in the SiO_2-Na_2O-B_2O_3 system, as tridymite is the equilibrium SiO_2 phase between 867°C and 1460°C.[47] Less than a day of isothermal exposure is needed for tridymite formation at temperatures at 1000°C and above. Below exposure of 900°C, tridymite + cristobalite formation within the reaction layer also occurs, but its formation is much slower than at higher temperatures. The formation of a thermally grown tridymite layer is anomalous as quartz is the equilibrium SiO_2 phase below 867°C.

The oxidation of SiC in dry $O_2(g)$ in the presence Na_2SO_4 and BN, differs from exposure without these species. Comparison to values generated from literature seen in Figure 3.16 and 3.17, show that BN and Na_2SO_4 increase the SiC consumption levels nearly 1-2 orders of magnitude relative to oxidation in dry $O_2(g)$ with and without the presence of BN. Figure 3.8 shows the hot corrosion of SiC with only Na_2SO_4 present does not cause a reaction below the melting temperature of Na_2SO_4. BN does little to alter the Na_2SO_4-induced hot corrosion of SiC behavior above the melting temperature due to rapid B volatility. Microscopy and elemental mapping of the reaction layer in this work seen in Figure 3.5, revealed a nearly continuous, lath-like Si- and O- containing film covered the SiC surface, and in a few areas the entire thickness of the reaction layer. This indicates that the reaction layer crystallized from the bottom of the melt, at the SiC-reaction layer interface, and grew towards the gas-melt interface. Crystallization of thermally grown SiO_2 formed during oxidation of SiC in pure environments behaves differently, as the formation of spherulites occur at the gas-scale interface, and proceed down towards the SiC surface.[3] Furthermore, The presence of Na_2SO_4 and BN rapidly crystallize thermally grown SiO_2 relative to environments without these species and at temperatures at which SiO_2 crystallization is not known to happen. Exposure without Na_2SO_4 at temperatures above 1200°C in clean environments may take days to weeks to fully crystallize thermally grown SiO_2 into cristobalite.[48] Oxidation at 1200°C and below in clean environments are not known to produce crystalline scales at all. This work showed that significant SiC oxidation occurred, and that crystalline scales formed within hours to days depending on temperature. Thus the oxidation of SiC in the presence of BN and Na_2SO_4 will rapidly crystallize the reaction layer.

There are at least four possible mechanisms that explain the flattening of SiC consumption at increased times. First, a mechanism put forth by Jacobson proposed that a highly porous reaction layer on α-SiC specimens exposed to Na_2SO_4, transformed into a relatively thick SiO_2 layer void of porosity. The transformation into a non-porous SiO_2 layer was attributed to the reduction in SiC consumption.[9] A high degree of porosity was observed in this work on specimen surfaces exposed at 1000°C (Figure 3.9 and 3.10) at times up to 3h versus those exposed at 800°C. Inward permeation of O_2(g), outgassing of CO(g) and volatile B-containing species could lead to the observed rapid oxidation at 1000°C. These pores disappear after nearly 3h at 1000°C, which corresponded to the time which cristobalite formation was first observed via XRD. However, no diffraction of the reaction layer was performed by Jacobson.[9] Second, Hagan found that a build-up of a dense and continuous SiO_2 layer was the reason for the plateau in SiC consumption. Third, the silica reaction layer crystallizing into a continuous tridymite layer is a possible mechanism to explain the reduction in SiC consumption after prolonged exposure. Hagan and this work showed that the reaction layer crystallized into tridymite. This work showed that at temperatures both above and below the melting temperature of Na_2SO_4, tridymite crystallization was observed to begin at the same time as the kinetic plateau observed in ICP-OES Si level measurements. Finally, B_2O_3 and Na_2SO_4 volatilization and consumption via reaction could also contribute to the kinetic plateau observed. At low temperatures Na_2SO_4 was present up to 24h at 800°C. The formation of tridymite peaks appeared after the volatilization of S between 24h-96h of exposure at 800°C. In summary, (1) reduction in porosity in the reaction layer, (2) formation of a continuous silica layer, (3) reaction layer crystallization, and (4) B_2O_3 and Na_2SO_4 volatilization and could all synergistically cause the observed flattening in SiC consumption. Further investigation is needed to determine the role each of these potential mechanism partake in flattening of SiC consumption rates.

3.4.2 Surface Degradation

The addition of BN to Na_2SO_4 deposit-induced hot corrosion of SiC not only decreases the onset temperature for corrosion, but also creates temperature dependent morphological attack on SiC surfaces. At temperatures of 900°C and below a non-uniform melt led to the formation of "rivulet" attack surface features, while at temperatures above 900°C a uniform melt resulted in surface pitting. Because of the general trend of lower viscosities with increasing temperature in sodium borosilicate melts, reaction layers formed well above 884°C resulted in uniform, surface wide melts, seen in Figures 3.3, 3.9 and 3.10.[62] This surface covering melt allowed for a more uniform reaction layer than those observed at lower temperatures. The formation of higher viscosity sodium borosilicate liquid droplets and lack of Na_2SO_4 melting at temperatures below 884°C resulted in non-uniform surface layers. These non-uniform surface layers allowed for the formation of rivulet surface attack features due to the irregular contour left by sodium borosilicate liquid droplets. The higher temperature exposure ($T>1000°C$) of SiC to both BN and Na_2SO_4 in this work formed localized pits similar to those observed by Jacobson and Hagan.[23, 25] These pits are attributed to localized attack at structural discontinues such as grain boundaries, resident porosity form the starting material, or pores built-up due to oxidation of the B and C sintering aids. Thus, exposure of SiC to BN + Na_2SO_4 creates a temperature dependent set of attack morphologies based upon the melting of the reaction layer.

3.5 Implications For Turbine Engine Application

Na_2SO_4 deposit-induced hot corrosion of uncoated CMCs or spalled regions of coated CMCs is a problem. Without BN present, Na_2SO_4 deposit-induced hot corrosion to SiC occurs only above the melting temperature of

Na_2SO_4 (T_m = 884°C). This type of hot corrosion increases SiC oxidation rates and generates deep pits in SiC surfaces. With BN present though, Na_2SO_4 deposit-induced hot corrosion occurs both above and below the melting temperature of Na_2SO_4. Liquid sodium borosilicate can form down to ~700°C due to several low-temperature eutectics in the SiO_2-Na_2O-B_2O_3 system. Thermally grown liquid sodium borosilicates allows for rapid transport of O_2(g) and increased SiC consumption relative to Na_2SO_4-only and BN-only environments. Along with consumption of SiC at these lower temperatures, wide-trenches or rivulets into SiC surfaces occurs. Above the melting temperature of Na_2SO_4, rapid oxidation and localized pitting of SiC still occurs similarly to the hot corrosion of SiC + Na_2SO_4. Given the behavior discussed in this dissertation chapter, SiC CMCs potentially could undergo accelerated oxidation across a wider range of temperatures in the presence of Na_2SO_4 + BN, than in the presence of only Na_2SO_4 or BN. Additionally, temperature dependent morphological attack into CMC surfaces can occur in the presence of both Na_2SO_4 + BN, creating a more complex attack morphology and fracture behavior. Hot corrosion below the melting temperature of Na_2SO_4 and rapid attack of SiC surfaces is problematic for SiC CMCs.

3.6 Conclusions

It was found that BN lowered the onset temperature of Na_2SO_4 deposit-induced hot corrosion of SiC by nearly 200°C below the melting temperature of Na_2SO_4. Without BN, Na_2SO_4 deposit-induced hot corrosion of SiC occurs at temperatures above the melting temperature of Na_2SO_4 (T_m=884°C). The hot corrosion of SiC initially produced a liquid thermally grown oxide due to low-melting eutectics in the SiO_2-Na_2O-B_2O_3 system, that over time crystallized in mixtures of the SiO_2 phases tridymite and cristobalite due to SiO_2 enrichment in the thermally grown oxide. The mixture of SiO_2, B_2O_3, and Na_2O led to an initial accelerated period of SiC oxidation that eventually ended due to the establishment of a (i) low-porosity,

(ii) crystalline SiO_2 reaction layer and also a (iii) Na_2SO_4 depleted layer. The time for crystallization of the reaction layer to occur was slower at lower temperatures, needing days at 800°C while only a few hours at 1000°C. The effect of BN on Na_2SO_4 deposit-induced hot corrosion of SiC at temperatures above the Na_2SO_4 melting temperature was minimal due to rapid B_2O_3 volatilization. Nearly equal amounts of SiC consumption occurred at 800°C and 1000°C after exposure for several days, despite the slower reaction kinetics at 800°C. Temperature dependent-attack into SiC surfaces was observed. Five µm deep rivulets tens of microns wide formed into SiC surfaces at 900°C and below, while localized, 10-30 µm deep pits formed at exposure temperatures above 900°C.

References

1. Zok FW. Ceramic matrix composites enable revolutionary gains in turbine efficiency. 2016;95:22–28.
2. Melissae Fellet. Ceramic-Matrix Composites Take The Heat. *MRS Bull*. 2015;40:916–7.
3. Presser V, Nickel KG. Silica on Silicon Carbide. *Crit Rev Solid State Mater Sci*. 2008;33(1):1–99.
4. Guy E. Oxidation Behavior of Silicon Carbide. *J Am Ceram Soc*. 1958;41(9):347–352.
5. Costello JA, Tressler ER. Oxidation Kinetics of Silicon Carbide Crystals and Ceramics: I, In Dry Oxygen. *J Am Ceram Soc*. 1986;69(9):674–681.
6. Costello JA, Tressler ER. Oxidation Kinetics of Hot-Pressed and Sintered α-SiC. *J Am Ceram Soc*. 1981;64(6):327–331.
7. Ramberg EC, Gary C, Spear KE, Tressler RE, Ramberg CF. Passive-Oxidation Kinetics of High-Purity Silicon Carbide from 800° to 1100°C. *J Am Ceram Soc*. 1996;79(11):2897–2911.
8. Jacobson NS, Smialek JL. Hot Corrosion of Sintered α-SiC at 1000°C. *J Am Ceram Soc*. 1985;68(8):432–439.
9. Jacobson NS. Kinetics and Mechanism of Corrosion of SiC by Molten Salts. *J Am Ceram Soc*. 1986;69(1):74–82.
10. Pareek V, Shores DA. Oxidation of Silicon Carbide in Environments Containing Potassium Salt Vapor. *J Am Ceram Soc*. 1991;74(3):556–563.
11. McFarland B, Opila EJ. Silicon Carbide Fiber Oxidation Behavior in the Presence of Boron Nitride. *J Am Ceram Soc*. 2018;101:5534–5551.
12. Wilson, Megan. Oxidation of SiC/BN/SiC Ceramic Matrix Composites and Their Constituents. PhD Thesis; University of Virginia, Materials Science and Engineering; Charlottesville, VA; 2018
13. Jacobson NS, Serene F, Arthur M, Haluk S. High-Temperature Oxidation of Boron Nitride: I, Monolithic Boron Nitride. *J Am Ceram Soc*. 1999;82(2):393–398.
14. Jacobson NS, Morscher GN, Bryant DR, Tressler RE. High-Temperature Oxidation of Boron Nitride: II, Boron Nitride Layers in Composites. *J Am Ceram Soc*. 1999;82(6):1473–1482.
15. Rockett TJ, Foster WR. Phase Relations in the System Boron Oxide–Silica. *J Am Ceram Soc*. 1965;48(2):75–80.
16. Rockett TJ, Foster WR. The System Silica-Sodium Tetraborate. *J Am Ceram Soc*. 1966;49(1):30–33.
17. Rockett TJ, Foster WR. The High-Silica Liquidus Surface of the System Na_2O-B_2O_3-SiO_2. *J Am Ceram Soc*. 1981;64(11):148-149.
18. Stearns CA, Kohl FJ, Rosner DE. Combustion System Processes Leading to Corrosive Deposits. San Diego, California: 1981
19. Pettit F. Hot Corrosion of Metals and Alloys. *Oxid Met*. 2011;76(1):1–21.
20. Luthra KL. Kinetics of the Low Temperature Hot Corrosion of Co-Cr-Al Alloys. *J Electrochem Soc*. 1985;132(6):1293–1298.

21. Goebel JA, Pettit FS. Na_2SO_4-induced accelerated oxidation (hot corrosion) of nickel. *Metall Trans*. 1970;1(7):1943–1954.
22. Stringer J. Hot Corrosion of High-Temperature Alloys. *Annu Rev Mater Sci*. 1977;7(1):477–509.
23. Hagan JM, Opila EJ. High-Temperature Na_2SO_4 Deposit-Assisted Corrosion of Silicon Carbide – I: Temperature and Time Dependence. *J Am Ceram Soc*. 2015;98(4):1275–1284.
24. Hagan JM, Opila EJ. High-temperature Na_2SO_4 deposit-assisted corrosion of silicon carbide–II: Effects of B, C, and Si. *J Am Ceram Soc*. 2017;100(2):761–773.
25. Jacobson NS, Smialek JL. Corrosion Pitting of SiC by Molten Salts. 1986;133(12):2615–2621.
26. Smialek JL, Jacobson NS. Mechanism of Strength Degradation for Hot Corrosion of α-SiC. *J Am Ceram Soc*. 1986;69(10):741–752.
27. Morey GW. The Ternary System Na_2O-B_2O_3-SiO_2. *J Soc Glass Technol*. 1951;35(167):270–283.
28. Haller W, Blackburn DH, Wagstaff FE, Charles RJ. Metastable Immiscibility Surface in the System Na_2O-B_2O_3-SiO_2. *J Am Ceram Soc*. 1969;53(1):34–39.
29. Charles RJ, Wagstaff FE. Metastable Immiscibility in the B_2O_3-SiO_2 System. *J Am Ceram Soc*. 1967;51(1):16–20.
30. Ahari-Ghanbari K, Cameron A. Phase Diagram of Na_2O-B_2O_3-SiO_2 System. *J Am Ceram Soc*. 1993;76(8):2017–2022.
31. Buerger MJ, Lukesh J. The Tridymite Problem. *Science*. 1952;95:20.
32. Stevens SJ, Hand RJ, Sharp JH. Polymorphism of Silica. *J Mater Sci*. 1997;32:2929–2935.
33. Rockett TJ. The Thermal Stability of Purified Tridymite. *Am Mineral*. 1967;52:1233–1239.
34. Fenner CN. Stability Relations of the Silica Minerals. *Am J Sci*. 1913;36(4):331–384.
35. Flörke OW. Strukturanomalien bei Tridimyt und Cristobalit. *Berichte Dtsch Keram Ges*. 1955;32:369–381.
36. Fenner CN. The Relations Between Tridymite and Cristobalite. *Trans Soc Glass Technol*. 1919;3:116.
37. Flörke OW. Des Kriställrten des SiO_2 und ihr Umwandlungsverhalten. *Berichte Dtsch Keram Ges*. 1961;38(3):89–97.
38. Flörke OW. Uber das Einstoffsystem SiO. *Naturwissenschaften*. 1956;43:419.
39. Holmquist SB. Conversion of Quartz to Tridymite. *J Am Ceram Soc*. 1961;44(2):82–86.
40. Tuttle OF, England JL. Preliminary Report on the System SiO_2-H_2O. *Bull Geol Soc Am*. 1955;66(1):149–152.
41. Kracek FC. The System Sodium Oxide-Silica. *J Phys Chem*. 1929;34(7):1583–1598.

42. Kracek FC. The Ternary System, K_2SiO_3-Na_2SiO_3-SiO_2. *J Am Chem Soc*. 1939;61(10):2863–2877.
43. Kracek FC. Phase Equilibrium Relations in the System, Na_2SiO_3-Li_2SiO_3-SiO_2. *J Am Chem Soc*. 1939;61(10):2863–2877.
44. Sastry BSR, Hummell FA. Studies in Lithium Oxide System: VII, Li_2O-B_2O_3-SiO_2. *J Am Ceram Soc*. 1960;43:23.
45. Schairer JF, Bowen NL. The System Na_2O-Al_2O_3-SiO_2. *Am J Sci*. 1956;254:129.
46. Levin EM, Cleek GW. The Systen Barium Oxide-Boric Oxide-Silica. *J Am Ceram Soc*. 1958;41:175.
47. Rockett TJ. Phase Relations in the Systems Silica, Boron Oxide-Silica, and Sodium Oxide-Boron Oxide-Silica. The Ohio State University; Mineralogy; 1963
48. Opila EJ. Variation of the Oxidation Rate of Silicon Carbide with Water-Vapor Pressure. *J Am Ceram Soc*. 1999;82(3):625–636.
49. Opila EJ, Hann RE. Paralinear Oxidation of CVD SiC in Water Vapor. *J Am Ceram Soc*. 1997;80(1):197–205.
50. Ogbuji LUJT, Opila EJ. A Comparison of the Oxidation Kinetics of SiC and Si_3N_4. *J Electrochem Soc*. 1995;142(3):925–930.
51. Presser V, Loges A, Hemberger Y, Nickel KG. Microstructural Evolution of Silica on Single-Crystal Silicon Carbide. Part I: Devitrification and Oxidation Rates. *J Am Ceram Soc*. 2009;92(3):724–731. https://doi.org/10.1111/j.1551-2916.2009.02930.x
52. Presser V, Loges A, Wirth R, Nickel KG. Microstructural Evolution of Silica on Single Crystal Silicon Carbide. Part II: Influence of Impurities and Defects. *J Am Ceram Soc*. 2009;92(8):1796–1805. https://doi.org/10.1111/j.1551-2916.2009.03085.x
53. Luthra KL. Some New Perspectives on Oxidation of Silicon Carbide and Silicon Nitride. *J Am Ceram Soc*. 1991;74(5):1095–1103. https://doi.org/10.1111/j.1151-2916.1991.tb04348.x
54. Opila EJ. Influence of Alumina Reaction Tube Impurities on the Oxidation of Chemically-Vapor-Deposited Silicon Carbide. *J Am Ceram Soc*. n.d.;78(4):1107–1110.
55. Fox DS, Opila EJ, Hann RE. Paralinear Oxidation of CVD SiC in Simulated Fuel-Rich Combustion. *J Am Ceram Soc*. 2000;83(7):1761–1767. https://doi.org/10.1111/j.1151-2916.2000.tb01461.x
56. John A. Coppola, Laurence N. Hailey, Carl H McMurtry. Sintered Alpha Silicon Carbide Ceramic Body Having Equiaxed Microstructure. n.d.
57. Browning R, Smialek J, Jacobson N. Mulitelement Mapping of α-SiC by Scanning Auger Spectroscopy. *Adv Ceram Mater*. 1987;4(2):773–79.
58. Hay RS, Fair GE, Bouffioux R, *et al.* Hi-Nicalon™-S SiC Fiber Oxidation and Scale Crystallization Kinetics. *J Am Ceram Soc*. 2011;94(11):3983–3991.

59. Hay RS, Fair GE, Bouffioux R, *et al.* Relationships Between Fiber Strength, Passive Oxidation and Scale Crystallization Kinetics of Hi-Nicalon™-S SiC Fibers. *J Am Ceram Soc*. 2011;94(11):3983–3991.
60. Wilson M, Opila EJ. A Review of SiC Fiber Oxidation with a New Study of Hi-Nicalon SiC Fiber Oxidation. *Adv Eng Mater*. 2016;18(10):1698–1709.
61. Lamkin MA, Riley FL, Fordham RJ. Oxygen mobility in silicon dioxide and silicate glasses: a review. *J Eur Ceram Soc*. 1992;10(5):347 – 367.
62. Brosh E, Pelton AD, Decterov SA. A Model to Calculate the Viscosity of Silicate Melts Part V: Borosilciate Melts Containing Alkali Metals. *Int J Mater Res*. 2012;103(5):537–550.

4 | High Temperature Na_2SO_4 Interaction with Air Plasma Sprayed $Yb_2Si_2O_7$-Si-SiC Coating System

4.1 Introduction

Silicon carbide (SiC) ceramic matrix composites (CMCs) have already entered service into GE Aviation's LEAP engines as non-load bearing components.[1, 2] However, further research and development is required for SiC CMCs to replace metallic load-bearing components in the hot-section of these engines. Monolithic SiC possesses many properties that make its usage in turbine engines desirable, including low density and superior high temperature capability. However, due to the brittle fracture behavior of monolithic SiC, a reinforcing SiC fiber phase is used to provide damage tolerance by hindering crack propagation through the composite material. This damage tolerance is achieved through a weakly bonded SiC fiber/SiC matrix (SiC_f/SiC_m) boron nitride (BN) interphase coating.[3–6] Despite the promise of these revolutionary materials, there is still uncertainty in predicting the high temperature oxidation and corrosion rate of SiC CMC components.[7]

Turbine engines create oxidizing conditions for SiC CMCs. It is well known that bulk SiC oxidizes at high temperature in dry $O_2(g)$ environments to form SiO_2 and CO(g), seen in Equation (4.1)[8]:

$$SiC + 3/2\ O_2(g) \rightarrow SiO_2 + CO(g) \tag{4.1}$$

This reaction is well studied, and closely follows the Deal-Grove oxidation model used to predict the formation of SiO_2 on silicon (Si).[9, 10] This thermally grown SiO_2 layer on SiC acts as a self-protective diffusion barrier limiting for further oxidation, but only in impurity-free, dry O_2 containing environments. Environmental impurities such as Na_2O and B_2O_3 form low-melting silicates, which allow for rapid oxygen transport through nonprotective, highly permeable surface reaction layers, accelerating SiC oxidation kinetics.[11–18] Upon exposure to steam, SiC simultaneously reacts to form SiO_2 then volatilizes into the gaseous silicon hydroxide species $Si(OH)_4$, seen below in Equations (4.2) and (4.3):

$$SiC + 3\ H_2O\ (g) \rightarrow SiO_2 + 3\ H_2(g) + CO(g) \tag{4.2}$$

$$SiO_2 + 2\ H_2O\ (g) \rightarrow Si(OH)_4(g) \tag{4.3}$$

Experimental and modeling efforts have shown that SiC recession rates in high velocity steam are ~1 μm/h at temperatures of ~1200°C.[19–24] As a result of the nonprotective nature of thermally grown SiO_2 in steam and impurity containing environments, the usage of ceramic environmental barrier coatings (EBCs) are required for SiC CMCs components to last thousands of hours in turbine engine environments. Successful EBCs must adhere well to CMC components, possess a low level of reactivity within the engine environment, and must slow the diffusion of inward permeating of oxidizing species to prevent environmental degradation to SiC CMCs.

Currently, thermal spray techniques such as air plasma spray (APS) are used to deposit EBCs onto SiC CMC components. This processing technique injects the coating materials as powders into a high-velocity plasma jet, which deposit as molten splats onto components. Due to the large temperature gradients experienced in this technique, deposited coatings retain a "splat" microstructure filled with microcracking, porosity, along with non-equilibrium and amorphous phases.[25] Additionally it is known that silica containing materials (i.e. silicates, mullite etc.) sprayed using APS volatilize in the jet forming SiO(g), resulting in a coating with a SiO_2-depleted composition. Porosity in EBCs deposited using APS can be as high as ~15 vol% and secondary phase content can be as high as ~25 vol% depending upon processing parameters.[26–29] Post-deposition annealing is generally used to alleviate residual stresses, promote formation of crystalline phases, and to restore stoichiometry.

A promising and widely studied EBC is ytterbium disilicate ($Yb_2Si_2O_7$), as this material meets many of the properties needed for a durable EBC. Furthermore, a silicon (Si) bonding layer is used between the $Yb_2Si_2O_7$ EBC (or topcoat) and SiC CMC components to prevent interfacial gas-phase induced porosity built-up from CO(g) produced during oxidation of SiC (Equation (4.1)). Oxidation of Si in both dry and wet O_2(g) environments produces a dense SiO_2 reaction product minimizing the liberation of gaseous species, seen in Equations (4.4) and (4.5):

$$Si + O_2(g) \rightarrow SiO_2(s) \tag{4.4}$$

$$Si + 2H_2O(g) \rightarrow SiO_2(s) + 2H_2(g) \tag{4.5}$$

This oxidation product is slow-growing, with growth kinetics described by the linear-parabolic Deal-Grove oxidation model.[9] The permeation of oxidizing species through the EBC topcoat causes oxidation of the underlying Si bond coat, leading to the build-up of a buried SiO_2 thermally grown oxide (TGO) between the $Yb_2Si_2O_7$ topcoat and Si bond coat.[30, 31] The oxidation product is reported to form β-cristobalite during exposure, which inverts to its low-temperature polymorph α-cristobalite upon cooling below ~200-300°C.[32–34] This phase transformation causes cracking due to a ~5% density increase upon cooling, causing concern for EBC durability. An additional environmental degradation mechanism for $Yb_2Si_2O_7$ EBCs is the high temperature interaction with siliceous deposits known as calcium magnesium aluminosilicates (CMAS). It was found that $Yb_2Si_2O_7$ reacts only above the melting temperature of CMAS deposits, which generally is no less than ~1200°C depending upon the CMAS composition. Conflicting observations on the stability of $Yb_2Si_2O_7$ materials in contact with CMAS have been reported, as some works observed the formation of the crystalline apatite phase $Ca_2Yb_8(SiO_4)_6O_2$ while others did not.[35–39] However, the interaction of $Yb_2Si_2O_7$ with Na_2SO_4 deposits, another known source of deposit-induced degradation in turbine engines, has received very little attention in literature.

Operation of turbine engines in marine environments, results in the ingestion of NaCl that reacts *in-situ* with S impurities in the fuel or environment, leading to the formation of Na_2SO_4, seen in Equation (4.6).[40]

$$2NaCl + SO_3\,(g) + H_2O(g) \rightarrow Na_2SO_4 + 2HCl(g) \tag{4.6}$$

Na_2SO_4 melts at 884°C, a significantly lower temperature than that associated with CMAS melting. Liquid Na_2SO_4 salts deposit onto metallic hot-section components in current turbine engines, leading to a form of attack known as hot corrosion, resulting in the rapid oxidation and surface pitting of hot-section components. Due to the known formation and deposition of Na_2SO_4 on metallic components, high temperature reactions with EBC coated SiC CMC components are also expected. Hot corrosion studies on mullite ($3Al_2O_3{\bullet}2SiO_2$) coated SiC substrates and stand-alone yttrium disilicate ($Y_2Si_2O_7$) revealed the formation of crystalline reaction products at the coating surface.[41, 42] No work has been performed on hot corrosion of $Yb_2Si_2O_7$ materials nor does a phase diagram exist for the Yb_2O_3-SiO_2-Na_2O system. However, research in synthesizing Yb_2O_3-SiO_2-Na_2O compounds has proven the existence of a sodium apatite phase $NaYb_9Si_6O_{26}$ along with $Na_3YbSi_2O_7$ and $NaYbSiO_4$ phases.[31, 32]

Due to the importance of EBCs systems for SiC CMCs in gas-turbine engines and known Na_2SO_4 deposit based-degradation of hot-section materials in current turbine engines, the high temperature interaction of Na_2SO_4 deposits on EBC systems employing a $Yb_2Si_2O_7$ topcoat with a Si bond coat must be understood. This work focuses on the interaction of

Na_2SO_4 with an APS $Yb_2Si_2O_7$-Si coated SiC CMC, with emphasis on morphology, degradation behavior, and phase content of the top coat as a function of time and temperature.

4.2 Experimental

4.2.1 Materials

High temperature testing of coating systems with Na_2SO_4 was performed on SiC CMCs with a Si bond coat and APS $Yb_2Si_2O_7$ top coat specimens provided by Rolls-Royce North America (Indianapolis, IN). Specimens with dimension 1.27 cm x 1.27 cm x 0.3175 cm were received in the as-sprayed condition.

4.2.2 Hot Corrosion Procedure

All coated CMC specimens were annealed for 2h at 1200°C in air using a heating rate of 15°C/min, to promote crystallization of amorphous Yb-Si-O into crystalline phases before reaction with Na_2SO_4. Na_2SO_4 was applied to $Yb_2Si_2O_7$ surfaces as an aqueous solution in the ratio of 3g of Na_2SO_4 to 100 mL of DI water. Water was evaporated in a convection oven (Forced Air Convection Oven, MTI, Richmond, CA) at 120°C until only Na_2SO_4 salt remained. Specimens were weighed using a high precision analytical balance (Mettler Toledo, Columbus, OH) before and after salt deposition to ensure Na_2SO_4 loadings of ~2.5 mg/cm^2. High temperature testing was performed in a horizontal tube furnace (CM Furnaces, Bloomfield, NJ) fitted with gas-tight, O-ring sealed stainless steel endcaps for controlled atmospheric testing. All testing was performed in high purity fused quartz tubes (99.99%, Quartz Scientific, Fairport Harbor, OH) with an OD and ID of 50 mm and 47cm, respectively. Specimens were loaded onto an Al_2O_3 boat (99.8%, CoorsTek, Golden, CO) and exposed at temperatures between 1000-1316°C for times between 1-240h in a flowing 100 sccm 0.1% (1000 ppm) SO_2-O_2 gaseous mixture. Specimens were loaded at temperature, endcaps sealed, and the 0.1% SO_2-O_2 gas mixture was initiated. Several minutes before ending experimentation, the sealed tube was flushed with dry O_2 allowing for removal of the 0.1% SO_2-O_2 gas mixture, and specimens were subsequently air quenched. A single specimen was exposed at each time and temperature.

4.2.3 Characterization

The interaction of Na_2SO_4 with the coating system was assessed using several characterization techniques. X-ray diffraction (XRD) was conducted to determine the formation of crystalline reaction products. Data were collected using a diffractometer (Empyrean PANalytical, Almelo, the Netherlands) with Cu Kα (λ=0.1541 nm) radiation, while peak identification was done using Highscore Plus software. The morphology and chemical composition of specimens in cross-section and plan-view were determined using scanning electron microscopy (SEM) (Quanta 650, FEI Company, Hillsboro, OR) and energy dispersive spectroscopy (EDS) (X-max 150, Oxford Instruments, Abingdon, England). Prior to cross-sectional analysis, specimens were mounted in epoxy, then sectioned using a diamond tipped low-speed saw in a non-aqueous, ethylene glycol lubricant to minimize the removal of water soluble phases. Polishing was performed using an ethylene-glycol based diamond suspension down to a mirror finish, with the final polishing step ending with 0.250 μm diameter diamond suspension. ImageJ software analysis was performed on three high-resolution SEM images for porosity and phase content analysis in the topcoat.

4.3 Results

4.3.1 Topcoat Surface Interaction with Na_2SO_4

A SEM image of an APS $Yb_2Si_2O_7$ topcoat-Si bond coat EBC system on a SiC CMC substrate in cross-section, after annealing can be seen in Figure 4.1. The top coat contained cracks, porosity and voids as a result of APS processing. ImageJ digital software analysis determined the Si bond coat was ~50 μm thick while the top coat was ~130 μm thick. The topcoat was ~7% porous by volume and comprised of 8 vol.% Yb_2SiO_5 balance $Yb_2Si_2O_7$. The same topcoat surface in plan-view can be seen in Figure 4.2a), while the topcoat near the surface can be seen in cross-section in Figure 4.2b). This

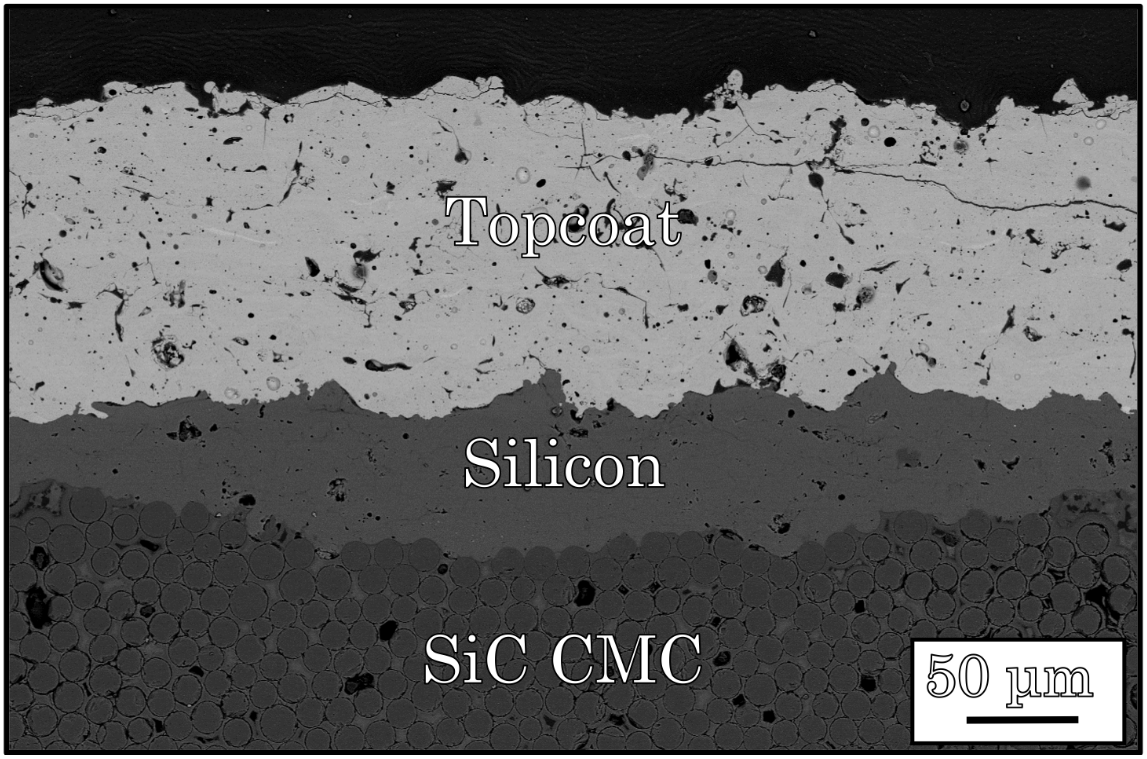

Figure 4.1. Backscattered SEM image of an APS $Yb_2Si_2O_7$ topcoat + Si bond coat EBC system on a SiC CMC substrate in cross-section after annealing for 2h at 1200°C in air.

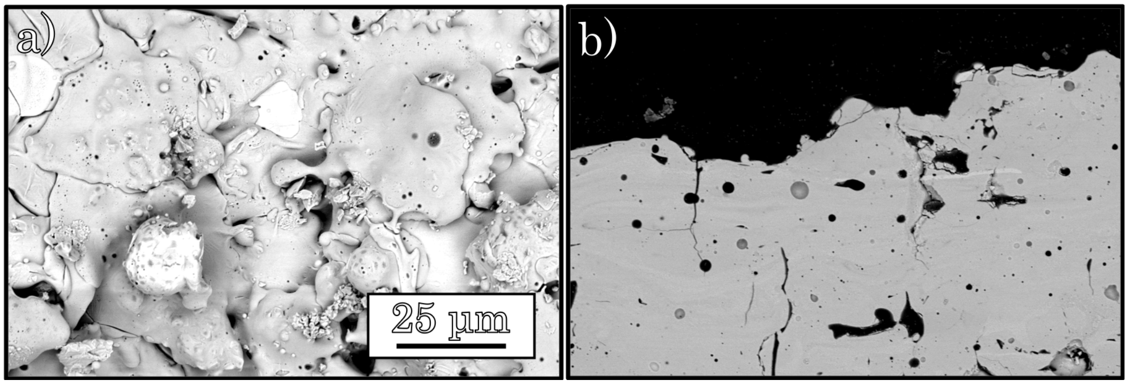

Figure 4.2. Backscattered SEM images of the topcoat in a) plan view and b) near the surface in cross-section after annealing for 2h at 1200°C in air.

coating system and its microstructure is representative of all specimens tested in this work.

A time and temperature dependent X-ray diffraction study on coatings post-exposure to Na_2SO_4 for times up to 240h at temperatures between 1000°C-1316°C can be seen in Figure 4.3. Examination of this figure reveals the post-annealed coating, before exposure to Na_2SO_4 and without any salt deposits on the surface, consists primarily of $Yb_2Si_2O_7$ and a small Yb_2SiO_5 phase fraction evident by low intensity Yb_2SiO_5 peaks at ~31° 2θ. All observed peaks post-exposure to Na_2SO_4 across the entire testing range belong to either $Yb_2Si_2O_7$ or Yb_2SiO_5. No Na_2SO_4 peaks were present after any exposure condition, presumably due to rapid reaction or volatilization, nor were any ternary Yb_2O_3-SiO_2-Na_2O compounds detected. $Yb_2Si_2O_7$ peaks exhibited high intensity across all testing conditions, while the Yb_2SiO_5 peak intensity varied across time and temperature, indicating changes in its phase content. Yb_2SiO_5 peaks after exposure at 1200°C and above were more intense than the peaks formed below 1200°C. These strong Yb_2SiO_5 peaks formed less than 1h into exposure at 1200°C and above, which provides evidence of a rapid reaction. However, the Yb_2SiO_5 peak intensity was not constant over time at these higher temperatures, as a decrease in intensity after exposure for 1h can be observed, especially for the 24h and 240h exposures. Similar diffraction studies performed on powder mixtures of $Na_2SO_4 + Yb_2Si_2O_7$ (and also $Na_2SO_4 + Yb_2SiO_5$) mixtures after exposure in air at temperatures between 1000°C-1400°C can be seen in Appendix D.

Microstructural analysis of topcoat surfaces revealed a reaction of Na_2SO_4 with the topcoat occurred after exposure at all times and temperatures, evident by the morphological changes seen in Figure 4.4. The reaction at 1000°C and 1100°C was sluggish, as after exposure for 240h only

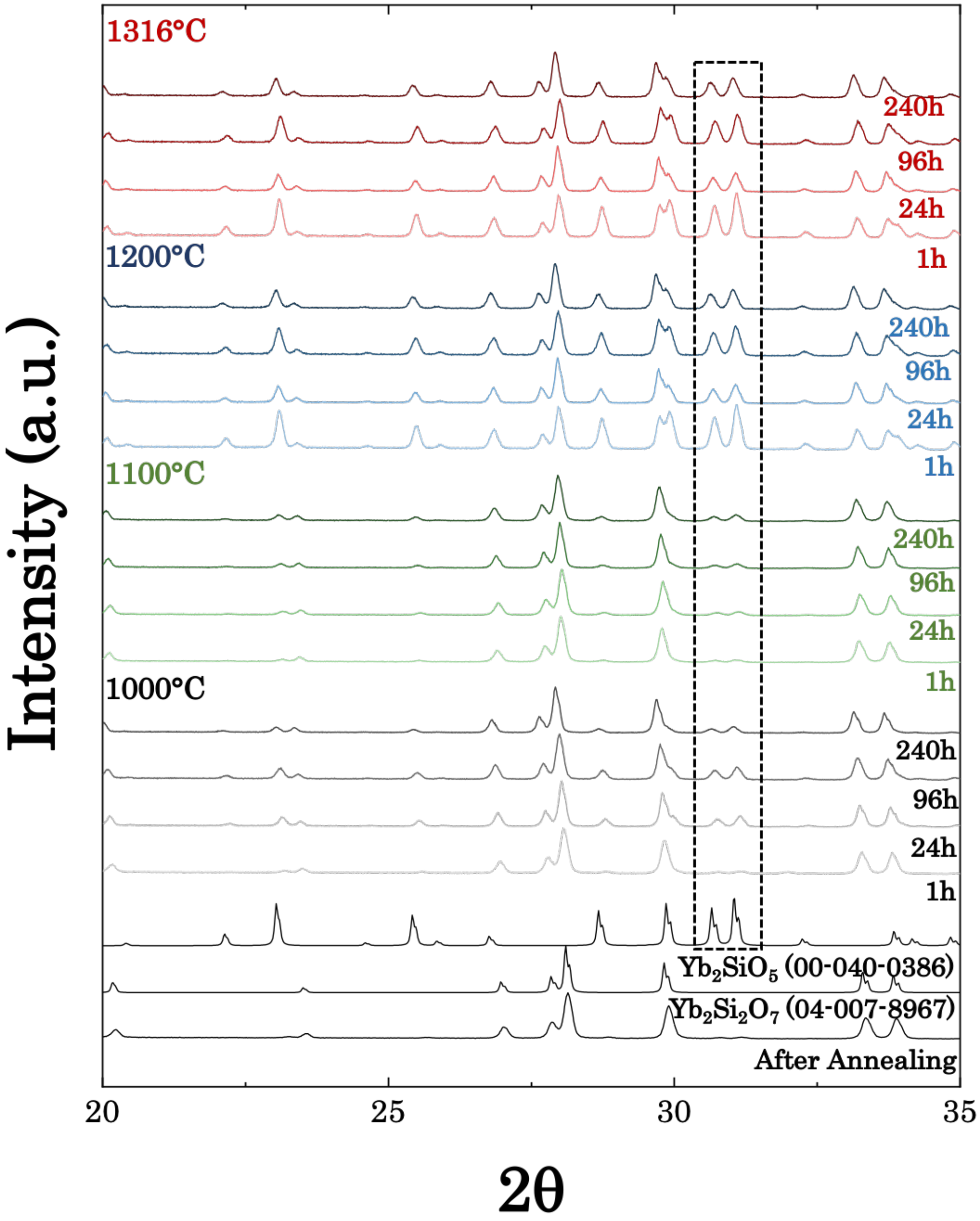

Figure 4.3. XRD patterns of air plasma sprayed $Yb_2Si_2O_7$-Si coated SiC CMC specimens after exposure to ~2.5 mg/cm^2 of Na_2SO_4 for times between 1-240h at 1000°C-1316°C in a gaseous 0.1% SO_2-O_2 environment. The dashed box represents the most intense diffracting peaks associated with Yb_2SiO_5.

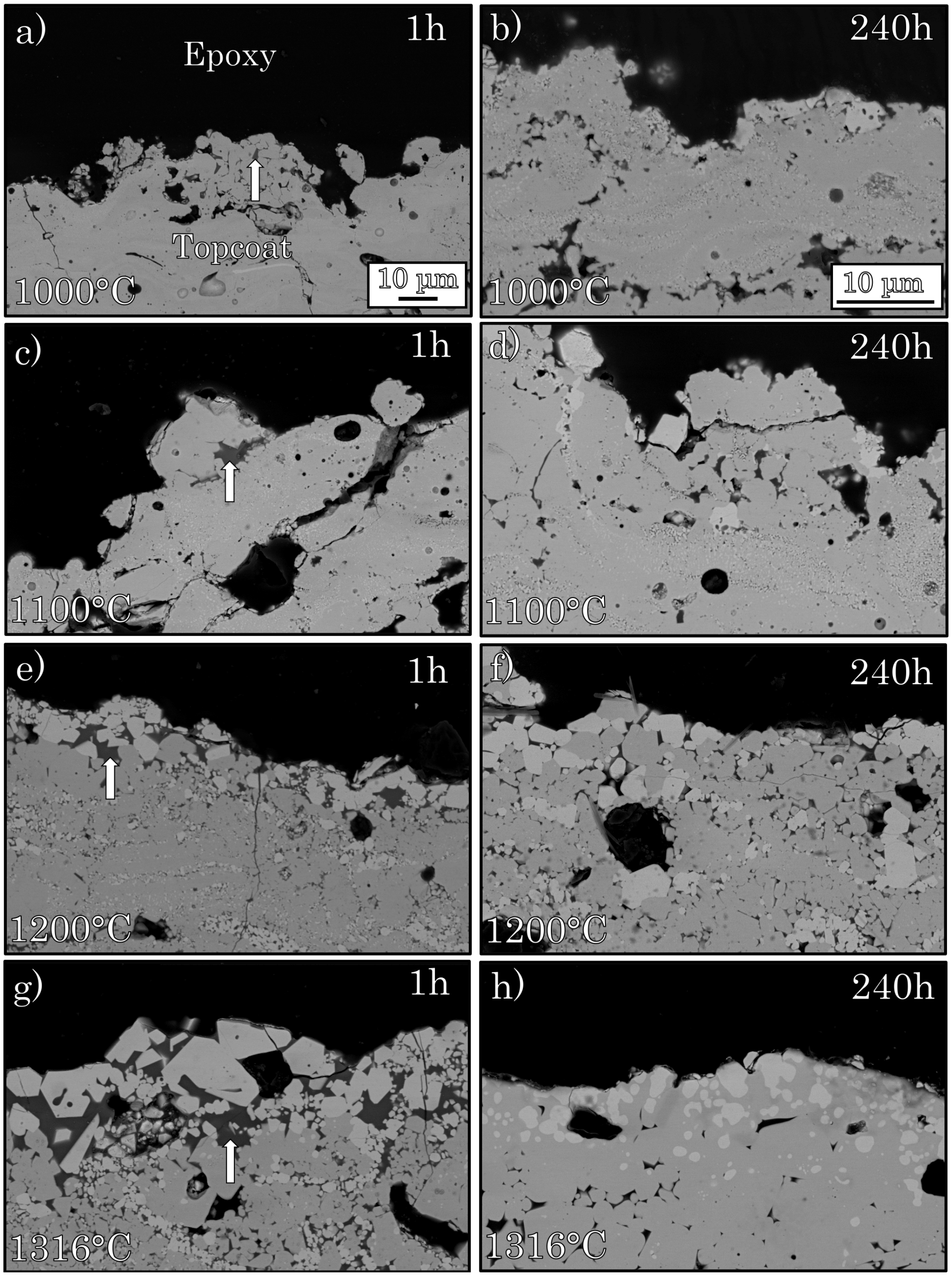

Figure 4.4. Backscattered SEM images of the topcoat surface in cross-section after exposure to ~2.5 mg/cm^2 of Na_2SO_4 for 1h (left) and 240h (right) at a)-b) 1000°C, c)-d) 1100°C, e)-f) 1200°C, and g)-h) 1316°C in a gaseous 0.1% SO_2-O_2 environment (arrows denote intergranular phase).

slight microstructural changes in the topcoat were observed, seen in Figures 4.4a)-4.d). The reaction kinetics were rapid at 1200°C and above, resulting in significant changes to the topcoat surface less than 1h into exposure, seen in Figure 4.4e) and 4.4h). Bright and medium contrast, granulated phases, along with an interpenetrating dark-phase at the coating surface can be observed at the coating surface after exposure for 1h denoted by the arrows in Figures 4.4a), c), e) and g). Exposure for 240h at these higher temperatures resulted in grain coarsening, disappearance of the black interpenetrating phase, and reduction in the bright-contrast phase below the surface (most apparent in Figure 4.4g). Localized chemical composition analysis performed on the surface of a topcoat after exposure for 96h at 1316°C using EDS point analysis can be seen in Figure 4.5. The composition measurement on the bright contrast phase (Point A) revealed a Yb:Si ratio of 1.9, consistent with Yb_2SiO_5, whilst the medium contrast phase (point B) determined a Yb:Si ratio of 1, consistent with of $Yb_2Si_2O_7$. The intergranular black contrast phase (point C) was confirmed to have Si, Na, and Yb, indicative of a silicate phase. Due to the electron beam interaction volume arising from the 10kV accelerating voltage extending into the surrounding region, parts of the Yb and Si signal generated from the silicate phase likely originate from neighboring $Yb_2Si_2O_7$ and Yb_2SiO_5 grains.

Microstructural characterization of topcoat surfaces after exposure to Na_2SO_4 can be seen in Figure 4.6. The morphology of the topcoat surfaces were hardly transformed after exposure to Na_2SO_4 for 1h at temperatures of 1100°C and below, seen in Figures 4.6a) and 4.6c). However, Na_2SO_4 completely transformed the topcoat from the splat-microstructure associated with APS coatings to a granulated microstructure in less than 1h after exposure at 1200°C and above. Prolonged exposure up to 240h increased the reaction at 1000°C and 1100°C but did very little to alter the granulated morphology at 1200°C and 1316°C, except that the intergranular, silicate phase was less pronounced.

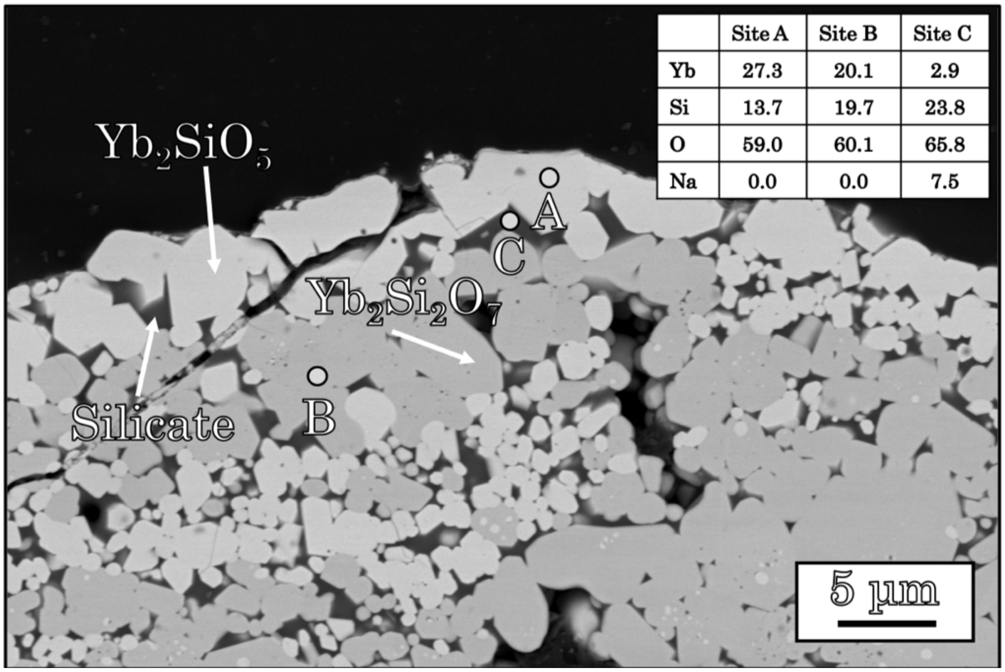

	Site A	Site B	Site C
Yb	27.3	20.1	2.9
Si	13.7	19.7	23.8
O	59.0	60.1	65.8
Na	0.0	0.0	7.5

Figure 4.5. Backscattered SEM image in cross-section of the topcoat after exposure to ~2.5 mg/cm^2 of Na_2SO_4 for 96h at 1316°C in a gaseous 0.1% SO_2-O_2 environment with composition analysis overlaid.

4.3.2 Na Penetration and Si Bond Coat Oxidation

An image of the topcoat/bond coat interface after the air anneal at 1200°C is shown as a baseline in Figure 4.7 for comparison to cross-sections after Na_2SO_4 exposure. The white arrow denotes the sub-micron Yb_2SiO_5 grains present in the topcoat after annealing. Compositional mapping and microscopy of the topcoat near the Si bond coat was performed on Na_2SO_4-exposed specimens for 1h and 240h at the 1000°C and 1316°C exposure temperatures to determine if the reaction of Na_2SO_4 with the topcoat was surface limited, seen in Figures 4.8 through 4.11. These SEM images and corresponding Yb, Si, Na, and O maps revealed that Na penetrated the topcoat rapidly, reaching the Si bond coat less than 1h after exposure 1000°C (Figure 4.8) and to within ~10 µm of the Si bond coat after exposure for 1h at 1316°C (Figure 4.9). The lack of S detected in the Na regions indicates rapid volatilization or reaction of Na_2SO_4 with the topcoat. The presence of Si, O

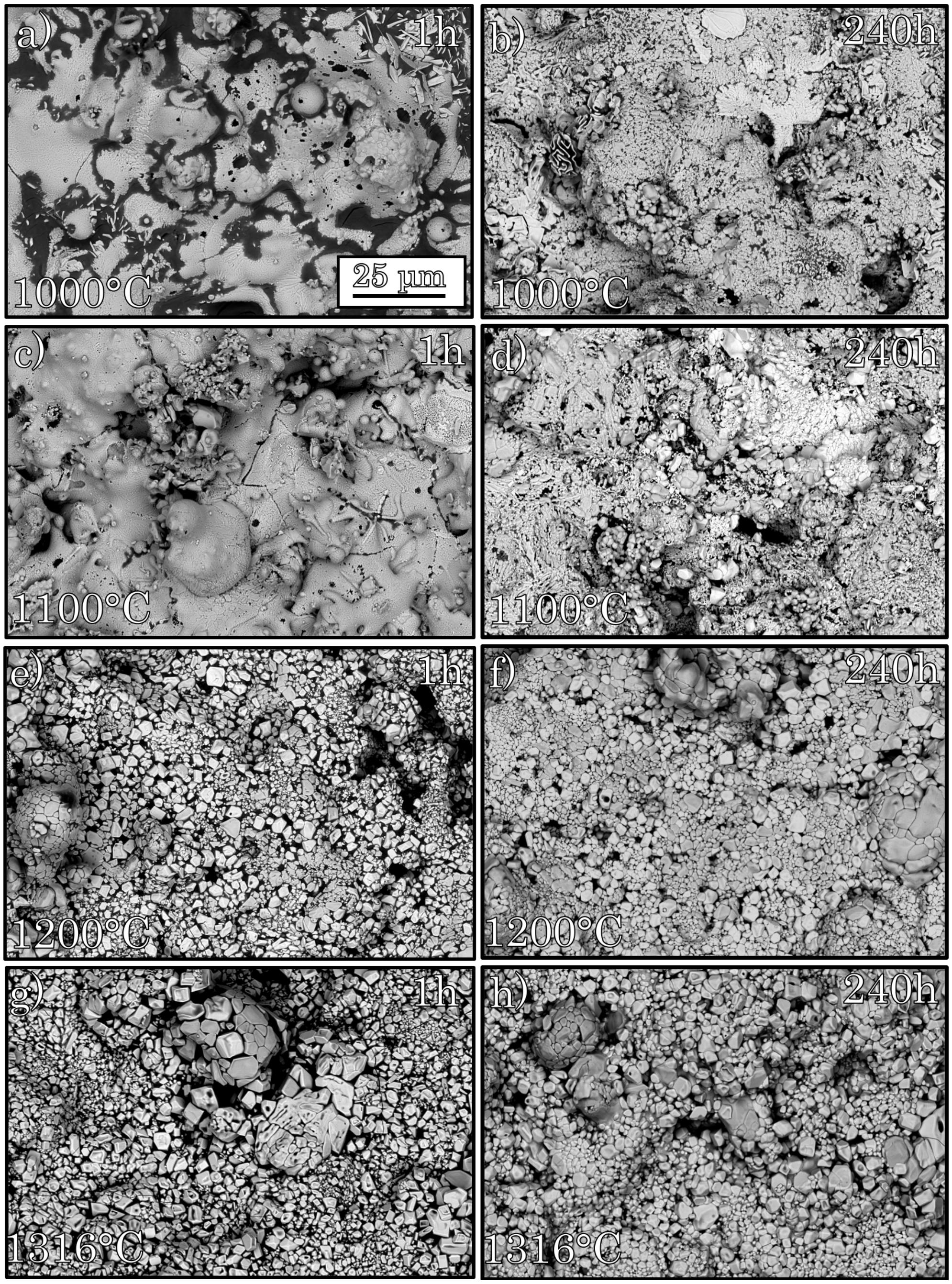

Figure 4.6. Backscattered SEM images of the surface of topcoats after exposure to ~2.5 mg/cm^2 of Na_2SO_4 for 1h (left) and 240h (right) at a)-b) 1000°C, c)-d) 1100°C, e)-f) 1200°C, and g)-h) 1316°C in a gaseous 0.1% SO_2-O_2 environment.

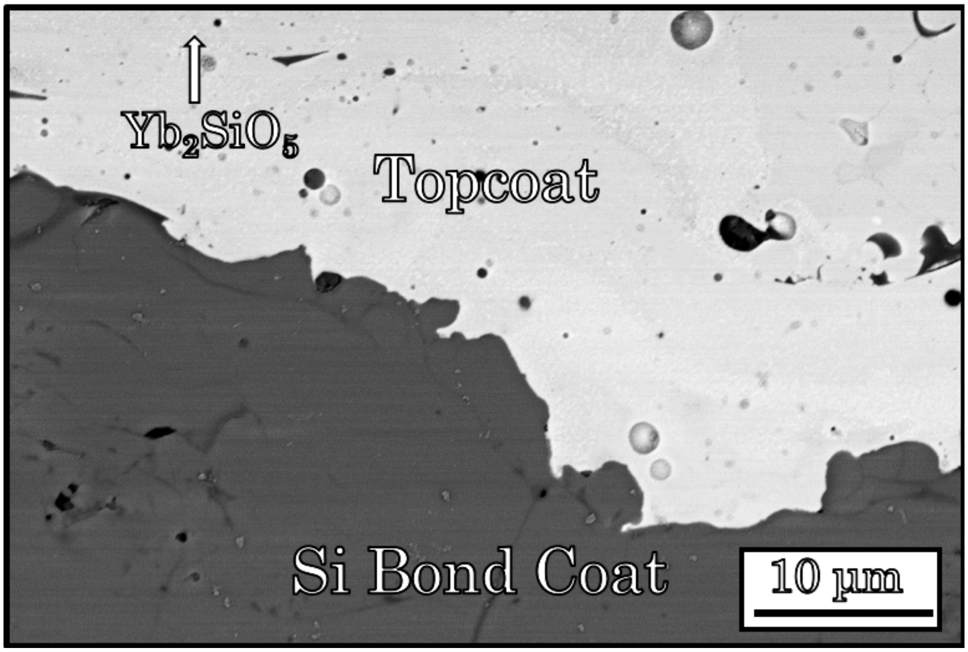

Figure 4.7. Backscattered SEM image of the topcoat-Si bond coat interface after annealing for 2h at 1200°C in air. The white arrow denotes sub-micron Yb_2SiO_5 grains within the topcoat.

and Yb alongside Na indicates that Na_2SO_4 reacted to form a silicate phase during exposure. Oxidation of the Si bond coat after 1h exposure at both 1000°C and 1316°C was also observed, evident by Si and O containing regions between the topcoat and Si bond coat no greater than 500 nm. The beginning of topcoat granulation at 1316°C can also be observed in Figure 4.9, evident by the presence of micron sized Yb_2SiO_5 grains. Similar microscopy coupled with elemental mapping of this interface after exposure for 240h at 1000°C and 1316°C can be seen in Figures 4.10 and 4.11. Elemental mapping revealed that the silicate phase was still present after exposure for 240h at both temperatures. However, due to the increased oxidation kinetics at 1316°C, a much thicker TGO formed at 1316°C than at 1000°C. The topcoat was also highly granulated with 5-10 µm diameter $Yb_2Si_2O_7$ granules after exposure at 1316°C (Figure 4.11), while hardly changed after exposure 1000°C (Figure 4.10). This indicates that the entire topcoat transformed from

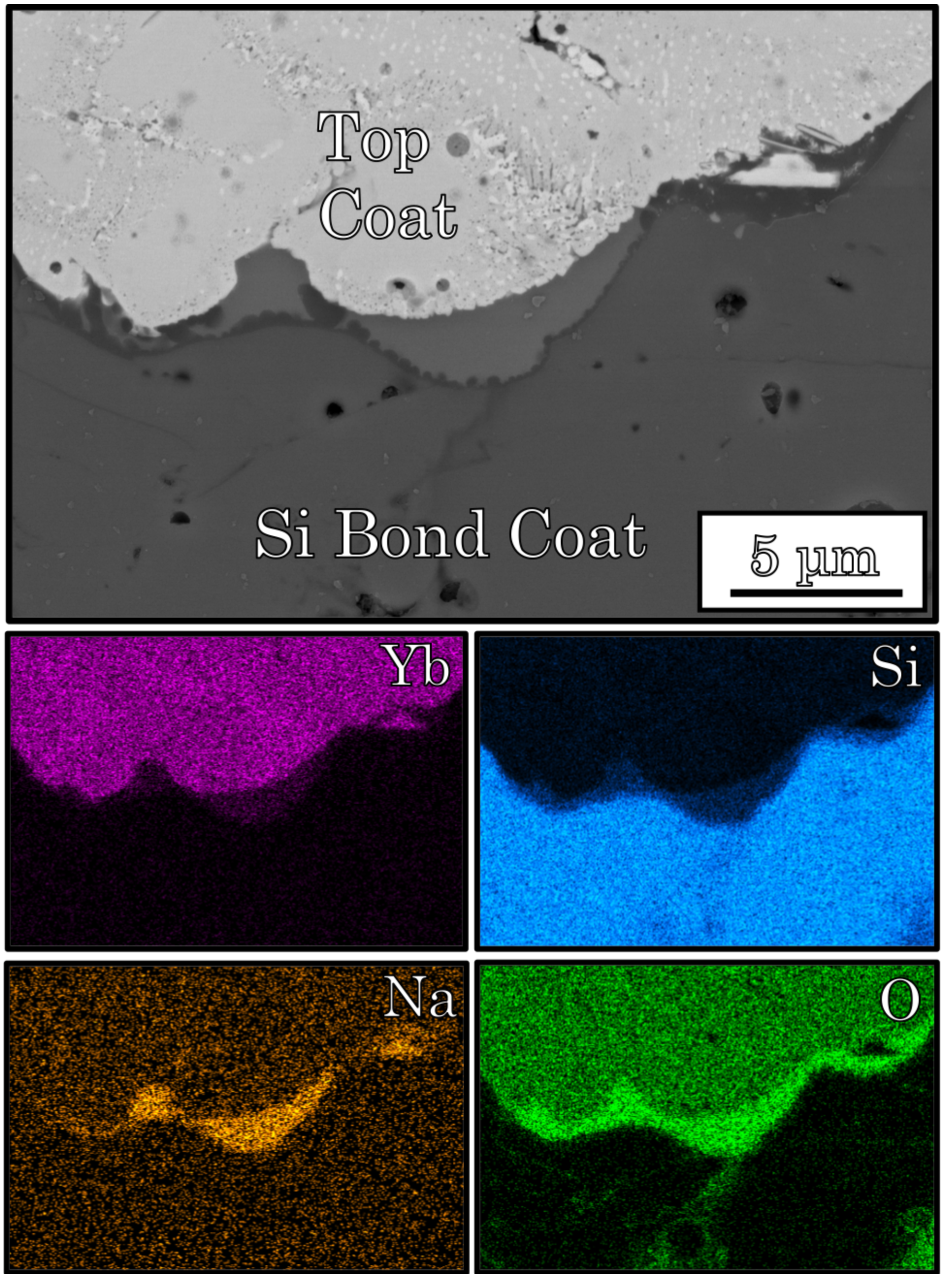

Figure 4.8. Backscattered SEM image and corresponding elemental Yb, Na, Si and O maps of the topcoat-Si interface in cross-section of an air plasma sprayed $Yb_2Si_2O_7$ specimen after exposure to ~2.5 mg/cm^2 of Na_2SO_4 for 1h at 1000°C in a gaseous 0.1% SO_2-O_2 environment.

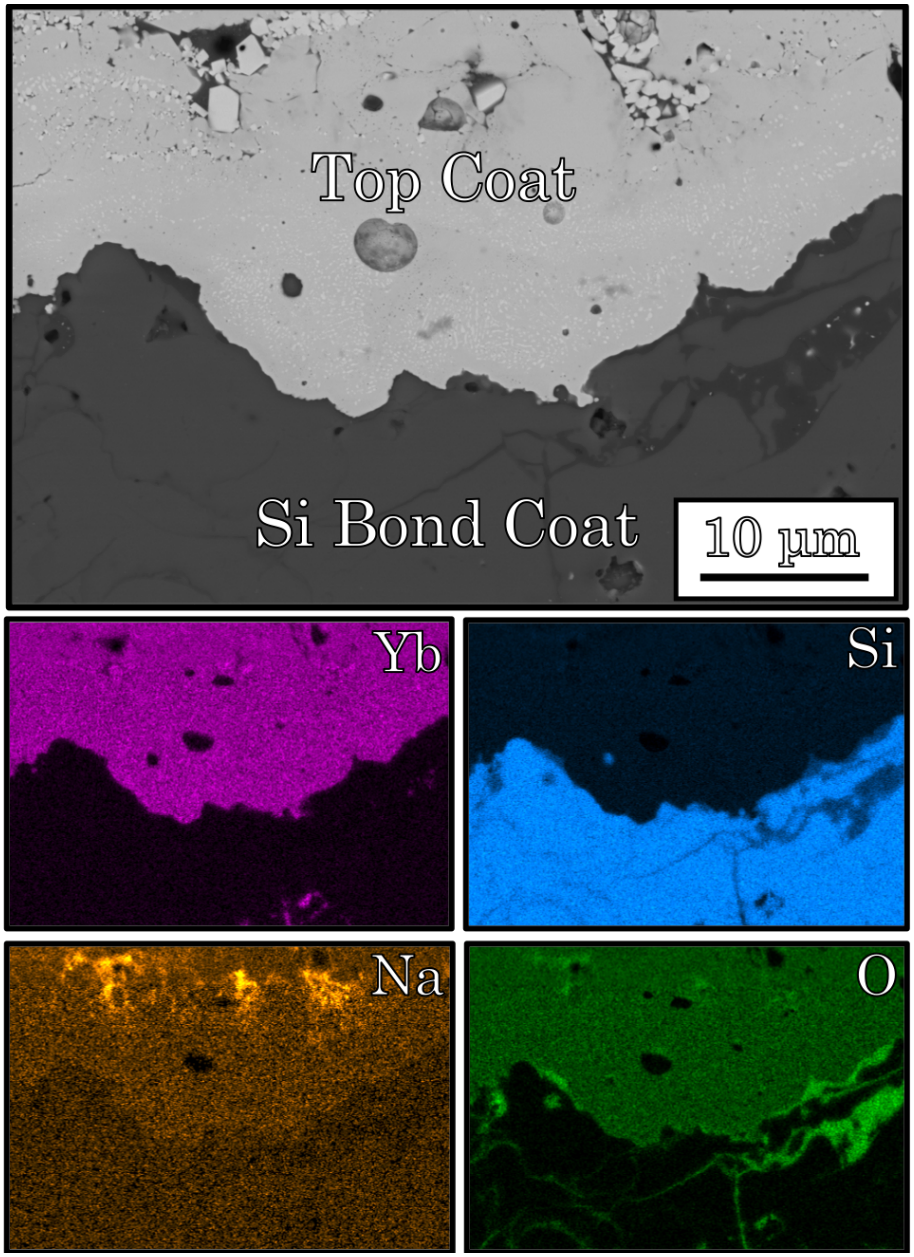

Figure 4.9. Backscattered SEM image and corresponding elemental Yb, Na, Si and O maps of the topcoat-Si interface in cross-section of an air plasma sprayed $Yb_2Si_2O_7$ specimen after exposure to ~2.5 mg/cm^2 of Na_2SO_4 for 1h at 1316°C in a gaseous 0.1% SO_2-O_2 environment.

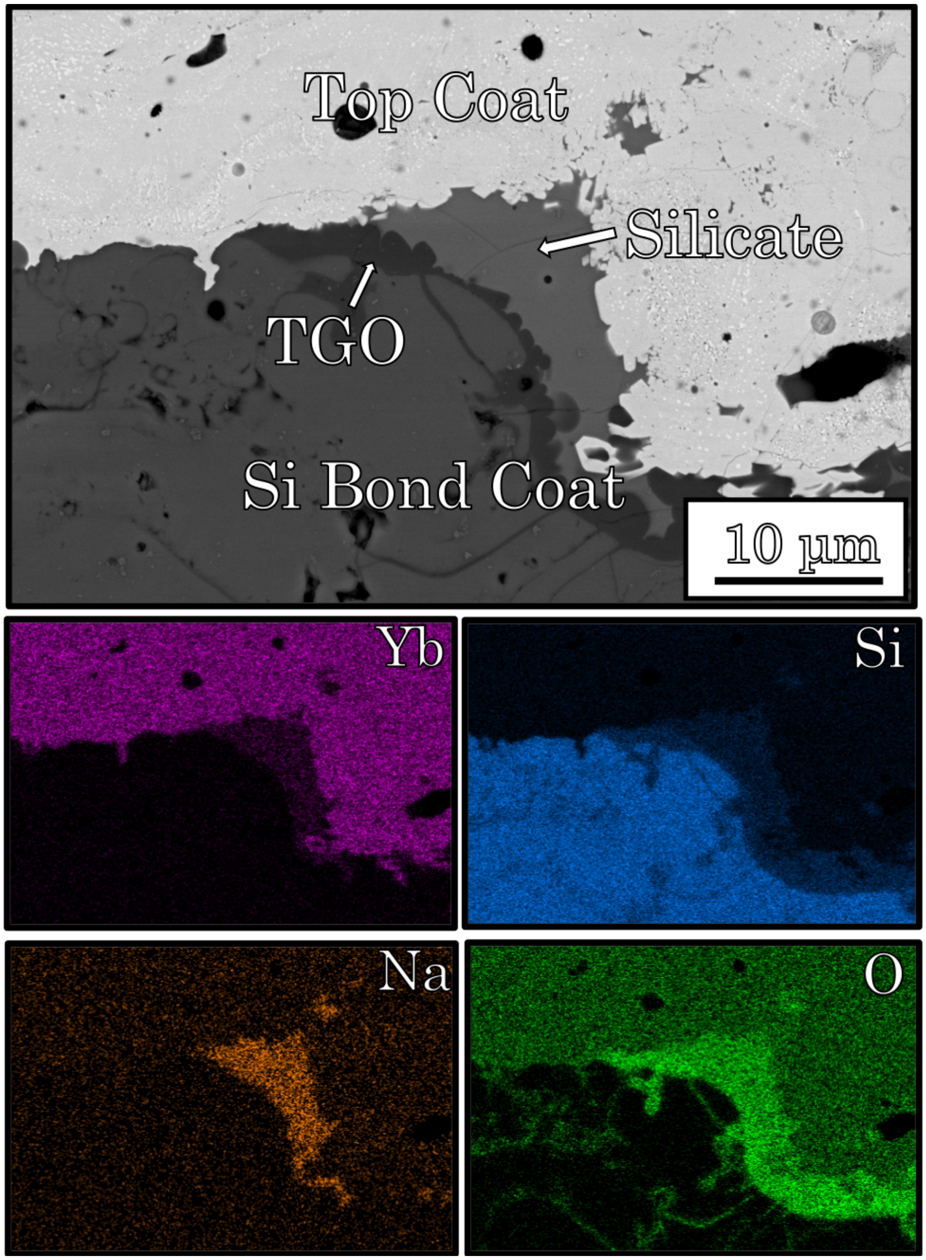

Figure 4.10. Backscattered SEM image and corresponding elemental Yb, Na, Si and O maps of the topcoat-Si interface in cross-section of an air plasma sprayed $Yb_2Si_2O_7$ specimen after exposure to ~2.5 mg/cm^2 of Na_2SO_4 for 240h at 1000°C in a gaseous 0.1% SO_2-O_2 environment.

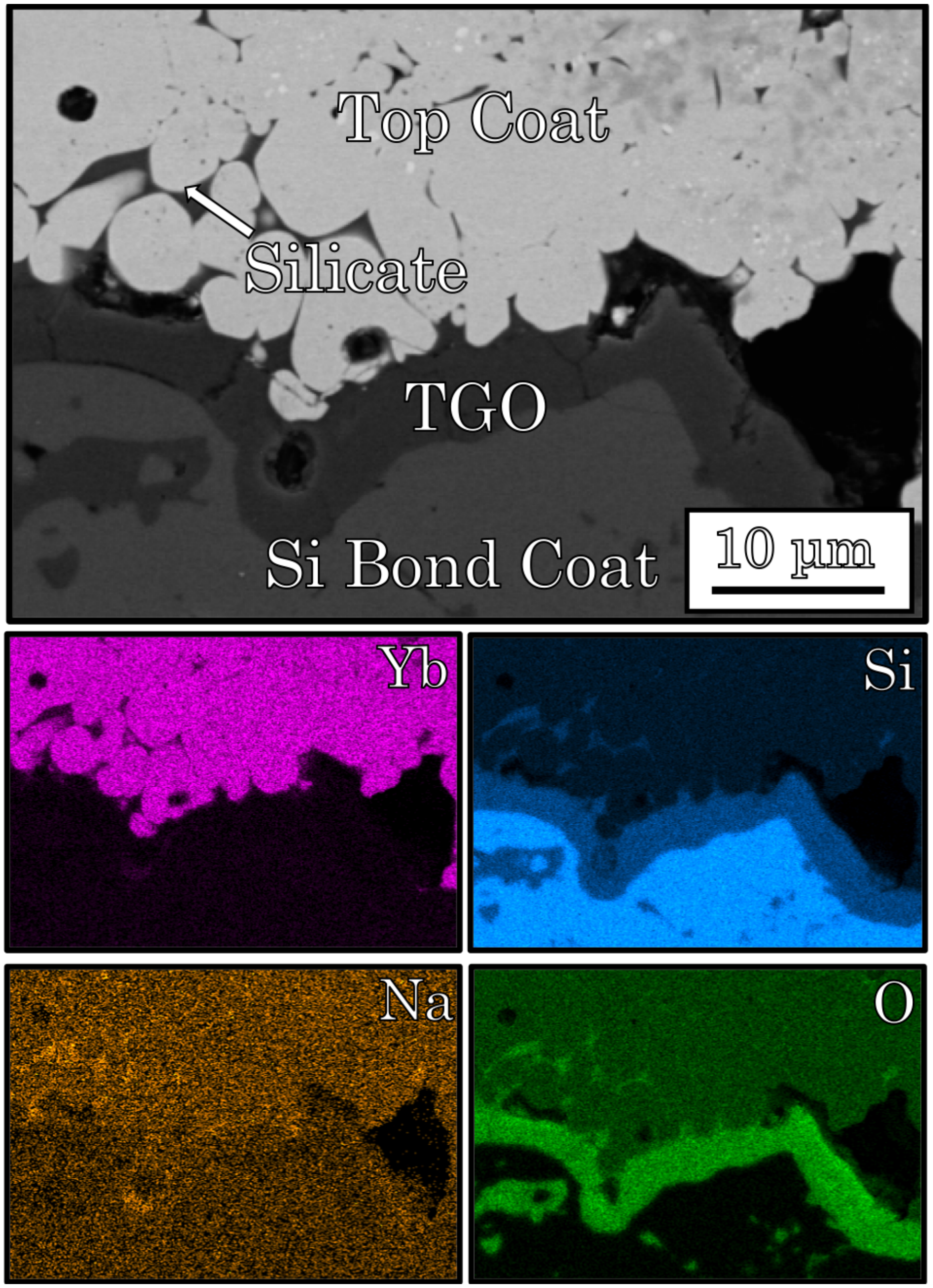

Figure 4.11. Backscattered SEM image and corresponding elemental Yb, Na, Si and O maps of the topcoat-Si interface in cross-section of an air plasma sprayed $Yb_2Si_2O_7$ specimen after exposure to ~2.5 mg/cm^2 of Na_2SO_4 for 240h at 1316°C in a gaseous 0.1% SO_2-O_2 environment.

a splat-microstructure to a granulated microstructure at 1316°C. Furthermore, comparison between the images in Figure 4.9 and 4.11 after 1h and 240h exposure at 1316°C, reveal reduced Yb_2SiO_5 content over time, as described in more detail in the next section.

4.3.3 Yb_2SiO_5 Volume Content Reduction

Due to the apparent reduction in Yb_2SiO_5 phase content from the topcoat during exposure at 1316°C (observed in Figures 4.4g) and 4.11), quantification of the Yb_2SiO_5 phase content in the topcoat during exposure at 1316°C was assessed. Contrast thresholding, using ImageJ digital software analysis was applied to several SEM images of the topcoat, and the Yb_2SiO_5 volume (in μm^3) was then calculated. The volume was calculated by first measuring the Yb_2SiO_5 area from several high resolution backscattered SEM images using ImageJ. Backscattered electron images allow for sufficient phase contrast to isolate Yb_2SiO_5 grains for ImageJ thresholding to be performed. This total Yb_2SiO_5 area measurement was then divided by the total horizontal field width of images analyzed, to create a normalized Yb_2SiO_5 area per length of sample analyzed in units of microns. This value was then multiplied by the area of the topcoat, assumed to be 1.27 cm squared, and by 0.93 due to the 7 vol. % porosity in the topcoat. The equation used to determine the Yb_2SiO_5 volume in topcoats can be seen below in Equation (4.7):

$$V_{Yb_2SiO_5} = (1\text{-}P)\ \frac{\sum A_{Yb_2SiO_5}}{\sum l}\ A_{topcoat} \qquad (4.7)$$

where $V_{Yb_2SiO_5}$ is Yb_2SiO_5 volume in the topcoat, P the porosity in the topcoat determined using ImageJ, $\sum A_{Yb_2SiO_5}$ the total Yb_2SiO_5 area in the topcoat determined using ImageJ, $\sum l$ the total length of all images analyzed using ImageJ, while $A_{topcoat}$ is the topcoat area. Examples of images thresholded using ImageJ software only showing Yb_2SiO_5 grains can be seen in Figure

4.12. An explanation on how ImageJ was used to determine Yb_2SiO_5 volume can be seen in Appendix E. The left-hand side of Figure 4.12 shows the each of the topcoats prior to thresholding after 1h (top) to 240h (bottom) exposure, while the right-hand side are the corresponding thresholded images containing only the Yb_2SiO_5 grains. Yb_2SiO_5 content in the topcoat changes slightly up to exposure for 96h seen in Figures 4.12b), d), and f) However, a clear decrease in Yb_2SiO_5 content after 240h exposure can be seen in Figure 4.10h), with the majority of Yb_2SiO_5 grains populating the topcoat surface. The average Yb_2SiO_5 volume in the topcoat is plotted as a function of time in Figure 4.13. The Yb_2SiO_5 volume in the topcoat clearly decreases over time, going from ~3.5×10^9 µm^3 to ~0.9×10^9 µm^3 , or a ~5x decrease between 1h and 240h. The relationship between Yb_2SiO_5 volume in the topcoat and time is seemingly linear, and resultantly a linear fit was applied to the dataset. The equation seen inlaid in Figure 4.12, was extrapolated to determine a time of ~328h or ~2 weeks at which zero Yb_2SiO_5 should remain in the coating. This value is only a few days more than the longest exposure time in this work. This calculation was made assuming the topcoat converted entirely from amorphous Yb-Si-O to crystalline $Yb_2Si_2O_7$ + Yb_2SiO_5 after annealing in air for 2h at 1200°C.

4.4 Discussion

4.4.1 Topcoat Reaction with Na_2SO_4

A reaction between ~2.5 mg/cm^2 of Na_2SO_4 and the $Yb_2Si_2O_7$ topcoat was observed. Regardless of time and temperature, the topcoat transformed into a 3-phase mixture consisting of $Yb_2Si_2O_7$, Yb_2SiO_5 and a sodium silicate phase. However, the reaction rate and morphological changes in the topcoat were highly dependent upon exposure time and temperature. Time and temperature dependent diffraction studies coupled with microscopy of the topcoat revealed the reaction with Na_2SO_4 rapidly (<1h) transformed the topcoat into a granulated microstructure at 1200°C and above. However, observable changes in the topcoat below 1200°C were minimal in 1h. The reaction with Na_2SO_4 was not limited to the coating surface though, as sodium silicate was found to exist at the Si bond coat ~1h into exposure at the lowest and highest temperatures tested in this work. Na_2SO_4 melted (T_m = 884°C) and then likely infiltrated through the porous topcoat (~8% porosity). It is also possible that at least some of this rapid infiltration could occur upon aqueous solution loading prior to exposure. The lack of S present in the Na containing regions indicates that during high temperature exposure, Na_2SO_4 transformed into a sodium silicate. Thus, a simplified stoichiometric reaction between Na_2SO_4 and $Yb_2Si_2O_7$ is provided in Equation (4.8):

$$Yb_2Si_2O_7 + Na_2SO_4 \rightarrow Yb_2SiO_5 + Na_2SiO_3 + SO_3(g) \qquad (4.8)$$

There was no evidence of any ternary Yb_2O_3-SiO_2-Na_2O compound reaction products, or residual Na_2SO_4 after all exposure conditions. This is a surprising result, as mixtures of many rare earth silicates with Na, including $Yb_2Si_2O_7$, are known to form ternary compounds. Felsche found that 1:9:12 molar ratios of Na_2CO_3:Yb_2O_3:SiO_2 at 1100°C for an undisclosed time period in air resulted in the formation of $NaYb_9Si_6O_{26}$. It is possible that C is needed to stabilize this phase, as Felsche used Na_2CO_3 for Na apatite synthesis, while also possible that sulfur present in Na_2SO_4 and in $SO_2(g)$ in this work destabilizes $NaYb_9Si_6O_{26}$. The effects of S on the high temperature reaction of with $Yb_2Si_2O_7$ materials have not been studied at this point in time. Another possibility to explain the lack of $NaYb_9Si_6O_{26}$ formation in this work, is the sluggish reaction kinetics, as it may need more than 240h to form. Additional Yb_2O_3-SiO_2-Na_2O ternary compounds other than $NaYb_9Si_6O_{26}$ have been reported in literature, and were also not observed to form in this work.[45, 46] No phase equilibria studies in the Yb_2O_3-SiO_2-Na_2O system have been performed at this point in time. Thus, phase equilibria studies in the Yb_2O_3-

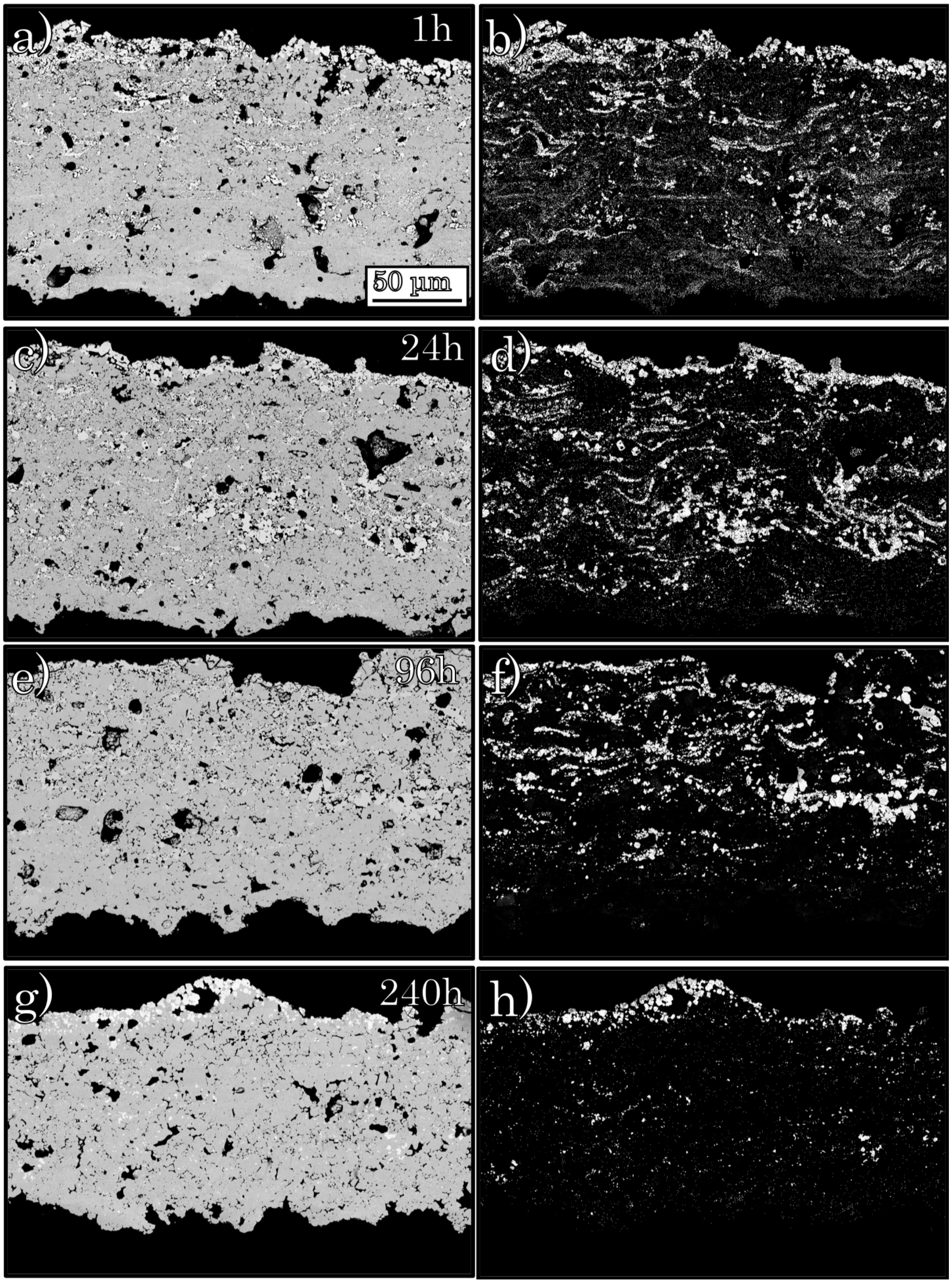

Figure 4.12. Backscattered SEM images of the topcoat in cross-section after exposure to ~2.5 mg/cm^2 of Na_2SO_4 for 240h at 1316°C in a gaseous 0.1% SO_2-O_2 environment with the Si bond coat removed and b)after thresholding using ImageJ software analysis showing only the Yb_2SiO_5 grains.

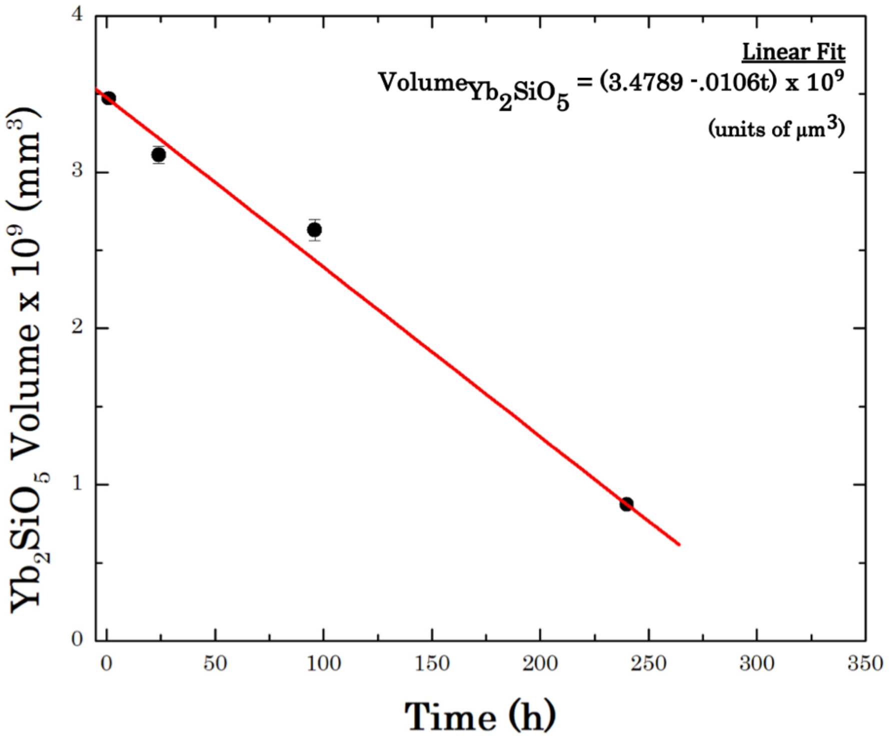

Figure 4.13. Plot showing the Yb_2SiO_5 volume (in μm^3) in air plasma sprayed $Yb_2Si_2O_7$ coatings after exposure to ~2.5 mg/cm^2 of Na_2SO_4 at 1316°C in a gaseous 0.1% SO_2-O_2 environment as a function of time.

SiO_2-Na_2O system are needed to understand the high-temperature interaction of Na_2SO_4 with $Yb_2Si_2O_7$ EBCs.

4.4.2 Topcoat Reaction with SiO_2 TGO

Along with the topcoat being reactive with Na_2SO_4, the topcoat is also reactive with the SiO_2 produced from Si bond coat oxidation. ImageJ measurements revealed a ~5x decrease in Yb_2SiO_5 volume in the topcoat between 1h to 240h during exposure at 1316°C. Visual observation of Yb_2SiO_5 removal from the topcoat revealed Yb_2SiO_5 grains mainly populated the topcoat surface after 240h exposure, as mostly $Yb_2Si_2O_7$ and silicate phases populate the bottom of the topcoat. This Yb_2SiO_5 depleted region is indicative of a moving reaction front towards the topcoat surface. Additionally, the Yb_2SiO_5 volume reduction in the topcoat follows linear kinetics, indicating a reaction-limited process occurs. This linear reduction of

Yb_2SiO_5 volume with time coupled with the upward moving Yb_2SiO_5 depleted region likely indicates that SiO_2 rapidly transports from the TGO through fast-diffusion pathways offered by the liquid silicate phase, and reacts with Yb_2SiO_5 in the topcoat. This microstructural evolution can easily be explained using relevant phase diagrams for this coating system.

Examination of the Yb_2O_3-SiO_2 phase diagram in Figure 4.14, reveals that the annealed topcoat comprised of 8 vol.% Yb_2SiO_5 balance $Yb_2Si_2O_7$ or 65.4 mol% SiO_2 balance Yb_2O_3, is an equilibrium mixture up to ~1750°C. However, the oxidation of the Si bond coat increases the SiO_2 content of the coating system, creating a thermodynamic driving force for reduction in Yb_2SiO_5 phase content in the topcoat due to reaction form $Yb_2Si_2O_7$. This occurs via a two-step reaction seen below in Equations (4.4) and (4.9):

$$Si + O_2(g) \rightarrow SiO_2 \tag{4.4}$$

$$Yb_2SiO_5 + SiO_2 \rightarrow Yb_2Si_2O_7 \tag{4.9}$$

$O_2(g)$ transports through the topcoat and then reacts with the Si bond coat via Equation (4.4). Once produced, SiO_2 then reacts with Yb_2SiO_5 grains in the topcoat to form $Yb_2Si_2O_7$ via Equation (4.9). The TGO forms between the topcoat and Si bond coat because Equation (4.4) happens at a faster rate than Equation (4.9), indicating different reaction rates are occurring in the coating system. Regardless of these rates, once all Yb_2SiO_5 is consumed from the topcoat, the coating system will consist of a phase pure $Yb_2Si_2O_7$ topcoat + silicate/ SiO_2 TGO / Si bond coat. Na_2SO_4 deposits change the coating system composition from a two-component Yb_2O_3-SiO_2 system to a three component Yb_2O_3-SiO_2- Na_2O system and increase the reaction kinetics of Equation (4.9) due to rapid transport kinetics through the liquid silicate phase. The reaction of a SiO_2 forming layer (i.e. Si, SiC) with EBC materials is not newly discovered. A highly studied early EBC candidate system was BaO-SrO-Al_2O_3-SiO_2 (BSAS) on a Si bond coat. This coating system was found to be unsuitable for service

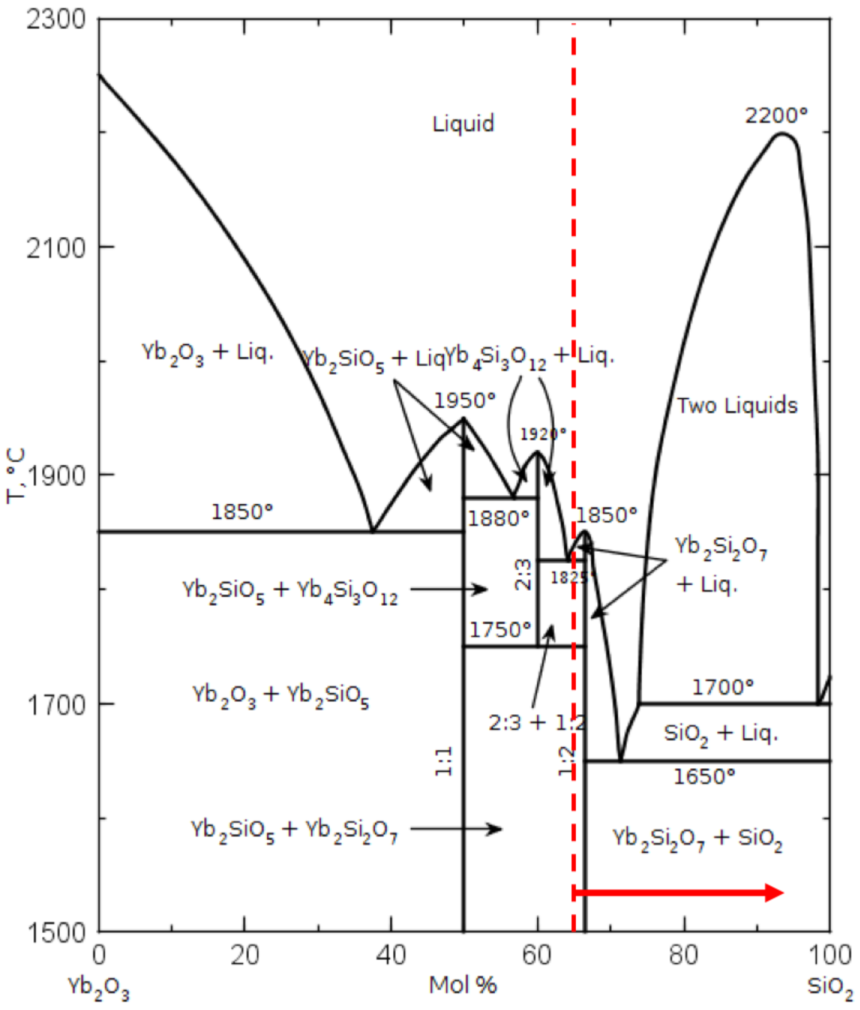

Figure 4.14. The experimental Yb_2O_3-SiO_2 binary phase diagram overlaid with a vertical dashed red line of the starting topcoat composition of 65.4 mol% SiO_2. The solid red arrow indicates the movement of the coating system composition towards the SiO_2 rich portion of the phase diagram due to Si bond coat oxidation.[49]

in turbine engines for long times and at temperatures above ~1100°C due to the formation of a glassy reaction layer between the BSAS topcoat and Si bond coat. Phase equilibrium analysis applied to this coating system revealed excess SiO_2 additions to a BSAS material lead to the formation of a liquid phase.[47] Other research has shown that a Y_2SiO_5 coating applied to a SiC substrate via RF magnetron sputtering reacted to form $Y_2Si_2O_7$.[48] Similar to the behavior seen in $Yb_2Si_2O_7$ topcoats tested in this chapter, SiO_2 additions to Y_2SiO_5 lead to the formation of $Y_2Si_2O_7$, as expected from similar phase equilibria in these systems.

4.5 Implications For Turbine Engine Application

The goal of an EBC system is to protect underlying SiC CMC components from reacting rapidly with the harsh combustion environment inside of a turbine engine. Thus, any degradation to EBC systems is problematic for SiC CMC components, including degradation from CMAS and Na_2SO_4 deposit based attack. CMAS degradation to EBCs occurs only above the CMAS melting temperature, which depending upon its composition is generally no less than ~1200°C. The work performed in this dissertation chapter provides evidence that Na_2SO_4 based deposits could pose a greater threat to EBC durability for $Yb_2Si_2O_7$ topcoat-Si bond coat EBC systems than CMAS deposits, as the reaction with Na_2SO_4 is not limited to the topcoat surface and occurs down to at least 1000°C, or nearly ~200°C less than temperatures which CMAS-deposit based attack is known to occur. Although not tested in this dissertation chapter, it is likely that Na_2SO_4 deposit-induced degradation is a problem for EBCs down to its melting temperature (T_m=884°C). The reaction with Na_2SO_4 is severe at 1200°C and above, but less reactive below 1200°C due to reduced reactions associated with lower temperatures. However, the reaction of Na_2SO_4 could be highly degrading to $Yb_2Si_2O_7$ EBCs at these lower exposure temperatures over the course of thousands of hours. Furthermore, the interaction of Na_2SO_4 with the $Yb_2Si_2O_7$ topcoat allows for the rapid removal of Yb_2SiO_5 grains from the topcoat due to reaction with the SiO_2 TGO. Fast-diffusion pathways offered by the liquid sodium silicate grain boundary phase allow for rapid transport within the coating system to occur. The reaction between the SiO_2 TGO and secondary Yb_2SiO_5 phases in the topcoat to form $Yb_2Si_2O_7$ lead to property changes over time within the EBC system due to composition and phase changes. This reaction should be evaluated more closely to better understand EBC durability.

4.6 Conclusions

The interaction of Na_2SO_4 with APS $Yb_2Si_2O_7$-Si-SiC CMC specimens for times up to 240h between 1000°C and 1316°C in a 0.1% SO_2-O_2(g) environment resulted in the formation of a three phase coating, comprised of $Yb_2Si_2O_7$, Yb_2SiO_5 and a liquid silicate. The reaction with Na_2SO_4 was not surface limited, as Na infiltrated the entire topcoat at the highest and lowest exposure temperatures in less than 1h. During exposure, infiltrated Na_2SO_4 reacted with the topcoat to form a sodium silicate. The topcoat transformed from a splat-microstructure, typical of APS deposition, into a granular microstructure of Yb_2SiO_5 and $Yb_2Si_2O_7$ grains, interpenetrated by a sodium silicate liquid phase. The microstructural transformation of the topcoat was gradual below 1200°C, needing 240h for significant microstructural changes to occur, while less than 1h was needed for the topcoat to significantly change at exposure temperatures of 1200°C and above. Additionally, a decrease in Yb_2SiO_5 volume content in the topcoat was observed due to reaction with the growing SiO_2 TGO and rapid SiO_2 transport through the interpenetrating sodium silicate phase. Nearly all Yb_2SiO_5 was reacted from the topcoat during exposure at 1316°C for 240h. It was predicted ~2 weeks is needed for removal of all Yb_2SiO_5 from the topcoat.

References

1. Zok FW. Ceramic Matrix Composites Enable Revolutionary Gains in Turbine Efficiency. 2016;95:22–28.
2. Melissae Fellet. Ceramic-Matrix Composites Take The Heat. *MRS Bull.* 2015;40:916–7.
3. Naslain RR. SiC-Matrix Composites: Nonbrittle Ceramics for Thermo-Structural Application. *Int J Appl Ceram Technol.* 2005;2(2):75–84.
4. Morscher GN, Yun HM, DiCarlo JA. In-Plane Cracking Behavior and Ultimate Strength for 2D Woven and Braided Melt-Infiltrated SiC/SiC Composites Tensile Loaded in Off-Axis Fiber Directions. *J Am Ceram Soc.* 2007;90(10):3185–3193.
5. Morscher GN, Yun HM, DiCarlo JA. Matrix Cracking in 3D Orthogonal Melt-Infiltrated SiC/SiC Composites with Various Z-Fiber Types. *J Am Ceram Soc.* 2005;88(1):146–153.
6. Morscher GN, DiCarlo JA, Kiser JD, Yun HM. Effects of Fiber Architecture on Matrix Cracking for Melt-Infiltrated SiC/SiC Composites. *Int J Appl Ceram Technol.* 2010;7(3):276–290.
7. Bansal N. Handbook of Ceramic Matrix Composites. Vol. 200. 2006:77–98.
8. Presser V, Nickel KG. Silica on Silicon Carbide. *Crit Rev Solid State Mater Sci.* 2008;33(1):1–99.
9. Deal BE, Grove AS. General Relationship for the Thermal Oxidation of Silicon. *J Appl Phys.* 1965;36(12):3770–3778.
10. Ramberg EC, Gary C, Spear KE, Tressler RE, Ramberg CF. Passive-Oxidation Kinetics of High-Purity Silicon Carbide from 800° to 1100°C. *J Am Ceram Soc.* 1996;79(11):2897–2911.
11. Jacobson NS. Corrosion of Silicon-Based Ceramics in Combustion Environments. *J Am Ceram Soc.* 1993;76(1):3–28.
12. Jacobson NS. Kinetics and Mechanism of Corrosion of SiC by Molten Salts. *J Am Ceram Soc.* 1986;69(1):74–82.
13. Jacobson NS, Smialek JL. Hot Corrosion of Sintered α-SiC at 1000°C. *J Am Ceram Soc.* 1985;68(8):432–439.
14. Hagan JM, Opila EJ. High-Temperature Na_2SO_4 Deposit-Assisted Corrosion of Silicon Carbide – I: Temperature and Time Dependence. *J Am Ceram Soc.* 2015;98(4):1275–1284.
15. Hagan JM, Opila EJ. High-temperature Na_2SO_4 deposit-assisted corrosion of silicon carbide–II: Effects of B, C, and Si. *J Am Ceram Soc.* 2017;100(2):761–773.
16. Carruth M, Baxter D, Oliveira F, Coley K. Hot-corrosion of silicon carbide in combustion gases at temperatures above the dew point of salts. *J Eur Ceram Soc.* 1998;18(16):2331 – 2338.
17. Jacobson NS, Morscher GN, Bryant DR, Tressler RE. High-Temperature Oxidation of Boron Nitride: II, Boron Nitride Layers in Composites. *J Am Ceram Soc.* 1999;82(6):1473–1482.

18. Lee SY, Park YS, Hsu PP, McNallan MJ. Synergistic Effects of Water Vapor and Alkali Chloride Vapors on the High-Temperature Corrosion of SiC-Based Ceramics. *J Am Ceram Soc*. 2003;86(8):1292–1298.
19. Opila EJ. Oxidation and Volatilization of Silica Formers in Water Vapor. *J Am Ceram Soc*. 2003;86(8):1238–1248.
20. Opila EJ. Variation of the Oxidation Rate of Silicon Carbide with Water-Vapor Pressure. *J Am Ceram Soc*. 1999;82(3):625–636.
21. Opila EJ, Hann RE. Paralinear Oxidation of CVD SiC in Water Vapor. *J Am Ceram Soc*. 1997;80(1):197–205.
22. Opila EJ, Fox DS, Jacobson NS. Mass Spectrometric Identification of Si–O–H(g) Species from the Reaction of Silica with Water Vapor at Atmospheric Pressure. *J Am Ceram Soc*. 1997;80(4):1009–1012.
23. Robinson RC, Smialek JL. SiC Recession Caused by SiO_2 Scale Volatility under Combustion Conditions: I, Experimental Results and Empirical Model. *J Am Ceram Soc*. 1999;82(7):1817–1825.
24. Opila EJ, Smialek JL, Robinson RC, Fox DS, Jacobson NS. SiC Recession Caused by SiO_2 Scale Volatility under Combustion Conditions: II, Thermodynamics and Gaseous-Diffusion Model. *J Am Ceram Soc*. 1999;82(7):1826–1834.
25. Davis JR, Committee ASMITSST. Handbook of Thermal Spray Technology. ASM International; 2004
26. Richards BT, Wadley HNG. Plasma spray deposition of tri-layer environmental barrier coatings. *J Eur Ceram Soc*. 2014;34(12):3069 – 3083.
27. Bakan E, Marcano D, Zhou D, Sohn YJ, Mauer G, Vaßen R. $Yb_2Si_2O_7$ Environmental Barrier Coatings Deposited by Various Thermal Spray Techniques: A Preliminary Comparative Study. *J Therm Spray Technol*. 2017;26(6):1011–1024.
28. Garcia E, Lee H, Sampath S. Phase and microstructure evolution in plasma sprayed $Yb_2Si_2O_7$ coatings. *J Eur Ceram Soc*. 2019;39(4):1477–1486.
29. Richards BT, Zhao H, Wadley HNG. Structure, composition, and defect control during plasma spray deposition of ytterbium silicate coatings. *J Mater Sci*. 2015;50(24):7939–7957.
30. Lee KN. $Yb_2Si_2O_7$ Environmental barrier coatings with reduced bond coat oxidation rates via chemical modifications for long life. *J Am Ceram Soc*. 2019;102(3):1507–1521.
31. Richards BT, Young KA, Francqueville F, Sehr S, Begley MR, Wadley HNG. Response of ytterbium disilicate–silicon environmental barrier coatings to thermal cycling in water vapor. *Acta Mater*. 2016;106:1 – 14.
32. Hatch DM, Ghose S. The α-β phase transition in cristobalite, SiO_2. *Phys Chem Miner*. 1991;17(6):554–562.
33. Hill VG, Roy R. Silica Structure Studies: V, The Variable Inversion in Cristobalite. *J Am Ceram Soc*. 1958;41(12):532–537.

34. Fenner CN. The Relations Between Tridymite and Cristobalite. *Trans Soc Glass Technol*. 1919;3:116.
35. Stolzenburg F, Johnson MT, Lee KN, Jacobson NS, Faber KT. The interaction of calcium–magnesium–aluminosilicate with ytterbium silicate environmental barrier materials. *Surf Coat Technol*. 2015;284:44–50.
36. Zhao H, Richards BT, Levi CG, Wadley HNG. Molten silicate reactions with plasma sprayed ytterbium silicate coatings. *Surf Coat Technol*. 2016;288:151 – 162.
37. Turcer LR, Krause AR, Garces HF, Zhang L, Padture NP. Environmental-barrier coating ceramics for resistance against attack by molten calcia-magnesia-aluminosilicate (CMAS) glass: Part II, β-Yb2Si2O7 and β-Sc2Si2O7. *J Eur Ceram Soc*. 2018;38(11):3914–3924.
38. Stokes JL, Harder BJ, Wiesner VL, Wolfe DE. High-Temperature thermochemical interactions of molten silicates with $Yb_2Si_2O_7$ and $Y_2Si_2O_7$ environmental barrier coating materials. *J Eur Ceram Soc*. 2019;39(15):5059–5067.
39. Costa G, Harder BJ, Wiesner VL, *et al.* Thermodynamics of reaction between gas-turbine ceramic coatings and ingested CMAS corrodents. *J Am Ceram Soc*. 2019;102(5):2948–2964.
40. Stearns CA, Kohl FJ, Rosner DE. Combustion System Processes Leading to Corrosive Deposits. San Diego, California: 1981
41. Sun Z, Li M, Li Z, Zhou Y. Hot corrosion of γ -$Y_2Si_2O_7$ in strongly basic Na_2CO_3 molten salt environment. *J Eur Ceram Soc*. 2008;28(1):259 – 265.
42. Ziqi S, Meishuan L, Yanchun Z. Kinetics and Mechanism of Hot Corrosion of γ -$Y_2Si_2O_7$ in Thin-Film Na_2SO_4 Molten Salt. *J Am Ceram Soc*. 2008;91(7):2236–2242.
43. Felsche J. Rare earth silicates with the apatite structure. *J Solid State Chem*. 1972;5(2):266 – 275.
44. Felsche J. The crystal chemistry of the rare-earth silicates. *Rare Earths*. Springer Berlin Heidelberg; 1973:99–197.
45. Latshaw AM, Wilkins BO, Chance WM, Smith MD, Loye H-C zur. Influence of rare earth cation size on the crystal structure in rare earth silicates, Na_2RESiO_4 (RE = Sc, Yb) and $NaRESiO_4$ (RE = La, Yb). *Solid State Sci*. 2016;51:59 – 65.
46. Latshaw AM, Yeon J, Smith MD, Loye H-C zur. Synthesis, structure, and polymorphism of $A_3LnSi_2O_7$ (A=Na, K; Ln=Sm, Ho, Yb). *J Solid State Chem*. 2016;235:100 – 106.
47. K.N. Lee, Fox DS, Eldridge JI, *et al.* Upper Temperature Limit of Environmental Barrier Coatings Based on Mullite and BSAS. *J Am Ceram Soc*. n.d.;86(8):1299–1306.
48. Mechnich P. Y_2SiO_5 coatings fabricated by RF magnetron sputtering. *Surf Coat Technol*. 2013;237:88–94.

49. Toropov NA, Bondar IA. Silicate of Rare Earth Elements. VI. Phase Diagrams for the Binary Systems Sm_2O_3-SiO_2 and Yb_2O_3-SiO_2 and a Comparison of them with Silicates of other Rare Earth Elements. *Uch Zap Kazan Gos Univ*. 1961;1372–1379.

5 | Na_2SO_4 Effects on Environmental Degradation of Si Bond Coats in EBC/CMC Systems For Application in Turbine Engines

5.1 Introduction

Silicon carbide (SiC) ceramic matrix composites (CMCs) are materials that will lower the operating costs and reduce harmful engine emissions in next-generation turbine engines due to their superior high temperature properties. These material have already entered service as non-load bearing components in GE Aviations LEAP engines.[1, 2] The CMCs are comprised of boron nitride (BN) coated, reinforcing SiC fibers embedded in a SiC matrix. Simulated turbine engine environmental testing has known that these materials react at unacceptably high rates in the presence of steam, with recession rates on the order of ~1 μm/h at temperatures of ~1200°C and above.[3, 4] This has necessitated the development and usage of environmental barrier coatings (EBCs) in order to reduce recession rates of SiC CMCs in steam. Combinations of several key properties make ytterbium disilicate ($Yb_2Si_2O_7$) a prime EBC material, and this material subsequently has been the focus of many studies.[5–20] Additionally, the oxidation rate of a metal Si bond coat layer between a $Yb_2Si_2O_7$ EBC and SiC CMC components has also been heavily investigated.[11, 20, 21] Currently, the $Yb_2Si_2O_7$ top coat + Si bond coat EBC system is state-of-the art. However, environmental degradation mechanisms affecting the durability of this coating system still remain uncertain, including the effect of Na_2SO_4 surface deposition on the underlying Si bond coat, the focus of this dissertation chapter.

It is well known that at elevated temperatures in oxidizing environments, stand-alone Si metal will oxidize to form a passivating SiO_2 layer, seen in Equation (5.1):

$$Si + O_2(g) \rightarrow SiO_2 \qquad (5.1)$$

This oxidation reaction is well described by the linear-parabolic Deal-Grove oxidation model.[22] This model mathematically predicts that at long times and temperatures relevant for turbine applications the oxidation rate of stand-alone Si will follow a single rate constant, known as the parabolic rate constant or k_p. Few studies have investigated the crystallization of thermally grown oxides (TGO) on Si bond coats, however several studies have reported the formation of a cristobalite TGO.[23–25] The accepted mechanism of thermally grown SiO_2, adopted from SiC oxidation studies, is that an amorphous SiO_2 forms initially, followed by surface-nucleated crystallization into cristobalite.[26–29] TGO crystallization becomes relevant at ~1300°C, but only up to the melting temperature of the Si bond coat (T_m = 1414°C).

Three SiO_2 polymorphs are known to exist in the SiO_2 system at ambient pressure up to the melting temperature of SiO_2 at 1723°C, namely quartz, tridymite, and cristobalite. A commonly accepted phase transition scheme in this system puts transition temperatures between quartz and tridymite at ~860°C and tridymite to cristobalite at ~1467°C,[30–34] while another scheme places a single transition between quartz and cristobalite at 1050°C, as tridymite is believed to be an impurity-stabilized phase.[35, 36] In EBC topcoat/Si bond coat/SiC CMC systems, inward permeation of oxidizing (i.e. O_2, H_2O) gaseous species through the EBC top coat leads to Si bond coat oxidation.[5, 6, 11] Thermally grown SiO_2 layers form amorphous or β-cristobalite at temperature, which then invert to α-cristobalite upon cooling through an inversion temperature between 200-300°C. This displacive β-to-α cristobalite phase transformation is of concern for EBC systems with a Si bond coat, as the ~5% density increase upon cooling leads to vertical cracking and partial delamination due to large tensile forces (~4 GPa) generated within the TGO. This cracking event could cause EBC delamination from SiC CMC components allowing for rapid recession.[37] However, the effect of Na_2SO_4 on Si bond coat oxidation kinetics and TGO crystallization is unknown. The inclusion of Na impurities into thermally grown SiO_2 on Si bond coats is of importance to SiC CMC component durability as Na_2SO_4 is a known environmental contaminant in turbine engines.

Turbine engines operating in a marine environment ingest NaCl and react with S impurities in the fuel or environment, causing the in-situ formation of Na_2SO_4, seen in Equation (5.2):[38]

$$2NaCl + SO_3(g) + H_2O(g) \rightarrow Na_2SO_4(l) + 2HCl(g) \tag{5.2}$$

Na_2SO_4 deposits cause rapid oxidation and pitting on metallic hot-section components in current turbine engines and are also expected to cause degrading reactions with SiC CMC components.[39] Testing of commercially sintered α-SiC, has shown rapid oxidation and pitting.[40, 41] The reaction of Na_2SO_4 deposits is expected to occur with the EBC top coat first, unless exposed CMC regions due to EBC spallation exist. It is unknown how Na_2SO_4 deposits will affect the environmental degradation of Si bond coats. Emphasis is placed on the Si bond coat oxidation kinetics, along with the structure, chemical composition and crack damage of the thermally grown SiO_2 oxide. Reactions with $Yb_2Si_2O_7$ EBC top-coat were explored in the previous chapter.

5.2 Experimental

5.2.1 Materials

High temperature testing of coating systems was performed on Si melt-infiltrated (MI) SiC CMC specimens (1.27 cm x 1.27 cm x 0.31 cm) provided by Rolls Royce North America (Indianapolis, IN). Specimens were coated using an air plasma spray process with a $Yb_2Si_2O_7$ top coat on a Si bond coat. Coated specimens were received in the as-sprayed condition without any post-spraying heat treatment.

5.2.2 Hot Corrosion Procedure

Prior to exposure, all specimens were annealed for 2h at 1200°C in air using a heating rate of 15°C/min, to promote crystallization of amorphous Yb-Si-O in the topcoat. An aqueous solution containing 3g of Na_2SO_4 and 100mL of DI water was thoroughly mixed, and then pipetted on specimen surfaces. Specimens were heated at 120°C in a convection oven (MTI. Richmond, CA) to evaporate water from specimen surfaces, leaving behind Na_2SO_4 only. Salt loadings of ~2.5 mg/cm^2 or ~4 mg given a sample surface area of 1.6 cm^2, were confirmed after deposition and convection oven drying using an analytical balance. High temperatures exposures were performed in a horizontal tube furnace (CM Furnaces, Bloomfield, NJ) fitted with gas-tight, O-ring sealed stainless steel endcaps for controlled atmospheric testing. Exposures were conducted at temperatures between 1000°C-1316°C for times between 1h-240h in a flowing 100 sccm 0.1% (1000 ppm) SO_2-O_2 gaseous mixture. Specimens were loaded into an Al_2O_3 boat, which was pushed into the hot-zone of the tube furnace at temperature. Several minutes before termination of testing, the gas mixture was switched to pure O_2(g) in the testing environment to remove the SO_2-O_2 gas mixture. Specimens were air quenched upon completion of exposure.

5.2.3 Characterization

Post-exposure, specimens were mounted in epoxy, cross-sectioned, and then polished for analysis along the topcoat-Si bond coat interface. Sectioning was performed using a diamond tipped low-speed saw in ethylene glycol-based media to minimize the removal of water-soluble reaction products. All polishing was performed using ethylene glycol diamond-based suspension disk, starting with a 15 μm diamond backed-disk and ending using 0.250 μm diameter suspension.

The microstructure of specimens was characterized using scanning electron microscopy (SEM) (Quanta 650, FEI Company, Hillsboro, OR) and the chemical composition was determined using energy dispersive spectroscopy (EDS) (Oxford Instruments, Abingdon, England). ImageJ software analysis was applied to SEM images for SiO_2 thickness measurement. A digitally applied grid with equally spaced lines was applied to 10 separate images with a horizontal field width of 50 μm, totaling 30 measurements per experimental condition. An average for each testing condition was taken while measured uncertainties were calculated as standard error.

Raman spectroscopy (Renishaw, Hoffman Estates, IL) was used to probe the vibrational structure of the reaction product formed between the $Yb_2Si_2O_7$ topcoat-Si bond coat. Calibration of the system was made using the Si 520.5 cm^{-1} peak from a single crystal Si wafer. A 514 nm laser coupled with a 50x objective lens provided a laser probe diameter of ~1.3 μm during measurement. Measurement of the TGO was performed using 50% laser power, a diffraction grating of 3000 lines per mm, and collection times ranging between 30-120s. Raman spectra were collected from a piece of α-cristobalite formed from devitrified fused SiO_2 that was annealed for 30h at 1500°C, and from the topcoat and Si bond coat to provide baseline spectra.

Transmission electron microscopy (TEM) (Titan, FEI, Hillsboro, OR) coupled with selected area electron diffraction (SAED) was also used to determine the microstructure and crystal structure of the TGO. A Ga^+ based focused ion beam (FIB)-SEM (Helios, FEI, Hillsboro, OR) was used to prepare specimens for TEM analysis. The region of interest was first protected with a platinum (Pt) layer deposited using an electron beam energy of 2kV and beam current of 6.4 μA. Ga^+ ion milling was done at an ion energy of 30 kV, with trench cuts performed first at an ion beam current of 9.3 nA, while J-cuts were performed at an ion beam current of 2.3 nA. Specimens were lifted out from the interface and mounted onto a Cu TEM grid. The reaction-layer specimens were attached using Pt deposition with a 24 pA ion current. FIB milling on the grid was performed first at an ion current of 430 pA and then 230 pA to reduce specimen thicknesses to ~100 nm. Finally, cleaning with the Ga ion beam of specimens was performed with an ion beam current of 80 pA. Imaging during the FIB process using the electron beam was done with an electron beam energy of 2kV and current of 100 nA in the unicolor, UC, monochromator mode, except for intermittent backscattered electron (BSE) imaging performed with electron beam energy at 10kV at a current of 0.8 μA. Imaging and selected area diffraction was performed using TEM (Titan 80-300, FEI, Hillsboro, OR) at an electron beam energy of 300 kV.

5.3 Results

5.3.1 Si Bond Coat Oxidation Kinetics

An SEM image of the APS $Yb_2Si_2O_7$ top coat-Si bond coat interface after annealing for 2h at 1200°C can be seen in Figure 5.1. Porosity, cracking, and sub-micron Yb_2SiO_5 precipitates are seen within the topcoat. An oxidation product between the topcoat and the Si bond coat was not observed after annealing. ImageJ analysis was used to determine ~7 vol. % porosity and 8 vol. % Yb_2SiO_5 in the topcoat. The average topcoat thickness was measured to be ~130 μm while the average Si bond coat thickness was ~50 μm. The Si bond coat was measured to be little as ~20 μm in thickness in some areas.

High temperature exposure to Na_2SO_4 in an 0.1% SO_2-O_2(g) environment led to the formation of a TGO phase at the topcoat-Si bond coat interface, that increased in thickness over time and temperature. SEM images of the topcoat-Si bond interface after exposure for 240h at temperatures between 1000°C and 1316°C can be seen in Figure 5.2. The TGO can most easily be seen between the topcoat and Si bond coat seen in Figure 5.2c) and 5.2d). Average thickness measurements of the TGO were made across time and temperature to assess Si bond coat oxidation kinetics, which can be seen in Figure 5.3a). Average TGO thicknesses after exposure for 240h were between ~0.7-1.5 μm at temperatures between 1000°C-1200°C and ~6 μm at exposure 1316°C. The uncertainty bars reported for the average TGO thickness in Figure 5.3a) are attributed to the variation in TGO thickness along the interface and not measurement error. An expected baseline comparison of TGO thickness in dry O_2(g) without Na_2SO_4 was

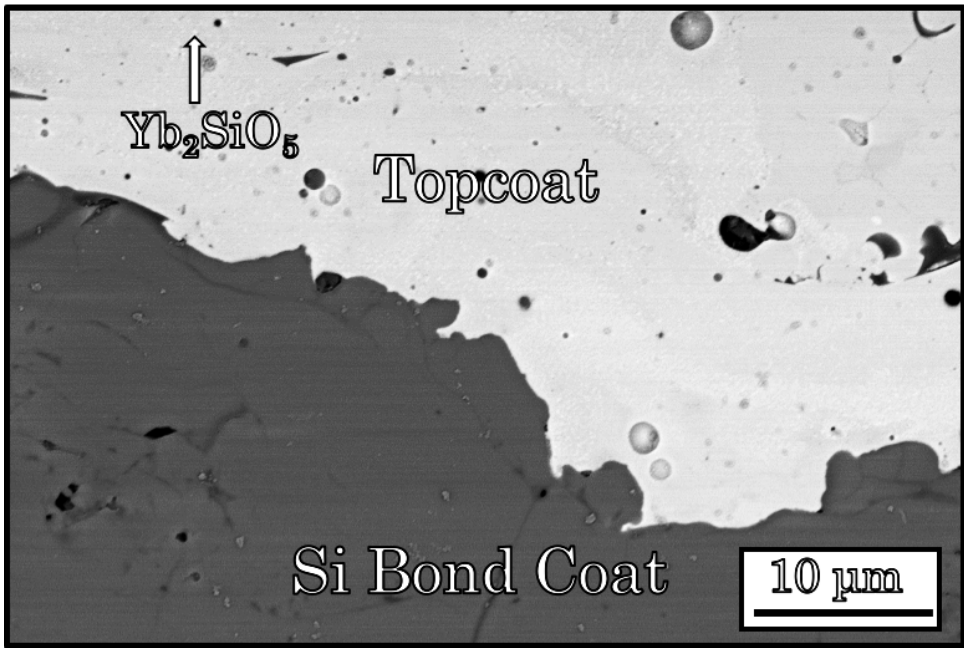

Figure 5.1. Backscattered electron SEM image of the $Yb_2Si_2O_7$ topcoat-Si bond coat interface after annealing for 2h at 1200°C in air.

calculated using the Deal-Grove model, which can be seen in Figure 5.3b).[22] It was assumed that the thermally grown SiO_2 layer calculated using the Deal-Grove model followed the parabolic oxidation equation, $x^2 = k_pt$, where x is the SiO_2 layer thickness, k_p the parabolic oxidation rate constant, and t time. This is reasonable even at 1000°C where the transition from linear-to-parabolic kinetics occurs at 2.3h. Reported k_p values tabulated in the original Deal-Grove work were used for 1000°C-1200°C, while a calculated k_p value of 0.098 µm^2/h was used for 1316°C.[22]. Comparing between average TGO thickness values reported in Figure 5.3a) and those predicted by the Deal-Grove model in Figure 5.3b), the Deal-Grove model predicts TGO's 1-2 µm thicker than those measured in the coating system at exposure temperatures between 1000°C-1200°C, while are slightly less than the values measured at 1316°C.

Only two works have published Si bond coat oxidation kinetics for $Yb_2Si_2O_7$-Si EBC systems, which were both performed at 1316°C in a 90%

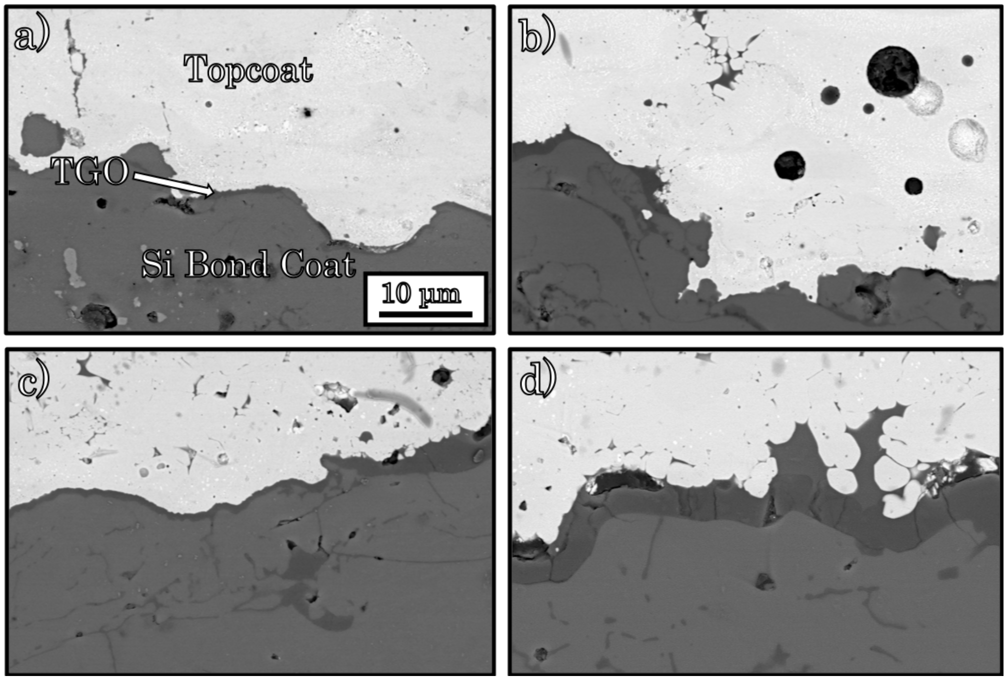

Figure 5.2. Backscattered electron SEM images of the topcoat-Si bond coat interface after exposure to ~2.5 mg/cm^2 of Na_2SO_4 for 240h at a)1000°C b)1100°C c)1200°C d)1316°C in a gaseous 0.1% SO_2-O_2 environment.

steam + 10 % O_2(g) environments.[11, 20] TGO thicknesses measured at 1316°C in this dissertation were compared against the values published in these works, which can be seen in Figure 5.4. Reported TGO values in this dissertation chapter (plotted in green) and values reported in literature (plotted in gold) can be seen in Figure 5.4a), while TGO thickness predicted by the Deal-Grove model in dry O_2(g) (plotted in green) and in 90% H_2O and 10% O_2(g) environments at 1316°C (plotted in gold) can be seen in Figure 5.4b). The raw data, reported k_p, and fitting parameters reported by both authors in literature and in the Deal-Grove model can be seen inlaid in both plots. The TGO thicknesses reported in the steam containing environments by Lee and Richards, produce TGOs less thick than that predicted by the Deal-Grove model. However, the Si bond coat oxidation kinetics reported by

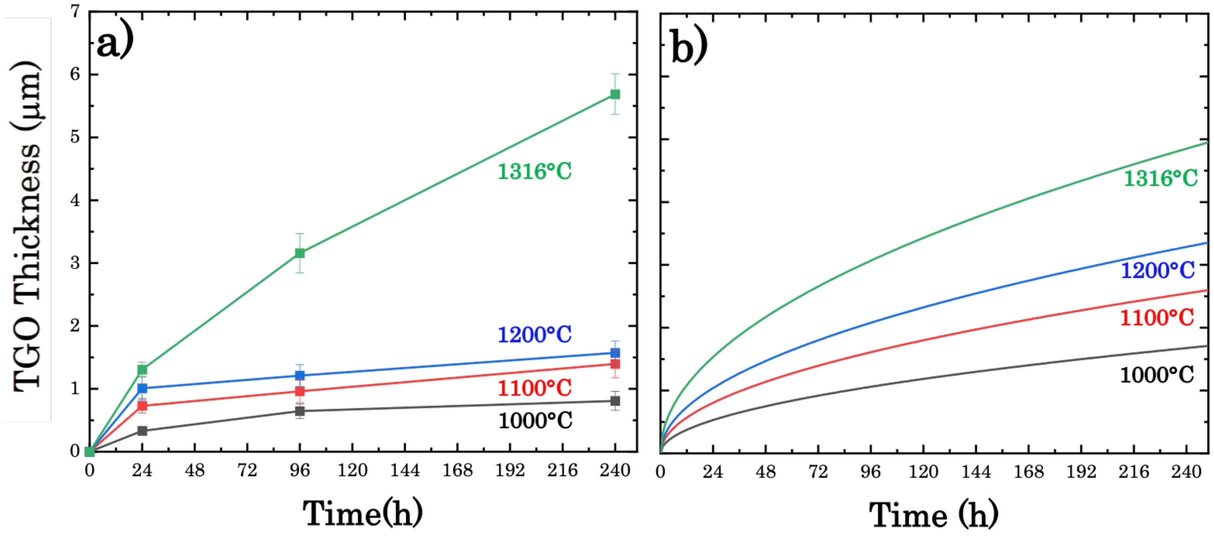

Figure 5.3. a) Plot of the average TGO layer thickness formed in the $Yb_2Si_2O_7$ topcoat + Si bond coat system after exposure to ~2.5 mg/cm^2 of Na_2SO_4 at temperatures between 1000-1316°C in a gaseous 0.1% SO_2 –O_2 environment as a function of time and values predicted b) by the Deal-Grove model for free-standing Si.[22]

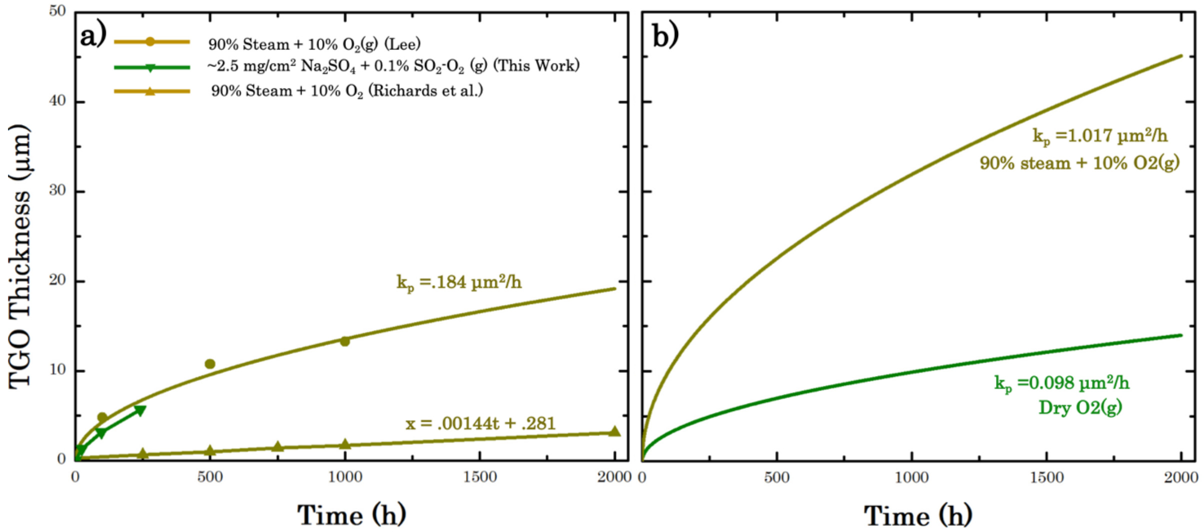

Figure 5.4 a) Plot of the average TGO thickness in $Yb_2Si_2O_7$ topcoat-Si bond coat EBC systems from this work (dark green) and reported in literature in 90% steam + 10% O_2(g) environments (dark yellow), while b) values as predicted by the Deal-Grove model for free-standing Si in dry O_2(g) (dark green) and 90% steam / 10% O_2(g) (dark yellow) environments at 1316°C.[11, 20, 22]

Richards et al. are nearly ~5x less than that predicted by Lee after 2000h of exposure, and even oxidizes slower than in dry O_2(g) despite the k_p for steam being ~10x higher than in dry O_2(g). The TGO thicknesses reported in this dissertation chapter are nearly equal to that reported by Lee, indicating similar oxidation kinetics occurred. The coatings used by Lee are microstructurally comparable to the topcoats tested in this dissertation chapter, while the coatings tested by Richards et al. were considerably more dense.

5.3.2 TGO Chemistry and Structure

Elemental composition analysis of the dark contrast TGO phase between the topcoat-Si interface after exposure for 96h at 1316°C was performed using EDS, seen in Figure 5.5. These local chemistry measurements in the topcoat reveal that point A had a Yb:Si ratio of 1.8, consistent with Yb_2SiO_5, while point B had a Yb:Si ratio of 1.1, consistent with $Yb_2Si_2O_7$. The dark contrast interpenetrating phase at point C was a mixture of Yb, Si, Na and K, consistent with a silicate phase filled with impurities. Potassium is likely an impurity from the testing environment or originated as an impurity during powder processing of the topcoat or bond coat materials. Due to the interaction volume generated from the 10 kV electron beam, it is possible that some of Yb signal is generated from the topcoat. The reaction product between the topcoat and Si layers at point D consisted only of Si and O and possessed a O:Si ratio of 1.9, consistent with SiO_2. The SiO_2 layer corresponding to point D was used for TGO thickness data reported in Figures 5.3 and 5.4.

Laser Raman spectroscopy performed on TGOs (in cross-section) formed after exposure for 240h at 1000°C and 1316°C revealed a rich vibrational spectrum, populated with many low-wavenumber peaks ranging from ~100 cm^{-1} - 1000 cm^{-1} which can be seen in Figure 5.6. It was determined that all of the observed peaks reported in Figure 5.6a) matched with the reference patterns for $Yb_2Si_2O_7$, α-cristobalite and the Si bond coat seen in

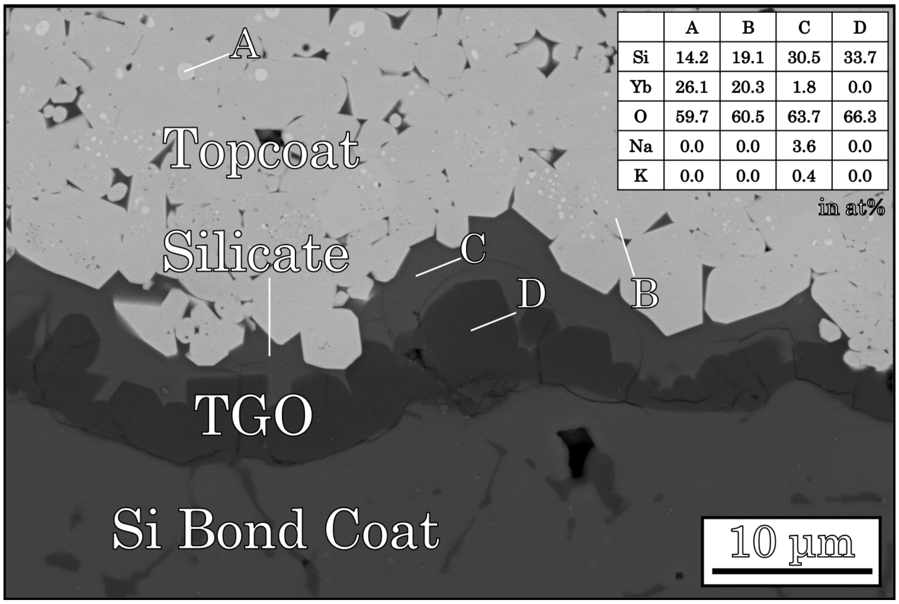

	A	B	C	D
Si	14.2	19.1	30.5	33.7
Yb	26.1	20.3	1.8	0.0
O	59.7	60.5	63.7	66.3
Na	0.0	0.0	3.6	0.0
K	0.0	0.0	0.4	0.0

in at%

Figure 5.5. Backscattered electron SEM image from a portion of the topcoat-Si bond coat interface after exposure to ~2.5 mg/cm^2 of Na_2SO_4 for 96h at 1316°C in a gaseous 0.1% SO_2 –O_2 environment overlaid with an inlaid table displaying elemental compositions (in at.%) collected from several points.

Figure 5.6b). The reference pattern for α-cristobalite has Raman active modes at 113, 230, 274, 278 416, and 783 cm^{-1}, $Yb_2Si_2O_7$ has modes at 145, 278, 370, 416, 485, 521, 669, 923, and 952 cm^{-1}, while the Si bond coat has peaks at 300, 514, 620 cm^{-1} and a broad peak centered at around 950 cm^{-1}. These measurements reveal Raman signal from the surrounding $Yb_2Si_2O_7$ topcoat and Si bond coat layers is generated due to sampling volume interaction. The Si bond coat peak at 514 cm^{-1} was strong from specimens exposed at 1100°C and below, much more than spectra collected from specimens exposed at 1100°C and above. Peaks at 924 and 953 cm^{-1} corresponding to $Yb_2Si_2O_7$ are present in all spectra collected, while strong peaks at 113, 230, 275, 416, and 785 cm^{-1} belonging to α-cristobalite are present in all spectra collected from TGOs formed at 1200°C and above. There is overlap between the 416 and 275 cm^{-1} α-cristobalite and $Yb_2Si_2O_7$ peaks, however the 113, 230, and 785 cm^{-1} peaks clearly identify the TGO as α-cristobalite despite the peak overlap. The

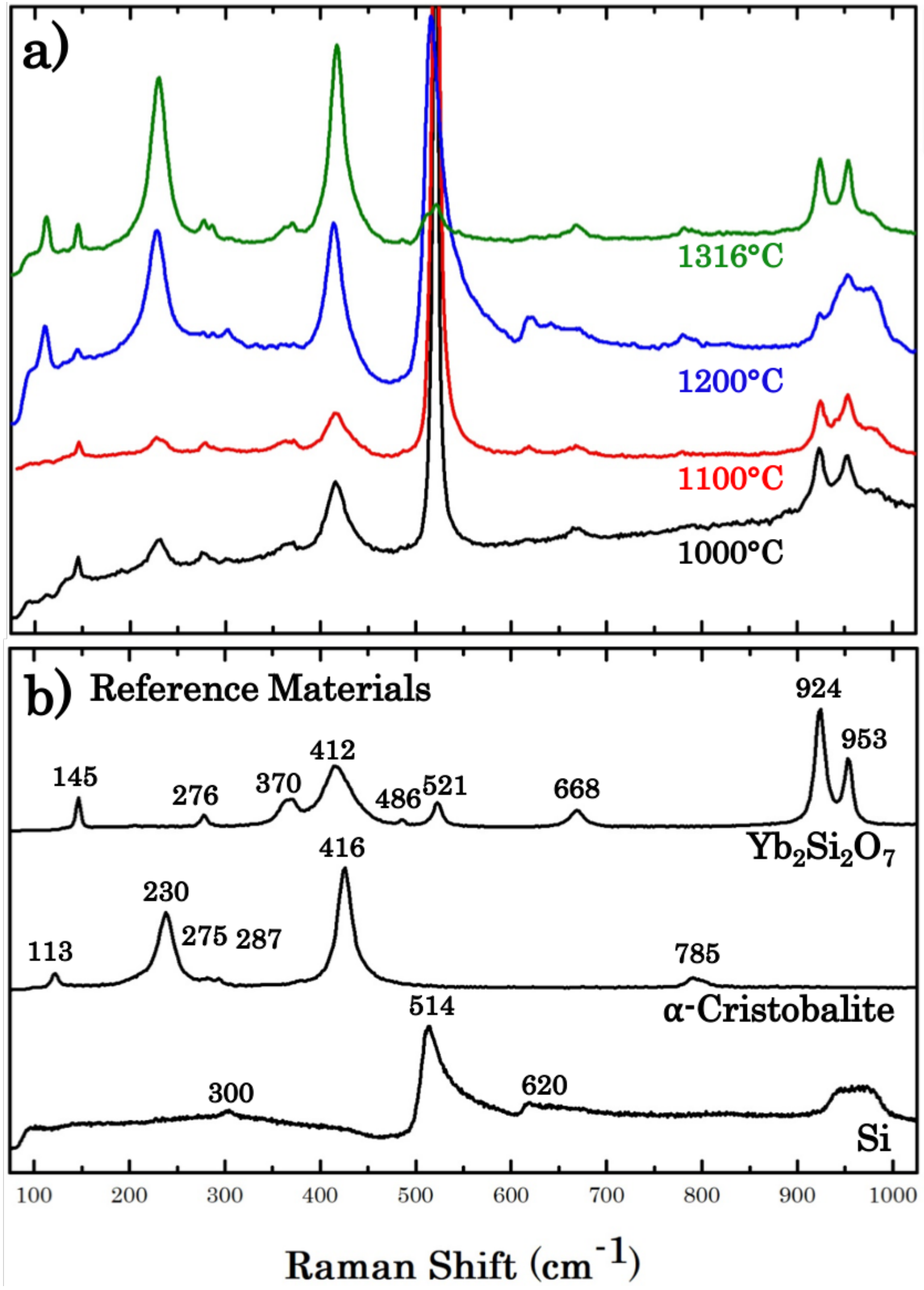

Figure 5.6. a) Plot of raman spectral data collected from the TGO formed after exposure to ~2.5 mg/cm^2 for 240h at 1000°C-1316°C in a gaseous 0.1% SO_2-O_2 environment and b) reference patterns for $Yb_2Si_2O_7$, α-cristobalite and the Si bond coat.

overlapping 416 and 275 cm^{-1} peaks still exist in the patterns for the TGOs formed at 1100°C and below, but only the 230 cm^{-1} peak belonging to α-cristobalite can be observed. The absence of the 113 cm^{-1} and 785 cm^{-1} peaks combined with the presence of the 230 cm^{-1} peak likely indicates that small amounts of α-cristobalite are present within the TGO or that the generated signal is weaker than the signal generated from TGOs formed at 1200°C and higher. Additional Raman spectral data can be seen in Appendix F.

Electron diffraction was performed on specimens after exposure for 1h and 240h at 1316°C to confirm Raman spectral measurements and also to determine crystallization kinetics. Three different areas along the TGO, hundreds of microns apart were examined to determine any possible variation in crystal structure. TEM images and the three areas where electron diffraction patterns were taken from (red circles) on a specimen exposed at 1h can be seen in Figure 5.7, while diffraction patterns from a specimen exposed for 240h can be seen in Figure 5.8. All of the TEM images are orientated similarly, with the polycrystalline Si bond coat on the right-hand side and the topcoat on the left-hand side. A several micron thick Pt layer can be seen in each of these images because of Pt deposition during FIB sample preparation. Adjacent to the Si bond coat is a highly crystalline layer ~1 μm thick in the 1h images and ~6 μm in the 240h images. The corresponding electron diffraction patterns can be seen displayed on the right-hand of their corresponding TEM images. Each of the three diffraction patterns taken per specimen reveal that the areas probed were single crystal and were on zone-axis directions. All diffraction patterns taken at 1h and 240h were indexed to the tetragonal SiO_2 phase α-cristobalite with space group $P4_122$ (PDF File #00-039-1425). The diffraction patterns in Figure 5.7a) and Figure 5.8c) produce forbidden (001), (002) and (100) type-diffraction spots that match well with the known α-cristobalite lattice constant values of 4.972 and 6.927 Å. These forbidden diffraction spots are likely due to multiple scattering of electrons due to increased sample

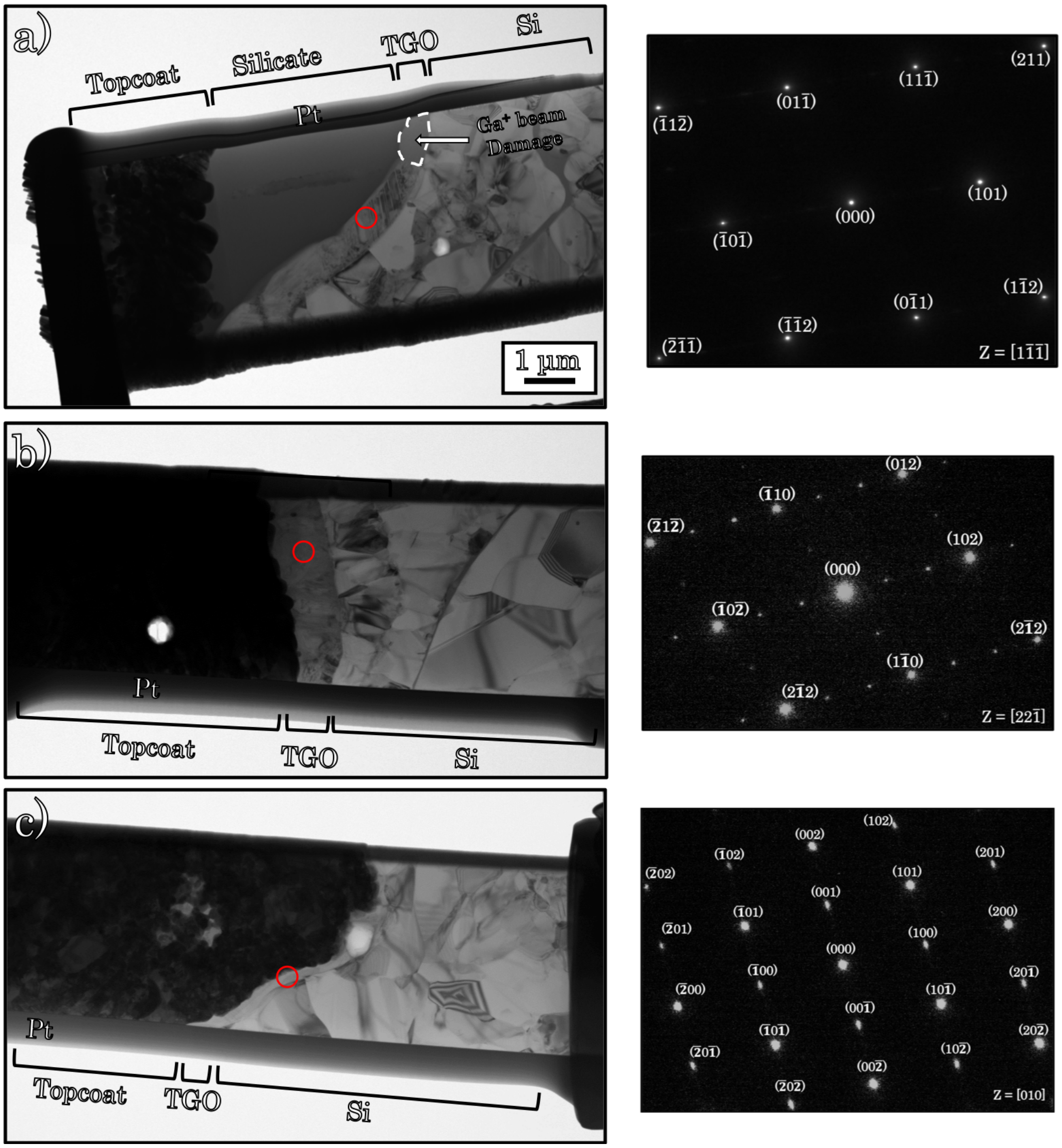

Figure 5.7. TEM images (left) showing several regions of the topcoat-Si bond coat interface after exposure to ~2.5 mg/cm^2 for 1h at 1316° in a gaseous 0.1% SO_2-O_2 environment and diffraction patterns (right) taken from areas circled in red.

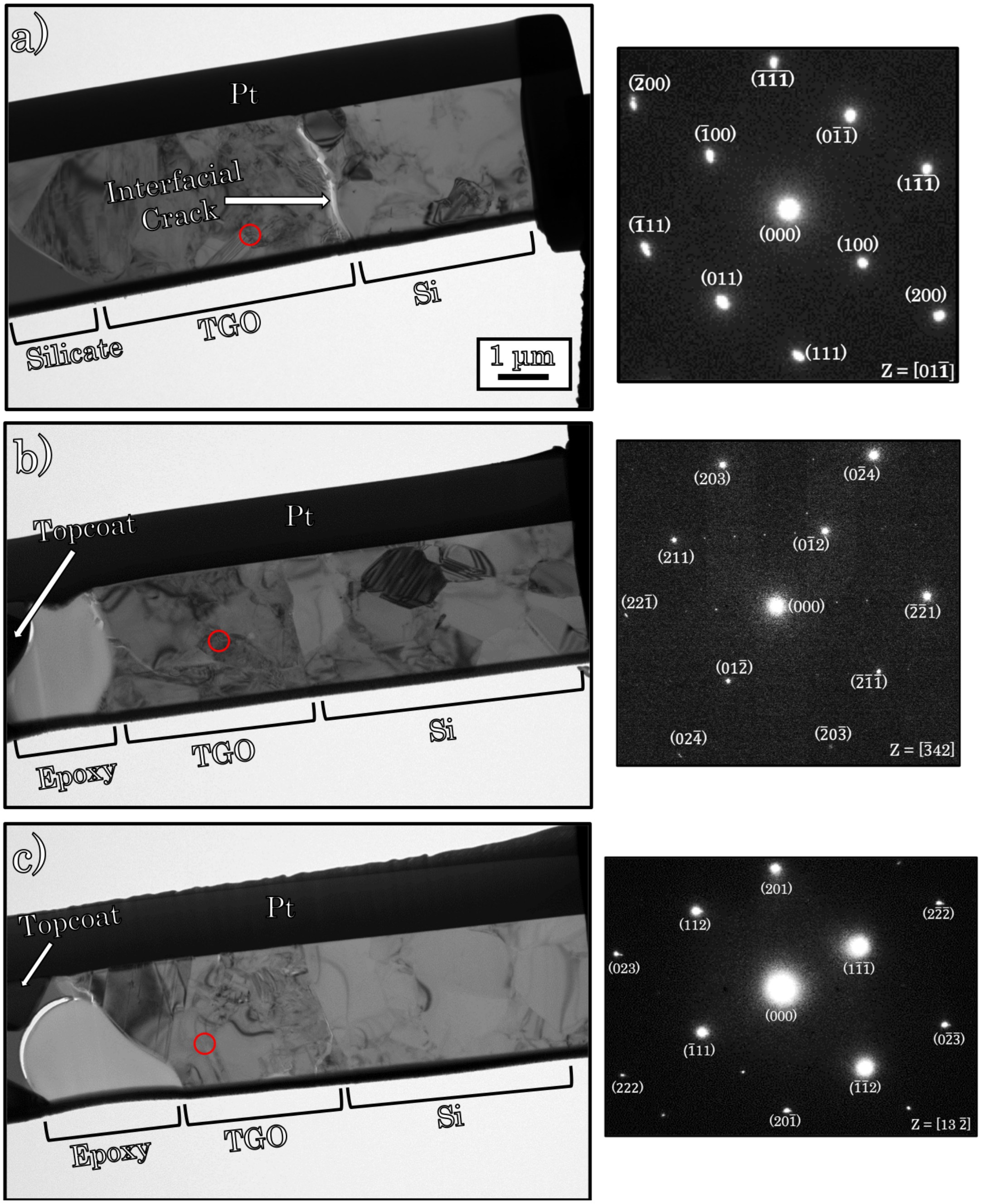

Figure 5.8. TEM images (left) showing several regions of the topcoat-Si bond coat interface after exposure to ~2.5 mg/cm^2 for 240h at 1316° in a gaseous 0.1% SO_2-O_2 environment and diffraction patterns (right) taken from areas circled in red.

thickness and low crystallographic symmetry in the TGO. Diffraction patterns seen in Figure 5.7b) and Figure 5.8b) produce diffraction spots that all match with α-cristobalite. An explanation on how these diffraction patterns were indexed can be seen in Appendix G.

During the process of preparing specimens for TEM analysis using Ga^+ ion based milling, it was observed that Ga^+ ion beam-damage induced amorphization of the TGO. Partial amorphization to the TGO layer can be seen in Figure 5.7a) in the region outlined in white, while amorphization of the entire TGO layer can be seen in Figure 5.9. Starting at the right-hand side of the TEM image in Figure 5.9 is the polycrystalline Si bond coat, while the topcoat can be seen on the left-hand side. Between these layers are two amorphous regions evident by their diffraction patterns, collected from the regions outlined in the red and blue circles. The region nearest the Si bond coat is amorphized α-cristobalite TGO, while the region nearest the topcoat is the silicate phase. A further explanation on how FIB-SEM was used to prepare specimens for TEM imaging an electron diffraction and additional examples of Ga^+ ion beam amorphization to crystalline TGOs can be seen in Appendix H.

Low-magnification SEM images of the topcoat + Si bond coat after exposure for 240h at 1000°C and 1100°C can be seen in Figure 5.10, while similar images after exposure for 240h at 1200°C and 1316°C can be seen in Figure 5.11. The TGO is hardly visible and no vertical cracking or delamination between the Si bond coat and topcoat at this magnification is observed below exposures of 1316°C. However, vertical cracking and delamination can easily be observed in the TGO at this magnification after exposure at 1316°C. Some portions of the TGO are adherent and vertically cracked, while other portions of the TGO are delaminated and missing from the specimen. Also unlike the TGOs formed in other specimens, porosity between the TGO-topcoat interface is present. Examination of the TGO after exposure for 1h at 1316°C seen in Figure 5.12, revealed that no vertical

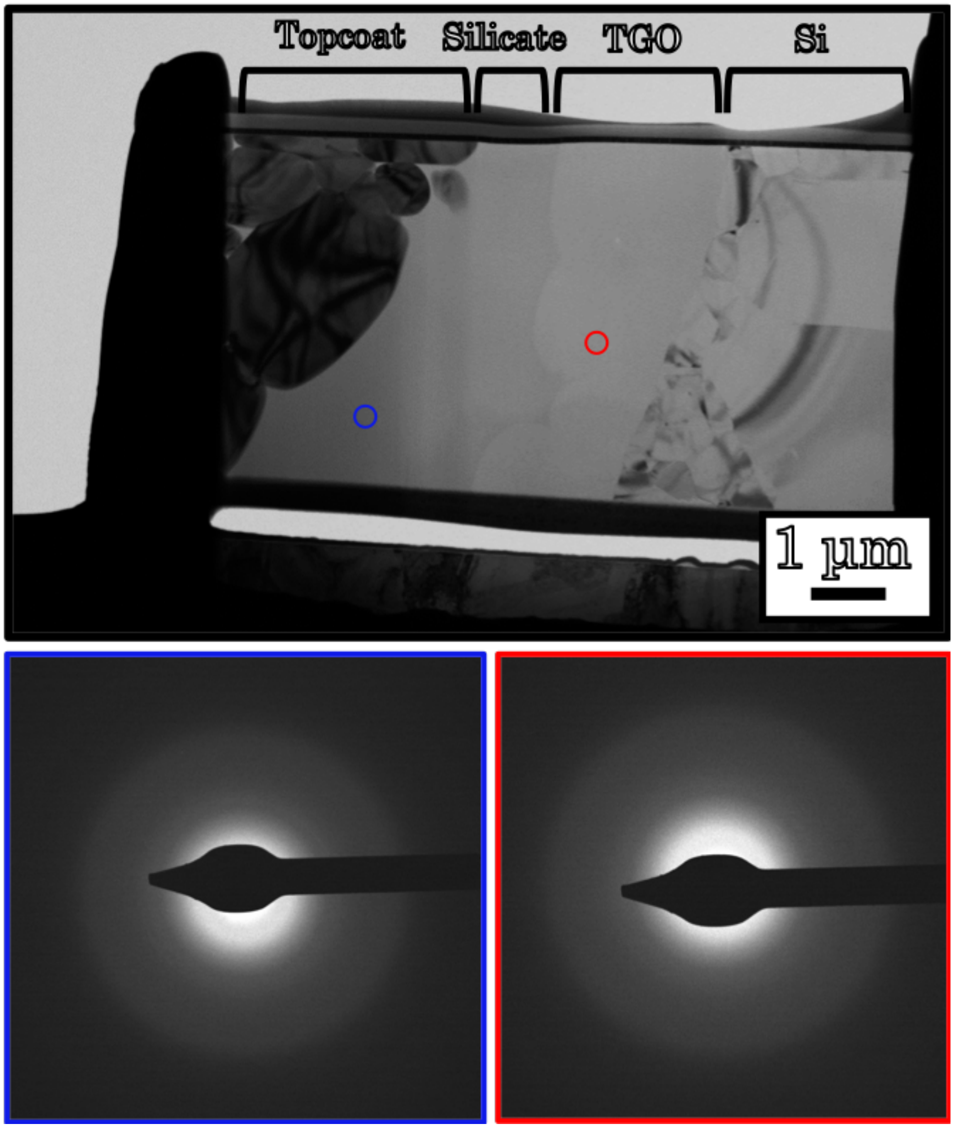

Figure 5.9. TEM image (top) showing a portion of topcoat-Si bond coat interface after exposure to ~2.5 mg/cm^2 for 96h at 1316° in a gaseous 0.1% SO_2-O_2 environment and diffraction patterns (bottom) taken from the areas circled in blue and red.

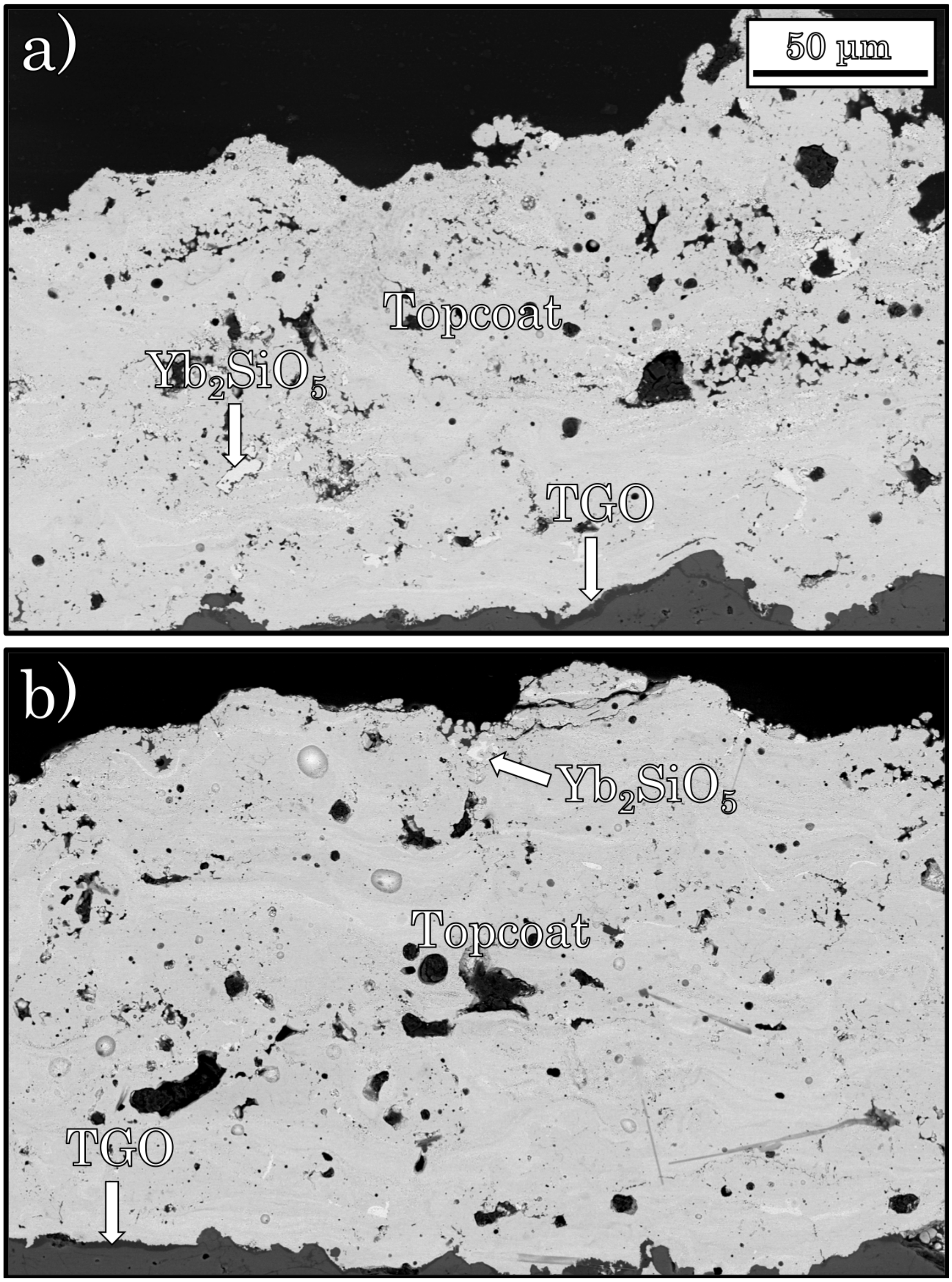

Figure 5.10. Backscattered electron SEM images from a portion of the topcoat after exposure to ~2.5 mg/cm^2 of Na_2SO_4 for 240h at a)1000°C and b) 1100°C in a gaseous 0.1% SO_2 –O_2 environment.

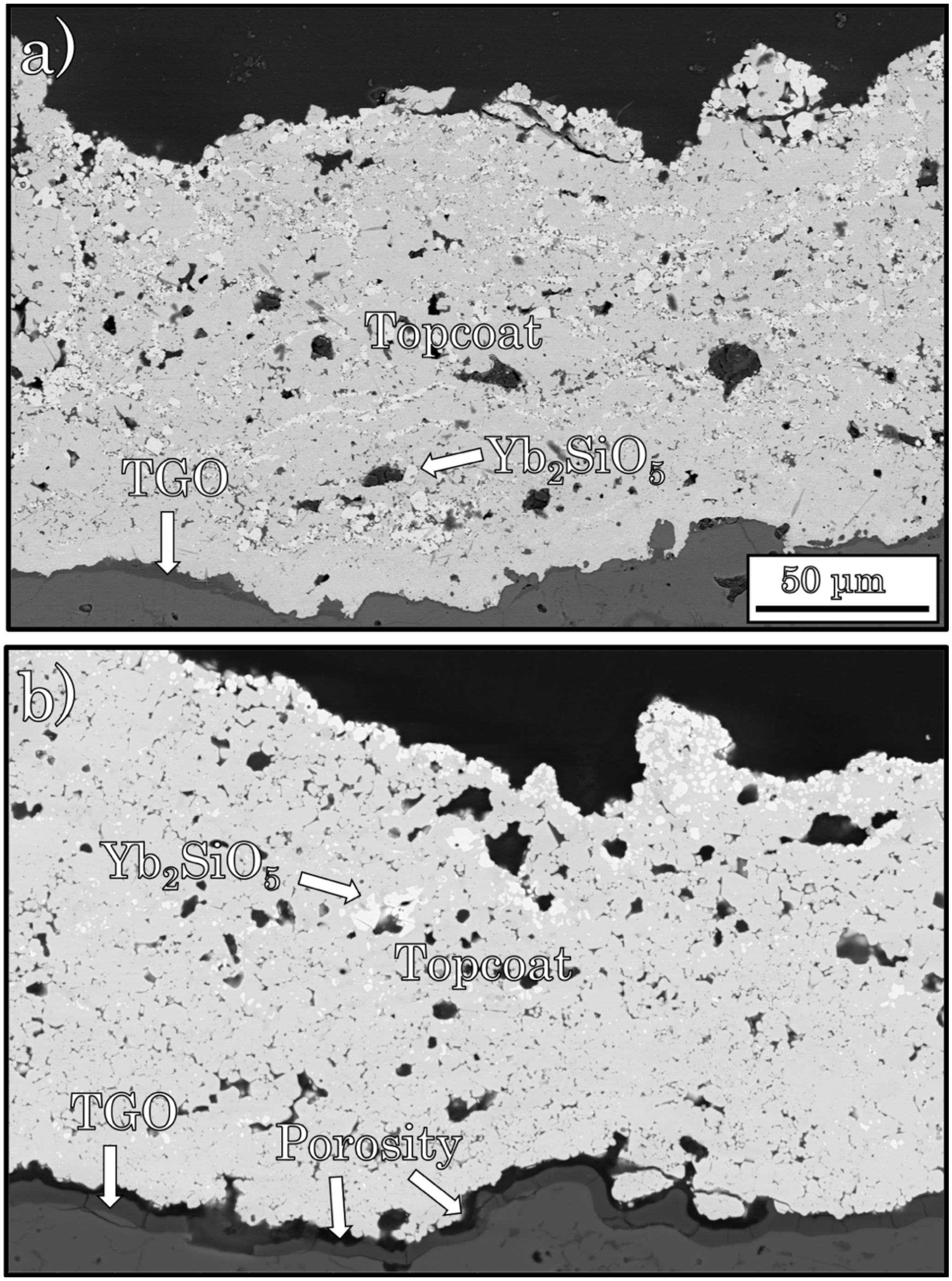

Figure 5.11. Backscattered electron SEM images from a portion of the topcoat after exposure to ~2.5 mg/cm^2 of Na_2SO_4 for 240h at a)1200°C and b) 1316°C in a gaseous 0.1% SO_2 –O_2 environment.

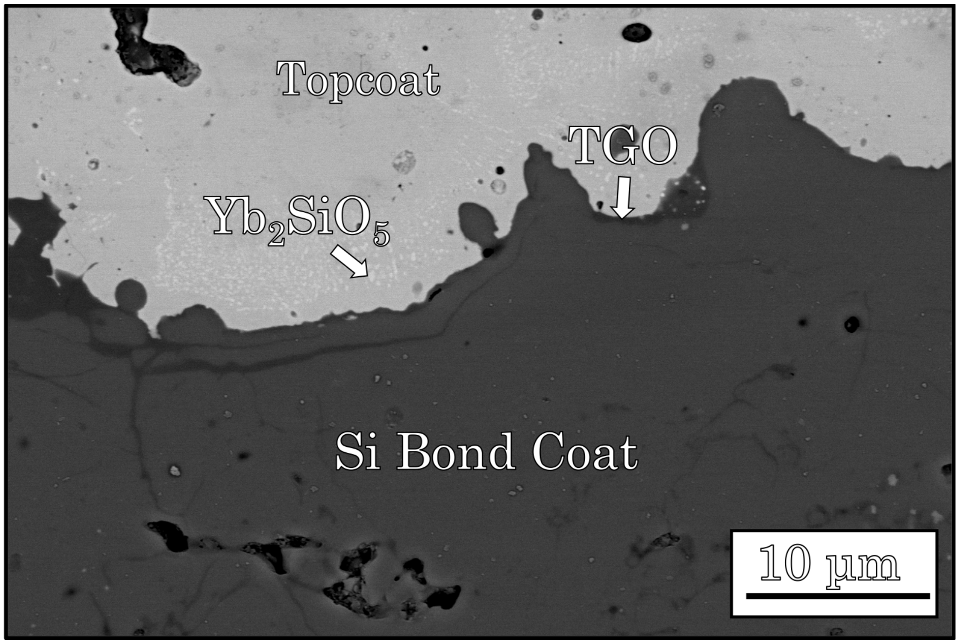

Figure 5.12. Backscattered electron SEM image from a portion of the topcoat-Si bond coat interface after exposure to ~2.5 mg/cm^2 of Na_2SO_4 for 1h at 1316°C in a gaseous 0.1% SO_2 –O_2 environment.

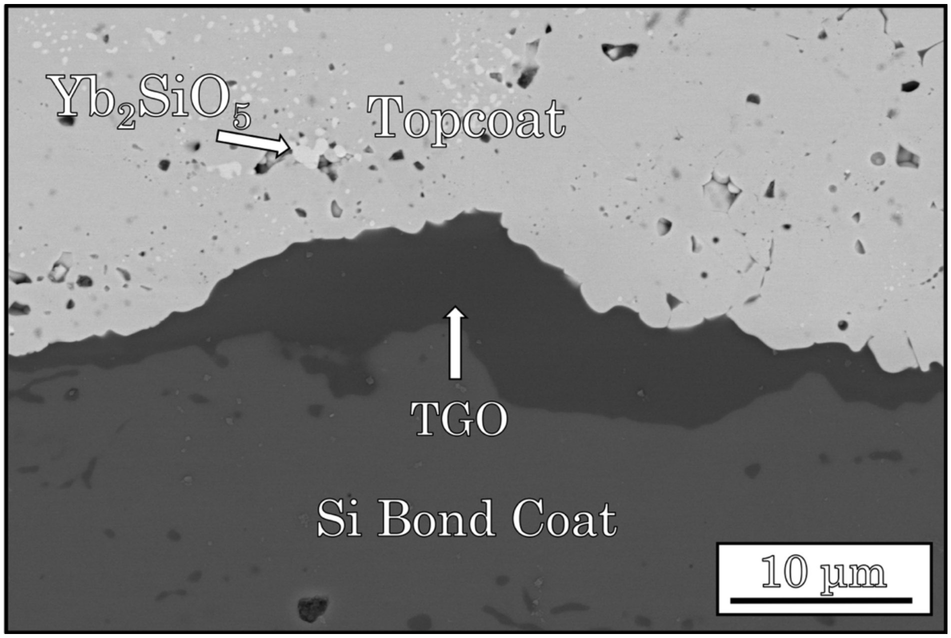

Figure 5.13. Backscattered electron SEM image from a portion of the topcoat-Si bond coat interface after exposure to ~2.5 mg/cm^2 of Na_2SO_4 for 96h at 1316°C in a gaseous 0.1% SO_2 –O_2 environment.

cracking, delamination, or porosity build-up at the TGO-topcoat interface within the coating system occurred. The TGO formed after exposure for 96h is up to 10 μm thick in some areas and is uncracked despite being cristobalite. More SEM images of the TGO across time and temperature can be seen in Appendix I.

5.4 Discussion

5.4.1 Si Bond Coat Oxidation Kinetics: Effects of Na_2SO_4 and Yb_2SiO_5

Exposure to Na_2SO_4 in a 0.1% SO_2-O_2(g) environment for times up to 240h at temperatures between 1000°C-1316°C led to the oxidation of the Si bond coat. A comparison to Si bond coat oxidation kinetics as predicted by the Deal-Grove model in dry O_2(g) were made. However, average TGO thickness measurements reported in this dissertation reveal the interaction of Na_2SO_4 with the coating system does not increase the overall oxidation kinetics of the Si bond coat significantly when compared to Deal-Grove model predictions. Exposure to Na_2SO_4 between 1000°C-1200°C produced TGOs ~1-2 μm thinner than those predicted by the Deal-Grove model, while exposure at 1316°C produced TGOs with thicknesses only slightly larger than those predicted by the Deal-Grove model (4.8 μm D&G vs. 5.7 ± 0.4 μm after 240h). It is known that stand-alone SiO_2 forming materials (i.e. Si, SiC, Si_3N_4) exhibit increased oxidation kinetics in the presence of Na-containing compounds such Na_2SO_4.[41–44] However, the observed contradictory reduction in Si bond coat oxidation kinetics, despite the presence of the oxidation rate increasing compound Na_2SO_4, is likely explained by slower O_2(g) transport rates through the topcoat. The ~130 μm thick topcoat itself could provide some oxidation protection as O_2(g) must first diffuse through the topcoat. The filling of empty space within the topcoat by the sodium silicate phase could also further reduce O_2(g) transport through topcoat. However, the reduced oxidation kinetics observed in the $Yb_2Si_2O_7$ topcoat-Si bond coat EBC system tested in this dissertation chapter may be partially attributed to an additional mechanism. As explained in the previous chapter of this dissertation, the SiO_2 TGO reacts with Yb_2SiO_5 in the topcoat to form $Yb_2Si_2O_7$. TGO formation and its subsequent reaction with Yb_2SiO_5 grains in the topcoat occurs, are expressed in Equations (5.1) and (5.3):

$$Si + O_2(g) \rightarrow SiO_2 \tag{5.1}$$

$$Yb_2SiO_5 + SiO_2 \rightarrow Yb_2Si_2O_7 \tag{5.3}$$

This indicates measurement of TGO thickness underestimates Si bond coat oxidation kinetics, as SiO_2 consumed from reaction with Yb_2SiO_5 is unaccounted for. An approximate value for the true average TGO thickness (x_{total}) is the sum of the measured TGO thickness ($x_{measured}$) reported in Figure 5.3a) and that consumed from reaction with Yb_2SiO_5 in Equation (5.3) ($x_{consumed}$):

$$x_{total} = x_{measured} + x_{consumed} \tag{5.4}$$

A value for $x_{consumed}$ can be calculated starting with density-mass-volume relations seen in Equation (5.5):

$$x_{consumed} = \frac{mass_{SiO_2}}{\rho_{SiO_2} A_{TGO}} \tag{5.5}$$

where $mass_{SiO_2}$ is the total mass of SiO_2 consumed by reaction with Yb_2SiO_5 in the top coat, ρ_{SiO_2} is the density of β-cristobalite (2.20 g/cm^3), and A_{TGO} is the surface area of the TGO, assumed to be 1.6 cm^2 or the surface area of specimens tested. The term $mass_{SiO_2}$ can be rewritten as:

$$mass_{SiO_2} = mol_{SiO_2} MW_{SiO_2} \tag{5.6}$$

where MW_{SiO_2} is the molecular weight of SiO_2 (60.08 g/mol) and mol_{SiO_2} are the number of moles of SiO_2 consumed by Yb_2SiO_5. According to Equation (5.3), for every 1 mol of SiO_2 produced from the oxidation of the Si bond coat, 1 mol of Yb_2SiO_5 will be consumed to produce 1 mol of $Yb_2Si_2O_7$. The term mol_{SiO_2} can thus be re-written as:

$$mol_{SiO_2} = mol_{Yb_2SiO_5} = \frac{\rho_{Yb_2SiO_5} |\Delta V_{Yb_2SiO_5}|}{MW_{Yb_2SiO_5}} \tag{5.7}$$

where $\rho_{Yb_2SiO_5}$ is the density of Yb_2SiO_5 (7.22 g/cm^3), $MW_{Yb_2SiO_5}$ is the molecular weight of Yb_2SiO_5 (454 g/mol) and $|\Delta V_{Yb_2SiO_5}|$ is equal to the difference in the absolute value of the change in volume of Yb_2SiO_5 (in units of μm^3) in the topcoat at the time of interest and t = 0h and is determined experimentally. The linear fit reported in Ch. 4 of this dissertation was used for $|\Delta V_{Yb_2SiO_5}|$. Thus, substituting Equations (5.6) and (5.7) in (5.5), an expression for $x_{consumed}$ can be re-written as:

$$x_{consumed} = \frac{|\Delta V_{Yb_2SiO_5}|}{A_{TGO}} \frac{MW_{SiO_2}}{MW_{Yb_2SiO_5}} \frac{\rho_{Yb_2SiO_5}}{\rho_{SiO_2}} \tag{5.8}$$

Plugging Equation (5.8) into Equation (5.2), the total amount TGO thickness (x_{total}) produced during exposure can be expressed as:

$$x_{total} = x_{measured} + \frac{|\Delta V_{Yb_2SiO_5}|}{A_{TGO}} \frac{MW_{SiO_2}}{MW_{Yb_2SiO_5}} \frac{\rho_{Yb_2SiO_5}}{\rho_{SiO_2}} \tag{5.9}$$

A plot of x_{total}, $x_{measured}$, and the TGO thickness predicted by the Deal-Grove model at 1316°C in dry O_2(g) without Na_2SO_4 can be seen in Figure 5.14. The

TGO thickness values predicted by the Deal-Grove model and $x_{measurement}$ are in reasonable agreement, while values for x_{total} are expectedly larger than $x_{measurement}$ values. Exposure after 240h results in the largest difference between x_{total} and $x_{measurement}$, nearly 6 µm. Thus, consumption of SiO_2 from the TGO by Yb_2SiO_5 in the topcoat does have significant effect on Si bond coat oxidation kinetics, and the determination of Si bond coat oxidation kinetics through TGO measurement are underestimated. Alternatively, Si bond coat consumed (x_{Si}) can be used as a metric for Si bond coat oxidation kinetics. The conversion of SiO_2 TGO thickness produced to thickness of Si bond coat consumed can be written as:

$$x_{Si} = \frac{MW_{Si}}{MW_{SiO_2}} \frac{\rho_{SiO_2}}{\rho_{Si}} = 0.46\ x_{SiO_2} \tag{5.10}$$

where MW_{Si} is the molecular weight of Si (28.09 g/mol), MW the molecular weight of SiO_2 (60.08 g/mol), ρ_{SiO_2} the density of β-cristobalite (2.20 g/cm^3), and ρ_{Si} the density of Si (2.33 g/cm^3). This equation demonstrates that for every 1 µm of Si bond coat consumed from oxidation, 2.17 µm of TGO is produced. Average TGO measurements predict ~2.8 µm of the Si bond coat is consumed after exposure for 240h, while 5.5 µm of the Si bond coat is consumed after accounting for reaction with Yb_2SiO_5 in the top coat. A difference of 3 µm in Si bond coat consumption occurs from neglecting the reaction with Yb_2SiO_5 in the topcoat, a significant value. If the oxidation behavior is extrapolated to the time in which all Yb_2SiO_5 in the topcoat reacts to form $Yb_2Si_2O_7$ (~327h), this difference is between 4-5 µm. Undoubtedly, the reaction of Yb_2SiO_5 with the TGO still occurs below exposure at 1316°C, but at a slower rate due to the temperature dependence of the reaction (Equation (5.3)). Thus times longer than ~327h are needed for removal of all Yb_2SiO_5 from the topcoat at exposure temperatures below 1316°C. As mentioned in the previous chapter of this dissertation, it was assumed that the entire

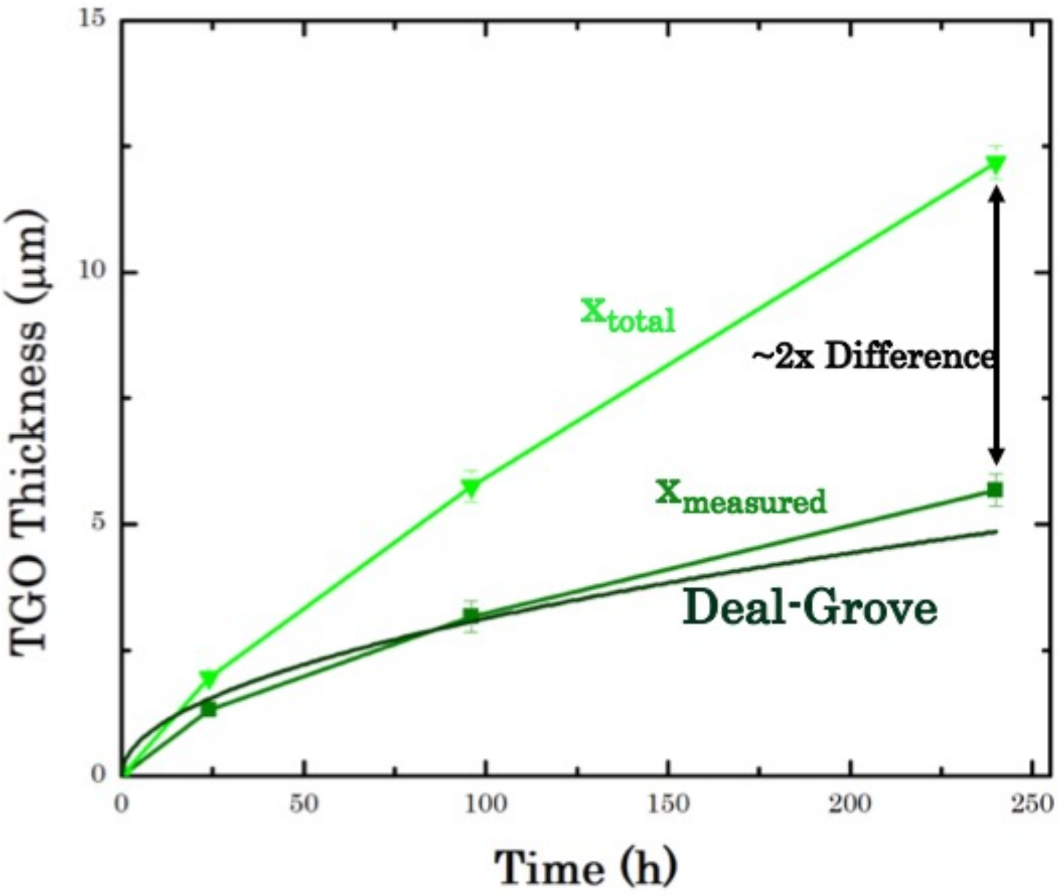

Figure 5.14. Plot of the average TGO thickness as predicted by the Deal-Grove Model (dark green) in dry O_2(g), measured TGO thickness (green) and total SiO_2 produced (bright green) considering SiO_2 loss from reaction with Yb_2SiO_5 after exposure to ~2.5 mg/cm$_2$ at 1316°C in a gaseous 0.1% SO_2 –O_2 environment as a function of time.

topcoat transformed from amorphous Yb-Si-O into crystalline $Yb_2Si_2O_7$ and Yb_2SiO_5 phases after annealing for 2h at 1200°C. The effect of Yb_2SiO_5 in the topcoat suppressing Si bond coat oxidation rates would be less pronounced if a solid-state instead of a liquid-phase transport mechanism occurs within the coating system. As previously mentioned, Si bond coat oxidation kinetics as predicted by the Deal-Grove model may be reduced due to slower O_2(g) transport through the silicate filled topcoat. This seems unlikely at least during exposure at 1316°C after considering SiO_2 loss from reaction with

Yb_2SiO_5 in the topcoats accounted for nearly twice as much SiO_2 produced than determined through average TGO thickness measurement. This indicates that something is increasing the oxidation rates at 1316°C despite the presence of the coating filling silicate phase. Incorporation of foreign ions (i.e. Al_2O_3, Na_2O) into the SiO_2 network even down to ppm levels are known to modify its tetrahedral framework. These low level network modifiers amounts are known to increase SiC oxidation rates by nearly an order of magnitude relative to high purity environments.[42, 45, 46] Given this information, the increased Si bond coat oxidation kinetics observed at 1316°C can be attributed to opening of the SiO_2 network of the TGO from Na_2O impurities, which allow for increased transport rates through the TGO to the underlying Si bond coat. EDS detection limits are generally at ~1000 ppm, which explains the missing Na signal in Figure 5.3, a value that is well above the Na levels known to cause network modification and increased oxidation rates of SiO_2 formers. Without measurement of Yb_2SiO_5 levels at lower exposure temperatures though, it is impossible to determine effect of Na network modification on Si bond coat oxidation kinetics below 1316°C. However, it is reasonable to assume that Si bond coat oxidation kinetics are enhanced at these lower temperatures relative to values predicted by the Deal-Grove model if SiO_2 loss from reaction with Yb_2SiO_5 in the topcoat could be accounted for.

Although not studied in this dissertation chapter, the reaction of steam with Si bond coats is also important due to its presence as a combustion product inside of turbine environments, an especially since Si oxidizes faster in steam versus dry $O_2(g)$ environments. Given exposure at the same temperature, k_p value ratios for oxidation of Si between 90% steam + 10% O_2 and dry $O_2(g)$ environments is ~10, indicating Si bond coats will be consumed 3.2 times faster than in dry $O_2(g)$. However, after calculating the effect of Yb_2SiO_5 on suppressing Si bond coat oxidation kinetics at 1316°C in $Yb_2Si_2O_7$

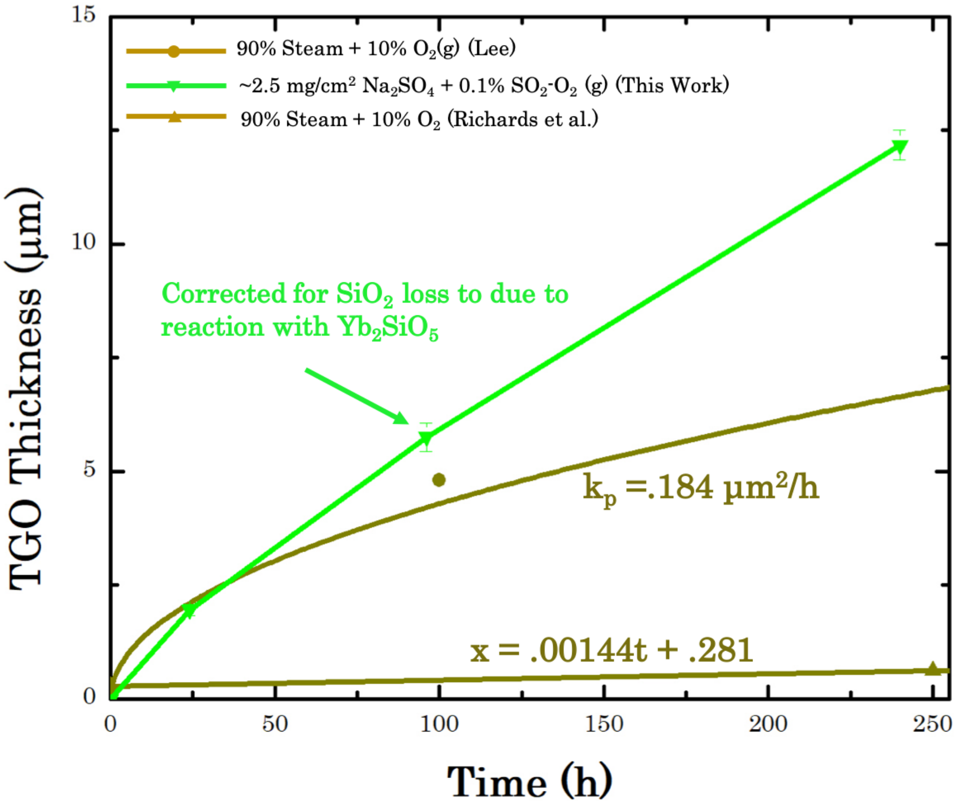

Figure 5.15. Plot of the average TGO thickness in $Yb_2Si_2O_7$ topcoat-Si bond coat EBC systems exposed at 1316°C reported in this work (bright green) and from literature (dark yellow). Values published in this work are corrected to account for SiO_2 loss from the TGO due to reaction with Yb_2SiO_5 in the topcoat.[11, 20]

topcoat-Si bond EBC systems tested in this dissertation chapter and the bond coat oxidation kinetics reported in literature by Richards et al.[20] and Lee[11], Na_2SO_4 + 0.1% SO_2-O_2(g) environments results in more rapid oxidation kinetics than in steam containing environments. Replotting of Figure 5.4a) in Figure 5.15 after considering SiO_2 loss from reaction with Yb_2SiO_5 in the topcoat, reveals Si bond coat oxidation occurred more rapidly in the presence of Na_2SO_4 than in Na_2SO_4-free and steam containing environments. The effect of both Na_2SO_4 and steam on Si bond coat oxidation has not been studied.

5.4.2 TGO Crystallization

Thermally grown oxides on SiO_2 formers (i.e. Si, SiC, Si_3N_4) are believed to initially form as amorphous SiO_2, which then devitrify into β-cristobalite sperhulites after prolonged exposure.[26] These β-cristobalite spherulites are surface nucleated, and then grow radially outward and down into the surrounding amorphous SiO_2 until the surrounding amorphous SiO_2 matrix is completely crystalline. The crystals crack due to a ~5% density increase upon cooling through the β-to-α cristobalite inversion temperature somewhere between ~200-300°C. Due to the formation of a SiO_2 TGO from the oxidation of the Si bond coat (Equation (5.1)), it is believed that TGOs will crystallize into cristobalite and display similar cracking behavior. This phase transformation is believed to be a major failure mechanism of EBCs. However, there have been no published studies definitively proving the crystallization and cracking behavior in $Yb_2Si_2O_7$ topcoat-Si bond coat based EBC systems. This work was able to provide the first evidence of TGO crystallization in $Yb_2Si_2O_7$ topcoat-Si bond coat based EBC systems. Both Raman laser spectroscopy and electron diffraction were able to show the TGO was the crystalline SiO_2 phase α-cristobalite. This suggests the TGO crystallized into β-cristobalite during exposure which then inverted to α-cristobalite upon cooling through the β-to-α cristobalite inversion. Electron diffraction + Raman laser spectroscopy performed on the TGO of a specimen exposed at 240h at 1316°C produced a vibrational spectrum and multiple diffraction patterns matching with α-cristobalite. TEM images revealed that the TGO was polycrystalline α-cristobalite. Due to the identically matching Raman spectra collected from TGOs formed during exposure at 1200°C and 1316°C, it is reasonable to assume the TGO formed at 1200°C is also α-cristobalite. The TGOs formed below 1200°C are likely comprised of small amounts of α-cristobalite evident by the weak Raman signal and missing 113 and 785 cm^{-1} peaks. Diffraction studies of the lower temperatures are needed to verify the α-cristobalite Raman spectral measurement from TGOs formed at these lower temperatures. It should be noted that FIB-SEM sample prep for electron diffraction studies caused significant damage to TGOs due to Ga^+ ion beam damage, leading to complete amorphization of the specimen analyzed. Depending upon the FIB-SEM settings, an amorphous or crystalline TGO structure was observed. Thicker Pt layers, several microns thick and a lower Ga^+ ion beam energy (5kV) for the final milling thinning step was employed to minimize this damage.

It was observed in the third chapter of this dissertation and it is well known in literature that Na-containing compounds including Na_2SO_4 cause SiO_2 crystallization into tridymite.[41, 47–53] Thus with this information, TGOs should crystallize into the high temperature β-tridymite phase during exposure, and then invert to one of its many low-temperature polymorphs upon cooling to room temperature. However, it is also well known that cristobalite can form in the tridymite range even in the presence of low levels of impurities including Na_2O, indicating partial solubility within the cristobalite structure.[27, 28, 46] Thus, the formation of the cristobalite TGO observed in this dissertation chapter could be explained by partial solubility of Na_2O and other impurities from the coating system which act to stabilize cristobalite. The TGO might exist as tridymite only once enough impurities within the coating system are present.

5.4.3 TGO Crack Damage

Usage of high purity SiO_2 glass is limited at high temperatures due to devitrification into cristobalite. This crystalline SiO_2 phase nucleates within the glass matrix or at its surface, and cracks upon cooling due to the large density increase cooling from β-to-α cristobalite. Similar cracking behavior has been observed in oxidation of SiO_2 forming materials, including Si and SiC.[24, 28, 54, 55] Due to the presence of α-cristobalite TGOs in the EBC system tested in this dissertation, similar cracking is expected. However, significant cracking (i.e. vertical, delamination) in TGO was only observed after exposure for 240h at 1316°C, despite the confirmed presence of α-cristobalite after exposure for 240h at all exposure temperatures and even after exposure for 1h at 1316°C. The TGO formed after exposure for 240h at 1316˚C had an average thickness of ~6 μm, the thickest TGO formed across all testing conditions. The other exposure conditions formed cristobalite TGOs that were crack-free relative to the 240h 1316˚C exposure, and were only 1-3 μm thick. Thus, it is reasonable to believe that relatively thin cristobalite TGOs can exist without significant cracking associated with the β-to-α cristobalite inversion. Examination of a TGO formed after exposure for 96h at 1316°C presented in Figure 5.13 indicates that the TGO in this region is also crack-free despite being α-cristobalite, but in some regions is ~10 μm thick. If the entire TGO is cristobalite, then there should be some cracking within this region. This uncracked, crystalline region despite being nearly 10 μm thick provides evidence that cracking may be localized to certain regions within the TGO. More work is needed to fully understand the cracking behavior in SiO_2 TGOs formed in in $Yb_2Si_2O_7$ topcoat-Si bond coat CMC systems across time and temperature, as crack damage associated with TGO crystallization into cristobalite is widely believed to be the primary failure mechanism in EBC systems.

5.5 Implications For Turbine Engine Application

Inward diffusion of oxidizing species (i.e. O_2(g), H_2O(g)) through the topcoat will cause the formation of a buried SiO_2 TGO between the EBC topcoat and Si bond coat, with increasing thickness over time. However, the rate at which this layer builds up over time cannot be predicted using published k_p values from the Deal-Grove model due to consumption of SiO_2 by reactive phases within the topcoat. Phase diagram analysis along with measurement of phase content within the topcoat over time can predict how much Si bond coat oxidation kinetics are underestimated. Analysis of the coating system tested in this dissertation chapter predicts that exposure for ~327h at 1316°C resulted in underestimation of Si bond coat consumption by an estimated 5-6 μm, thus revealing not all SiO_2 produced from Si bond coat oxidation lies in the TGO between the EBC topcoat and Si bond coat. Thus, Si bond coat oxidation kinetics within EBC topcoat + Si bond coat systems should account for consumption by reactive phases within the topcoat. Regardless of the effect of reactive phases within an EBC topcoat has on Si bond coat oxidation kinetics, the presence of Na will increase the oxidation kinetics of Si bond coats due to network modification of the SiO_2 TGO. This increase in Si bond coat oxidation will occur even if Na modification of the SiO_2 network is at ppm levels. EBC systems employing a Si bond coat should therefore be designed to keep Na species away from the TGO.

Currently a major failure mechanism in EBC system is attributed to the crystallization of the SiO_2 TGO into cristobalite. This phase is known to induce severe cracking upon inverting through the β-to-α inversion, resulting in delamination and thus is a concern for EBC durability. Significant cracking associated with this phase transformation was observed only after exposure for 240h at 1316°C. Cristobalite TGOs 1-3 μm thick formed at 1000°C and above were found to be hardly cracked and highly adherent within the coating system. This indicates EBCs with relatively thin (<3-5 μm) cristobalite TGOs may not undergo catastrophic cracking.

5.6 Conclusions

Si bond coat oxidation kinetics and crystallization of the TGO in a $Yb_2Si_2O_7$ topcoat-Si bond coat EBC systems exposed to ~2.5 mg/cm^2 Na_2SO_4 was studied. The TGO growth kinetics cannot be predicted using the Deal-Grove model for three reasons: (i) transport of oxidant to the reaction interface may be decreased by the $Yb_2Si_2O_7$ topcoat (ii) SiO_2 consumption due to reaction with Yb_2SiO_5 in the topcoat leads to underestimation of SiO_2 production (or Si bond coat consumption) (iii) Na_2O inclusions within the TGO present from Na_2SO_4 deposition will increase the TGO growth rate due to enhanced transport through the SiO_2 TGO due to SiO_2 network modification. The effect of the topcoat on transport was not considered in this dissertation chapter. TGOs formed at exposure temperatures below 1316°C were on average ~0.75-1 μm less thick than that predicted by the Deal-Grove model. Average TGO thickness measurements relative to values predicted by the Deal-Grove oxidation model at 1316°C were only slightly increased in the presence of Na_2SO_4 only. However, when SiO_2 consumed by reaction with Yb_2SiO_5 in the topcoat at 1316°C is added to the average TGO thickness measurements, nearly ~2x as much SiO_2 is produced (or Si bond coat consumed) than that determined by average TGO thickness measurement. The TGO likely crystallized into β-cristobalite during all exposure temperatures, which transformed to α-cristobalite upon cooling through the β-to-α cristobalite inversion. The TGO crystallization occurred rapidly, doing so in less than 1h during exposure at 1316°C. Significant vertical cracking and delamination within the TGO was only observed after exposure for 240h at 1316°C. This indicates EBCs with relatively thin (<3-5 μm) cristobalite TGOs may not undergo catastrophic cracking generally associated with the β-to-α cristobalite inversion. Additionally, formation of porosity between the topcoat and TGO was also only observed after exposure for 240h at 1316°C.

References

1. Zok FW. Ceramic Matrix Composites Enable Revolutionary Gains in Turbine Efficiency. 2016;95:22–28.
2. Melissae Fellet. Ceramic-Matrix Composites Take The Heat. *MRS Bull*. 2015;40:916–7.
3. Robinson RC, Smialek JL. SiC Recession Caused by SiO_2 Scale Volatility under Combustion Conditions: I, Experimental Results and Empirical Model. *J Am Ceram Soc*. 1999;82(7):1817–1825.
4. Opila EJ, Smialek JL, Robinson RC, Fox DS, Jacobson NS. SiC Recession Caused by SiO_2 Scale Volatility under Combustion Conditions: II, Thermodynamics and Gaseous-Diffusion Model. *J Am Ceram Soc*. 1999;82(7):1826–1834.
5. Lee KN. Current status of environmental barrier coatings for Si-Based ceramics. *Surf Coat Technol*. 2000;133–134:1 – 7.
6. Rohbeck N, Morrell P, Xiao P. Degradation of ytterbium disilicate environmental barrier coatings in high temperature steam atmosphere. *J Eur Ceram Soc*. 2019;39(10):3153–3163.
7. Stolzenburg F, Johnson MT, Lee KN, Jacobson NS, Faber KT. The interaction of calcium–magnesium–aluminosilicate with ytterbium silicate environmental barrier materials. *Surf Coat Technol*. 2015;284:44–50.
8. Wada M, Matsudaira T, Kawashima N, Kitaoka S, Takata M. Mass transfer in polycrystalline ytterbium disilicate under oxygen potential gradients at high temperatures. *Acta Mater*. 2017;135:372 – 381.
9. Zhong X, Niu Y, Huang L, *et al.* Microstructure and Thermal Properties of Atmospheric Plasma-Sprayed $Yb_2Si_2O_7$ Coating. *J Therm Spray Technol*. 2017;26(1):203–210.
10. Bakan E, Marcano D, Zhou D, Sohn YJ, Mauer G, Vaßen R. $Yb_2Si_2O_7$ Environmental Barrier Coatings Deposited by Various Thermal Spray Techniques: A Preliminary Comparative Study. *J Therm Spray Technol*. 2017;26(6):1011–1024.
11. Lee KN. $Yb_2Si_2O_7$ Environmental barrier coatings with reduced bond coat oxidation rates via chemical modifications for long life. *J Am Ceram Soc*. 2019;102(3):1507–1521.
12. Ueno S, Ohji T, Lin H-T. Recession behavior of $Yb_2Si_2O_7$ phase under high speed steam jet at high temperatures. *Corros Sci*. 2008;50(1):178 – 182.
13. Bakan E, Sohn YJ, Kunz W, Klemm H, Vaßen R. Effect of processing on high-velocity water vapor recession behavior of Yb-silicate environmental barrier coatings. *J Eur Ceram Soc*. 2019;39(4):1507–1513.
14. Stokes JL, Harder BJ, Wiesner VL, Wolfe DE. High-Temperature thermochemical interactions of molten silicates with $Yb_2Si_2O_7$ and $Y_2Si_2O_7$ environmental barrier coating materials. *J Eur Ceram Soc*. 2019;39(15):5059–5067.

15. Poerschke DL, Sluytman JSV, Wong KB, Levi CG. Thermochemical compatibility of ytterbia–(hafnia/silica) multilayers for environmental barrier coatings. *Acta Mater.* 2013;61(18):6743 – 6755.
16. Costa GCC, Jacobson NS. Mass spectrometric measurements of the silica activity in the Yb_2O_3–SiO_2 system and implications to assess the degradation of silicate-based coatings in combustion environments. *J Eur Ceram Soc.* 2015;35(15):4259–4267.
17. Zhao C, Wang F, Sun Y, Zhou Y. Synthesis and characterization of β-$Yb_2Si_2O_7$ powders. *Ceram Int.* 2013;39(5):5805 – 5811.
18. Xu Y, Yan Z. Investigation on the preparation of Si/mullite/$Yb_2Si_2O_7$ environmental barrier coatings onto silicon carbide. *J Rare Earths.* 2010;28(3):399 – 402.
19. Shu-Bin W, Yan-Ru L, Yan-Xia C. Synthesis of Single-Phase β-$Yb_2Si_2O_7$ and Properties of Its Sintered Bulk. *Int J Appl Ceram Technol.* 2015;12(6):1140–1147.
20. Richards BT, Young KA, Francqueville F, Sehr S, Begley MR, Wadley HNG. Response of ytterbium disilicate–silicon environmental barrier coatings to thermal cycling in water vapor. *Acta Mater.* 2016;106:1 – 14.
21. Sullivan RM. Reformulation of oxide growth equations for oxidation of silicon bond coat in environmental barrier coating systems. *J Eur Ceram Soc.* 2019;39(16):5403–5409.
22. Deal BE, Grove AS. General Relationship for the Thermal Oxidation of Silicon. *J Appl Phys.* 1965;36(12):3770–3778.
23. Richards BT, Begley M, Wadley HNG. Mechanisms of Ytterbium Monosilicate/Mullite/Silicon Coating Failure During Thermal Cycling in Water Vapor. *J Am Ceram Soc.* n.d.;98(12):4066–4075.
24. Haynes JA, Lance MJ, Cooley KM, Ferber MK, Lowden RA, Stinton DP. CVD Mullite Coatings in High-Temperature, High-Pressure Air–H_2O. *J Am Ceram Soc.* 2000;83(3):657–659.
25. Cojocaru CV, Lévesque D, Moreau C, Lima RS. Performance of thermally sprayed Si/mullite/BSAS environmental barrier coatings exposed to thermal cycling in water vapor environment. *Surf Coat Technol.* 2013;216:215 – 223.
26. Luthra KL. Some New Perspectives on Oxidation of Silicon Carbide and Silicon Nitride. *J Am Ceram Soc.* 1991;74(5):1095–1103.
27. Ogbuji LUJT, Opila EJ. A Comparison of the Oxidation Kinetics of SiC and Si_3N_4. *J Electrochem Soc.* 1995;142(3):925–930.
28. Opila EJ. Variation of the Oxidation Rate of Silicon Carbide with Water-Vapor Pressure. *J Am Ceram Soc.* 1999;82(3):625–636.
29. Opila EJ, Hann RE. Paralinear Oxidation of CVD SiC in Water Vapor. *J Am Ceram Soc.* 1997;80(1):197–205.
30. Fenner CN. Stability Relations of the Silica Minerals. *Am J Sci.* 1913;36(4):331–384.

31. Fenner CN. The Relations Between Tridymite and Cristobalite. *Trans Soc Glass Technol*. 1919;3:116.
32. Flörke OW. Des Kriställrten des SiO_2 und ihr Umwandlungsverhalten. *Berichte Dtsch Keram Ges*. 1961;38(3):89–97.
33. Flörke OW. Strukturanomalien bei Tridimyt und Cristobalit. *Berichte Dtsch Keram Ges*. 1955;32:369–381.
34. Flörke OW. Uber das Einstoffsystem SiO. *Naturwissenschaften*. 1956;43:419.
35. Buerger MJ, Lukesh J. The Tridymite Problem. *Science*. 1952;95:20.
36. Rockett TJ. The Thermal Stability of Purified Tridymite. *Am Mineral*. 1967;52:1233–1239.
37. Padture NP. Environmental degradation of high-temperature protective coatings for ceramic-matrix composites in gas-turbine engines. *Npj Mater Degrad*. 2019;3(1):11.
38. Stearns CA, Kohl FJ, Rosner DE. Combustion System Processes Leading to Corrosive Deposits. San Diego, California: 1981
39. Pettit F. Hot Corrosion of Metals and Alloys. *Oxid Met*. 2011;76(1):1–21.
40. Jacobson NS. Corrosion of Silicon-Based Ceramics in Combustion Environments. *J Am Ceram Soc*. 1993;76(1):3–28.
41. Hagan JM, Opila EJ. High-Temperature Na_2SO_4 Deposit-Assisted Corrosion of Silicon Carbide – I: Temperature and Time Dependence. *J Am Ceram Soc*. 2015;98(4):1275–1284.
42. Zheng Z, Tressler RE, Spear KE. The Effect of Sodium Contamination on the Oxidation of Single Crystal Silicon Carbide. *Corros Sci*. 1992;33(4):545–556.
43. Jacobson NS. Kinetics and Mechanism of Corrosion of SiC by Molten Salts. *J Am Ceram Soc*. 1986;69(1):74–82.
44. Guy E. Oxidation Behavior of Silicon Carbide. *J Am Ceram Soc*. 1958;41(9):347–352.
45. Opila EJ. Influence of Alumina Reaction Tube Impurities on the Oxidation of Chemically-Vapor-Deposited Silicon Carbide. *J Am Ceram Soc*. n.d.;78(4):1107–1110.
46. Venezia AM, Parola V [La, Longo A, Martorana A. Effect of Alkali Ions on the Amorphous to Crystalline Phase Transition of Silica. *J Solid State Chem*. 2001;161(2):373–378.
47. Hagan JM, Opila EJ. High-temperature Na_2SO_4 deposit-assisted corrosion of silicon carbide–II: Effects of B, C, and Si. *J Am Ceram Soc*. 2017;100(2):761–773.
48. Rockett TJ, Foster WR. The High-Silica Liquidus Surface of the System Na_2O-B_2O_3-SiO_2. *J Am Ceram Soc*. 1981;64(11):148-149.
49. Rockett TJ. Phase Relations in the Systems Silica, Boron Oxide-Silica, and Sodium Oxide-Boron Oxide-Silica. The Ohio State University; Mineralogy; 1963

50. Kracek FC. The System Sodium Oxide-Silica. *J Phys Chem*. 1929;34(7):1583–1598.
51. Kracek FC. The Ternary System, K_2SiO_3-Na_2SiO_3-SiO_2. *J Am Chem Soc*. 1939;61(10):2863–2877.
52. Kracek FC. Phase Equilibrium Relations in the System, Na_2SiO_3-Li_2SiO_3-SiO_2. *J Am Chem Soc*. 1939;61(10):2863–2877.
53. Morey GW. The Ternary System Na_2O-B_2O_3-SiO_2. *J Soc Glass Technol*. 1951;35(167):270–283.
54. Ainger FW. The formation and devitrification of oxides on silicon. *J Mater Sci*. 1966;1(1):1–13.
55. Tortorelli PF, More KL. Effects of High Water-Vapor Pressure on Oxidation of Silicon Carbide at 1200°C. *J Am Ceram Soc*. 2003;86(8):1249–1255.

6| Conclusions

Valuable new insights into the high-temperature reaction behavior of Na_2SO_4 with SiC CMCs and $Yb_2Si_2O_7$ + Si bond coat EBC systems were provided in this dissertation. The reaction kinetics, reaction products, morphological features of the reaction products and SiC surfaces, and application of phase diagram analysis to predict thermodynamics trend were all explored using numerous characterization techniques, including bench-top weight change, macro-imaging, scanning electron microscopy (SEM), transmission electron microscopy (TEM), x-ray diffraction (XRD), inductively coupled plasma optical emission spectroscopy, (ICP-OES), energy-dispersive spectroscopy (EDS), dual-beam focused ion beam scanning electron microscopy, (FIB-SEM) and optical profilometry. It was shown that exposure of various SiC fibers relevant for application in SiC CMCs, SiC CMC chemical constituents, SiC CMCs with a $Yb_2Si_2O_7$ topcoat + Si bond coat EBC system to Na_2SO_4 results in several possible of degradation mechanisms, including granulation of $Yb_2Si_2O_7$ EBC topcoats and reaction to form Yb_2SiO_5 and Na silicates, increased TGO growth kinetics and crystallization, formation of low-melting sodium borosilicate phases due to reaction with the BN matrix fiber interphase, and rapid SiC fiber corrosion and pitting. Each of these degradation mechanisms should be considered for usage of SiC CMCs in Na containing and high-temperature, marine environment applications.

7| Recommendations For Future Work

This dissertation was able to determine many aspects of the high temperature reaction of Na_2SO_4 with a SiC CMC and $Yb_2Si_2O_7$ + Si bond coat EBC system. However, several areas of further research could further improve the understanding of this interaction and the general performance of EBC systems. Further areas of research to be considered include: *(i)* Crystallization kinetics of oxide formated on SiC fibers in the presence of Na_2SO_4 at temperatures other than 1000°C should be performed. Additionally, crystallization kinetics of thermally grown SiO_2 with and without Na_2SO_4 present should be performed. *(ii)* The sensitivity of fiber oxidation kinetics to Na_2SO_4 impurities should be investigated across a wide range of temperatures. *(iii)* Repeat high-temperature tests similar to those in Ch. 3 of this dissertation but with varying levels of BN and Na_2SO_4 to compare SiC consumption, crystallization kinetics, and pitting behavior. *(iv)* Below 867°C, the equilibrium crystalline SiO_2 phase in the Na_2O-B_2O_3-SiO_2 system is quartz. However, the thermally grown SiO_2 layer formed after several days of exposure at 800°C and below observed in Ch.3 of this dissertation chapter, was a mixture of cristobalite + tridymite. Repeat studies below 867°C but for longer times should be performed to determine when or if thermally grown SiO_2 crystallizes into quartz. *(v)* Phase equilibria data for nearly all RE_2O_3-Na_2O and RE_2O_3-SiO_2-Na_2O (RE for rare earth) systems, where RE = Y, Sc and all lanthanide elements is lacking. However, due to the usage of rare earth based coatings in EBC systems and known formation of Na_2SO_4 inside of turbine engines, reaction product formation is difficult to predict. Will all rare earth base materials form low melting sodium silicates that enhance Si bond coat oxidation like that observed in Ch.4 and 5 of this dissertation form? *(vi)* Ch.4 and Ch.5 revealed that Si bond coat oxidation kinetics were underestimated by nearly ~2x after exposure for 240h at 1316°C until the reaction of the SiO_2 TGO with Yb_2SiO_5 in the topcoat was accounted for. The stability of the TGO-topcoat interface should be taken into account to more accurately determine Si bond coat oxidation kinetics. This effect should be studied or at least accounted for in other EBC materials employing a Si bond coat. *(vii)* Similar oxidation kinetics and cracking-and-crystallization studies like that performed in Ch.5 of this dissertation should be performed for $Yb_2Si_2O_7$ topcoat + Si bond coat EBC systems in steam containing environments with and without Na_2SO_4. The phase of the TGO should be characterized using techniques including electron diffraction, Raman spectroscopy, an electron diffraction back scattered (EBSD). *(viii)* It was determined in Ch.5 of this dissertation that the TGOs several microns in thickness could be highly crack-free despite the β-to-α cristobalite inversion occurring. TGO cracking was observed for only the specimen exposed for 240h at 1316°C. To rule out the possibility that cracking did not occur from sample preparation, a sectioning and polishing study should be performed. A carefully planned auto-polishing + hand-polishing procedure coupled with precision sectioning should be performed to determine how much cracking in the TGO is attributed to sample preparation. *(ix)* A serious effort to determine the diffusion kinetics of O_2 and H_2O through an EBC topcoat should be performed. The effects of porosity volume content, porosity connectivity, grain size + shape, grain boundary density and crystallographic anisotropy of air plasma sprayed topcoats should be taken into account. Additionally, $^{18}O_2$ and $H_2{}^{18}O$ diffusion in single crystal and polycrystalline EBC materials at temperatures relevant for turbine engine service should also be performed to gather diffusion data as these data are lacking in literature.

Appendix A | Electron Beam Amorphization of Crystalline SiO_2

TEM imaging (Titan, FEI, Hillsboro, OR) and electron diffraction was performed to determine the morphology and crystal structure of thermally grown SiO_2 layers formed on SiC fibers (Ch.2) and between $Yb_2Si_2O_7$ topcoat and Si bond coat layers (Ch.5) after exposure to Na_2SO_4. As reported in these two dissertation chapters, crystalline SiO_2 TGOs formed on both SiC fibers and between the $Yb_2Si_2O_7$ topcoat and Si bond coat layers. During TEM imaging of these crystalline SiO_2 reaction layers though, it was observed that the crystalline reaction layers amorphized within seconds upon focusing the 300 kV electron beam onto the crystalline SiO_2 regions. The scale formed on Hi Nicalon amorphized completely, easily seen by the removal of the large grain and twinned regions seen in Figure A.1a) and A.1b). Hi magnification imaging of the α-cristobalite scale formed between the $Yb_2Si_2O_7$ top coat-Si bond coat which can be seen in Figure A.2a)-b) resulted in a circular amorphized region as a result of beam focusing. These results indicate that crystalline SiO_2 layers are highly sensitive to electron beam irradiation damage during TEM imaging, and make hi-magnification imaging and diffraction difficult.

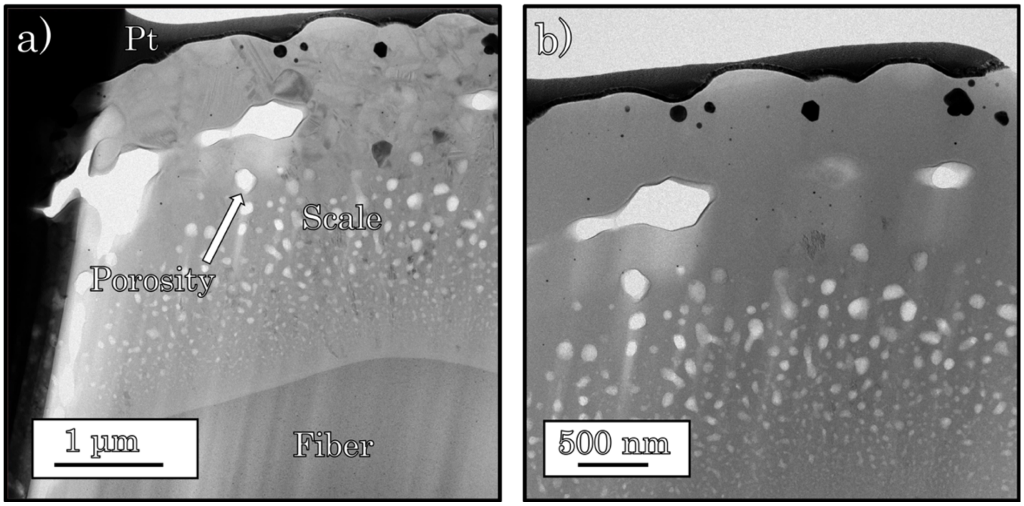

Figure A.1 TEM image of a Hi Nicalon fiber after exposure to ~60 µg/cm^2 of Na_2SO_4 for 24h at 1000°C in a gaseous 0.1% SO_2-O_2 environments a) before and b) after electron beam amorphization.

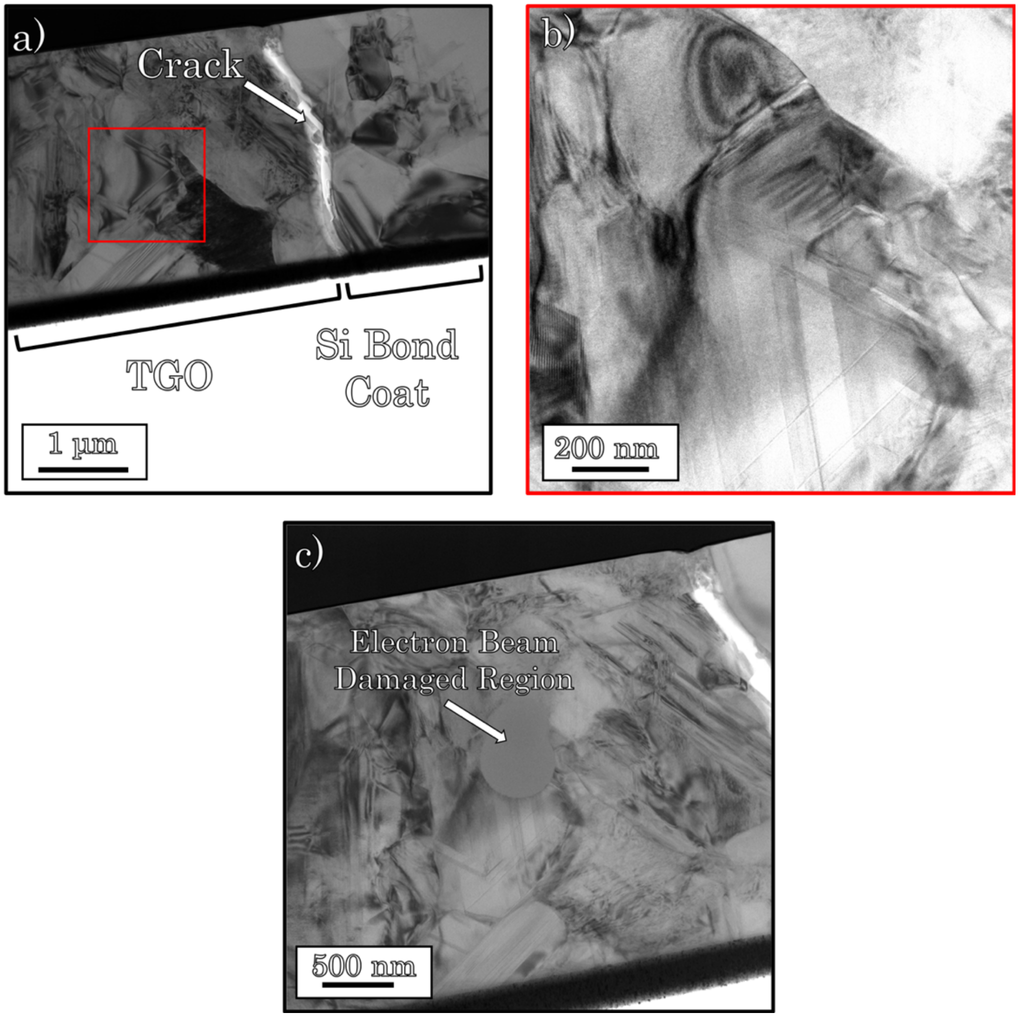

Figure A.2. a) TEM image of an α-cristobalite TGO formed between the $Yb_2Si_2O_7$ topcoat + Si bond coat after exposure to ~2.5 mg/cm^2 for 240h at 1316°C in a gaseous 0.1% SO_2-O_2 environment and b) higher magnification image outlined in red before and c) after electron beam amorphization.

Appendix B | Fiber Diameter Recession Measurements

Oxide thickness measurements (Figure 2.16) were used to assess the oxidation kinetics of SiC fibers after exposure to Na_2SO_4 in Ch.2. In addition to measuring oxide thickness, fiber diameter recession measurement was also employed to quantify oxidation kinetics, which can be seen in Figure B.1. These measurements were determined by measuring the fiber diameter using SEM images from fibers after exposure to ~60 $\mu g/cm^2$ of Na_2SO_4 between 0.75h-24h at 1000°C across ~20 fibers. Hi Nicalon experienced the most fiber recession after exposure for 24h and did not experience a kinetic plateau, which is consistent with behavior discussed in Ch.2. However, the fiber diameter recession behavior of Hi Nicalon S, Sylramic, and Sylramic iBN fibers is different than the oxidation behavior discussed in Ch. 2. Given the reported experimental uncertainty, it is difficult to conclude if Hi Nicalon S fibers exhibited a kinetic plateau, which was observed in oxide thickness measurements. Less than 500 nm of fiber diameter recession occurred for Sylramic and Sylramic iBN fibers up to 6h of exposure, while zero or negative fiber diameter recession occurred after exposure for 24h, indicating that these fibers possibly increased in thickness over time. These negative fiber diameter recession measurements present interpretational challenges.

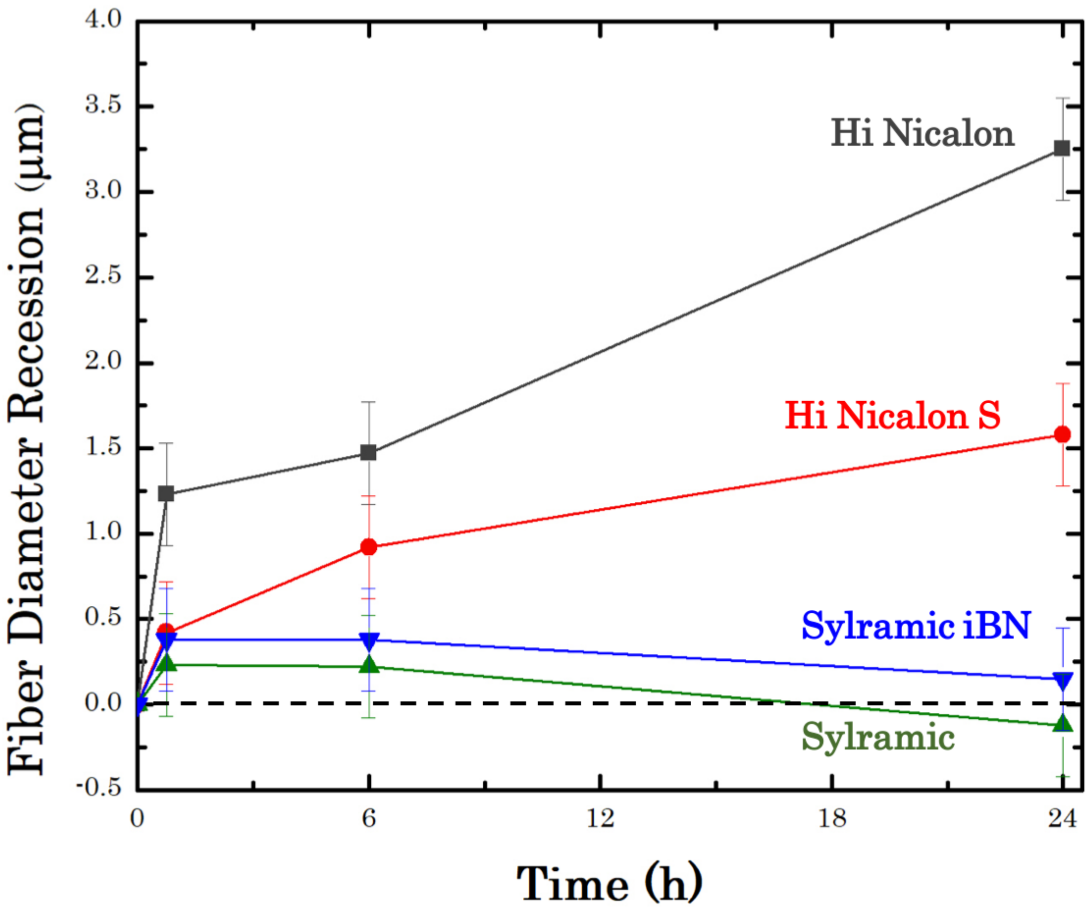

Figure B.1. Plot showing the fiber diameter recession for Hi Nicalon (dark gray) Hi Nicalon S(red), Sylramic(green), and Sylramic iBN(blue) after exposure to ~60 μg/cm^2 of Na_2SO_4 for 0.75h-24h at 1000°C in a gaseous 0.1% SO_2-O_2 environment.

Appendix C | Validation of ICP-OES Measurement of SiC Consumption

The composition of the reaction product formed on BN-coated Hexoloy (α-SiC) substrates after exposure to ~2.5 mg/cm^2 of Na_2SO_4 for times up to 144h at temperatures between 700°C-1100°C was measured using inductively coupled plasma optical emission spectroscopy (ICP-OES) in Ch.3 of this dissertation. Along with ICP-OES composition measurement of the thermally grown layer, bench-top weight change measurement was performed using an analytical balance. Specimens were weighed before and after salt loading, and then after high-temperature exposure. Specimens were then soaked in the two-step water and hydrofluoric acid digestion, and then weighed after removal from the digestion to determine total amount of SiC consumed during exposure. The Si levels of the corrosion products (sodium borosilicate + SiO_2) measured using ICP-OES, was converted to SiC consumed. The calculation was made assuming the SiC specimens tested possessed 1:1 C and Si stoichiometry. These values were calculated for both time and temperature dependent testing, and were compared to benchtop weight change values measured before salt loading and after removal of the corrosion products from digestion. As seen in the temperature dependent comparison plot in Figure C.1 and time dependent Figure C.2, there is only ~10% disagreement between ICP-OES and benchtop weight change measurements. This indicates that ICP-OES was able to accurately determine SiC consumption levels in the reaction product reported in Ch.3 of this dissertation.

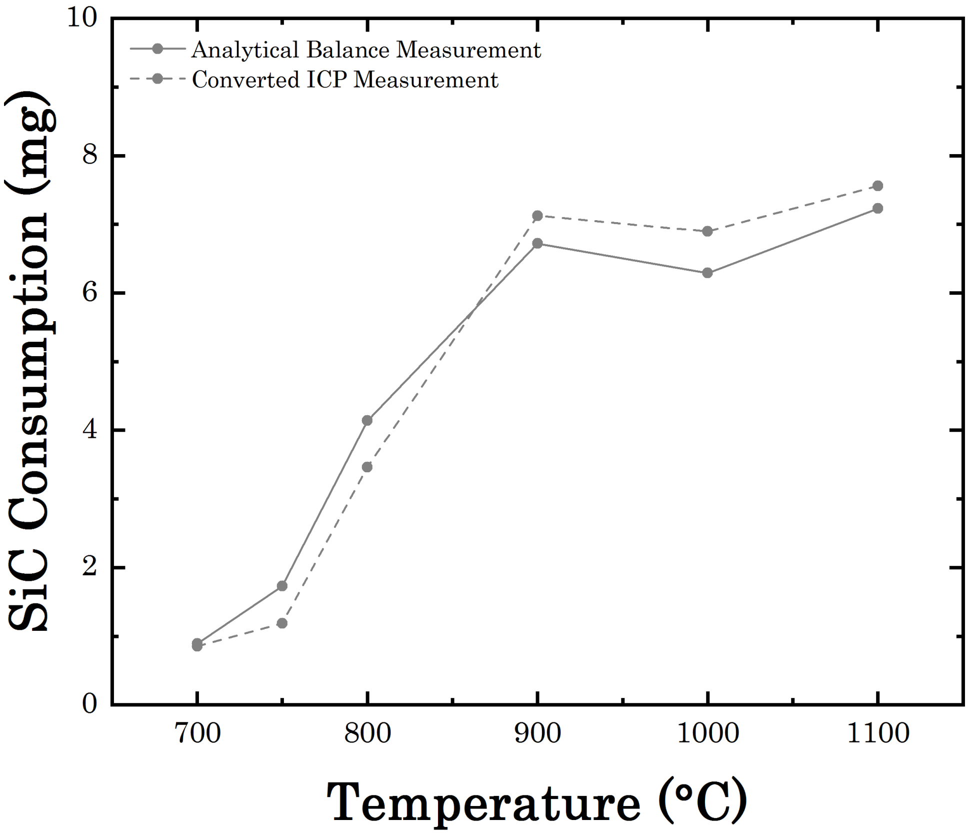

Figure C.1. Plot showing the amount of SiC consumed (in mg) determined from ICP-OES measurement (solid line) and benchtop weight change (dash) from specimens after exposure to ~2.5 mg/cm^2 of Na_2SO_4 for 24h at temperature between 700°C-1100°C in a gaseous 0.1% SO_2-O_2 environment.

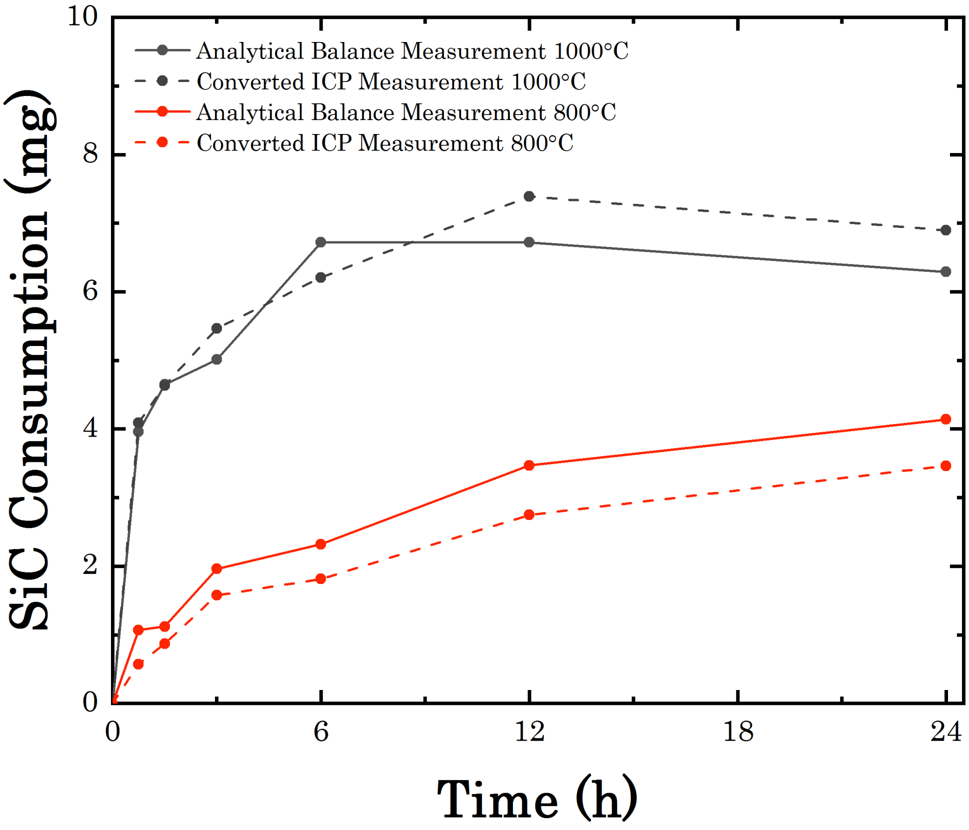

Figure C.2. Plot showing the amount of SiC consumed (in mg) determined from ICP-OES measurement (solid line) and benchtop weight change (dash) from specimens after exposure to ~2.5 mg/cm^2 of Na_2SO_4 for 0.75h-24h at 800°C (red) and 1000°C (dark grey) in a gaseous 0.1% SO_2-O_2 environment.

Appendix D | Phase Formation in $RE_2Si_2O_7$ + Na_2SO_4 and RE_2SiO_5 + Na_2SO_4 (RE + Y, Yb) Powder Mixtures Fired Between 900°C-1400°C in Air

Introduction

Other than the diffraction studies presented in Ch.4 of this dissertation, there currently lacks any phase relation studies in the Yb_2O_3-SiO_2-Na_2O ternary system. Synthesis of some ternary compounds have been reported in literature though.[1–3] Currently, the only phase relation study reported for all RE_2O_3-SiO_2-Na_2O (RE = rare earth) systems where RE includes all lanthanides, Y, and Sc, is for RE = Y.[4, 5] However, RE_2O_3-SiO_2-Na_2O compositions with 50 mol.% SiO_2 and higher were studied. Crystalline ternary compounds with melting temperatures above 1300°C were identified in the Y_2O_3-SiO_2-Na_2O system. This work found that multiple Y_2O_3-SiO_2-Na_2O compounds exist, and of most relevance to EBCs, is the reaction of Na_2O with the line compound $Y_2Si_2O_7$ to produce multiple ternary compounds. Due to the interest of rare earth silicates of the form RE_2SiO_5 and $RE_2Si_2O_7$ (RE = Y, Yb) as EBC materials, understanding their high temperature phase formation with Na_2SO_4 deposits is relevant.

Experimental

Powdered mixtures containing 2g of 5, 10, and 50 wt% high purity Na_2SO_4 balance $RE_2Si_2O_7$ or RE_2SiO_5 (RE = Y, Yb) were weighed using an analytical benchtop balance and subsequently mixed homogenously. These loose powder mixtures were placed inside of a Pt crucible which was placed inside of an Al_2O_3 support boat. High temperature firings were performed inside of a horizontal tube furnace, for times up to several hours to days at temperatures between 900°C-1400°C in air. All three (5, 10, and 50 wt% Na_2SO_4) mixtures were fired simultaneously at temperature. A high-purity fused quartz tube with OD 50mm and ID 47mm was used for testing. Upon completion of firing, the powder-filled Pt crucibles were removed from high temperature and then air quenched. These fired, powder mixtures were ground down using a mortar and pestle and phase analysis was subsequently performed to identify newly formed phases using x-ray diffraction (Empyrean, Panalytical, Netherlands). The phases identification was performed using HighScore software.

Results

Diffraction results from the $RE_2Si_2O_7$ + 5, 10 and 50 wt.% Na_2SO_4 mixtures (RE = Y, Yb) after firing can be seen in Figures D.1-D.6. The temperatures and subsequent firing times for each of these mixtures can be seen next to each diffraction pattern. The phase formation in all three of the mixtures $Yb_2Si_2O_7$ was relatively simple, as the only newly formed crystalline phase was Yb_2SiO_5. The strongest Yb_2SiO_5 diffraction peaks around ~30-31° 2θ can be seen outlined in the dashed red box in Figures D.1-D.3. These outlined Yb_2SiO_5 peaks are most noticeable in all mixtures at exposures temperatures of 1100°C and higher, indicating Yb_2SiO_5 formation occurs faster at higher temperature. No ternary Yb_2O_3-SiO_2-Na_2O reaction products formed across the entire testing range. There are a series of strong crystalline Na_2SO_4 peaks centered at ~32° 2θ in the 50 wt% mixture seen in Figure D.3. These strong Na_2SO_4 peaks are presumably a result of Na_2SO_4 crystallization into two different polymorphs (T_m=884°C) upon quenching. Na_2SO_4 was not present in the 5 and 10 wt.% mixtures presumably due to a combination of volatilization, amorphous phase formation, or existing below the detection limits of XRD (~5 vol.%). As already discussed in Ch. 4 of this dissertation, Yb_2SiO_5 formation occurred due to SiO_2 removal from $Yb_2Si_2O_7$, leading to the formation of a sodium silicate phase which is expressed in Equation (D.1):

$$Yb_2Si_2O_7 + Na_2SO_4 \rightarrow Yb_2SiO_5 + Na_2SiO_3 + SO_3(g) \qquad (D.1)$$

Due the low-melting temperature of the sodium silicate, crystalline sodium silicate is not detected. Furthermore, due to sluggish reaction kinetics

Yb_2SiO_5 XRD signal is too weak to measure at temperatures below 1100°C. Yb_2SiO_5 formation below 1100°C is likely even though it was not observed.

The diffraction results for the $Y_2Si_2O_7$ + 5, 10, and 50 wt% Na_2SO_4 mixture firings can be seen in Figures D.4-D.6. Unlike the reaction of Na_2SO_4 with $Yb_2Si_2O_7$, which only formed Yb_2SiO_5, the reaction of Na_2SO_4 with $Y_2Si_2O_7$ is more complicated as $Y_2Si_2O_7$, Y_2O_3-SiO_2-Na_2O crystalline compounds, and Na_2SO_4 were detected across the three mixtures and temperature range, which can be seen in Figured D.4-D.6. Due to these large number of phases, reference pattern matching like that seen in Figures D.1-D.3 is difficult to visualize due to the large number of peaks and peak overlap. The phases formed in $Y_2Si_2O_7$ + 5, 10, and 50 wt.% Na_2SO_4 mixtures after firing are listed in Table D.1 for further convenience. A main distinction between the reaction of Na_2SO_4 with $Y_2Si_2O_7$, is that unlike the reaction with $Yb_2Si_2O_7$, crystalline Y_2O_3-SiO_2-Na_2O reaction products, namely $NaY_9Si_6O_{26}$, $NaY_3Si_2O_7$, and $NaYSi_2O_6$ are produced. Across the entire mixture range, the main reaction products are $NaY_9Si_6O_{26}$ and $NaYSi_2O_6$. However, a $NaY_3Si_2O_7$ reaction product formed after exposure of a 50 wt.% Na_2SO_4 mixture at 1400°C. Na_2SO_4 is only detected in the 50 wt.% mixture, presumably due to volatilization + low phase content in the lower Na_2SO_4-containing mixtures.

Diffraction patterns for the RE_2SiO_5 + 5, 10 and 50 wt.% Na_2SO_4 (RE = Y, Yb- mixtures after firing can be seen in Figures D.7-D.12. The temperatures and associated firing times can be seen next to each diffraction pattern. Unlike the $RE_2Si_2O_7$ (RE = Y,Yb) firings, reaction of Na_2SO_4 with both RE_2SiO_5 (RE = Y,Yb) produced no new crystalline phases across the entire testing range. This indicates that both Yb_2SiO_5 and Y_2SiO_5 are either unreactive with Na_2SO_4, or have sluggish reaction kinetics producing a reaction product whose phase content is below the detection limits of XRD. Due to the stability of RE_2SiO_5 (RE = Y, Yb) with Na_2SO_4, no chemical reaction equation can be written. Lastly, just like in the $RE_2Si_2O_7$ + Na_2SO_4

mixtures, crystalline Na_2SO_4 was detected only in the 50 wt.% mixture, as Na_2SO_4 was not present in the 5 and 10 wt.% mixtures.

	900°C	1100°C	1200°C	1300°C	1400°C
$Y_2Si_2O_7$ + 5 wt. % Na_2SO_4	Na_2SO_4 $Y_2Si_2O_7$	$NaY_9Si_6O_{26}$ $NaYSi_2O_6$ $Y_2Si_2O_7$	$NaY_9Si_6O_{26}$ $NaYSi_2O_6$ $Y_2Si_2O_7$	$NaY_9Si_6O_{26}$ $Y_2Si_2O_7$	$NaY_9Si_6O_{26}$
$Y_2Si_2O_7$ + 10 wt. % Na_2SO_4	$Y_2Si_2O_7$ Na_2SO_4	$NaY_9Si_6O_{26}$ $NaYSi_2O_6$ $Y_2Si_2O_7$	$NaY_9Si_6O_{26}$ $NaYSi_2O_6$ $Y_2Si_2O_7$	$NaY_9Si_6O_{26}$ $Y_2Si_2O_7$	$NaY_9Si_6O_{26}$ $Y_2Si_2O_7$
$Y_2Si_2O_7$ + 50 wt. % Na_2SO_4	$Y_2Si_2O_7$ Na_2SO_4	$NaY_9Si_6O_{26}$ $NaYSi_2O_6$ Na_2SO_4 $Y_2Si_2O_7$	$NaY_9Si_6O_{26}$ $NaYSi_2O_6$ Na_2SO_4 $Y_2Si_2O_7$	$NaY_9Si_6O_{26}$ Na_2SO_4	$NaY_9Si_6O_{26}$ $NaY_3Si_2O_7$ Na_2SO_4

Table D.1. List of phases formed from $Y_2Si_2O_7$ + 5, 10, and 50 wt.% Na_2SO_4 mixtures after firing for various times at temperature between 900°C-1400°C in air.

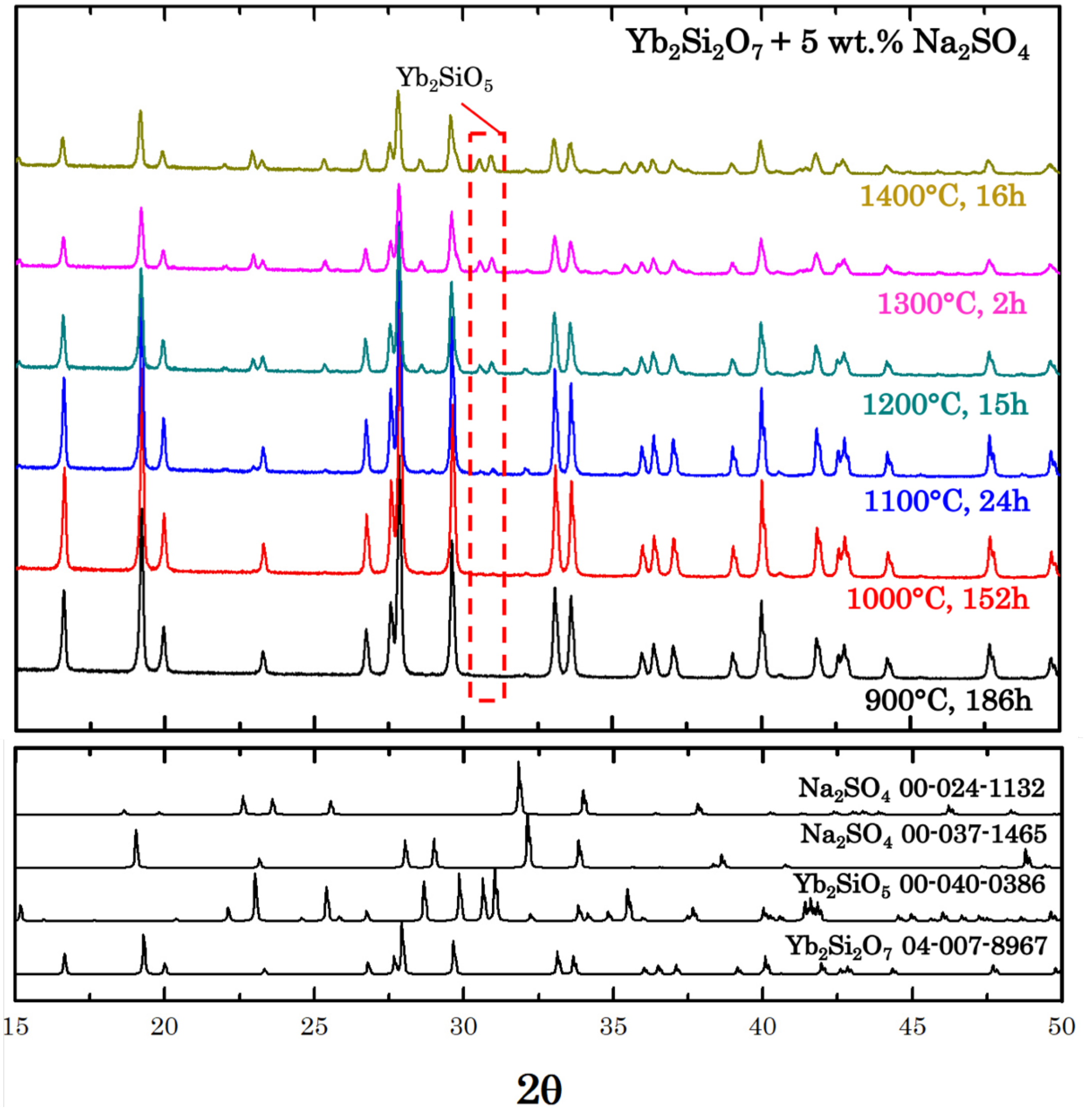

Figure D.1. Diffraction patterns of powdered $Yb_2Si_2O_7$ + 5 wt% Na_2SO_4 mixture after exposure for various times between 900°C-1400°C in air.

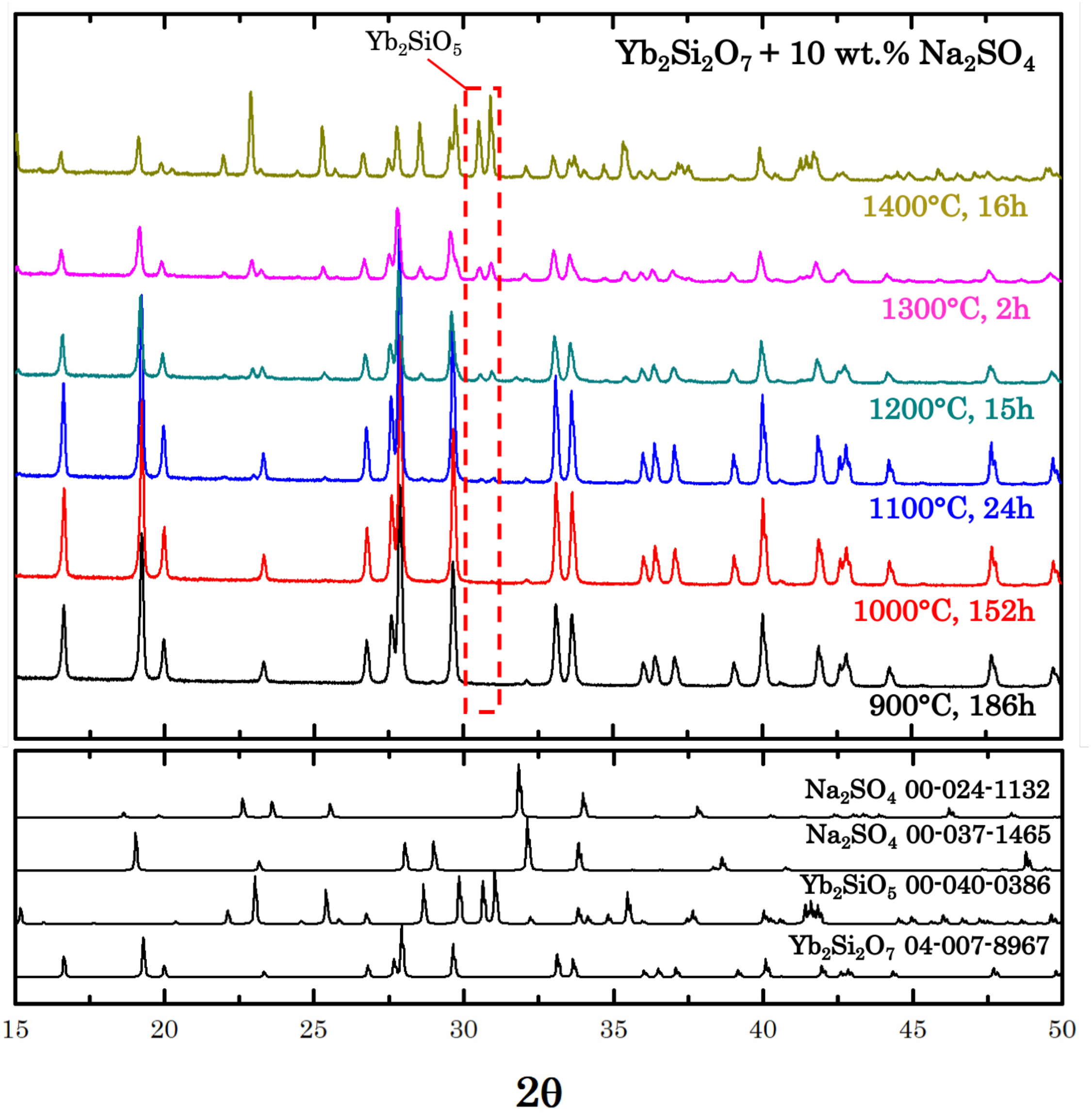

Figure D.2. Diffraction patterns of powdered $Yb_2Si_2O_7$ + 10 wt% Na_2SO_4 mixture after exposure for various times between 900°C-1400°C in air.

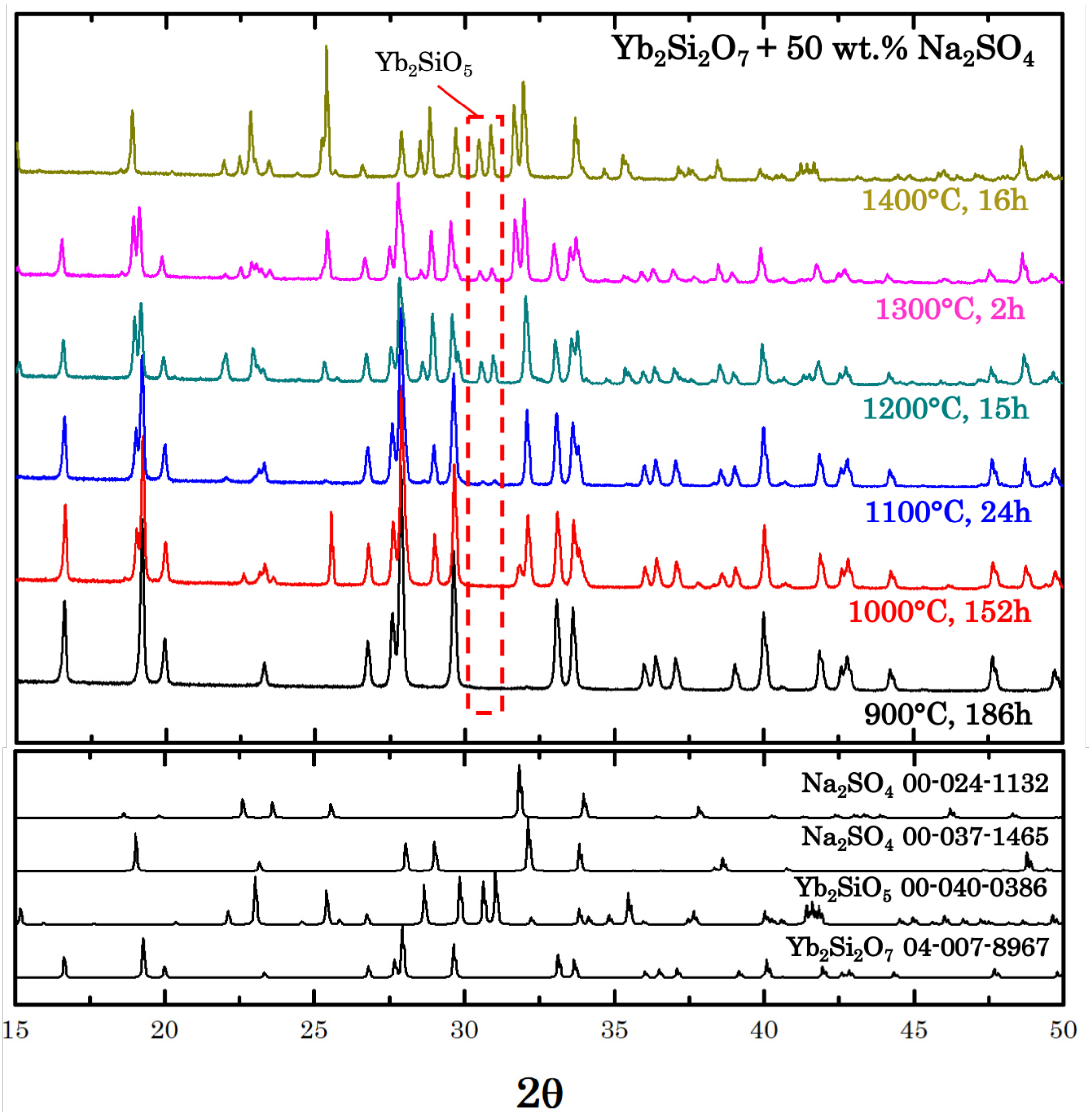

Figure D.3. Diffraction patterns of powdered $Yb_2Si_2O_7$ + 50 wt% Na_2SO_4 mixture after exposure for various times between 900°C-1400°C in air.

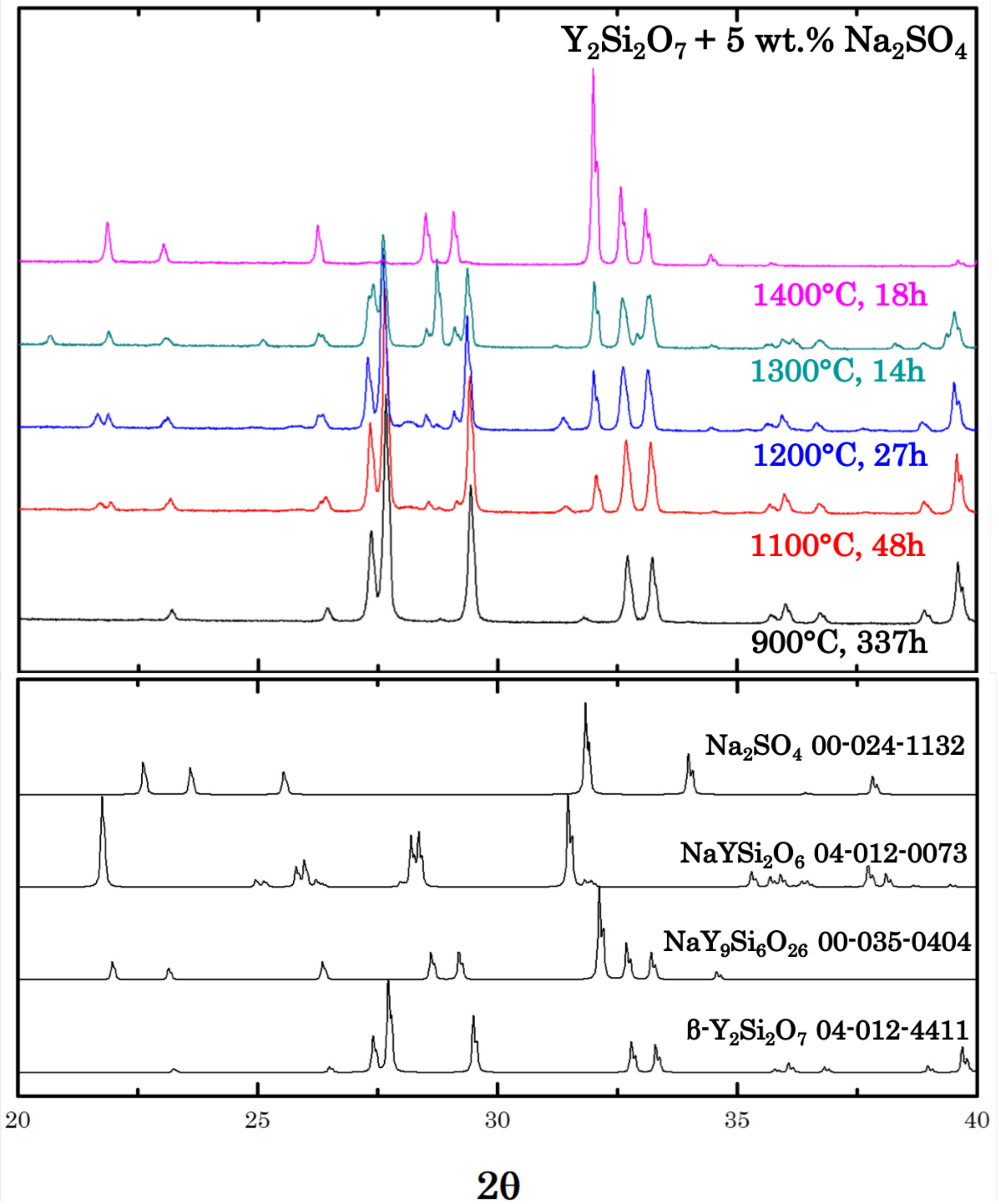

Figure D.4. Diffraction patterns of powdered $Y_2Si_2O_7$ + 5 wt% Na_2SO_4 mixture after exposure for various times between 900°C-1400°C in air.

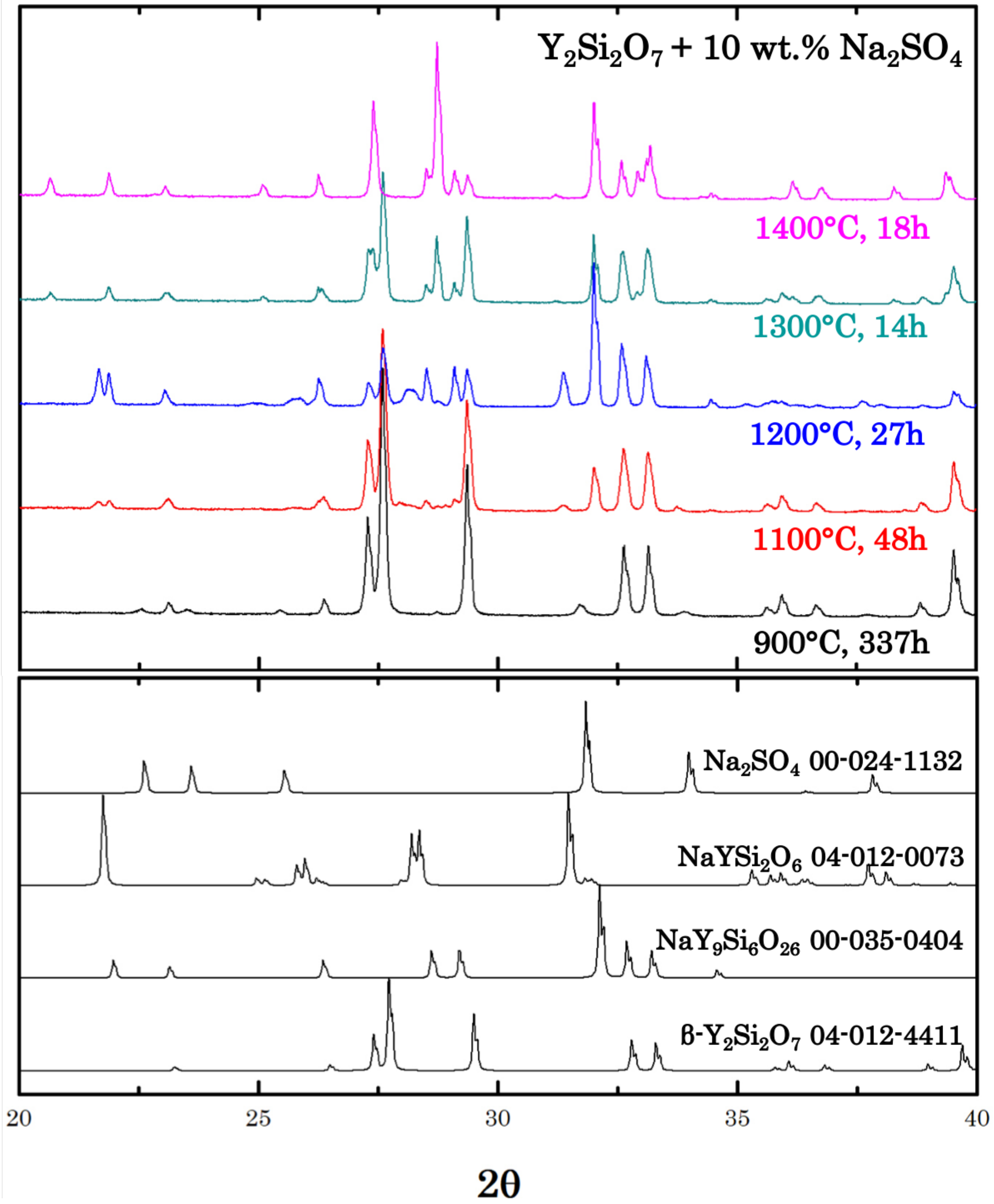

Figure D.5. Diffraction patterns of powdered $Y_2Si_2O_7$ + 10 wt% Na_2SO_4 mixture after exposure for various times between 900°C-1400°C in air.

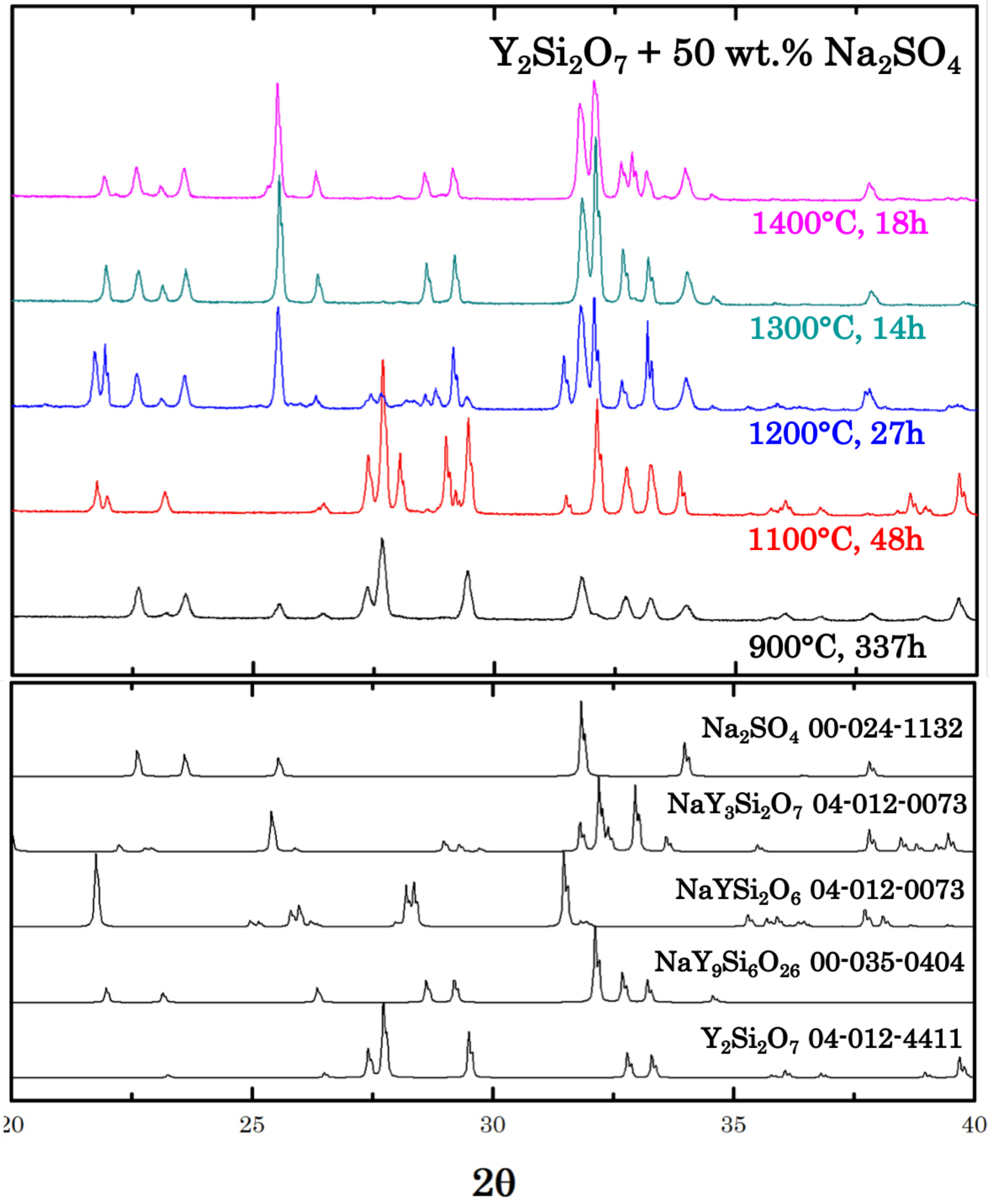

Figure D.6. Diffraction patterns of powdered $Y_2Si_2O_7$ + 50 wt% Na_2SO_4 mixture after exposure for various times between 900°C-1400°C in air.

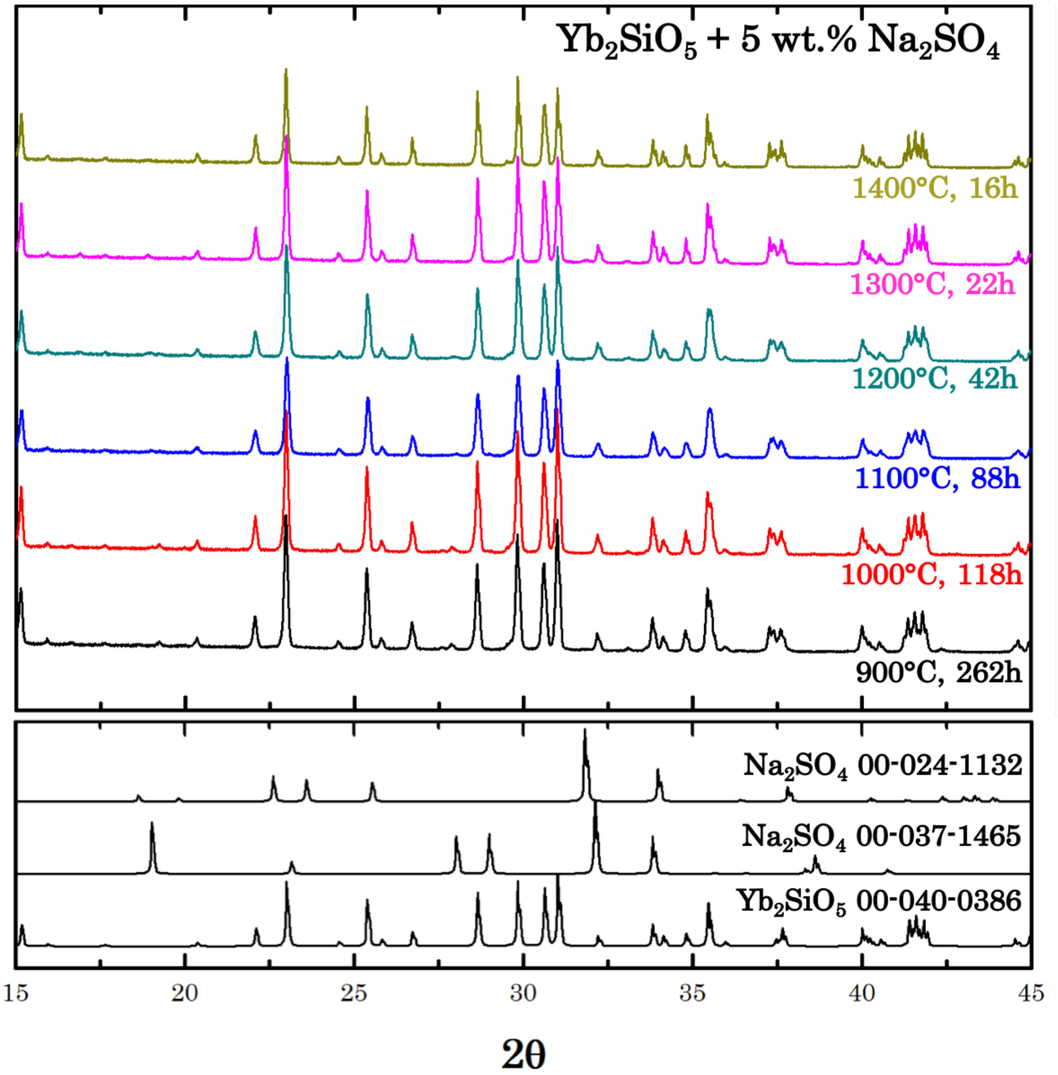

Figure D.7. Diffraction patterns of powdered Yb_2SiO_5 + 5 wt% Na_2SO_4 mixture after exposure for various times between 900°C-1400°C in air.

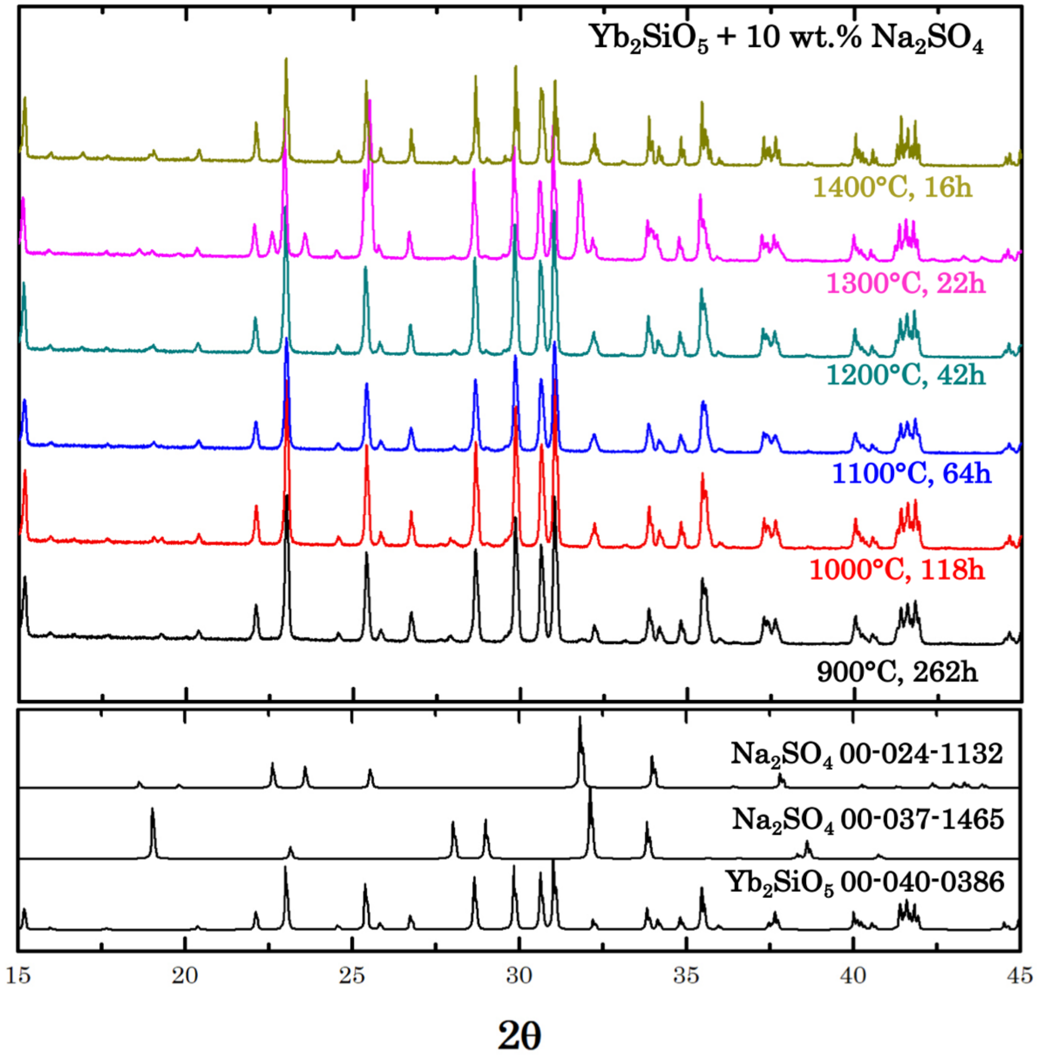

Figure D.8. Diffraction patterns of powdered Yb_2SiO_5 + 10 wt% Na_2SO_4 mixture after exposure for various times between 900°C-1400°C in air.

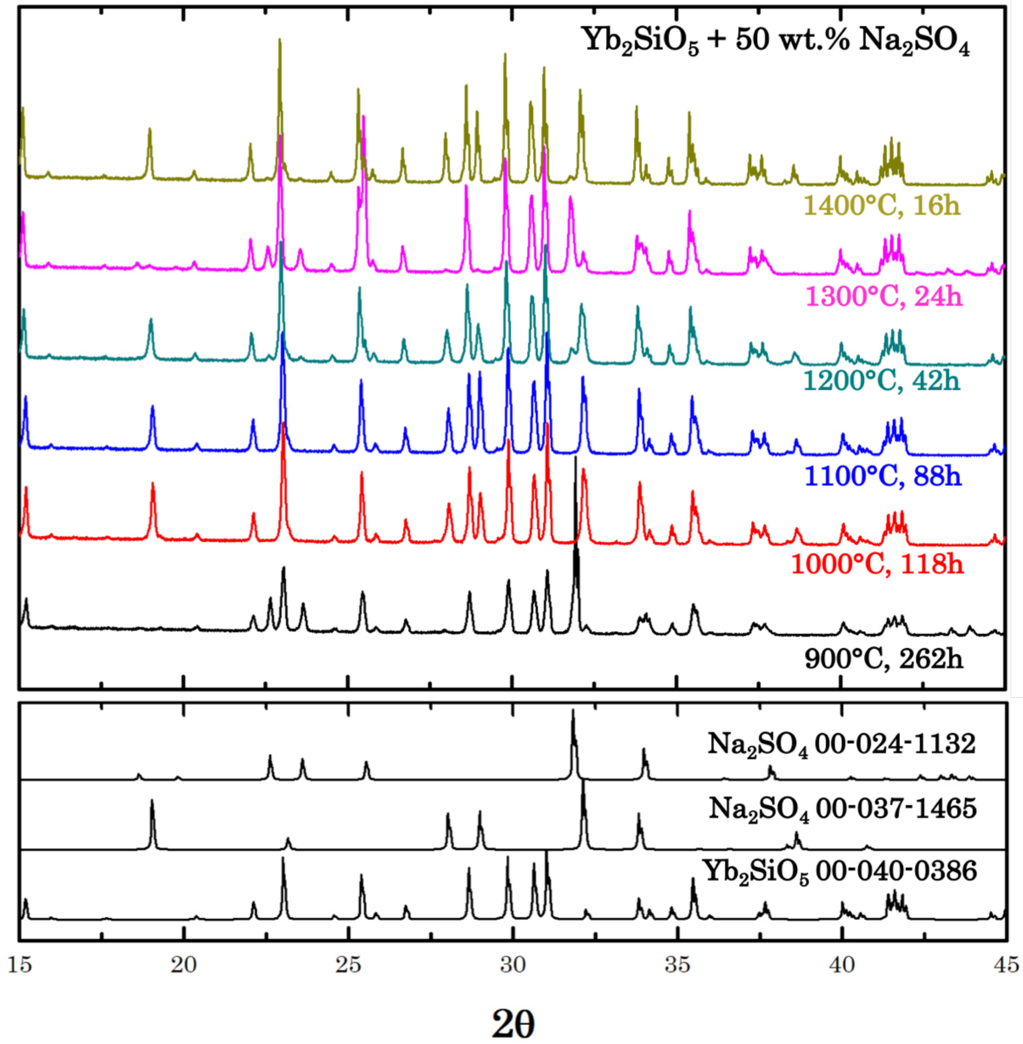

Figure D.9. Diffraction patterns of powdered Yb_2SiO_5 + 50 wt% Na_2SO_4 mixture after exposure for various times between 900°C-1400°C in air.

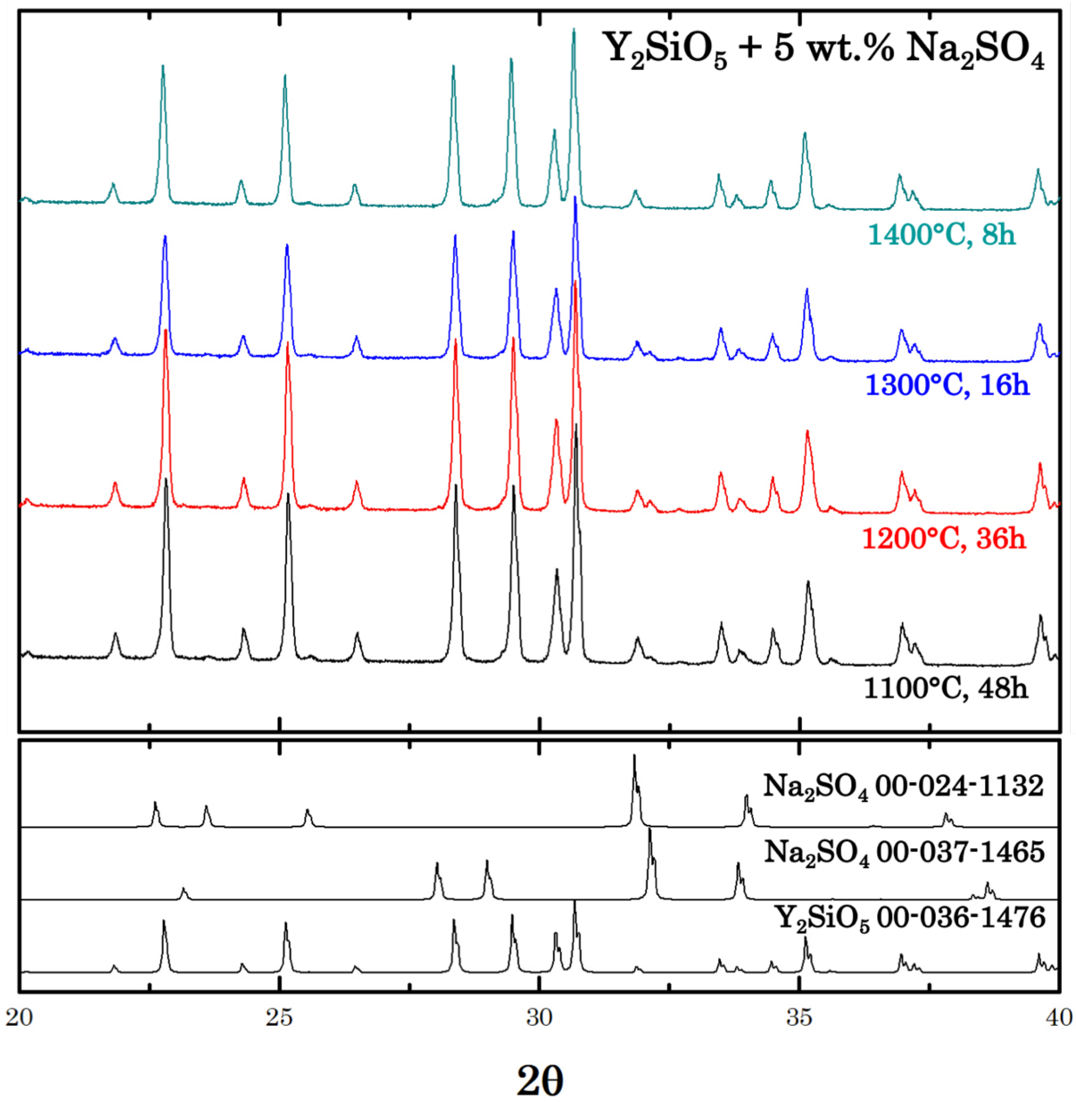

Figure D.10. Diffraction patterns of powdered Y_2SiO_5 + 5 wt% Na_2SO_4 mixture after exposure for various times between 1100°C-1400°C in air.

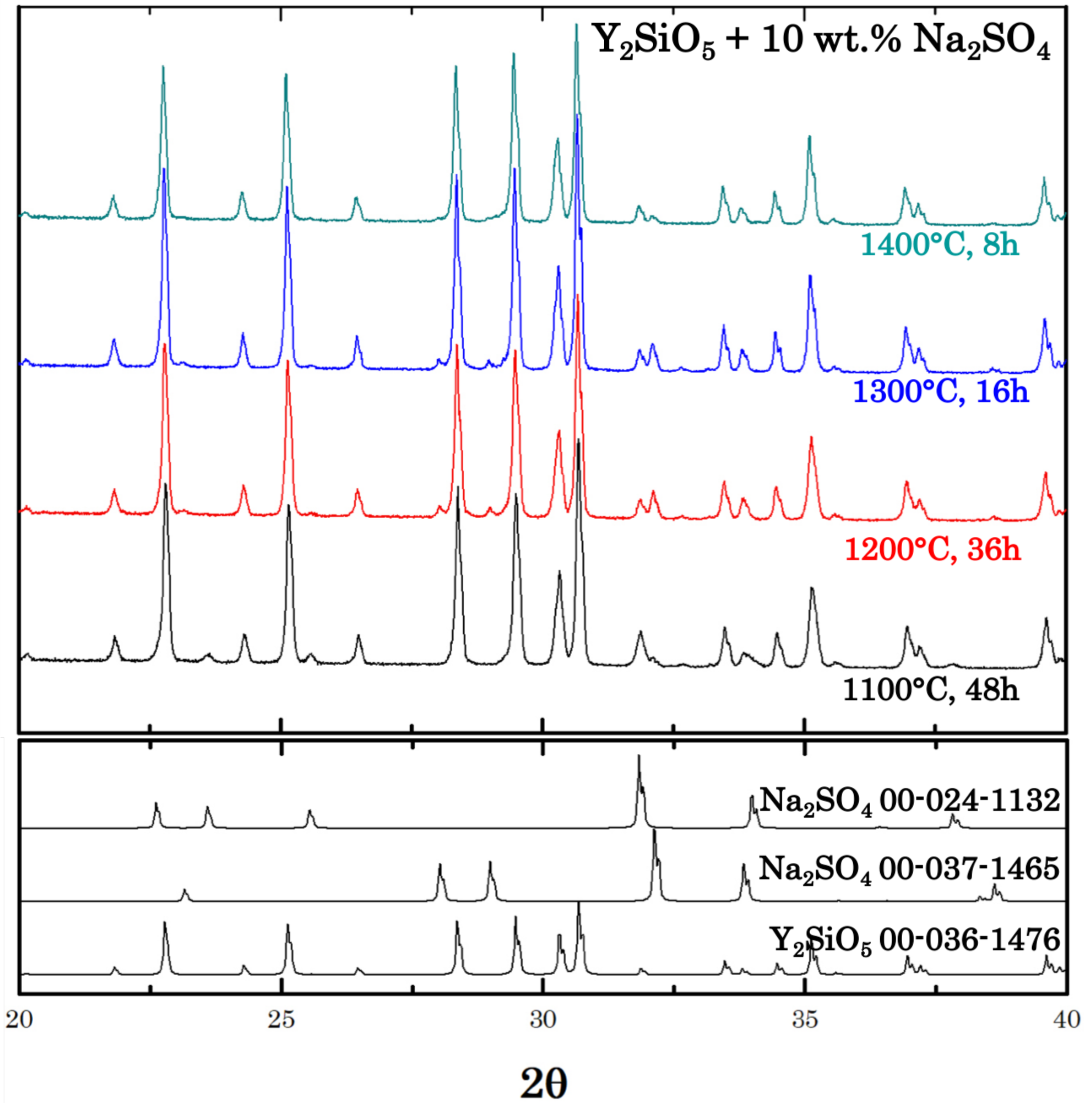

Figure D.11. Diffraction patterns of powdered Y_2SiO_5 + 10 wt% Na_2SO_4 mixture after exposure for various times between 1100°C-1400°C in air.

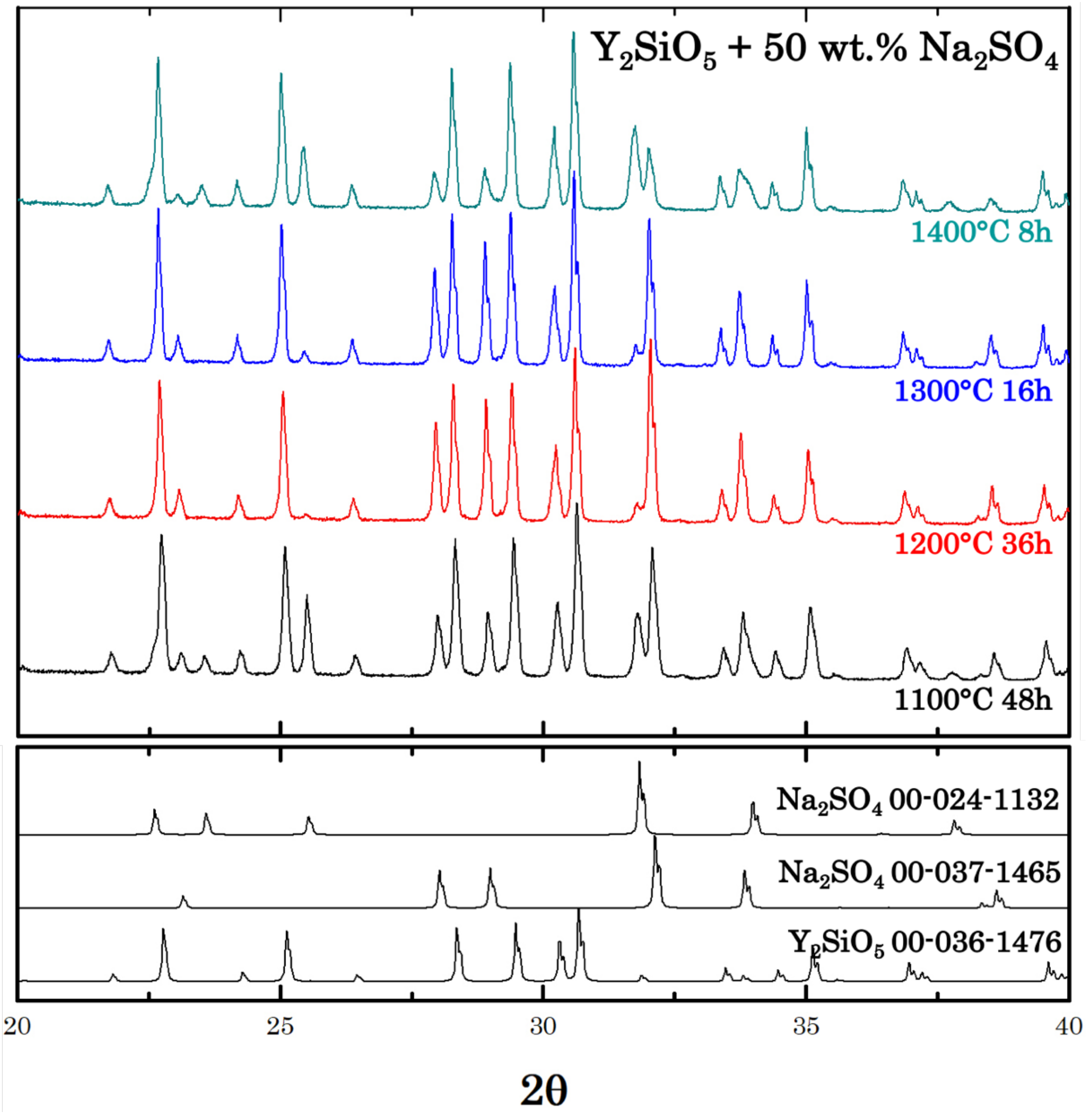

Figure D.12. Diffraction patterns of powdered Y_2SiO_5 + 50 wt% Na_2SO_4 mixture after exposure for various times between 1100°C-1400°C in air.

References

1. Latshaw AM, Wilkins BO, Chance WM, Smith MD, Loye H-C zur. Influence of rare earth cation size on the crystal structure in rare earth silicates, Na_2RESiO_4 (RE = Sc, Yb) and $NaRESiO_4$ (RE = La, Yb). *Solid State Sci*. 2016;51:59 – 65.
2. Latshaw AM, Yeon J, Smith MD, Loye H-C zur. Synthesis, structure, and polymorphism of $A_3LnSi_2O_7$ (A=Na, K; Ln=Sm, Ho, Yb). *J Solid State Chem*. 2016;235:100 – 106.
3. Felsche J. Rare earth silicates with the apatite structure. *J Solid State Chem*. 1972;5(2):266 – 275.
4. Lee FC, Marr J, Gunawardane RP, Glasser F. Phase relations at liquidus temperatures in the Na_2O-Y_2O_3-SiO_2 system. 1991;90:8–11.
5. Lee FC, Marr J, Glasser FP. Compounds in the Na_2O-Y_2O_3-SiO_2 system. *Ceram Int*. 1981;7(2):43–47.

Appendix E | Description of ImageJ Analysis Calculation for Determination of Yb_2SiO_5 Volume Content Within $Yb_2Si_2O_7$ Topcoats

This appendix explains how the Yb_2SiO_5 content, reported in Figure 4.13 of Ch.4 of this dissertation, within $Yb_2Si_2O_7$ topcoats measured over time was quantified using ImageJ. A step-by-step explanation can be seen below:

Sample Prep

1) Before Yb_2SiO_5 content in the topcoat could be determined, a polished cross-section of specimens was first made. A surface finish with the final polishing step down to a 0.250 μm diameter polishing suspension was sufficient.

Image

2) An SEM image taken with a backscattered (BSE) detector using the highest possible resolution settings was used. Backscattered imaging allows for excellent Yb_2SiO_5 contrast within the topcoat. An image of the entire topcoat with the scale bar included and with the highest possible resolution settings was taken.

Software Analysis

3) After taking high resolution SEM images of the entire topcoat, the Yb_2SiO_5 content in the topcoat was performed using ImageJ software analysis. The micrograph of interest was opened in ImageJ software under File → Open.

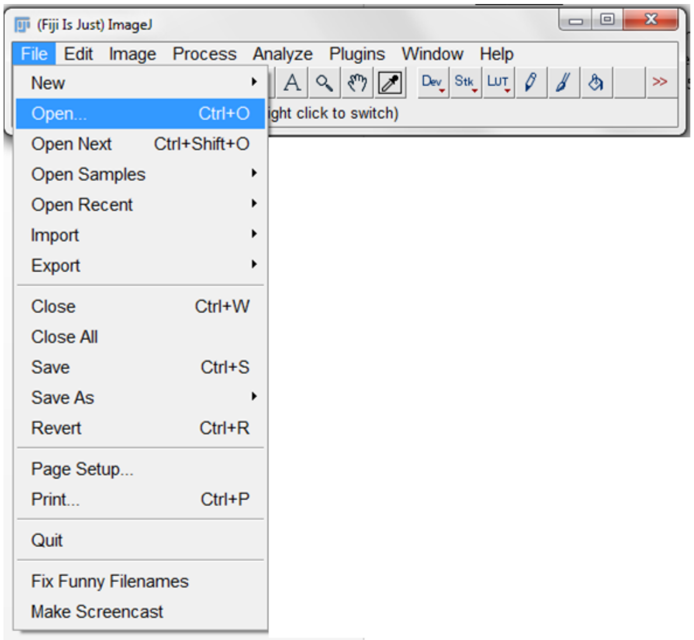

4) Once the SEM image was opened, the line tool calibrated the number of pixels per length in the micrograph (This is why a scale bar is needed). Left-click on the icon and then align the marker line to be the exact length of the scale bar. Shift was held while dragging the mouse to ensure the line only lengthened along one-dimension.

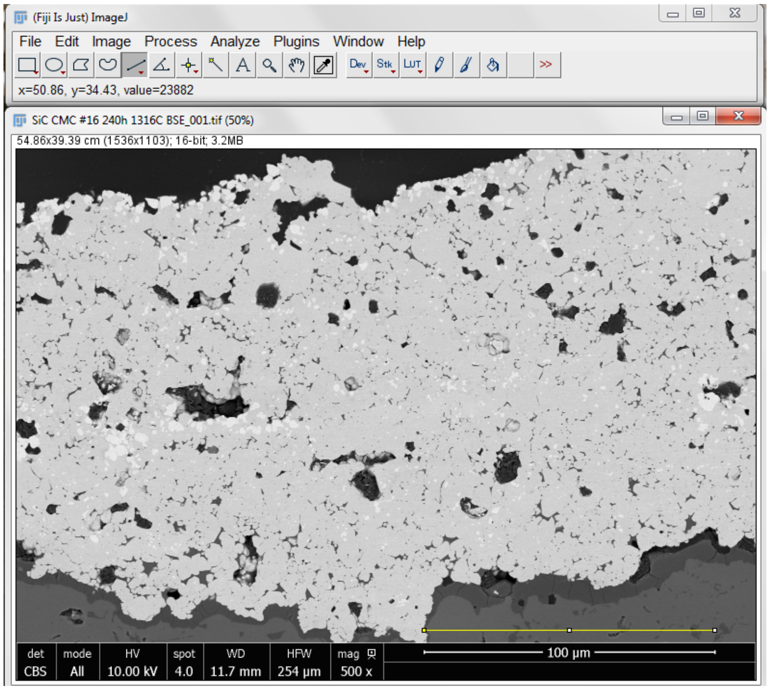

x=50.86, y=34.43, value=23882

54.86x39.39 cm (1536x1103); 16-bit; 3.2MB

5) Once the line icon was the exact length of the scale bar on the micrograph, the number of pixels per length of the line to the length of the scale bar was calibrated after clicking Analyze → Set Scale. The length of the scale bar was entered into “Known distance” and the units of the scale bar were entered into “Unit of length”.

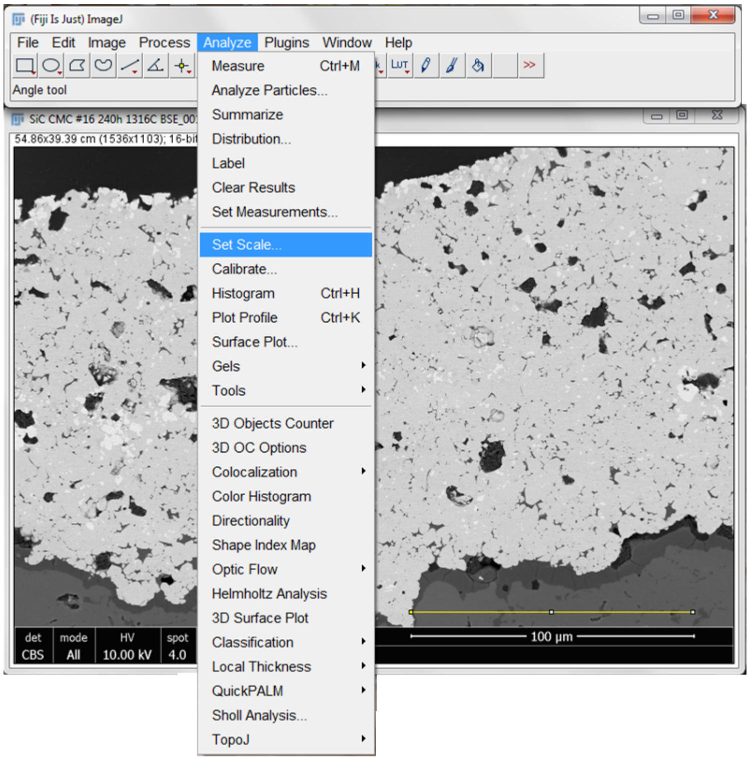

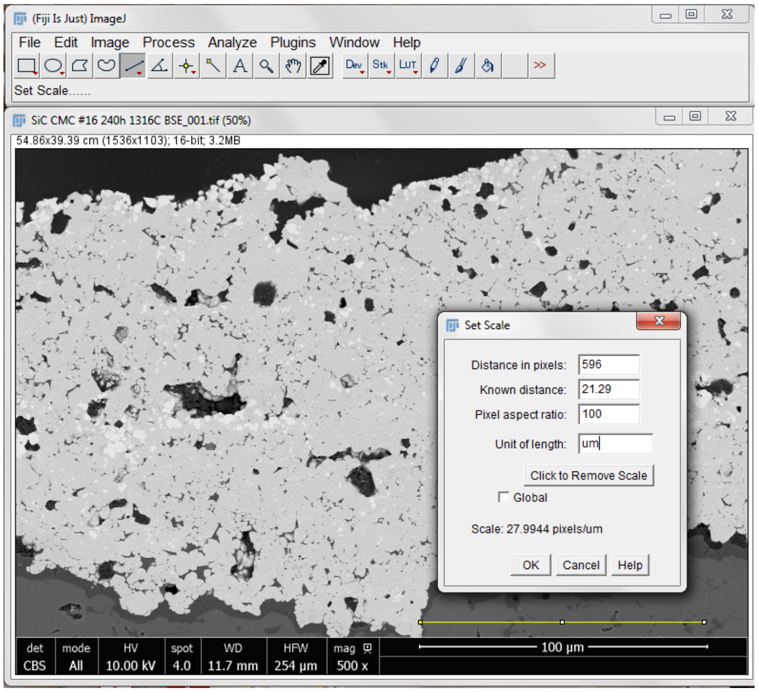

Set Scale......

SiC CMC #16 240h 1316C BSE_001.tif (50%)

54.86x39.39 cm (1536x1103); 16-bit; 3.2MB

Distance in pixels: 596
Known distance: 21.29
Pixel aspect ratio: 100
Unit of length: um
☐ Global
Scale: 27.9944 pixels/um

det	mode	HV	spot	WD	HFW	mag
CBS	All	10.00 kV	4.0	11.7 mm	254 µm	500 x

100 µm

6) Once the values were entered, Analyze →Measure was selected (Ctrl + M on the keyboard works as well). The length reported in this table was the same "Known distance" value entered or the scale bar length.

7) The square icon was selected and a box was placed around the coating system in the SEM image. Image → Crop was selected, and the area outside of the box was cropped out.

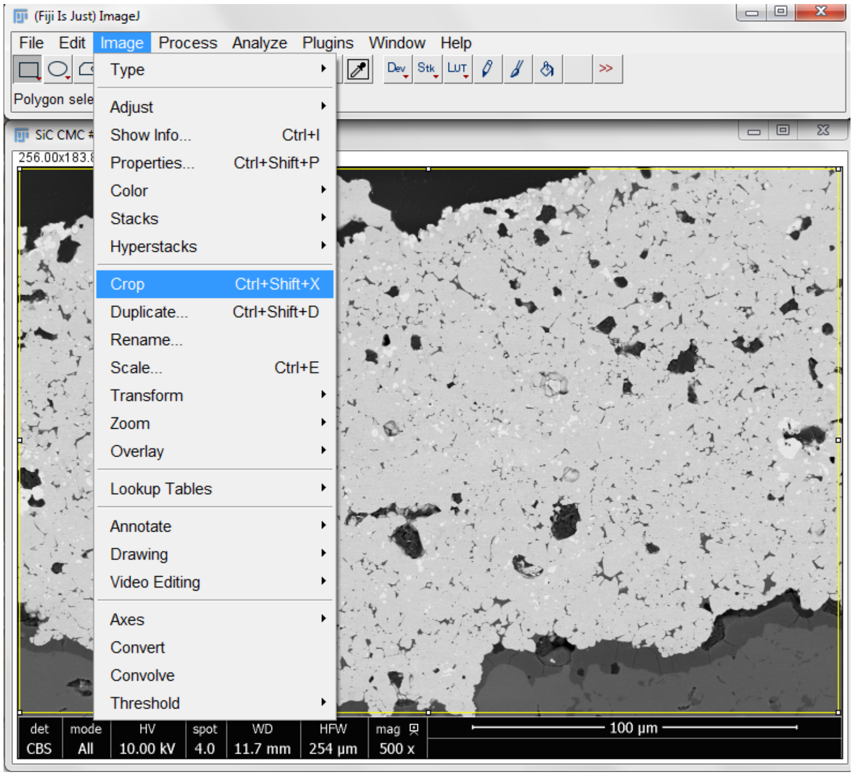

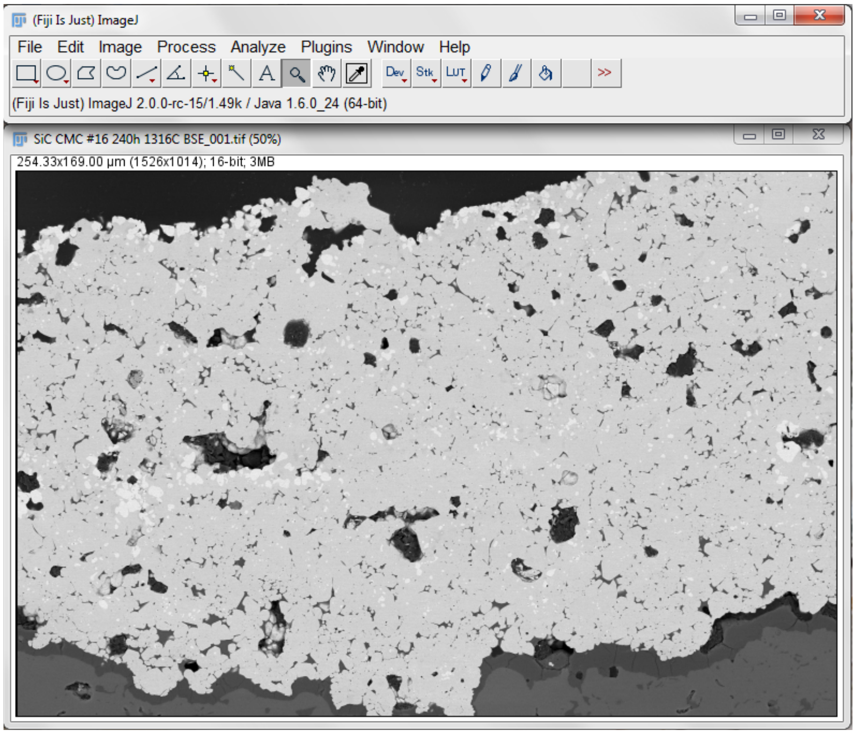

(Fiji Is Just) ImageJ 2.0.0-rc-15/1.49k / Java 1.6.0_24 (64-bit)

SiC CMC #16 240h 1316C BSE_001.tif (50%)

254.33x169.00 µm (1526x1014); 16-bit; 3MB

8) After the image was cropped, the Yb_2SiO_5 measurement can be made. The image was converted to an 8-bit format under Image → Type → 8-bit. This converts the image to an 8-bit format, which can be contrast thresholded to include only Yb_2SiO_5

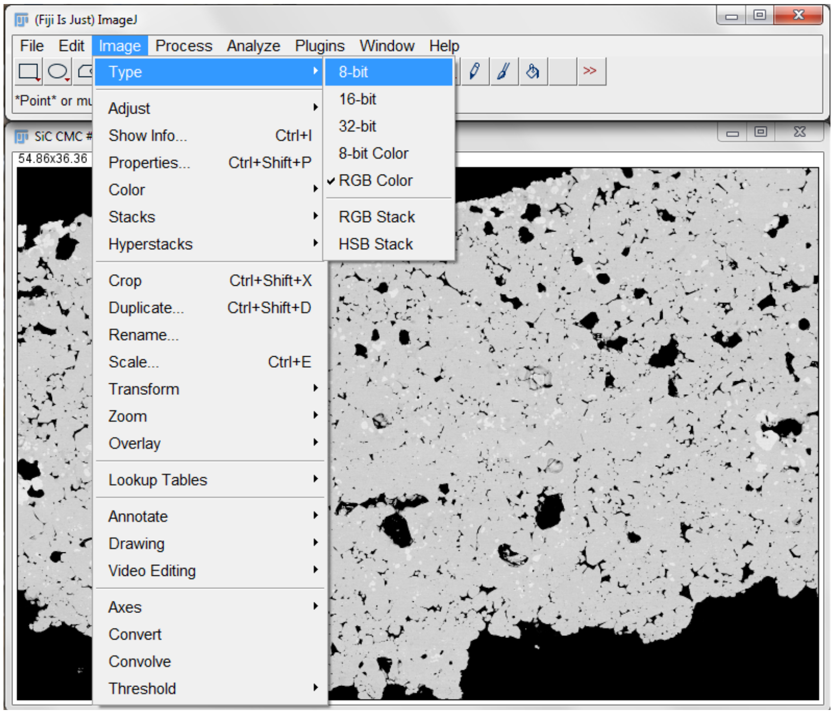

9) Image → Adjust → Threshold was selected. This allows only for Yb_2SiO_5 grains within the topcoat to be selected for quantification.

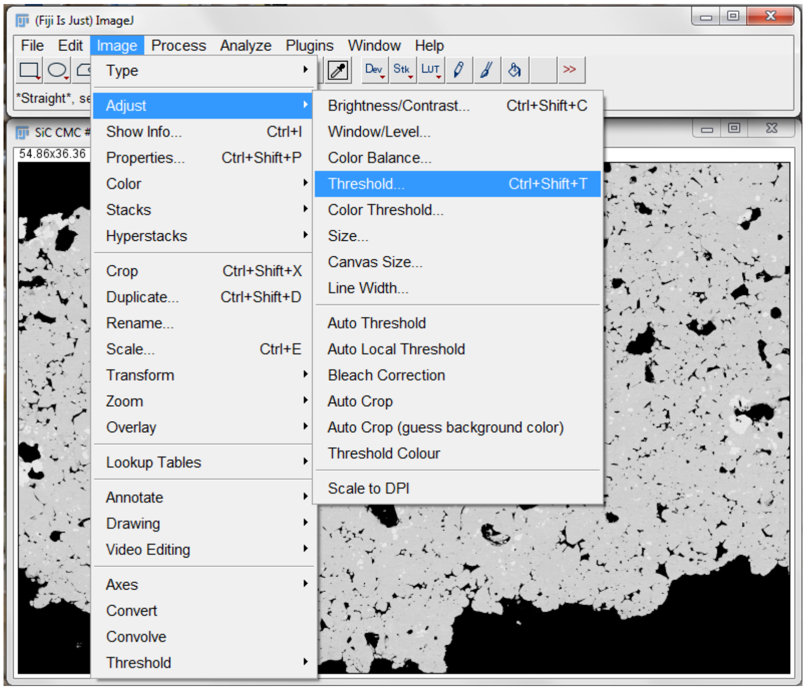

10) Once the “Threshold” side-window opens, Yb_2SiO_5 phase content within the topcoat was analyzable. Within the “Threshold” icon are two sliding bars, each which can be adjusted between a value of 0-255. The top sliding bar was adjusted until only the Yb_2SiO_5 grains in the topcoat were isolated. After an acceptable value was selected, the Yb_2SiO_5 content was measured (Ctrl + M). The Yb_2SiO_5 content (in area) value is reported in the results table under the area column.

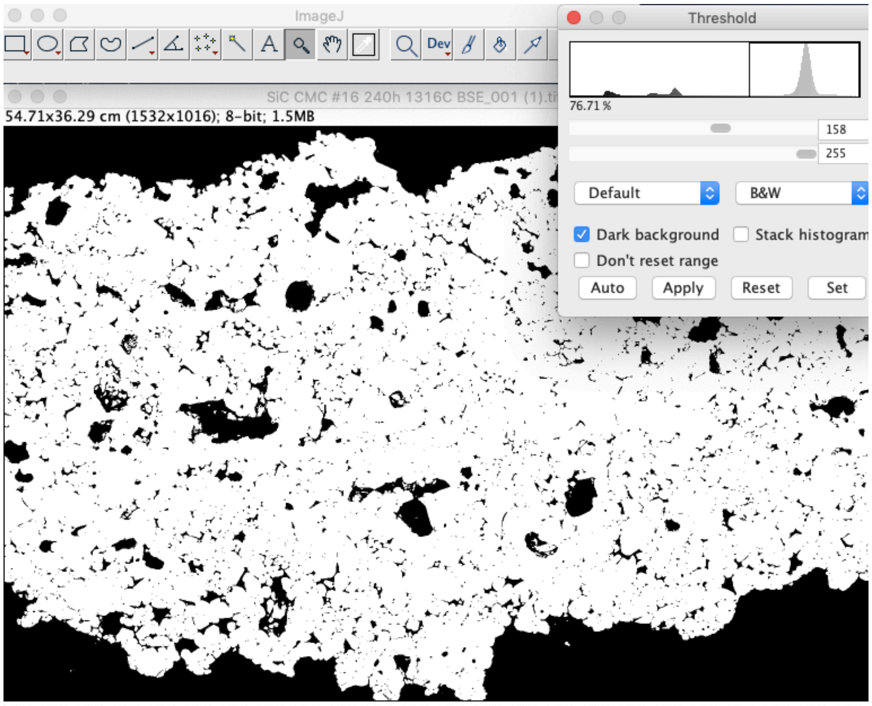

SiC CMC #16 240h 1316C BSE_001 (1).ti

54.71x36.29 cm (1532x1016); 8-bit; 1.5MB

76.71 %

158

255

Default

B&W

☑ Dark background

☐ Stack histogram

☐ Don't reset range

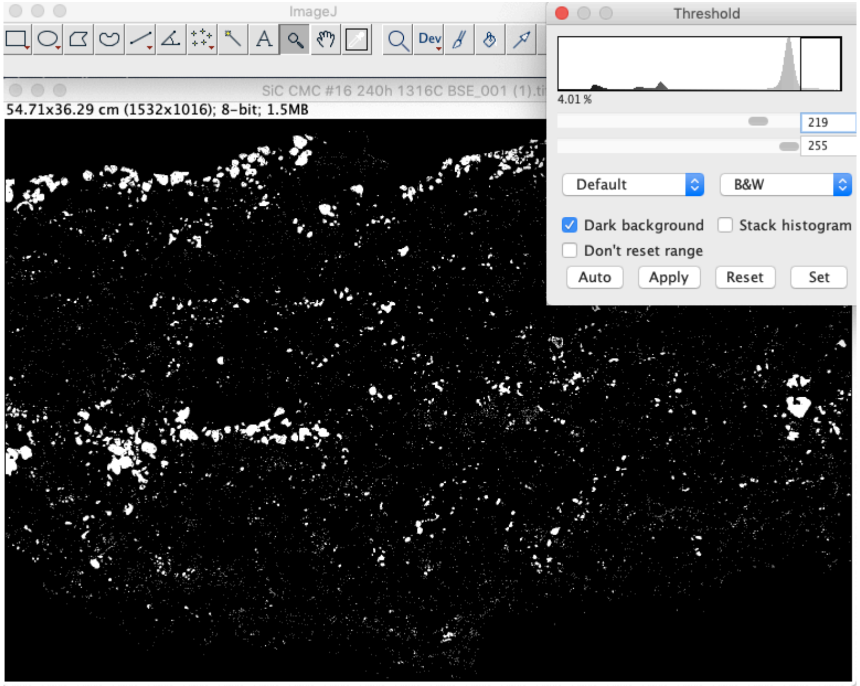

SiC CMC #16 240h 1316C BSE_001 (1).ti

54.71x36.29 cm (1532x1016); 8-bit; 1.5MB

4.01 %

219

255

Default

B&W

☑ Dark background

☐ Stack histogram

☐ Don't reset range

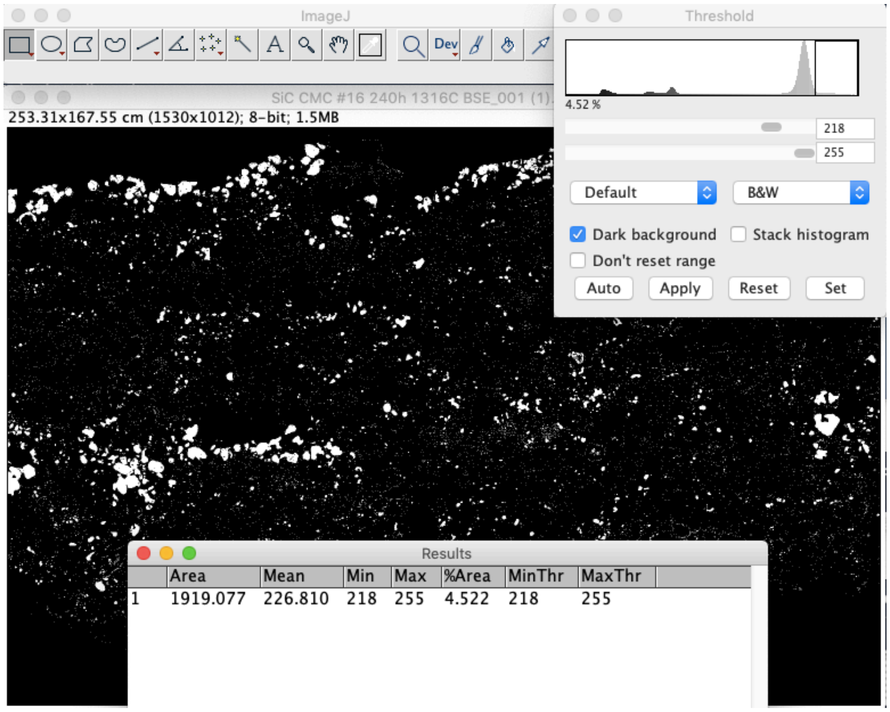

SiC CMC #16 240h 1316C BSE_001 (1).

253.31x167.55 cm (1530x1012); 8-bit; 1.5MB

4.52 %

218

255

Default

B&W

☑ Dark background

☐ Stack histogram

☐ Don't reset range

	Area	Mean	Min	Max	%Area	MinThr	MaxThr
1	1919.077	226.810	218	255	4.522	218	255

Appendix F| TDTR Characterization + Additional Raman Spectral Analysis of α-Cristobalite TGOs Formed on Specimen Exposed for 240h at 1316°C

Along with the temperature dependent Raman data presented in Ch.5 of this dissertation (Figure 5.6), additional Raman spectral data collected from a TGO formed after exposure to ~2.5 mg/cm^2 of Na_2SO_4 for 240h at 1316°C is seen in Figure F.1. Five spectral acquisitions were taken from different regions of the TGO of this specimen, seen in Figure F.1a), while the reference patterns for $Yb_2Si_2O_7$, α-cristobalite and the Si bond coat phases can be seen in Figure F.1b) The five spectra collected from the TGO have peaks belonging to all three phases in the coating system. Peaks at 113, 229, 277, and 788 cm^{-1} all belong to α-cristobalite, peaks at 145, 486, 669, 924 and 953 cm^{-1} belong to $Yb_2Si_2O_7$, while the single peak at 516 cm^{-1} belongs to α-cristobalite. These additional Raman spectra indicate that the entire TGO formed after exposure for 240h at 1316°C is likely α-cristobalite. The additional peaks are generated from the surrounding layers due to laser beam interaction volume exceeding the TGO. The same collection settings as described in the experimental section of Ch.5 was used for spectral acquisition for the Raman spectra reported in this appendix. Additionally, the spectrum from Spot 1 in Figure F.1a) is the same spectrum reported in Figure 5.6 in Ch.5 of this dissertation.

Another characterization technique known as time-domain reflectance (TDTR) was also used for phase determination of the TGO formed on the same specimen exposed for 240h at 1316°C. TDTR is an optical pump-probe technique used to measure the thermal properties of materials, including thermal conductivity. A detailed description this technique is presented in a comprehensive literature review by Braun et al.[1] The technique used in this appendix was developed by the ExSite (Experimental and Simulations in Thermal Engineering) Lab in the Mechanical Engineering Department at UVA. Prior to measurement, a mirror-finish, polished to a 50 nm colloidal

SiO_2 suspension, was applied to the specimen surface. A region around the TGO was nano-indented to help identify later during thermal mapping measurement. TDTR measurement spatially determined the thermal conductivity over a 80 μm x 100 μm region of the $Yb_2Si_2O_7$ topcoat + Si bond coat interface. An SEM image of the area probed in the $Yb_2Si_2O_7$ topcoat + Si bond coat EBC system and corresponding thermal conductivity can be seen in Figure F.2. Sadly, due to delamination cracking of the TGO from the Si bond coat and porosity build-up between the topcoat and TGO, mapping between the SEM image in Figure F.2b) and the corresponding thermal map in Figure F.2c) the layer is difficult to see. However, the corresponding thermal conductivity map indicates the region around the TGO has a thermal conductivity of ~2.6-2.7 W/mK indicated by the bright green color. Previous work by Olson et al. measured the thermal conductivity of surface nucleated cristobalite from a specimen of devitrified fused quartz after exposure in steam at 1316°C using TDTR. TDTR on the devitrified α-cristobalite regions of the fused quartz sample determined a thermal conductivity value of 2.69 W/mK. The value determined from the TGO on this specimen and that published by Olson et al. are nearly identical and are thus in good agreement. This was the only specimen whose TGO was thicker than the ~1-5 μm spatial resolution limit of the TDTR system. Thus, electron diffraction, laser raman spectroscopy, and TDTR were all used to confirm the TGO formed on a specimen exposed to ~2.5 mg/cm^2 of Na_2SO_4 for 240h at 1316°C was α-cristobalite.

Note: I would like to thank Hans Olson for all of the thermal conductivity measurements and data analysis and Dr. John Gaskins for the nano-indentation help!

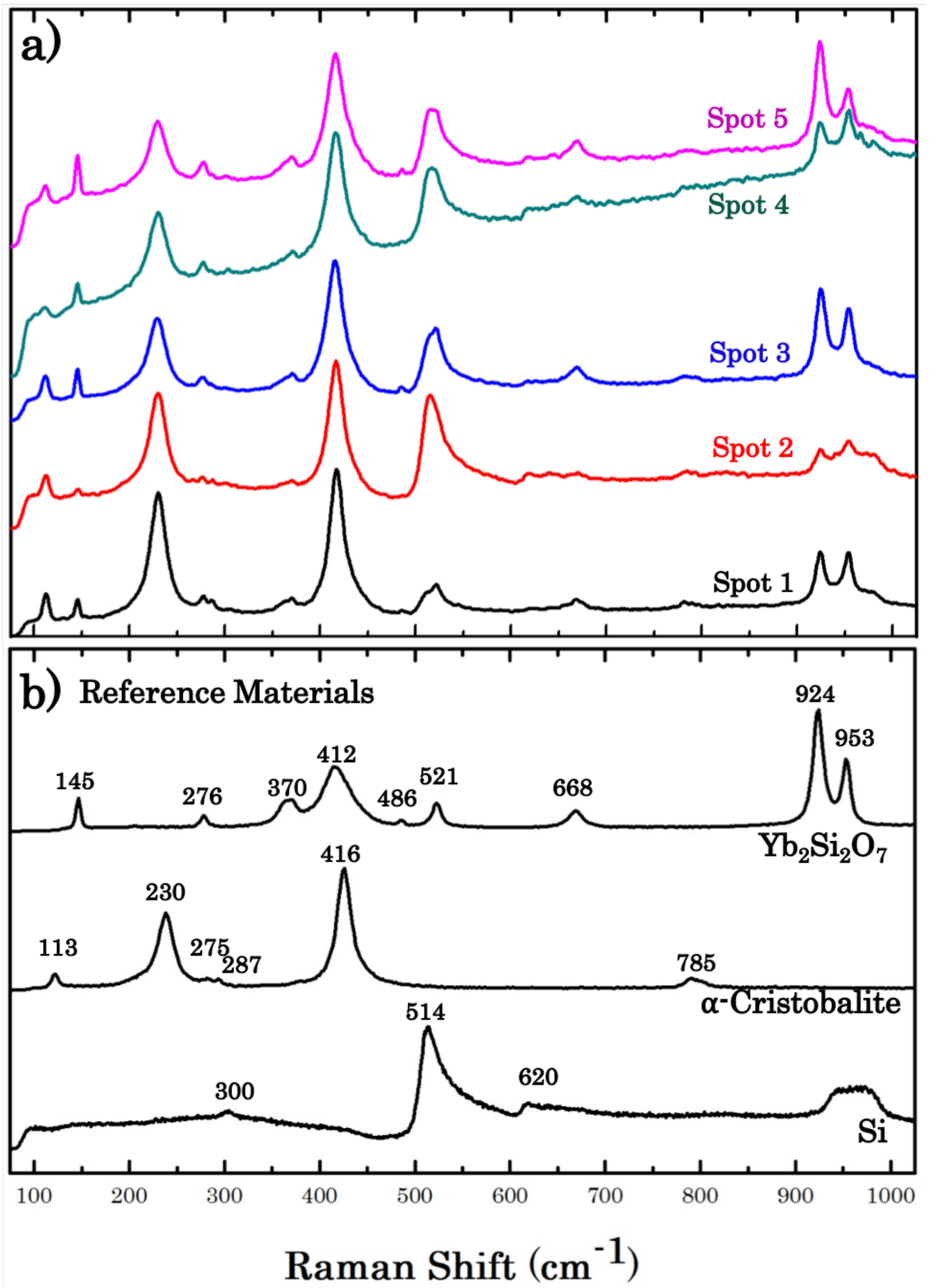

Figure F.1. a) Raman spectra collected from the TGO and b) reference patterns for $Yb_2Si_2O_7$, α-cristobalite, and Si bond coat from a $Yb_2Si_2O_7$ topcoat-Si bond coat specimen after exposure to ~2.5 mg/cm^2 of Na_2SO_4 for 240h at 1316°C in a gaseous 0.1% SO_2-O_2 environment.

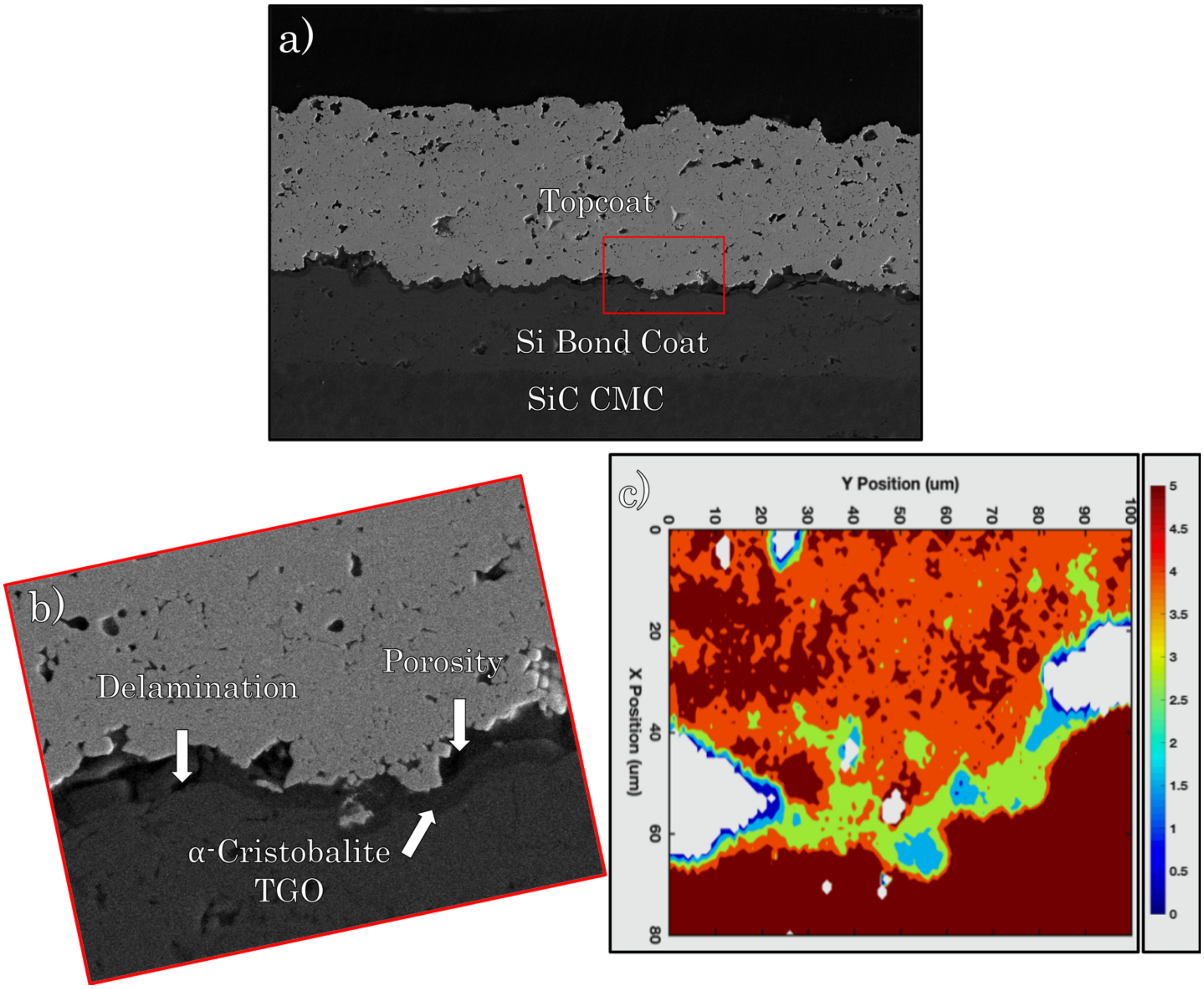

Figure F.2. a) Backscattered SEM image of the $Yb_2Si_2O_7$ topcoat- Si bond coat SiC CMC specimen, b)higher magnification SEM image and c) corresponding thermal conductivity map collected using TDTR system for the $Yb_2Si_2O_7$ topcoat-Si bond coat interface of a specimen after exposure to ~2.5 mg/cm^2 of Na_2SO_4 for 240h at 1316°C in a gaseous 0.1% SO_2-O_2 environment. The thermal conductivity map scale bar is in units of W/mK.

References

1. Braun JL, Olson DH, Gaskins JT, Hopkins PE. A steady-state thermoreflectance method to measure thermal conductivity. *Rev Sci Instrum*. 2019;90(2):024905.
2. Olson DH, Gaskins JT, Tomko JA, *et al.* Local thermal conductivity measurements to determine the fraction of α-cristobalite in thermally grown oxides for aerospace applications. *Scr Mater*. 2020;177:214–217.

Appendix G | Explanation of Dual Beam FIB-SEM Sample Preparation for TEM + Electron Diffraction and Examples of Ga^+ Ion Beam Damage to Crystalline SiO_2 TGO

Extensive TEM imaging and electron diffraction work was performed to determine the crystal structure of the TGO formed between the $Yb_2Si_2O_7$ topcoat-Si bond coat during exposure between 1-240h at 1316°C. The results of this structural characterization are explained in great detail in Ch.5 of this dissertation. Sample preparation for TEM imaging and electron diffraction was performed using a FEI Helios Dual-Beam FIB-SEM. This appendix discusses the (i) general sample preparation methods and (ii) Ga^+ ion beam amorphization to the α-cristobalite TGO during ion milling.

Before any ion milling could be performed, a thin conductive Au-Pd conductive coating was deposited onto specimen surfaces to prevent charging. With the exception of the Si bond coat, the TGO and topcoat are highly non-conductive materials and easily charge, making consistent Pt deposition and ion milling nearly impossible. An example of an area that was used for imaging and diffraction before ion milling occurred can be seen in Figure G.1. After a region of interest was Pt-coated, a protective Pt layer was deposited onto the surface of all specimens to prevent damage to sample surfaces. All Pt layer were deposited across the topcoat-TGO-Si bond coat layers, and were generally several microns thick. Once the Pt layer was deposited, an area several microns away from the coated area was milled inwards towards the Pt covered region, which can be seen in Figure G.2. The other side of the Pt covered region was then similarly milled inwards, which can be seen in Figure G.3. The sample was tilted to 52.5°, and a J-cut or undercut was performed to mill away the bottom of the sample. Only a small portion of the milled region was left attached to the specimen after this step. A needle was then precision inserted next to the partially milled region and Pt was deposited to attach the partially milled region to the needle. The small portion still connecting the milled region to the specimen was milled away, and the sample was *in-situ* lifted out from the specimen and transferred over to a copper (Cu) multi-sample holder within the chamber. The lifted-out sample was placed inside in one of the sample holding regions within the Cu sample holder, and Pt was then deposited to secure the specimen to the Cu sample-holder. The Cu sample holder was filled with multiple specimens and a higher magnification image of a region of the Cu sample holder filled with a specimen can be seen in Figures G.4 and G.5. This sample preparation process was repeated for all specimens analyzed using TEM and electron diffraction. A region of the topcoat-Si bond coat after exposure to Na_2SO_4 for 240h at 1316°C and before and after Pt deposition and ion milling can be seen in Figure E.6a).

As mentioned in Ch.5 of this dissertation, many samples were prepared for TEM imaging and electron diffraction using FIB-SEM. Many samples per experimental condition were prepared for diffraction to confirm if the entire TGO was crystalline. However, after preparing several samples for microscopy and diffraction, it was discovered partial and sometimes even complete Ga^+ ion beam amorphization to the crystalline α-cristobalite TGO occurred. Examples of Ga^+ ion beam damage to samples exposed to Na_2SO_4 between 24h-240h at 1316°C in a gaseous 0.1% SO_2-O_2 with thin Pt layers can be seen in Figures G.7-G.9. The specimen exposed for 24h and 96h underwent partial amorphization, as denoted by the dashed outline region, while the specimen exposed for 240h underwent full amorphization except for a small region at the bottom of the image.

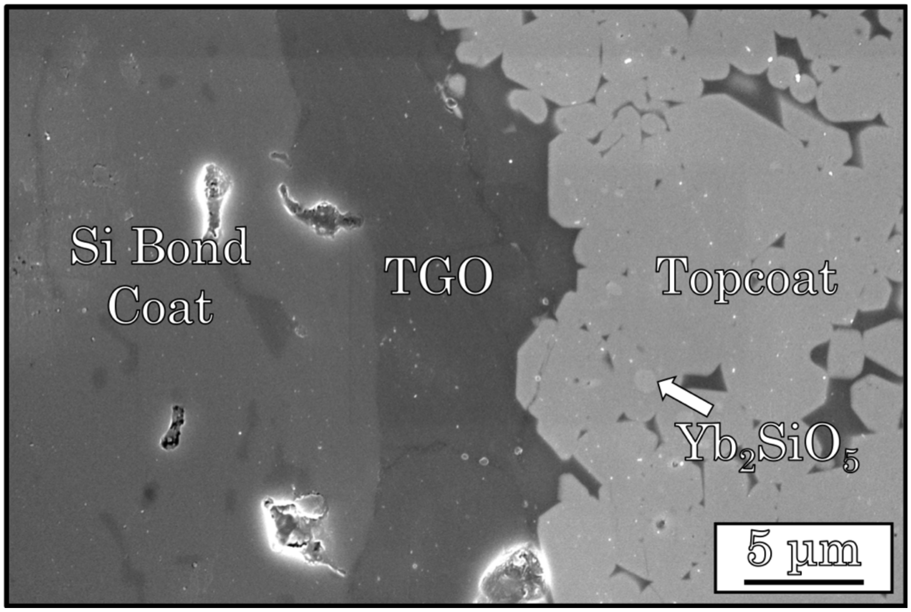

Figure G.1. SEM image showing the topcoat-Si bond coat interface after exposure to ~ 2.5 mg/cm^2 of Na_2SO_4 for 240h at 1316°C in a gaseous 0.1% SO_2-O_2 environment.

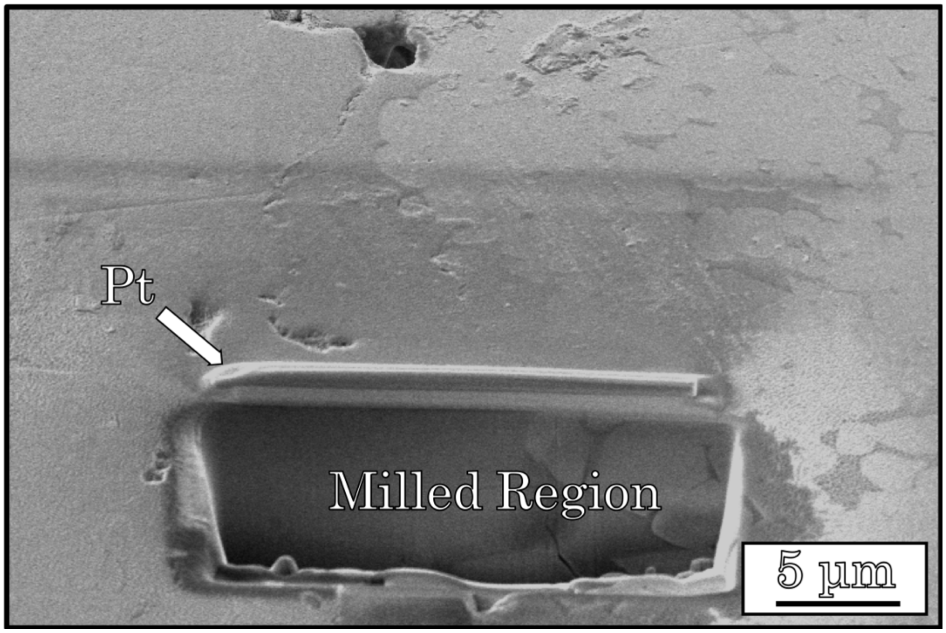

Figure G.2. SEM image showing the topcoat-Si bond coat interface with a surface deposited Pt layer with one side ion milled away.

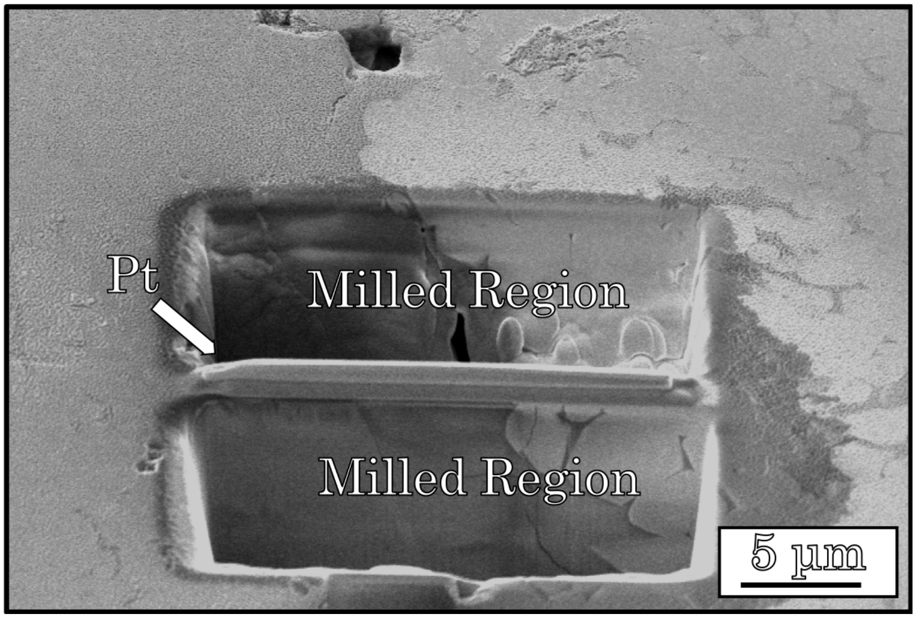

Figure G.3. SEM image showing the topcoat-Si bond coat interface with a surface deposited Pt layer with two sides ion milled away.

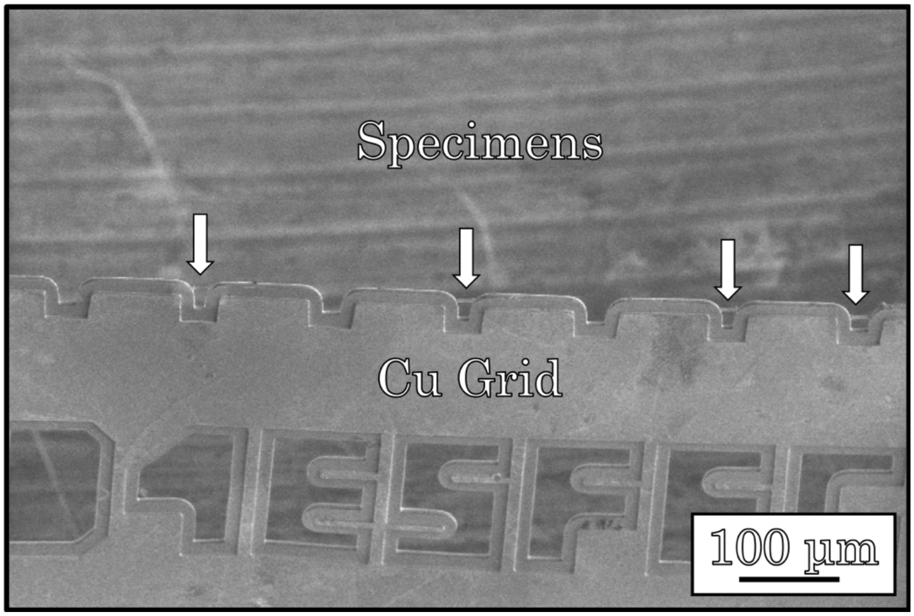

Figure G.4. SEM image showing the Cu grid sample holder filled with several milled samples removed from topcoat specimens.

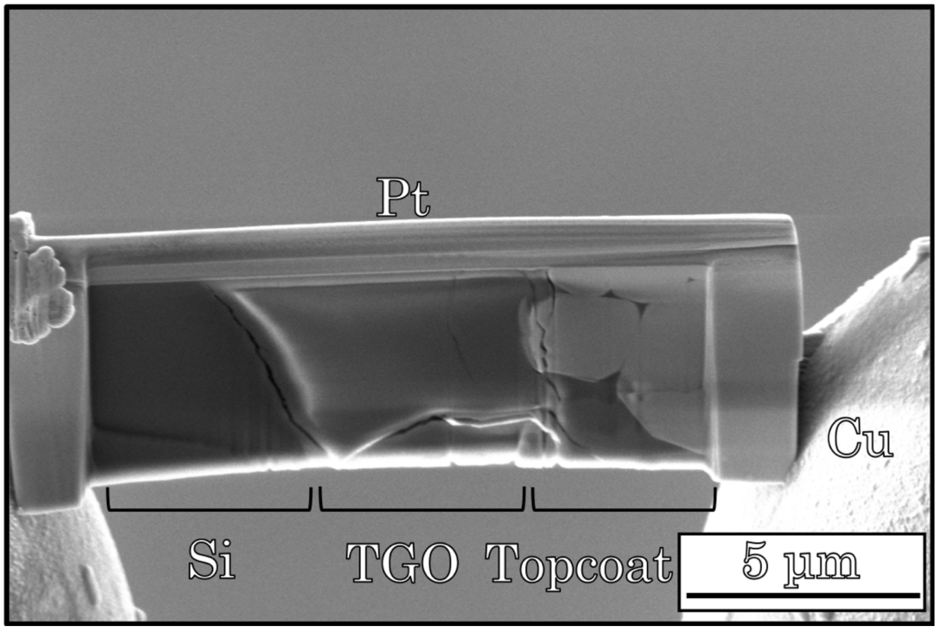

Figure G.5. A SEM image showing inside a region of the Cu multi-sample holder filled with an ion milled sample from the topcoat-Si bond coat interface of a specimen after exposure to ~2.5 mg/cm^2 of Na_2SO_4 for 240h at 1316°C in a gaseous 0.1% SO_2-O_2 environment.

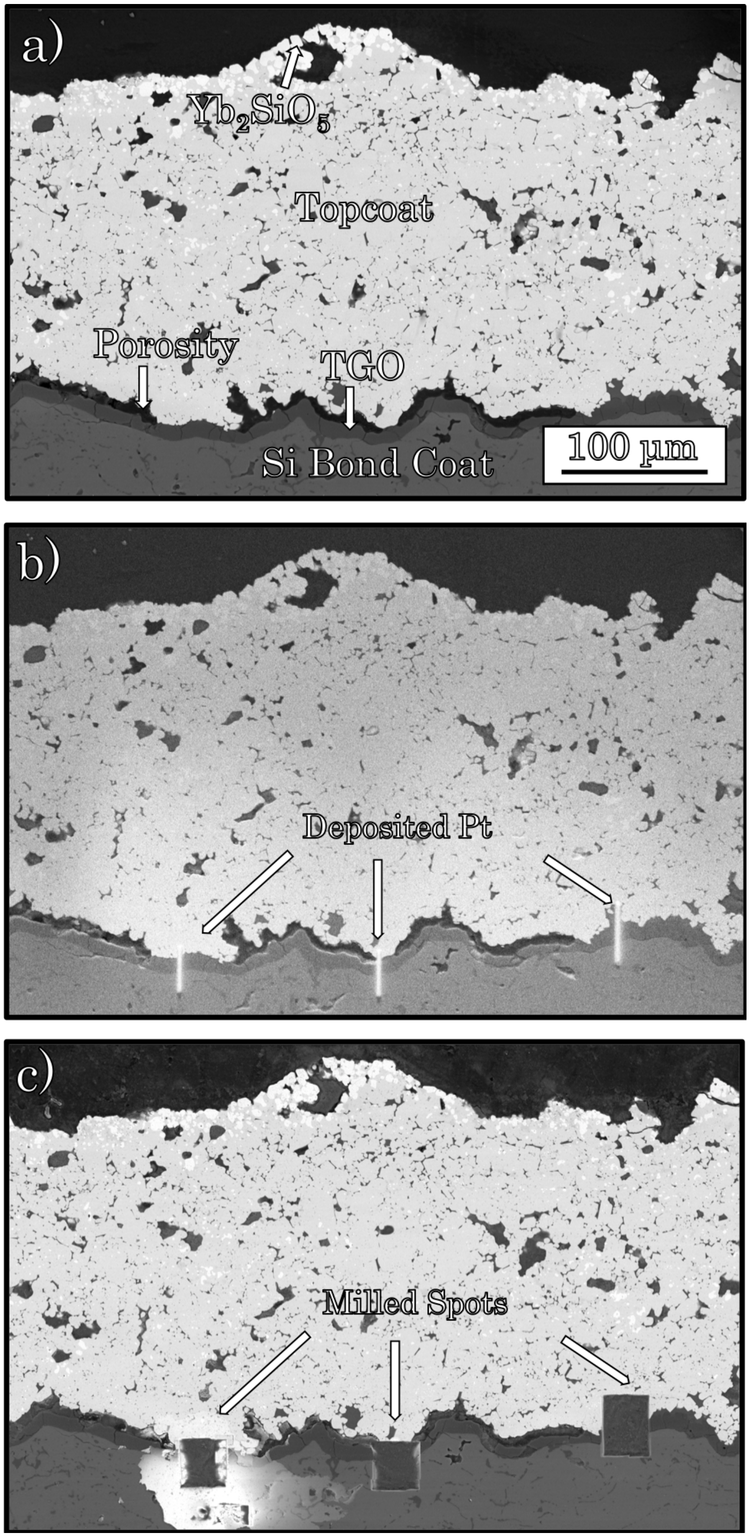

Figure G.6. SEM images showing the topcoat-Si bond coat interface a) after exposure to ~2.5 mg/cm^2 for 240h at 1316°C in gaseous 0.1% SO_2-O_2 environment and the same area after b) Pt deposition and c) ion milling

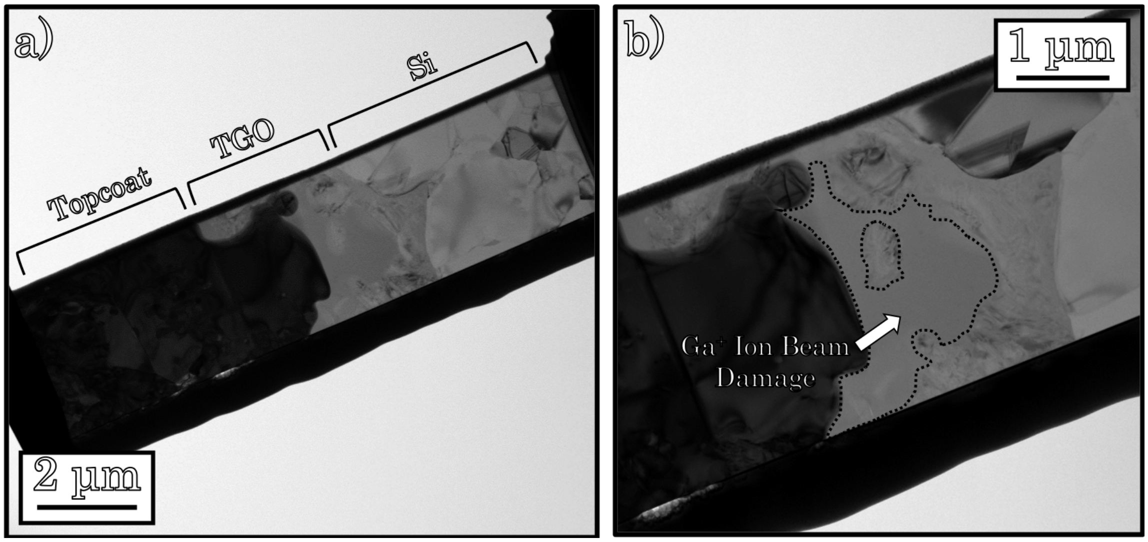

Figure G.7. a) TEM image of the $Yb_2Si_2O_7$ topcoat-Si bond coat interface after exposure to ~2.5 mg/cm^2 of Na_2SO_4 for 24h at 1316°C in a gaseous 0.1% SO_2-O_2 environment. b) Ga ion beam damage can be seen in the black-outlined region.

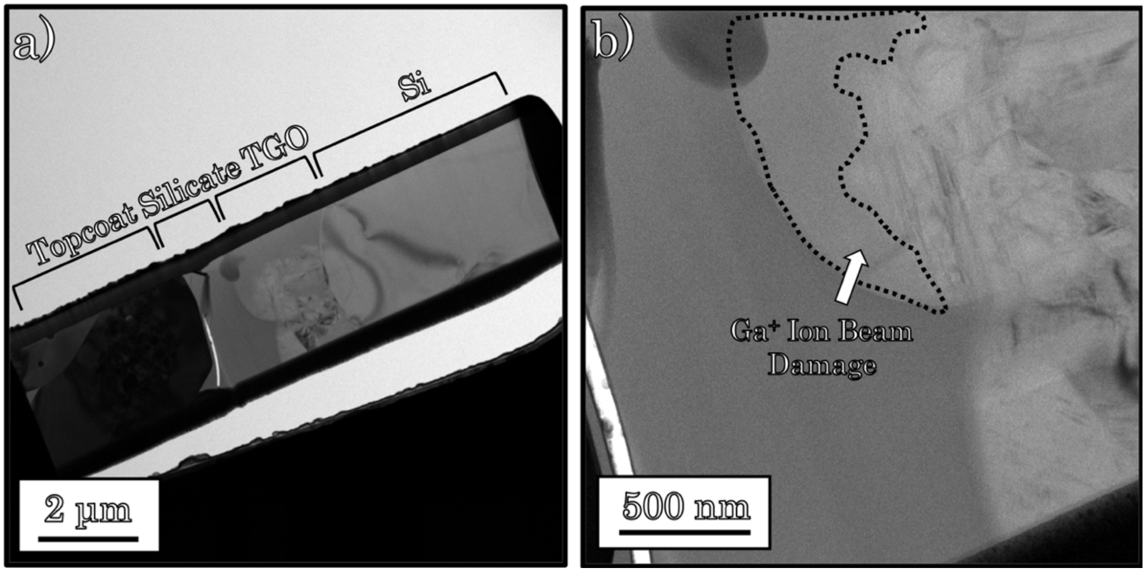

Figure G.8 a) TEM image of the $Yb_2Si_2O_7$ topcoat-Si bond coat interface after exposure to ~2.5 mg/cm^2 of Na_2SO_4 for 96h at 1316°C in a gaseous 0.1% SO_2-O_2 environment. The TGO is highly crystalline except near the top of the image, which can be seen at b) higher magnification in the area outline by the black-dashed region.

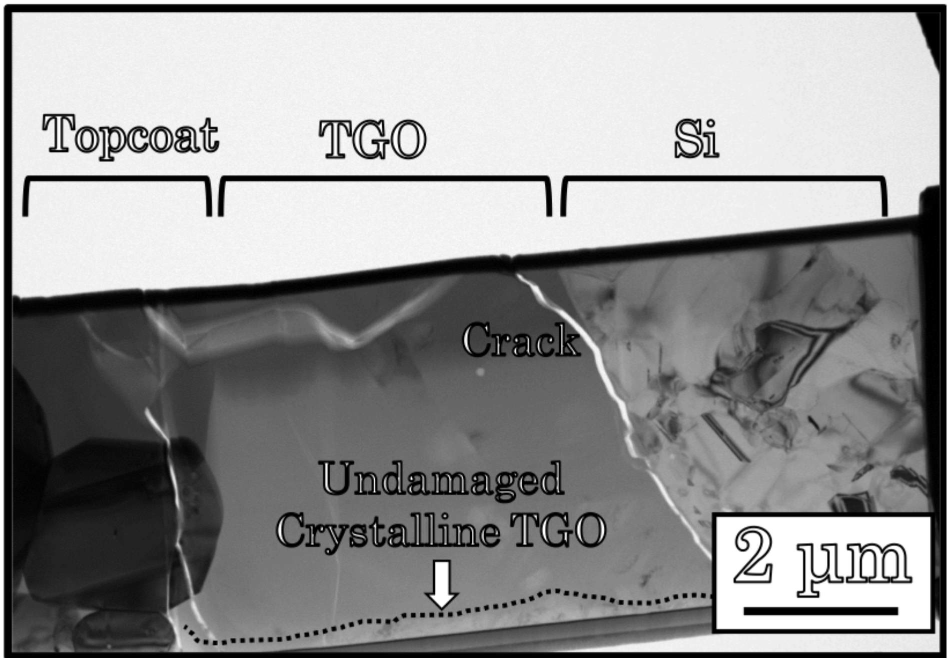

Figure G.9. TEM image of the $Yb_2Si_2O_7$ topcoat-Si bond coat interface after exposure to ~2.5 mg/cm^2 of Na_2SO_4 for 240h at 1316°C in a gaseous 0.1% SO_2-O_2 environment. The TGO is completely amorphized from Ga^+ ion beam damage except for a small undamaged crystalline region near the bottom of the image.

Appendix H | Crystallographic Data For α-Cristobalite and Procedure For Indexing α-Cristobalite Electron Diffraction Patterns

It was observed in Ch.5 of this dissertation exposure to Na_2SO_4 led to the formation of a SiO_2 thermally grown oxide (TGO) between the $Yb_2Si_2O_7$ topcoat + Si bond coat due to Si bond coat oxidation. Selected area electron diffraction was used for determining the crystal structure of TGOs formed from Si bond coat oxidation, as reported in Ch.5. Crystallographic data were needed to index the diffraction pattern data. These requisite data were taken from PDF file number 00-039-1425, which can be seen tabulated in Table H.1. Single-crystal electron diffraction patterns were analyzed using ImageJ software. The multi-step procedure used for indexing is described below:

1) After loading the electron diffraction file into ImageJ and calibrating the scale bar length to number of pixels, measure the distance between the zone center (center diffraction spot) and nearest three diffraction spots. These measured values are the reciprocal inverse ($1/d_{hkl}$) interplanar spacing for the family of planes corresponding to that diffraction spot. The inverse of these values gives the real-space interplanar spacings (d_{hkl}) of the diffracted crystal. The line connecting the zone center to each diffraction spot also corresponds to a vector in reciprocal space identified as $\vec{r}_i^{\,*}$, where the subscript i denotes some arbitrary reciprocal-space vector. With the zone center taken as the vertex, take angle measurements between reciprocal-space vectors $\vec{r}_i^{\,*}$ and $\vec{r}_j^{\,*}$ along with $\vec{r}_i^{\,*}$ and $\vec{r}_k^{\,*}$. These two angle measurements suffice for indexing the entire diffraction pattern.

(hkl)	$1/d_{hkl}$ (Å^{-1})	d_{hkl} (Å)		
101	2.4754	4.0397	Lattice	Tetragonal
110	2.8452	3.5147	Space Group	$P4_12_12$
111	3.1889	3.1359	Lattice Constants	a = b = 4.973 Å, c = 6.924 Å
102	3.5197	2.8412	Unit Cell Angles	$\alpha = \beta = \gamma = 90°$
200	4.0203	2.4874		
112	4.0527	2.4675		
201	4.2704	2.3417		
211	4.9516	2.1179		
202	5.1831	1.9294		
113	5.3434	1.8715		
220	5.6848	1.7591		
004	5.7792	1.7303		
203	5.9094	1.6922		
104	6.1167	1.6349		
301	6.2028	1.6121		
213	6.2449	1.6013		
310	6.3610	1.5721		
222	6.3798	1.5675		

Table H.1. Interplanar spacings and relevant crystallographic for α-Cristobalite as listed in PDF file 00-039-1425.

2) Because α-cristobalite is the suspected phase of the TGO, comparison between measured d-spacing and tabulated d-spacing values can be made. Once the family of planes (hkl) has been identified, indexing can be performed by comparing the measured and calculated angles between reciprocal vectors. Given the tetragonal symmetry of α-cristobalite, calculated angles can be determined using Equation H.1:

$$\mathrm{Cos}\theta = \frac{\frac{h_i h_j + k_i k_j}{a^2} + \frac{l_i l_j}{c^2}}{\sqrt{\frac{h_i^2 + k_i^2}{a^2} + \frac{l_i^2}{c^2}}\sqrt{\frac{h_j^2 + k_j^2}{a^2} + \frac{l_j^2}{c^2}}} \qquad \text{(H.1)}$$

Where h_i,k_i and l_i are the miller indices for reciprocal vector d_i, h_j, k_j and l_j are the miller indices for reciprocal vector d_j, and a and c are the lattice constants for α-cristobalite listed in Table H.1. The inverse of this equation will allow for calculation of the angle θ.

3) However, this is not a straight-forward calculation, as a mixing and matching of miller indices for a pair of reciprocal vectors $\vec{r}_i^*$ and $\vec{r}_j^*$, have to be input into Equation (H.1). This mixing and matching of hkl indices occurrs until the measured angle and the calculated angle from Equation G.1 are within ~1%. An excelsheet or a program in Python/Java can be written to help automate this calculation.

4) Once matched, these correctly identified reciprocal vectors are added together (i.e. $\vec{r}_i^* + \vec{r}_j^*$, $-\vec{r}_i^* + \vec{r}_j^*{}_j$, $\vec{r}_i^* - \vec{r}_j^*$ etc.) together until all diffraction spots are indexed.

5) Take the cross-product between $\vec{r}_i^*$ and $\vec{r}_j^*$ to determine the zone axis.

6) Lastly, the dot product between each reciprocal vector and the zone axis vector is taken to ensure orthogonality. If all of the dot products are zero, then the pattern has been correctly indexed.

Worked Example:

An explanation how the diffraction patterns reported in Ch. 5 were indexed is explained using the electron diffraction pattern reported in Figure 5.7a) as an example. An unindexed diffraction pattern labeled with reciprocal vectors $\vec{r}_1^*$, $\vec{r}_2^*$, and $\vec{r}_3^*$ and the angles between reciprocal vectors $\vec{r}_1^*$ and $\vec{r}_2^*$ (θ_1), an angle between $\vec{r}_1^*$ and $\vec{r}_3^*$ (θ_2) can be seen in Figure H.1. The associated d-spacings and angles measured using ImageJ are reported in Table H.2. The d-spacing measurements indicate that these three vectors likely belong to the family of (101), (111) and (211) planes of α-cristobalite, as there is only 1% disagreement between measured and accepted values. θ_1 was measured to be 55.8°, while θ_2 was measured to be 25.7°.

Bad Match:

$$\vec{r}_1^* = (101),\ h_1 = 0,\ k_1 = 1,\ l_1 = 1$$

$$\vec{r}_2^* = (\bar{1}10),\ h_2 = -1,\ k_2 = -1,\ l_2 = 0$$

$$\mathrm{Cos}\theta_1 = \frac{\frac{h_1h_2 + k_1k_2}{a^2} + \frac{l_1l_2}{c^2}}{\sqrt{\frac{h_1^2 + k_1^2}{a^2} + \frac{l_1^2}{c^2}}\ \sqrt{\frac{h_2^2 + k_2^2}{a^2} + \frac{l_2^2}{c^2}}} = \frac{\frac{-1}{a^2}}{\sqrt{\frac{1}{a^2} + \frac{1}{c^2}}\ \sqrt{\frac{2}{a^2}}} = -0.57$$

$$\theta_1 = 125.1° \text{ (measured value of } 55.8°)$$

Without knowing the exact miller indices of $\vec{r}_1^*$ and $\vec{r}_2^*$, an initial guess was made to reveal their indices. It was believed (incorrectly) that $\vec{r}_1^*$ was (101) and $\vec{r}_2^*$ was ($\bar{1}$10). Plugging these values into Equation (H.1) and solving for θ_1 gave a value of 125.1°, which is too high. A different set of indices were picked this time.

Good Match:

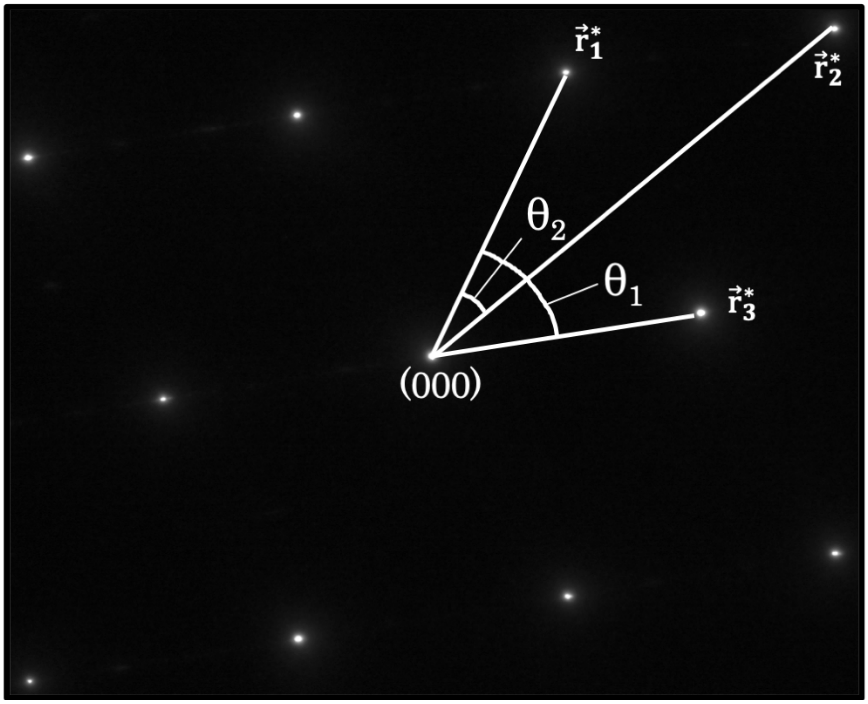

Figure H.1. Diffraction pattern from Figure 5.7a) with reciprocal vectors and angles denoted.

Vector	1/d_{hkl} ($Å^{-1}$)	d_{hkl} (Å)	Possible Planes	d_{hkl} ref. (Å)	Δ%
$\vec{r}_1^*$,	2.492	*4.013*	(101)	*4.040*	0.7
$\vec{r}_2^*$,	2.869	*3.486*	(110)	*3.515*	0.8
$\vec{r}_3^*$,	4.711	*2.123*	(211)	*2.118*	0.2

Angle	Value (°)
θ_1	55.8
θ_2	29.9

Table H.2. Raw data measured using ImageJ software from the electron diffraction pattern reported in Figure 5.7a) of Ch.5 of this dissertation.

$$\vec{r}_1^* = (101),\ h_1 = 1,\ k_1 = 0,\ l_1 = 1$$

$$\vec{r}_2^{\,*} = (110),\ h_2 = 0,\ k_2 = 1,\ l_2 = -1$$

$$\mathrm{Cos}\theta_1 = \frac{\frac{-1}{a^2} + \frac{0}{c^2}}{\sqrt{\frac{1}{a^2} + \frac{1}{c^2}}\ \sqrt{\frac{2}{a^2} + \frac{0}{c^2}}} = -0.34$$

$$\theta_1 = 54.9° \text{ (measured value of } 55.8°\text{)}$$

Thus, reciprocal vectors $\vec{r}_1^{\,*}$ and $\vec{r}_2^{\,*}$ are (101) and (110). Addition of these two vectors indicate $\vec{r}_3^{\,*}$ is (211). Plugging the $\vec{r}_1^{\,*}$ and $\vec{r}_3^{\,*}$ hkl values into Equation (H.1) determined a θ_2 value of 29.5° compared to a measured value of 29.9°. The cross-product between $\vec{r}_1^{\,*}$ and $\vec{r}_2^{\,*}$ gives a zone axis of $z = [1\bar{1}\bar{1}]$. Vectors $\vec{r}_1^{\,*}$ and $\vec{r}_2^{\,*}$ were added to index the remaining diffraction spots. The dot product of all indexed reciprocal vectors and the zone axis indicate a success attempt at indexing.

$[101]\cdot[1\bar{1}\bar{1}] = 1 + 0 - 1 = 0$	$[110]\cdot[1\bar{1}\bar{1}] = 1 - 1 + 0 = 0$
$[211]\cdot[1\bar{1}\bar{1}] = 2 - 1 - 1 = 0$	$[01\bar{1}]\cdot[1\bar{1}\bar{1}] = 0 - 1 + 1 = 0$
$[01\bar{2}]\cdot[1\bar{1}\bar{1}] = 0 + 4 - 4 = 0$	$[\bar{1}1\bar{2}]\cdot[1\bar{1}\bar{1}] = -1 - 1 + 2 = 0$
$[\bar{2}\bar{1}\bar{1}]\cdot[1\bar{1}\bar{1}] = -2 + 1 + 1 = 0$	$[\bar{1}1\bar{2}]\cdot[1\bar{1}\bar{1}] = -1 - 1 + 2 = 0$
$[0\bar{1}1]\cdot[1\bar{1}\bar{1}] = 0 + 1 - 1 = 0$	$[1\bar{1}2]\cdot[1\bar{1}\bar{1}] = 1 + 1 - 2 = 0$
$[\bar{1}0\bar{1}]\cdot[1\bar{1}\bar{1}] = -1 + 0 + 1 = 0$	

A fully indexed diffraction pattern for α-cristobalite with a zone axis of $[1\bar{1}\bar{1}]$ is seen in Figure H.2. The procedure described in this appendix allowed for easy indexing for the other diffraction patterns reported in Ch.5 of this dissertation.

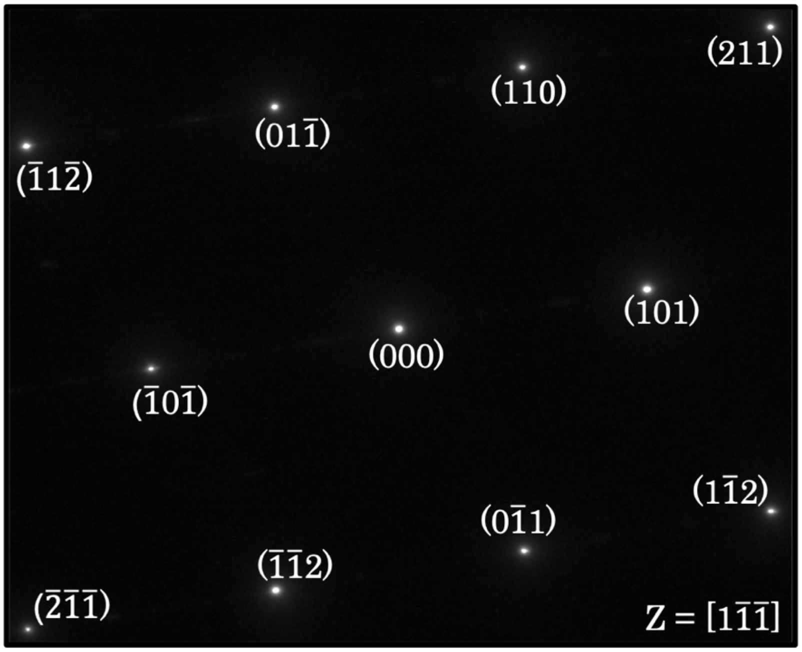

Figure H.2. Fully indexed single crystal electron diffraction pattern identifying the TGO as α-cristobalite. The same electron diffraction pattern reported in Figure 5.7a) of Ch.5 of this dissertation.

Note:

I would like to thank Dr. Helge Heinrich and my officemate and fellow classmate Eric Hoglund for assisting in electron diffraction patterns analysis. Ch.5 of this dissertation could not have happened without you. *Vielen Dank*!!!

Appendix I| SEM Images of TGOs Formed After Exposure for 240h Between 1000°C-1316°C

The structure of thermally grown SiO_2 oxides (TGOs) formed between the $Yb_2Si_2O_7$ topcoat + Si bond coat after exposure to Na_2SO_4 were presented in Ch.4 and Ch. 5 of this dissertation. The reaction of Na_2SO_4 lead to the formation of sodium silicate filled topcoat from the topcoat surface all the way down to the TGO. It was discovered from electron diffraction and laser raman spectroscopy measurement determined the TGO was α-cristobalite after exposure for 240h at temperatures between 1000°C-1316°C and also formed in less than 1h at 1316°C. This phase forms upon cooling from high temperature at which β-cristobalite is the stable phase. The β-to-α cristobalite transformation occurs between 200°C-300°C, and is associated with a high-degree of cracking. Despite the presence of this low temperature phase across all of the specimens analyzed, significant vertical cracking in the TGO and delamination from the Si bond coat was only observed in specimens exposed for 240h at 1316°C. More SEM images of the topcoat topcoat + Si bond coat interface after exposure for 240h at temperatures between 1000°C-1316°C can be seen in Figures I.1-4. SEM images after exposure between times of 1h-96h at 1316°C can be seen in Figures I.5-7. As seen in these Figures, there is hardly any observable cracking in the TGO even at the 2500x magnification used.

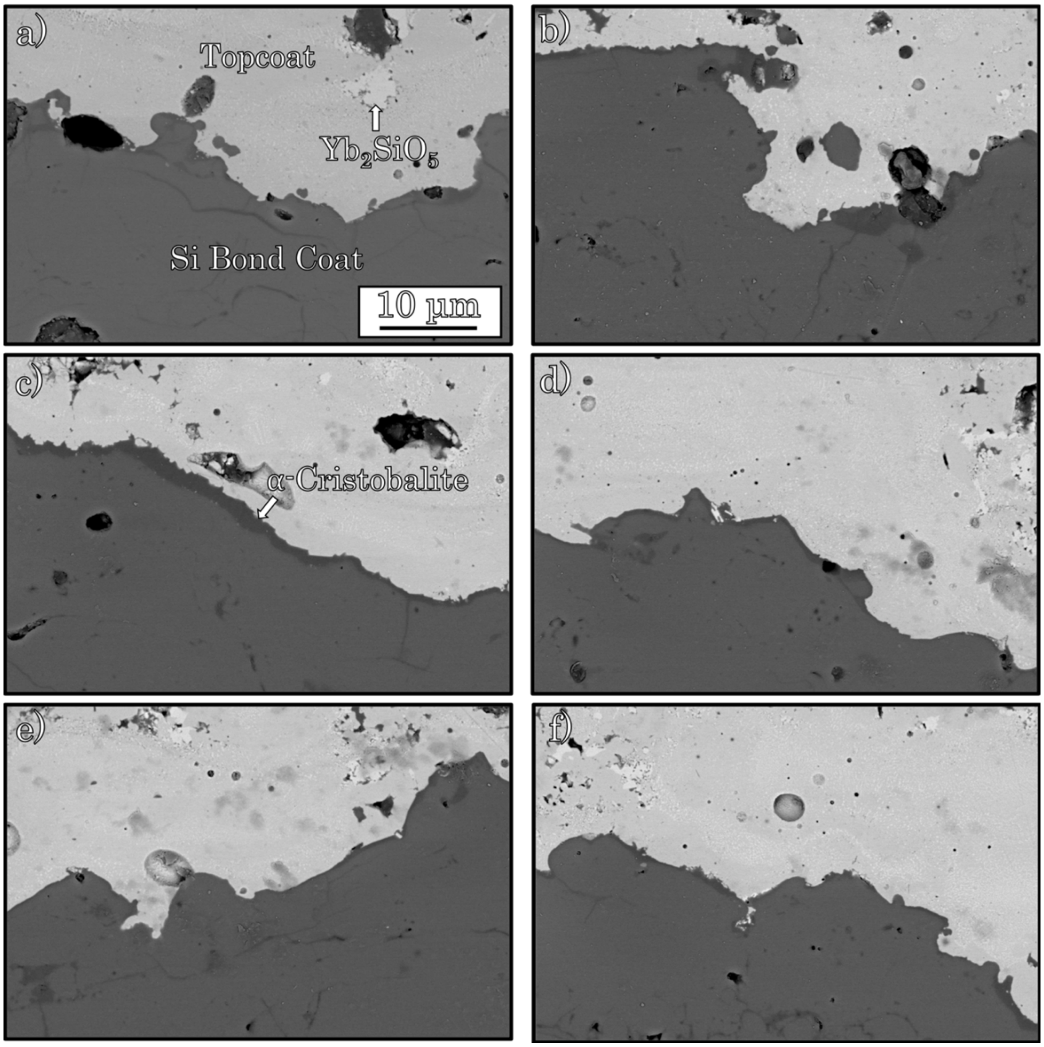

Figure I.1. Multiple SEM images of the topcoat-Si bond coat interface after exposure to ~2.5 mg/cm^2 of Na_2SO_4 for 240h at 1000°C in a gaseous 0.1% SO_2-O_2 gaseous.

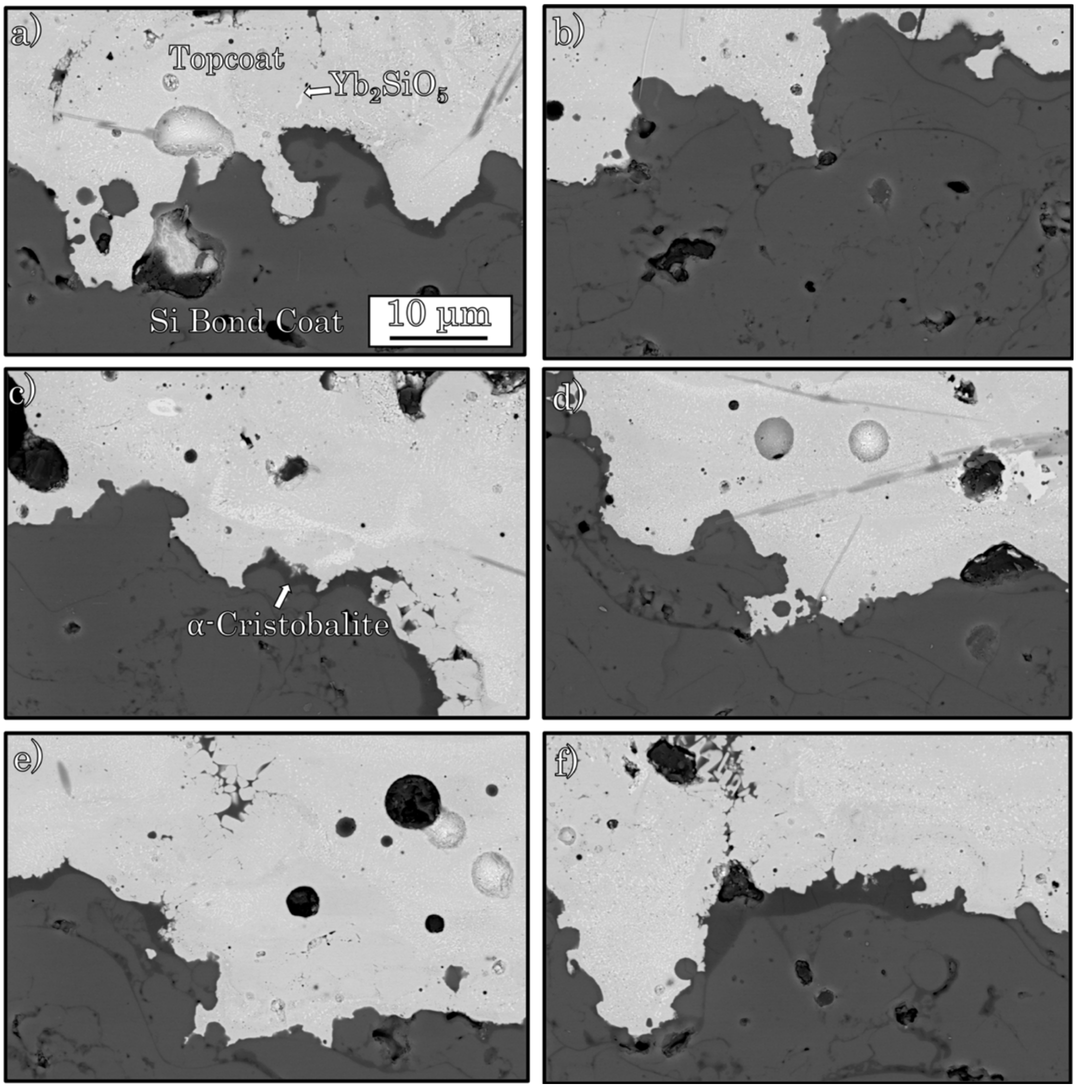

Figure I.2. Multiple SEM images of the topcoat-Si bond coat interface after exposure to ~2.5 mg/cm^2 of Na_2SO_4 for 240h at 1100°C in a gaseous 0.1% SO_2-O_2 gaseous.

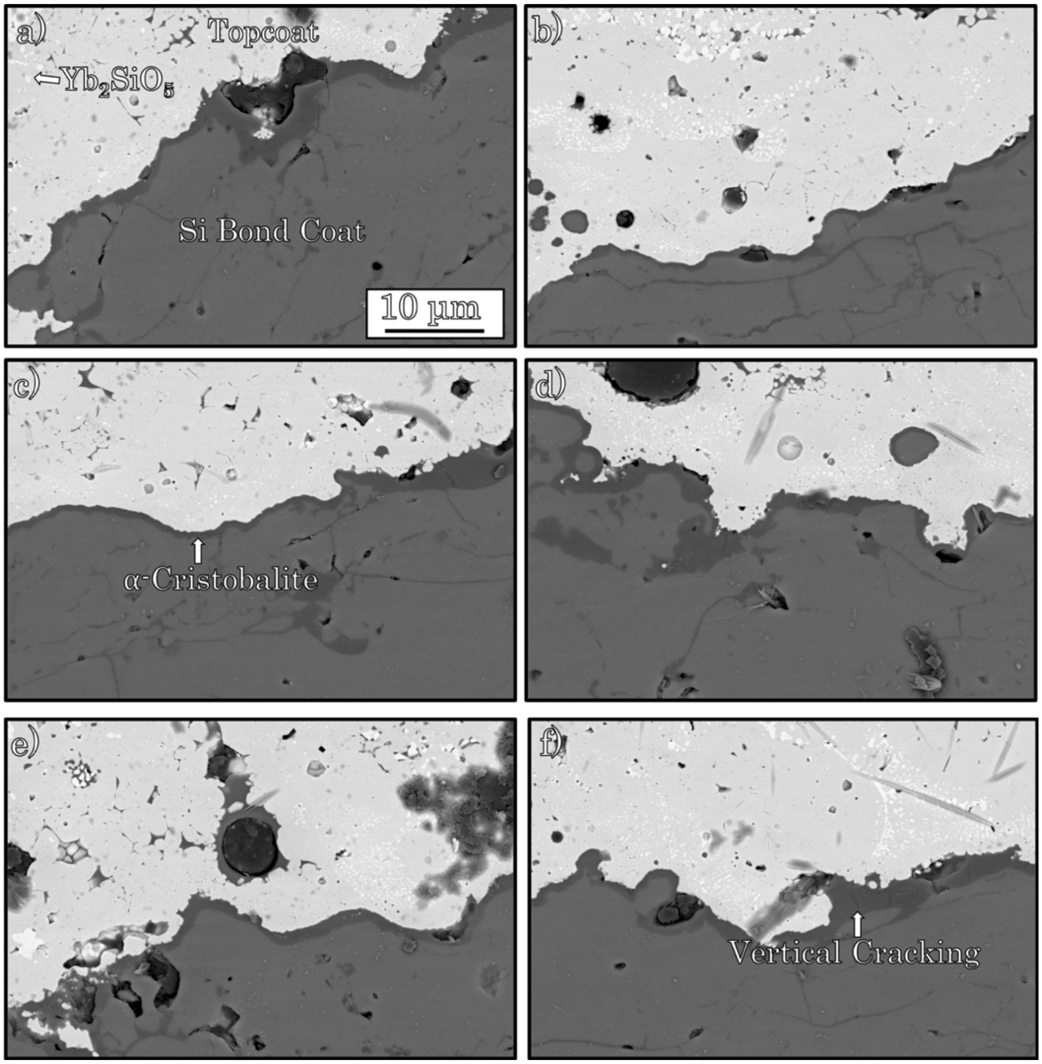

Figure I.3. Multiple SEM images of the topcoat-Si bond coat interface after exposure to ~2.5 mg/cm^2 of Na_2SO_4 for 240h at 1200°C in a gaseous 0.1% SO_2-O_2 gaseous.

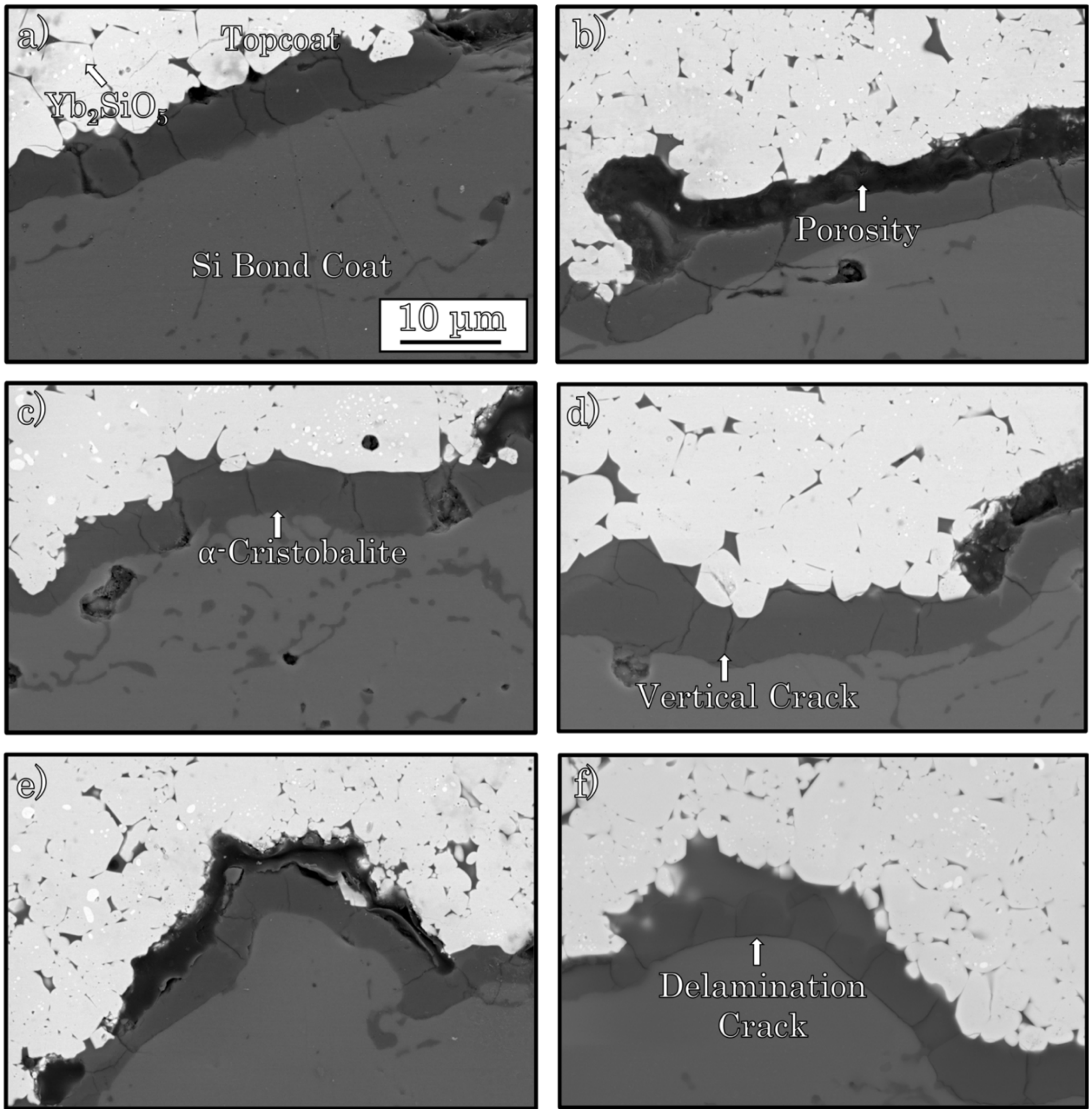

Figure I.4. Multiple SEM images of the topcoat-Si bond coat interface after exposure to ~2.5 mg/cm^2 of Na_2SO_4 for 240h at 1316°C in a gaseous 0.1% SO_2-O_2 gaseous.

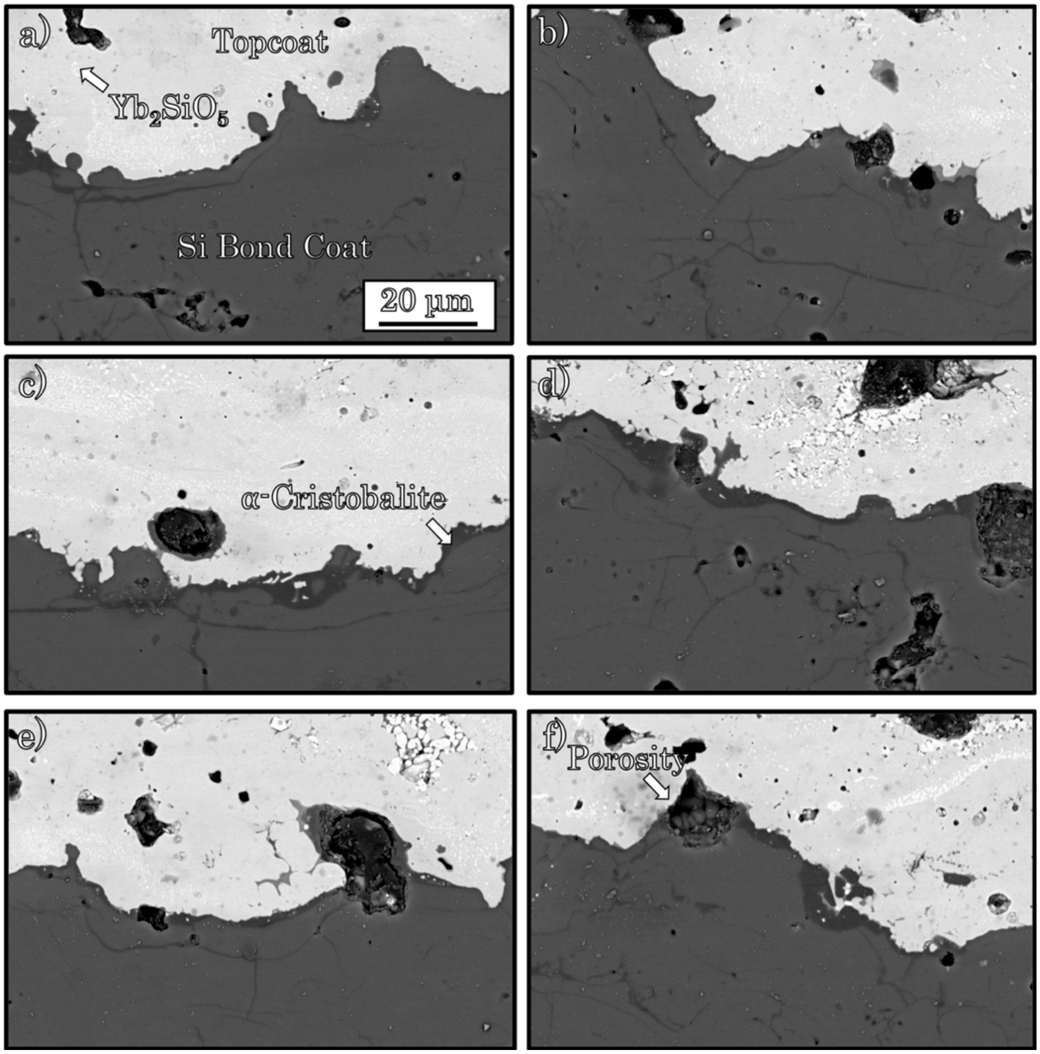

Figure I.5. Multiple SEM images of the topcoat-Si bond coat interface after exposure to ~2.5 mg/cm^2 of Na_2SO_4 for 1h at 1316°C in a gaseous 0.1% SO_2-O_2 gaseous.

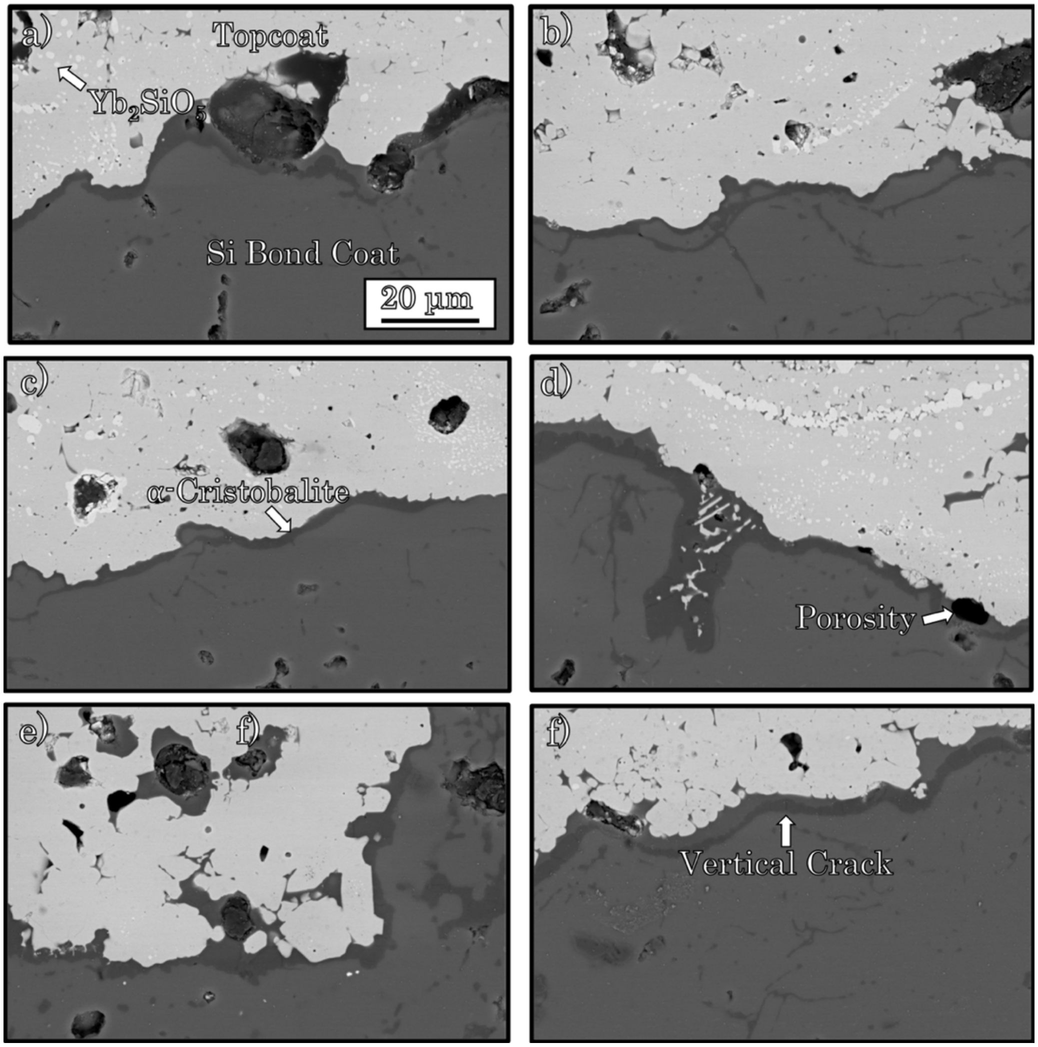

Figure I.6. Multiple SEM images of the topcoat-Si bond coat interface after exposure to ~2.5 mg/cm^2 of Na_2SO_4 for 24h at 1316°C in a gaseous 0.1% SO_2-O_2 gaseous.

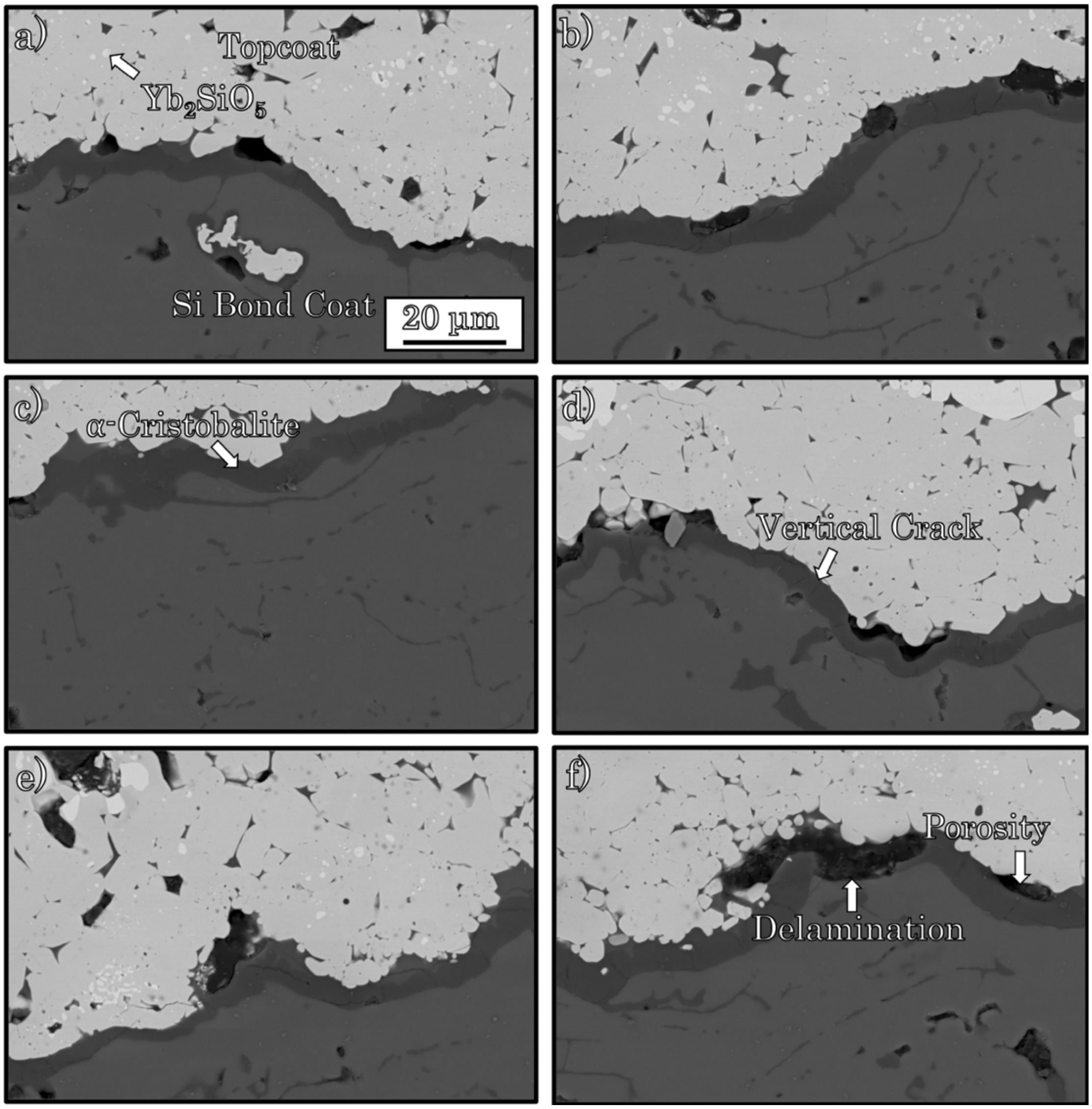

Figure I.7. Multiple SEM images of the topcoat-Si bond coat interface after exposure to ~2.5 mg/cm^2 of Na_2SO_4 for 96h at 1316°C in a gaseous 0.1% SO_2-O_2 gaseous.